ISSN 2518-7198 (Print)
ISSN 2663-5089 (Online)

BULLETIN
OF THE KARAGANDA UNIVERSITY

PHYSICS
Series

№ 3(111)/2023

Special issue

Functional Nanomaterials and Alternative Energy

Guest Editor:
Associate Professor, PhD Ng Annie

ISSN 2663-5089 (Online)
ISSN-L 2518-7198 (Print)
Индексі 74616
Индекс 74616

ҚАРАҒАНДЫ УНИВЕРСИТЕТІНІҢ ХАБАРШЫСЫ

ВЕСТНИК КАРАГАНДИНСКОГО УНИВЕРСИТЕТА

BULLETIN OF THE KARAGANDA UNIVERSITY

ФИЗИКА сериясы

Серия ФИЗИКА

PHYSICS Series

№ 3(111)/2023

Арнайы шығарылым / Специальный выпуск / Special Issue

Функционалды наноматериалдар және баламалы энергетика
Функциональные наноматериалы и альтернативная энергетика
Functional Nanomaterials and Alternative Energy

Шілде–тамыз–қыркүйек
30 қыркүйек 2023 ж.
Июль–август–сентябрь
30 сентября 2023 г.
July–August–September
July 30th, 2023

1996 жылдан бастап шығады
Издается с 1996 года
Founded in 1996

Жылына 4 рет шығады
Выходит 4 раза в год
Published 4 times a year

Қарағанды, 2023
Караганда, 2023
Karaganda, 2023

Редакцияның мекенжайы: 100024, Қазақстан, Қарағанды қ., Университет к-сі, 28
Тел.: +7 701 531 4758; факс: (7212) 35-63-98.
E-mail: vestnikku@gmail.com; karabekova71@mail.ru
Сайты: physics-vestnik.ksu.kz

Қарағанды университетінің хабаршысы. «Физика» сериясы.
ISSN-L 2518-7198 (Print). ISSN 2663-5089 (Online).

Меншік иесі: «Академик Е.А. Бөкетов атындағы Қарағанды университеті» КЕАҚ.

Қазақстан Республикасы Ақпарат және қоғамдық даму министрлігімен тіркелген. 30.09.2020 ж. № KZ38VPY00027378 қайта есепке қою туралы куәлігі.

Басуға 29.09.2023 ж. қол қойылды. Пішімі 60×84 1/8. Қағазы офсеттік. Көлемі 22,75 б.т. Таралымы 200 дана. Бағасы келісім бойынша. Тапсырыс № 87.

«Акад. Е.А. Бөкетов ат. Қарағанды ун-ті» КЕАҚ баспасының баспаханасында басылып шықты.
100024, Қазақстан, Қарағанды қ., Университет к-сі, 28. Тел. (7212) 35-63-16. E-mail: izd_kargu@mail.ru

Адрес редакции: 100024, Казахстан, г. Караганда, ул. Университетская, 28
Тел.: +7 701 531 4758. Факс: (7212) 35–63–98.
E-mail: vestnikku@gmail.com; karabekova71@mail.ru
Сайт: physics-vestnik.ksu.kz

Вестник Карагандинского университета. Серия «Физика».
ISSN-L 2518-7198 (Print). ISSN 2663-5089 (Online).

Собственник: НАО «Карагандинский университет имени академика Е.А. Букетова».

Зарегистрирован Министерством информации и общественного развития Республики Казахстан. Свидетельство о постановке на переучет № KZ38VPY00027378 от 30.09.2020 г.

Подписано в печать 29.09.2023 г. Формат 60×84 1/8. Бумага офсетная. Объем 22,75 п.л. Тираж 200 экз. Цена договорная. Заказ № 87.

Отпечатано в типографии издательства НАО «Карагандинский университет им. акад. Е.А. Букетова». 100024, Казахстан, г. Караганда, ул. Университетская, 28. Тел.(7212) 35-63-16. E-mail:izd_kargu@mail.ru

Postal address: 28, University Str., 100024, Karaganda, Kazakhstan
Tel.: +7 701 531 4758; Fax: (7212) 35-63-98.
E-mail: vestnikku@gmail.com; karabekova71@mail.ru
Web-site: physics-vestnik.ksu.kz

Bulletin of the Karaganda University. "Physics" Series.
ISSN-L 2518-7198 (Print). ISSN 2663-5089 (Online).

Proprietary: NLC "Karagandy University of the name of academician E.A. Buketov".

Registered by the Ministry of Information and Social Development of the Republic of Kazakhstan. Rediscount certificate No. KZ38VPY00027378 dated 30.09.2020.

Signed in print 29.09.2023. Format 60×84 1/8. Offset paper. Volume 22,75 p.sh. Circulation 200 copies. Price upon request. Order № 87.

Printed in the Publishing house of NLC "Karagandy University of the name of acad. E.A. Buketov".
28, University Str., Karaganda, 100024, Kazakhstan. Tel. (7212) 35-63-16. E-mail: izd_kargu@mail.ru

МАЗМҰНЫ — СОДЕРЖАНИЕ — CONTENT

DOI 10.31489/2023PH3/6-15

UDC: 620.91

T. Serikova[1,2], G. Bizhanova[1,3], Hanlin Hu[4], Annie Ng[1,3,*]

[1] *Department of Electrical and Computer Engineering, School of Engineering and Digital Sciences, Nazarbayev University, Astana, Kazakhstan;*
[2] *Department of Mathematics, School of Science and Humanities, Nazarbayev University, Astana, Kazakhstan;*
[3] *National Laboratory of Astana, Nazarbayev University, Astana, Kazakhstan;*
[4]*Hoffmann Institute of Advanced Materials Postdoctoral Innovation Practice Base Shenzhen Polytechnic Nanshan District, Shenzhen, P.R. China*
(e-mail: annie.ng@nu.edu.kz)

Recent UpdateonPerovskite/Organic Tandem Solar Cells

The emergence of multiple-junction photovoltaics (PVs) has presented a remarkable opportunity to overcome the Shockley-Queisser limit of single-junction solar cells. Recently, perovskite solar cells (PSCs) and organic photovoltaics (OPVs) are two of the most promising new-generation PVs, which have gained widespread attention in the PV community due to their exceptional rapid growth in their power conversion efficiencies (PCEs). Combining PSCs and OPVs in tandem structures offers numerous advantages, such as the ability to tune the bandgap of absorbers to regulate the absorption bands and enhance transparency. The use of thin-film technology ensures that the devices are lightweight and flexible, which is particularly advantageous for certain applications. Furthermore, both PSCs and OPVs are low-cost, making them attractive for large-scale deployment in the future. These advantages will make PSC/OPV tandem devices promising for applications beyond traditional silicon-based PVs. This review provides an up-to-date account on the recent progress of PSC/OPV tandem PVs. The state-of-the-art fabrication techniques and material engineering on the properties of PSC and OPV sub cells as well as their functional layers are discussed. A perspective guidance is also given to direct the future development of this type of tandem PVs. This paper provides an insight into the development of PSC/OPV tandem PVs, providing researchers with a roadmap to advance this technology further and unlock its full potential in the field of renewable energy.

Keywords: Perovskites, organic photovoltaics, tandem solar cells, device engineering.

Introduction

Due to the high energy demands and the risks caused by global warming, developing alternative energy sources is essential to address these urgent challenges. Solar energy is a promising renewable source of energy, which is safe, cost-effective and clean. In order to utilize solar energy, photovoltaics (PVs) are the key device for converting the solar energy to electrical energy. The history of the PV effect was discovered by the French physicist, Alexandre-Edmond Becquerel in 1839. The first practical application of photovoltaic (PV) technology was realized in 1954 with the development of the first silicon (Si) solar cell, which achieved a power conversion efficiency (PCE) of 6 % [1]. Nowadays PV technologies are classified into three generations. PV cells based on single-junction silicon wafers (monocrystalline and multicrystalline) and gallium arsenide (GaAs) are considered 1st generation PV technologies. Recently, the PCE of the single-junction GaAs and crystalline Si PV have reached 26.8 % and 29.1 %, respectively [2]. The 2nd generation of PV technologies utilizes thin-film materials such as amorphous silicon (a-Si), cadmium telluride (CdTe), and copper indium gallium selenide (CIGS) to achieve a more cost-effective device architecture for single junction devices, while they typically have a lower PCE compared to first-generation PV technologies. Currently, the highest efficiencies of CIGS, CdTe and a-Si: H thin-film solar cells are 23.6 %, 22.1 % and 14.0 %, respectively. The 3rd generation of solar cells is based on the emerging materials such as conductive polymers, organic dyes, quantum dots (QDs) and perovskites, etc. This type of emerging PVs provides promising alternatives of conventional Si-based PVs systems, ensuring more cost-effective manufacturing processes and offering a wide range of potential applications. The certified record PCEs of emerging PVs are 25.8 %, 19.2 %, 18.1 % and 13 % for perovskite solar cells (PCSs), organic photovoltaics (OPVs), QD cells and dye-sensitized cells, respectively [2]. Among different types of third-generation PV technologies, PSCs and OPVs are currently the two most promising examples, with rapidly PCEs being recorded for both technologies. PSCs are based on perovskite materials with a chemical formula of ABX_3 (A — monovalent cations, B — divalent metal cations, and X — halogen ions). The halide perovskite materials have gained tremendous attention from researchers due to their excellent optoelectronic properties, such as

high light absorption coefficients, tunable band-gaps, long carrier diffusion lengths and carrier lifetime, as well as high carrier mobility [3]. Recently, the invention of NFAs (NFA) with a broader absorption range and tunable energy levels has also made a significant breakthrough in materials properties of polymer: NFA system, leading to very promising performance of OPVs [4].

It is noteworthy that the single junction devices face critical problems that limit their efficiency. The first challenge is thermalization loss, caused by thermal relaxation when the energy of an absorbed photon is greater than the bandgap (Eg) of the device. The second issue is photon transmission loss, where photons with energy below the bandgap cannot be absorbed [5]. The theoretical PCE limit in single junction devices was determined as 33.7 % (Shockley and Queisser (SQ) limit) [6]. Currently the existing single junction devices are approaching SQ limit. Development of multi-junction solar cells can be the solution to surpass the SQ limit by connecting 2 or more subcells with complementary absorption spectra in a tandem structure. It was calculated that a PCE of around 46.1 % can be theoretically achieved by the tandem devices [5]. Nowadays, a lot of investigations have been performed on PSCs/Si tandem structure and a record PCE of 33.2 % have been recently announced [2]. However, the large difference of lifetime between silicon and PSCs hinders the progress of their commercialization. The expensive fabrication processes and opaque properties of Si also limit its potential for widespread use in conditions that require transparency or flexibility. On the other hand, perovskite/organic tandem solar cells have attracted increasing attention as these two types of PVs possess compatible material and device properties, making them a good pair in tandem structures. PSCs and OPVs can be fabricated by similar cost-effective thin-film deposition techniques on both rigid and flexible substrates. The bandgap of absorbers and transparency of the absorbers can be tuned according to the requirements of the applications, creating more freedom in tailoring the tandem device properties for future innovative products. Nevertheless, the PSC/OPV tandem PVs are still in the stage of research, the potential for further growth in PCE will be significant as the theoretical calculations have shown that a PCE higher than 30 % is achievable for this type of tandem PVs [7-9]. To provide prospective guidance for further studies of PSC/OPV tandem PVs, the recent achievements in this area are summarized, which provides analysis of the properties of each subcell and functional layer in the tandem structures, and outlines future directions for the development of this type of PSC/ OPV tandem technology in the PV community.

T a b l e

Summary of perovskite/organic Tandem solar cells

	Sub cell	2T/ 4T	Tandem configuration	Band-gap, (eV)	V_{oc} (V)	J_{SC} (mA/ cm^2)	FF (%)	PCE (%)	Ref.
1	$FA_{0.8}Cs_{0.2}Pb(I_{0.5}Br_{0.5})_3$	2T	MgF_2/ Glass/ITO/MeO-2PACz/WBG/PEAI /$PC_{61}BM$/ AZO NP / SnO_X / InO_X / MoO_X/NBG /C_{60} / BCP / Ag	1.85	2.15	17.90	80	23.1 %	[10] *(2022)*
	PM6: Y6: PC61BM (1:1.2:0.2)			1.33					
2	$Cs_{0.25}FA_{0.75}Pb(I_{0.6}Br_{0.4})_3$	2T	ITO/NiO_X/BPA/WBG/ C_{60}/BCP/ IZO/ MoO_X/ NBG / PNDIT-F3N /Ag	1.79	2.06	14.83	77.20	23.60 %	[11] *(2022)*
	PM6: Y6: P71CBM			1.36					
3	$MAPbI_2Br$ + $Pb(SCN)_2$)	2T	ITO/Poly-TPD/WBG/ PCBM/BCP/Au/MoO_3/ NBG /PFN-Br/Ag	1.7	1.94	13.12	78.7	20.03	[12] (2022)
	PM6: Y6			1.3*					
4	$MAPbI_{2.5}Cl_{0.5}$	2T	ITO/PVBT-SO_3/WBG/ $PC_{61}BM$/ C_{60}-ionene/Ag/MoO_3/ NBG/C_{60}-ionene/ Ag	1.6*	1.86	12.4	79	19.2	[13] (2022)
	PM6: Y6			1.31*					
5	$FA_{0.8}Cs_{0.2}Pb(Br_{0.4}I_{0.6})_3$	2T	MgF2/Glass/ITO/2PACz/ WBG/C_{60}/SnO_2/PEDOT: PSS/NBG/PFN-Br/ Ag	1.78	1.83	13.8	69.4	17.6	[14] (2022)
	PTB7-Th: IEICO-4F			1.24					
6	$FA_{0.6}MA_{0.4}Pb(I_{0.6}Br_{0.4})_3$ + ClFA	2T	ITO/2PACz/WBG/C_{60}/ BCP/ Ag/MoO_X/NBG/PDINN/Ag	1.79	1.88	15.7	74.6	22.0	[15] (2022)
	PTB7-Th: BTPV-4Cl-eC9			1.22					

7	$MA_{0.96}FA_{0.1}PbI_2Br(SCN)_{0.12}$	2T	ITO/poly-TPD/WBG/ PCBM/BCP/Au/MoO_3/ NBG/PFN-Br/Ag	1.75*	1.96	13.8	78.4	21.2	[16] (2022)
	PM6: CH1007			1.31*					
8	$CsPbI_{1.8}Br_{1.2}$/TACl	2T	ITO/SnO_2/WBG/TACl/ PBDB-T/MoO_3/Au/ZnO/ PFN/ NBG/MoO_3/Al	1.93	2.05	13.36	76.82	21.04	[17] (2021)
	PM6: Y6			1.4					
9	$CsPbI_2Br$	2T	ITO/ZnO/WBG/poly-TPD/MoO_3/Ag/PFN-Br/ NBG/MoO_3/Ag	1.91*	1.96	13.3	80.8	21.1	[18] (2021)
	PM6: Y6-BO			1.3*					
10	$CsPbI_2Br$	2T	ITO/SnO_2/ZnO/WBG /PTAA/MoO_3/Au/ZnO/ NBG/MoO_3/Ag	1.91*	1.96	13.07	80.8	20.9	[19] (2021)
	D18: Y6			1.33*					
11	$CsPbI_2Br$	2T	ITO/ZnO/SnO_2/WBG/ PDCBT / MoO_3/Ag/ZnO/ NBG /MoO_3/Ag	~1.9	1.95	12.5	76	18.4	[20] (2020)
	PM6: Y6			1.31*					
12	$CsPbI_2Br$	2T	ITO/ZnO/SnO_2/WBG/ PDCBT / MoO3/Ag/ZnO /NBG /MoO3/Ag	~1.9	1.86	12.9	75	18.1	[20] (2020)
	PTB7-Th: O6T-4F			1.24*					
13	$FA_{0.8}MA_{0.02}Cs_{0.18}PbI_{1.8}Br_{1.2}$	2T	ITO/NiOx/WBG/ C_{60} / BCP/ Ag/ MoO_X/ NBG/ TPBi/ Ag	1.77	1.902	13.05	83.1	20.6 (19.54)	[21] (2020)
	PBDBT-2F: Y6: $PC_{71}BM$			1.41					
14	$CsPbI_2Br$	2T	TO/SnO_2/WBG/ P3HT/ MoO_3/Ag/PFN-Br/ NBG/MoO_3/Ag	1.91	1.82	13.2	71.68	17.24	[22] (2020)
	PTB7-Th: IEICO-4F			1.24					
15	$Cs_{0.1}(FA_{0.6}MA_{0.4})_{0.9}Pb(I_{0.6}Br_{0.4})_3$	2T	ITO/PTAA/WBG/ PMABr/ PCBM/BCP/Ag/ M-PEDOT/NBG/ Bis-C60/BCP/Ag	1.74	1.85	11.52	70.98	15.13	[23] (2020)
	PBDB-T: SN6IC-4F			1.3					
16	$CsPbI_2Br$	2T	(ITO)/SnO_2/WBG/ PTAA/MoO_3/Au/ZnO/ NBG/MoO_3/Ag	1.92	1.71	11.98	73.4	15.04	[24](2019)
	PTB7-Th: COi8DFIC: $PC_{71}BM$			1.2					
17	$MAPbI_3$	2T	ITO/PEDOT: PSS/WBG/$PC_{61}BM$/C_{60}-SB/Ag/ MoO_3/ NBG/C_{60}-N/Ag	1.5	1.63	13.1	75.1	16	[25] (2016)
	PCE-10: PC71BM			1.46*					
18	$CH_3NH_3PbI_3$	2T	ITO/PEDOT: PSS/NBG/ PFN/TiO_2/ PEDOT: PSS PH500/PEDOT: PSS 4083/WBG/$PC_{61}BM$/ PFN/Al	1.52	1.52	10.05	67	10.23	[26] (2015)
	PBSeDTEG8: $PC_{61}BM$			1.28					
19	$CsPbI_2Br$	4T	ITO/SnO_2/ZnO/ WBG/ HTL/ MoO_3/ITO + ITO/PEDOT: PSS/NBG/PDIN/Ag	1.92	1.26	13.9	73.99	21.25	[27] (2022)
	D18-Cl-B: N3: $PC_{61}BM$			1.31*	0.84	27.37	78.6		
20	$CsPbBr_3$	4T	ITO/ZnO/WBG/ Spiro-OMeTAD/ transfer laminated PH1000+ ITO/ZnO/NBG/MoO_3/Al	2.3	1.38	6.15	70.5	14.03	[28] (2018)
	PBDB-T-SF: IT-4F			1.46*	0.88	12.18	75.2		

* *The values are calculated from the published EQE or absorption spectra.*

1. **Narrow-bandgap subcell**

The use of materials and device structures as well as the corresponding latest photovoltaic performance based on PSC/OPV tandem PVs are summarized in Table [10-28]. Nowadays, the majority of works use OPVs as the narrow bandgap subcells with a range from 1.20 eV to 1.46 eV in a tandem structure with PSCs. The absorber layer is composed of blending polymer donor, NFA and/or fullerene acceptors in an optimized ratio. The NFA based material system becomes the dominant absorber in OPVs used in tandem structure with PSC. In comparison with OPVs based on fullerene derivatives, NFA based devices have further enhanced absorption properties due to tunable energy levels and wider absorption range of the active layer [29]. Additionally, a lower driving force is needed for NFA based OPV to overcome the exciton binding energy, which leads to minimum V_{OC}losses and higher J_{SC} [29-30]. Moreover, it is found that NFA based devices are more stable under the light with minor burn-in losses [30]. Y6 and IEICO-4F are commonly used as NFA materials in the OPV subcell of the tandem devices, with the absorption spectra extended to near infrared (NIR) region and a peak absorption at 810 nm and 865 nm, respectively [4]. The OPVs with an active layer composed of non-fullerene acceptors (NFA) blended with common polymer donors, such as PM6, a member of the PBDB-T family, and PTB7-Th, have exhibited high PCEs over 14 % in single-junction solar cells [30]. Due to their excellent optoelectronic properties, this type of OPV has been widely used in tandem structures with PSCs. The recent development of copolymer D18 with a high hole mobility of 1.59×10^{-3} cm^2 V^{-1} s^{-1} blended with Y6 in the single-junction OPV has demonstrated a promising certificated PCE of 17.6 % [31]. The D-A copolymer donor D18 blended with NFA has been also applied in OPVs tandem with PSCs in 2T and 4T structures, for which both of the tandem structures exhibit a PCE of ~21 % [19],[27], indicating a huge potential of this type of OPV subcell for future development of high-efficiency PSC/OPV tandem PVs. The absorption onset for the D18, PM6 and PTB7-Th in thin films is 625 nm, 688 nm and 785 nm respectively, corresponding to an optical bandgap of 1.98 eV, 1.80 eV and 1.58 eV [30-31]. The absorption spectra of narrow-bandgap NFAs are complementary to those of common polymer donors used in OPVs, ensuring a wide absorption range extended to the long-wavelength region, which makes NFA based OPV sub cells well-suited for using in tandem structures with wide bandgap PSCs.

The non-radiative recombination which reduces the charge transport efficiency in OPV subcell, is one of the major challenges in achieving high-performance devices. By using fullerene as additives in the binary bulk heterojunction (BHJ) to form a ternary blend system, which enables better photovoltaic performance of OPVs as well as the overall efficiency of the tandem devices. It is found that adding an optimized amount of fullerene additives to the NFA based bulk BHJ active layer can introduce multiple positive effects, such as improved molecular packing for better carrier transport, enhanced light harvesting power, and better energy alignment etc. [10], [21], [24], [32-33]. In addition to enhancement of carrier transport, ternary OPVs are more flexible in controlling complementary absorption bands of the donor and acceptor components in the active layer to optimize the absorption range of the OPV subcell. Brinkmann *et al*. [10] added an optimized amount of PC61BM into the PM6: Y6 blend for improving the blend morphology of the photoactive layer, resulting in enhanced charge transportation and reduced non-radiative recombination in the PSC/OPV tandem solar cells, yielding a PCE of 17.5 % of OPV sub cell and 23.1 % for tandem with a PSC [10]. The high non-radiative recombination rate is one of the reasons for the low external quantum efficiency (EQE) of the OPVs. The EQE spectrum of binary PM6: Y6 extends beyond 900 nm and ternary cells exhibit enlarged EQE beyond 85 % at $\lambda > 650$ nm [10], which is suitable for use in tandem solar cells with a wide-gap front-cell. Other works reported by Chen *et al.* [21] and Zeng *et al.* [24] also used techniques of adding fullerene derivatives to form a ternary system in fabrication of OPVs. Jeong *et al.* [34] reported an improved PCE from 14.9 % to 15.6 % can be obtained from OPVs based on a ternary blend system by forming the BHJ blend with a fullerene self-assembled monolayer (C60-SAM). The OPVs with this ternary system were also found to retain 90 % of their original PCE after 8 hours of illumination. Similar approach of incorporation of PC71BM into the binary system has been reported by Chen *et al.* [11]. The OPVs based on the system of PBDBT-2F: Y6: PC71BM (1:1.2:0.2) possess balanced charge carrier transports, yielding a PCE of 15.8 % and a high PCE of 20.6 % (certified as 19.54 %) for 2T PSC/OPV monolithic tandem device.

Although the BHJ structure is widely used in OPVs, the random mixing of materials to form donor-acceptor blends creates challenges in controlling the morphology of the resultant active layer, reducing the batch-to-batch reproducibility. Recently, a sequential layer-by-layer (LBL) fabrication technique has been reported to increase the control of morphology formation and promote vertical phase separation in the OPVs. Qin *et al.* [15] have compared the fabrication techniques for forming LBL and BHJ structure and found the advantages of using LBL technique for preparing the rear OPV subcell based on PTB7-Th: BTPV-4Cl-eC9.

It is found that application of LBL leads to a better phase of the donor and acceptor, which can decrease the trap density and inhibit the non-radiative recombination [15]. The thin films in the LBL structure can facilitate charge extraction and transport at the interconnecting layer (ICL). The LBL-OPV subcell exhibits a higher J_{SC} and FF compared to the BHJ based device. The J_{SC} and FF of the LBL-OPV subcell are 28.6 mA cm^{-2} and 69.2 %, respectively, while those of the BHJ-based device are 27.8 mA cm^{-2} and 65.2 %, showing LBL as an effective technique for improving the performance of OPVs. A PCE of 22 % can be realized by fabricating 2T-tandem based on PSC/LBL-OPV. It is also interesting to note that the OPV subcells in monolithic tandem devices are usually fabricated in a regular structure (p-i-n), which can be due to the feasibility of deposition methods of preparing typical high-performance functional layers for OPVs and matching with the well-established inverted structures of organo-metal halide-based PSCs.

2. **Wide-bandgapsubcell**

The perovskite materials are commonly used in the wide-bandgap front cells in the tandem devices. The organic-inorganic hybrid perovskites (i.e. multiple cation mixed halide perovskite) and Cs-based all-inorganic perovskites (e.g. $CsPbI_2Br$, $CsPbI_{1.8}Br_{1.2}$) are the two major absorbers used in the PSCs. The bandgap of the perovskites can be tuned by changing the amount of monovalent cations and halogen ions in the range of 1.5 — 2.3 eV [15]. However, the chemical instability of organic–inorganic perovskites upon exposure to moisture, UV-light, and heat caused by the weakly bound of organic components in the hybrid crystal structure is still a critical problem for the device compliance with specific application requirements [35]. The use of all-inorganic perovskites such as $CsPbI_{3-x}Br_x$(x = 0, 1, 2, and 3) as light-harvesters by completely replacing organic cations with inorganic Cs^+ ions has emerged as a promising technology for improving the thermal stability of PSCs.

The defects in the bulk of perovskites and at the material interfaces are the key factors that lead to non-radiative charge recombination resulting in poor device efficiency and stability. Tremendous works have been done on passivation engineering of single junction PSCs [36], but they are also useful to implement in PSC/OPV tandem devices. *Li et al.* [23] used phenmethylammonium bromide (PMABr) as an interlayer between perovskite film and ETL, to passivate the defects in grain boundaries of $Cs_{0.1}(FA_{0.6}MA_{0.4})_{0.9}Pb(I_{0.6}Br_{0.4})_3$. The PL and TRPL results show that using PMABr for passivation increased the PL photon energy, resulting in a blueshift of PL peaks and suppressed nonradiative recombination, yielding a PCE of 15.13 % for the tandem device [23]. Qin *et al.* used chloro-formamidinium (ClFA) to passivate bulk defects in the $FA_{0.6}MA_{0.4}Pb(I_{0.6}Br_{0.4})_3$ based PSCs. It is also found that the use of CIFA leads to formation of bigger grains and more uniform film, resulting in reduction of trap density and better vertical charge transport, yielding a final PCE of 22.0 % in tandem with OPVs [15]. Intensive research has been also done on improving the quality of the interface between the perovskite and charge transport layers, since defects are likely concentrated at the material interface and lead to severe carrier recombination. Brinkmann *et al.* [10] have implemented passivation strategies, by modification of the perovskite surface with phenethylammonium iodide (PEAI), which promotes the formation of a 2D perovskite capping layer. The insertion of PEAI leads to notable lowering of the perovskite valence band maximum, which avoids photogenerated holes from reaching the electron extraction layer (EEL) and thereby facilitates selective extraction of electrons. As a result, a PSC/OPV tandem device with a remarkable PCE of 23.1 % and excellent stability of more than 1000 hours can be achieved [10]. Chen *et al.* [11] applied benzylphosphonic acid(BPA) for passivating the interface between NiOx and $Cs_{0.25}FA_{0.75}Pb(I_{0.6}Br_{0.4})_3$. Their tandem devices exhibited improved band alignment, reduced non-radiative recombination and better operational stability, yielding a PCE of 23.6 %.

Device architecture also plays an important role in determining the performance of PSC/OPV tandem devices. The PSCs can be fabricated in the n-i-p regular structure or inverted p-i-n structure. Notably, a compelling correlation has been observed based on the analysis of existing scientific literature. The inverted p-i-n structure is commonly employed for inorganic-organic hybrid PSC in tandem structure with the OPV subcell. The adoption of the inverted structure has demonstrated enhanced device stability and PCE in hybrid single-junction PSCs. These improvements are attributed to the increase of charge carrier lifetime and the diffusion coefficient as well as enhancement of charge collection efficiency, resulting in an enhanced performance of PSCs [37]. Meanwhile, owing to non-availability of corrosive additives in the inverted device configuration and hydrophobicity of the PCBM layer, the device stability can be enhanced in the ambient atmosphere [37]. In contrast, an n-i-p structure is almost exclusively used for all-inorganic Cs based PSCs in the tandem devices, with the electron transport layer deposited on the substrate followed by the

perovskite active layer and hole transport layer. This is not surprising, as high efficiency Cs-based all-inorganic PSCs have not been demonstrated in p-i-n structure for single-junction devices.

3. Other Constituent layers

The interconnecting layer (ICL) is one of the key components in the development of high-performance 2-terminal monolithic devices. Requirements for good interconnecting layers include high transparency, minimum optical losses, good interface for efficient recombination of holes and electrons generated from WBG and NBG sub cells. Moreover, minimum current leakage is obligatory for the interconnecting layer. The ICL in PSC/OPV tandem devices consists of carrier recombination layer (CRL) sandwiched between hole transporting layer (HTL) and electron transporting layer (ETL) (or known as EEL and hole extraction layer (HEL), respectively). The commonly used CRLs are thermally evaporated ultra-thin metal like Ag, Au or transparent conductive oxides such as indium tin oxide (ITO). The CRL has to be used for tandem devices. Otherwise, devices exhibit poor performance due to the Schottky barrier between the HTL and ETL. By inserting a CRL between the top and bottom cells, this barrier can be reduced, allowing charge carriers to recombine efficiently. Additionally, the CRL can improve the ohmic contact between the top and bottom cells, enhancing the overall performance of the tandem solar cell. Brinkmann *et al.* [10] developed an interconnection between sub cells using InO_x layer prepared by low-temperature atomic layer deposition (ALD) (80 °C) with a precise control of layer thickness. This approach has led to notable improvements in the *J-V* characteristics of PSC/OPV tandem solar cells and rendering the $SnO_x/InO_x/MoO_x$ ohmic contact. Chen *et al.* have found that 4-nm-thick sputtered indium zinc oxide (IZO) ICL can also reduce optical losses as well as V_{oc} loss in the WBG PSC by interfacial passivation. These improvements cause a promising PCE of 23.60 % (certified 22.95 %) for PSC/OPV tandem devices [11]. Xu *et al.* [14] demonstrated metal-free ICL PSC/OPV tandem devices based on ALD grown SnO_2 and solution-processed PEDOT: PSS. The use of metal-free ICL can simplify the device fabrication process and thus reduce the cost for future manufacturing. This type of tandem device has good outdoor stability and exhibits a PCE of 17.6 % [14].

For PSC/OPV tandem devices, the most commonly used HTLs are MoO_x, Poly-TPD, 2PACz/MeO-2PACz while the ETLs are ZnO, SnO_2, NiO_x, PCBM. A double layer of ETL based on ZnO and SnO_2 is also popularly used in all-inorganic Cs based PSCs [19], [20], and [27]. The thickness of the ETLs in the ICLs plays a critical role in affecting the performance of monolithic PSC/OPV devices. A very thin ETL can lead to inefficient electron extraction from the WBG sub cell to the ICLs, while too thick ETL can also inhibit electron extraction and compromise tandem device performance [12].

The deposition techniques used for constructing tandem devices should be also carefully considered. The processing techniques directly impact the film thickness, interface quality, crystal structures, and morphology of the layers, consequently influencing the overall performance of the tandem devices. For 2T-PSC/OPV tandem devices, the majority of the functional layers are prepared by the spin-coating processes, which is one of the most economical approaches among the thin-film deposition techniques such as e-beam deposition, magnetron sputtering and thermal evaporation etc. The spin-coating technique is straightforward to use under laboratory conditions while it is not suitable for large-scale production, and it can lead to composition inhomogeneities in the layers of the devices. Other thin-film deposition methods, which are compatible with solution-processed films, have been attempted during monolithic tandem device fabrication. One of them is thermal evaporation, it is a common deposition technique in PSC/OPV tandem device for preparing the thin metal layers of Ag or Au as the CRL and the electrode, as well as depositing ETL and HTL materials such as C_{60}/BCP/TPBi and MoO_3 respectively [10], [11], [16], [20-22]. The thermal evaporation has its advantages such as capability to control the film thickness, low contamination risks as well as high compatibility with the solution-processed layers. It is also capable of preparing flexible samples at low substrate temperature [38-39].

Apart from ICL, the external coating such as anti-reflective layers on the devices can reduce the light reflection at the surface of incoming light. Brickmann *et al.* [10] and Troughton *et al.* [14] utilized MgF_2 as an antireflective layer. The direct effect of the antireflective coating on the efficiency of the tandem device was not discussed in these studies while it is predicted that approximately 1 % reduction in reflection between the range of 400-800 nm can be achieved [40]. Given the promising results, the use of anti-reflective layers such as MgF_2 or other materials is an interesting area for research to further enhance the light harvesting ability of tandem PVs.

4. Perspective on future development PSC/OPV Tandem

The scientific community has made notable advances in developing efficient tandem PV devices using emerging materials. Among these, PSC/Si-based tandem devices have been extensively researched and

currently hold the highest PCE record of 33.2 % [2]. However, the mismatch in the lifetime of perovskite and silicon remains a significant obstacle for practical applications. Furthermore, silicon cannot be used for the construction of semi-transparent tandem solar cells, which limits the potential applications of PSC/Si tandem devices. The certified record PCE of 23.1 % has been achieved for PSC/OPV tandem devices [10], demonstrating the potential of using it as one of the future alternatives to conventional photovoltaics. The tunability of bandgap and transparency in PSCs and OPVs is a distinct advantage, ensuring a wide range of future innovative applications, such as smart PV windows with thermochromic functions and colorful PVs for aesthetically oriented projects and other building-integrated PVs (BIPVs). However, despite the promising progress made in the development of PSC/OPV tandem devices, there is still a scarcity of research focused on their engineering for practical applications. This is because some limitations still need to be overcome before PSC/OPV tandem devices can become commercially viable.

One of the major challenges is large-scale manufacturing of tandem structure which involves more fabrication steps compared to their corresponding single junction devices. Currently, the common reported active areas for PSC/OPV tandem devices range from 1.74 mm^2 [10] to 1 cm^2 [13, 23], which are still limited for practical applications that require large-scale deployment, and thus it is very crucial to develop effective thin-film deposition techniques for fabrication of larger devices while maintaining high efficiency is necessary. For example, blade coating, slot-die coating, spray coating and inkjet printing should be intensively investigated for preparing PSCs and OPVs while the vacuum deposition process such as thermal evaporation can be used for preparing uniform large-scale perovskite thin films and metal oxides carrier transport layers. Despite the ability to tune the bandgaps of both the perovskite and organic absorber layer in OPVs, the majority of reported PSC/OPV 2-terminal monolithic tandem devices are based on a front wide-bandgap perovskite subcell and a rear narrow- bandgap OPV subcell. This is due to the higher processing temperature required for PSCs, such as the conversion of precursors and perovskite crystallization, compared to the fabrication processes of OPVs. The high processing temperature steps of perovskite can cause the degradation of the underlying OPV properties. The possible solution is to develop pre-synthesized inks of perovskite, such as quantum dot dispersion solutions [41], and carrier transport materials, and investigate effective deposition of these inks to avoid high-temperature processing steps of PSC fabrication. Only with a maturity of diverse thin-film deposition methods can the freedom of PSC/OPV combination be largely enhanced, and this is crucial for advancing the practical viability of this type of tandem PVs. On the other hand, the development of transparent electrodes and the use of flexible substrates are also essential for enabling more diverse applications of PSC/OPV tandem PV in the future. The materials such as graphene with good flexibility [42] and sputtered ITO with desirable transparency and conductivity have been widely demonstrated for application in OPV and PSCs [43-44]. However, the compatibility of large-scale processing and the potential for induced damages on the thin films underneath during high-energy deposition processes should be carefully addressed.

Device stability and lifetimes of PSC/OPV tandem PVs are other critical considerations in the development of their practical applications. Both PSCs and OPVs are sensitive to environmental factors such as moisture, heat, and UV exposure etc., which can lead to device degradation over time. Researchers are exploring various strategies to improve device stability, including encapsulation techniques [45], material and device engineering [30-31], [46] etc. and achieved significant advancements. Despite the fact that PSC and OPV still have shorter lifetimes compared to Si at the current stage, their low material and fabrication costs can provide a cost-effective replacement option. Therefore, they could potentially be employed in certain applications that do not require a long product lifespan, which could be beneficial to indoor applications and portable electronic devices, where cost-effective replacement options are desirable and product lifetimes are relatively short due to frequent upgrades. This will be an incremental step towards future practical application of PSC/OPV PVs. With continued research and development, this technology will become a commercially viable option for a broader range of applications.

Acknowledgements

A.N. acknowledges the financial support from the Science Committee of the Ministry of Education and Science of the Republic of Kazakhstan (Scientific Research Grant no. AP14869983, AP19576154) and Nazarbayev University (Grant no. 021220CRP0422).

References

1 El Chaar, L., Lamont, L. A. & El Zein, N. (2011). Review of photovoltaic technologies. *Renewable and Sustainable Energy Reviews, 15(5), 2165-2175*. https://doi.org/10.1016/j.rser.2011.01.004

2 Best Research-Cell Efficiencies Chart. Retrieved from https://www.nrel.gov/pv/cell-efficiency.html

3 Roy, P., Sinha, N. K., Tiwari, S. & Khare, A. (2020). A review on perovskite solar cells: Evolution of architecture, fabrication techniques, commercialization issues and status. *Solar Energy, 198, 665-688*. https://doi.org/10.1016/j.solener.2020.01.080

4 Zhao, F., Zhang, H., Zhang, R., Yuan, J., He, D., Zou, Y. & Gao, F. (2020). Emerging Approaches in Enhancing the Efficiency and Stability in Non-Fullerene Organic Solar Cells. Adv. *Energy Mater., 10, 2002746*. https://doi.org/10.1002/aenm.202002746

5 Zhou, J., Huang, Q., Ding, Y., Hou, G. & Zhao, Y. (2022). Passivating contacts for high-efficiency silicon-based solar cells: From single-junction to tandem architecture. *Nano Energy, 92, 106712*. https://doi.org/10.1016/j.nanoen.2021.106712

6 Shockley, W. & Queisser, H. J. (1961). Detailed Balance Limit of Efficiency of p-n Junction Solar Cells. *Journal of Applied Physics, 32, 510-519.* https://doi.org/10.1063/1.1736034

7 Yan, C., Huang, J., Li, D. & Li, G. (2021). Recent progress of metal-halide perovskite-based tandem solar cells. *Mater. Chem. Front., 5, 4538-4564.* https://doi.org/10.1002/adma.202002228

8 Jiang, Y. & Qi, Y. (2021). Metal halide perovskite-based flexible tandem solar cells: next-generation flexible photovoltaic technology. *Mater. Chem. Front., 5, 4833-4850.* https://doi.org/10.1039/D1QM00279A

9 Wu, S., Liu, M. & Jen, A. (2023). Prospects and challenges for perovskite-organic tandem solar cells. *Joule, 7(3), 484-502*. https://doi.org/10.1016/j.joule.2023.02.014

10 Brinkmann, K. O., Becker, T. & Zimmermann, F. et al. (2022). Perovskite–organic tandem solar cells with indium oxide interconnect. *Nature 604, 280–286*. https://doi.org/10.1038/s41586-022-04455-0

11 Chen, W., Zhu, Y. & Xiu, J. et al. (2022). Monolithic perovskite/organic tandem solar cells with 23.6 % efficiency enabled by reduced voltage losses and optimized interconnecting layer. *Nat. Energy 7, 229–237.* https://doi.org/10.1038/s41560-021-00966-8

12 Xie, Y.-M., Niu, T., Yao, Q., Xue, Q., Zeng, Z., Cheng, Y., Yip, H. -L. & Cao, Y. (2022). Understanding the role of interconnecting layer on determining monolithic perovskite/organic tandem device carrier recombination properties. *Journal of Energy Chemistry, 71, 12-19.* https://doi.org/10.1016/j.jechem.2022.03.019

13 Zhang, Z., Cueto, C., Ding, Y., Yu, L., Russell, T. P., Emrick, T. & Liu, Y. (2022). High-Performance 1 cm^2 Perovskite-Organic Tandem Solar Cells with a Solvent-Resistant and Thickness-Insensitive Interconnecting Layer. *ACS Applied Materials & Interfaces, 14(26), 29896-29904.* https://doi.org/10.1021/acsami.2c06760

14 Xu, H., Merino, L. T., Koc, M., Aydin, E., Zhumagali, S., Haque, M. A., Yazmaciyan, A., Sharma, A., Villalva, D. R., Hernandez, L. H., De Bastiani, M., Isikgor, F. H., Troughton, J., De Wolf, S., Yerci, S. & Baran, D. (2022). Metal-Free Interconnecting Layer for Monolithic Perovskite/Organic Tandem Solar Cells with Enhanced Outdoor Stability. *ACS Applied Energy Materials, 5(11), 14035-14044.* https://doi.org/10.1021/acsaem.2c01749

15 Qin, S., Lu, C., Jia, Z., Wang, Y., Li, S., Lai, W., Shi, P., Wang, R., Zhu, C., Du, J., Zhang, J., Meng, L. & Li, Y., (2022). Constructing Monolithic Perovskite/Organic Tandem Solar Cell with Efficiency of 22.0 % via Reduced Open-Circuit Voltage Loss and Broadened Absorption Spectra. *Adv. Mater., 34, 2108829*. https://doi.org/10.1002/adma.202108829

16 Xie, Y.-M., Yao, Q., Zeng, Z., Xue, Q., Niu, T., Xia, R., Cheng, Y., Lin, F., Tsang, S. -W., Jen, A. K.-Y., Yip, H.-L. & Cao, Y., (2022). Homogeneous Grain Boundary Passivation in Wide-Bandgap Perovskite Films Enables Fabrication of Monolithic Perovskite/Organic Tandem Solar Cells with over 21 % Efficiency. *Adv. Funct. Mater. 32*, 2112126. https://doi.org/10.1002/adfm.202112126

17 Chen, W., Li, D., Chen, X., Chen, H., Liu, S., Yang, H., Li, X., Shen, Y., Ou, X., Y. (M.),, Jiang, L., Li, Y. & Li, Y., (2022). Surface Reconstruction for Stable Monolithic All-Inorganic Perovskite/Organic Tandem Solar Cells with over 21 % Efficiency. *Adv. Funct. Mater., 32*, 2109321. https://doi.org/10.1002/adfm.202109321

18 Wang, P., Li, W., Sandberg, O. J., Guo, C., Sun, R., Wang, H., Li, D., Zhang, H., Cheng, S., Liu, D., Min, J., Armin, A. & Wang, T. (2021). Tuning of the Interconnecting Layer for Monolithic Perovskite/Organic Tandem Solar Cells with Record Efficiency Exceeding 21 %. *Nano Letters, 21(18), 7845-7854.* https://doi.org/10.1021/acs.nanolett.1c02897

19 Liu, L., Xiao, Z., Zuo, C. & Ding, L. (2021). Inorganic perovskite/organic tandem solar cells with efficiency over 20 %. *Journal of Semiconductors, 42(2), 020501.* https://doi.org/10.1088/1674-4926/42/2/020501

20 Xie, S., Xia, R., Chen, Z., Tian, J., Yan, L., Ren, M., Li, Z., Zhang, G., Xue, Q., Yip, H.-L. & Cao, Y. (2020). Efficient monolithic perovskite/organic tandem solar cells and their efficiency potential. *Nano Energy, 78, 105238.* https://doi.org/10.1016/j.nanoen.2020.105238

21 Chen, X., Jia, Z., Chen, Z., Jiang, T., Bai, L., Tao, F., Chen, J., Chen, X., Liu, T., Xu, X., Yang, C., Shen, W., Sha, W. E. I., Zhu, H. & Yang, Y. (2020). Efficient and Reproducible Monolithic Perovskite/Organic Tandem Solar Cells with Low-Loss Interconnecting Layers. *Joule, 4(7), 1594-1606*. https://doi.org/10.1016/j.joule.2020.05.005

22 Lang, K., Guo, Q., He, Z., Bai, Y., Yao, J., Wakeel, M., Alhodaly, M. Sh., Hayat, T. & Tan, Z. (2020). High Performance Tandem Solar Cells with Inorganic Perovskite and Organic Conjugated Molecules to Realize Complementary Absorption. *The Journal of Physical Chemistry Letters, 11*(22), *9596-9604*. https://doi.org/10.1021/acs.jpclett.0c02794

23 Li, Z., Wu, S., Zhang, J., Lee, K. C., Lei, H., Lin, F., Wang, Z., Zhu, Z. & Jen, A. K. Y. (2020). Hybrid Perovskite-Organic Flexible Tandem Solar Cell Enabling Highly Efficient Electrocatalysis Overall Water Splitting. *Adv. Energy Mater., 10, 2000361*. https://doi.org/10.1002/aenm.202000361

24 Zeng, Q., Liu, L., Xiao, Z., Liu, F., Hua, Y., Yuan, Y. & Ding, L. (2019). A two-terminal all-inorganic perovskite/organic tandem solar cell. *Science Bulletin, 64(13), 885-887*. https://doi.org/10.1016/j.scib.2019.05.015

25 Liu, Y., Renna, L. A., Bag, M., Page, Z. A., Kim, P., Choi, J., Emrick, T., Venkataraman, D. & Russell, T. P. (2016). High Efficiency Tandem Thin-Perovskite/Polymer Solar Cells with a Graded Recombination Layer. *ACS Appl. Mater. Interfaces, 8, 11, 7070–7076.* https://doi.org/10.1021/acsami.5b12740

26 Chen, C., Bae, S., Chang, W., Hong, Z., Li, G., Chen, Q., Zhou H. & Yang Y. (2015). Perovskite/polymer monolithic hybrid tandem solar cells utilizing a low-temperature, full solution process. *Mater. Horiz., 2, 203-211*. https://doi.org/10.1039/C4MH00237G

27 Liu, L., Xiao, H. & Jin, K. et al. (2023). 4-Terminal Inorganic Perovskite/Organic Tandem Solar Cells Offer 22 % Efficiency. *Nano-Micro Lett., 15, 23*. https://doi.org/10.1007/s40820-022-00995-2

28 Chen, W., Zhang, J., Xu, G., Xue, R., Li, Y. W., Zhou, Y., Hou, J. & Li, Y. F. (2018). A Semitransparent Inorganic Perovskite Film for Overcoming Ultraviolet Light Instability of Organic Solar Cells and Achieving 14.03 % Efficiency. *Adv. Mater. 30, 1800855*. https://doi.org/10.1002/adma.201800855

29 Zhang, J., Tan, H.S. & Guo, X. et al. (2018). Material insights and challenges for non-fullerene organic solar cells based on small molecular acceptors. *Nat Energy 3,* 720–731. https://doi.org/10.1038/s41560-018-0181-5

30 Hou, J., Inganäs, O. & Friend, R. et al. (2018). Organic solar cells based on non-fullerene acceptors. *Nat. Mater. 6*(17), 119–128. https://doi.org/10.1038/nmat5063

31 Liu, Q., Jiang, Y., Jin, K., Qin, J., Xu, J., Li, W., Xiong, J., Liu, J., Xiao, Z., Sun, K., Yang, S., Zhang, X. & Ding, L. (2020). 18 % Efficiency organic solar cells. *Science bulletin, 65(4),* 272–275. https://doi.org/10.1016/j.scib.2020.01.001

32 Bi, P., Zhang, S., Chen, Z., Xu, Y., Cui, Y., Zhang, T., Ren, J., Qin, J., Hong, L., Hao, X. & Hou, J. (2021). Reduced non-radiative charge recombination enables organic photovoltaic cell approaching 19 % efficiency. *Joule, 5*(9), 2408-2419. https://doi.org/10.1016/j.joule.2021.06.020

33 Xie, Y., Li, T., Guo, J., Bi, P., Xue, X., Ryu, H. S., Cai, Y., Min, J., Huo, L., Hao, X., Woo, H. Y., Zhan, X. & Sun, Y. (2019). Ternary Organic Solar Cells with Small Nonradiative Recombination Loss. *ACS Energy Letters, 4*(5), 1196-1203. https://doi.org/10.1021/acsenergylett.9b00681

34 Jeong, S., Rana, A., Kim, J. -H., Qian, D., Park, K., Jang, J. -H., Luke, J., Kwon, S., Kim, J., Tuladhar, P. S., Kim, J. -S., Lee, K., Durrant, J. R. & Kang, H., (2023). New Ternary Blend Strategy Based on a Vertically Self-Assembled Passivation Layer Enabling Efficient and Photostable Inverted Organic Solar Cells. *Adv. Sci.* 2206802. https://doi.org/10.1002/advs.202206802

35 Faheem, M. B., Khan, B., Feng, C., Farooq, M. U., Raziq, F., Xiao, Y. & Li, Y. (2020). All-Inorganic Perovskite Solar Cells: Energetics, Key Challenges, and Strategies toward Commercialization. *ACS Energy Letters, 5*(1), 290-320. https://doi.org/10.1021/acsenergylett.9b02338

36 Aidarkhanov, D., Ren, Z., Lim, C-K., Yelzhanova, Z., Nigmetova, G,.Taltanova, G., Baptayev, B., Liu, F., Cheung, S., Balanay, M., Baumuratov, A., Djurišić, A., So, S., Surya, C., Prasad, P. & Ng, A. (2020). Passivation engineering for hysteresis-free mixed perovskite solar cells. *Solar Energy Materials and Solar Cells, 215,* 110648. https://doi.org/10.1016/j.solmat.2020.110648

37 Raj, A., Kumar, M. & Anshul. (2021). Recent advancement in inorganic-organic electron transport layers in perovskite solar cell: current status and future outlook. *Materials Today Chemistry, 22,* 100595. https://doi.org/10.1016/j.mtchem.2021.100595

38 Lee, J.-H., Kim, B. S., Park, J., Lee, J.-W. & Kim, K., (2022) Opportunities and Challenges for Perovskite Solar Cells Based on Vacuum Thermal Evaporation. *Adv. Mater. Technol.* 2200928. https://doi.org/10.1002/admt.202200928

39 Wang, S., Li, X., Wu, J., Wen, W. & Qi, Y. (2018). Fabrication of efficient metal halide perovskite solar cells by vacuum thermal evaporation: A progress review. *Current Opinion in Electrochemistry, 11,* 130-140. https://doi.org/10.1016/j.coelec.2018.10.006

40 Chundi, N., Das, B., Reddy, K. Prasad, M., Koppoju, S., Ramasamy, E. & Sakthivel, S. (2020). Single layer hollow MgF2 nanoparticles as high-performance omnidirectional broadband antireflective coating for solar application. *Solar Energy Materials and Solar Cells, 215,* 110680. https://doi.org/10.1016/j.solmat.2020.110680

41 Davletiyarov, B., Akmurzina, K., Seralin, A., Bizhanova, G., Baptayev, B., Balanay, M. & Ng. A. (2022). Investigation of Synthesis and Deposition Methods for Cesium-Based Perovskite Quantum Dots for Solar Cell Applications. *Eurasian Chem. - Technol. J., 24*(3), 241-249. https://doi.org/10.18321/ectj1437

42 Zhang, Y., Ng, S-W., Lu, X. & Zheng, Z. (2020). Solution-Processed Transparent Electrodes for Emerging Thin-Film Solar Cells. *Chem. Rev. 120,* 4, 2049–2122. https://doi.org/10.1021/acs.chemrev.9b00483

43 Srivishnu, K. S., Markapudi, P. R., Sundaram, S., Giribabu & Semitransparent, L. (2020). Perovskite Solar Cells for Building Integrated Photovoltaics: Recent Advances. *Energies, 16,* 889. https://doi.org/10.3390/en16020889

44 Ren, Z., Zhou, J., Zhang, Y., Ng, A., Shen, Q., Cheung, S. H., Shen, H., Li, K., Zheng, Z., So, S.K., Djurišić, A.B. & Surya, C. (2018). Strategies for high performance perovskite/crystalline silicon four-terminal tandem solar cells. *Solar Energy Materials and Solar Cells, 179,* 36-44. https://doi.org/10.1016/j.solmat.2018.01.004.

45 Dong, Q., Liu, F., Wong, M., Tam, H., Djurišić, A., Ng, A., Surya, C., Chan, W. K. & Ng, C. (2016). Encapsulation of Perovskite Solar Cells for High Humidity Conditions. ChemSusChem., *9,* 18. https://doi.org/10.1002/cssc.201600868.

46 Ng, A., Liu, X., Jim, W., Djurišić, A., Lo, K., Li, S. & Chan, W. (2014). P3HT: PCBM solar cells — The choice of source material. *J. Appl. Polym. Sci., 131*. https://doi.org/10.1002/app.39776

Т. Серікова, Г. Бижанова, Ханлин Ху, Энни Нг

Перовскитті органикалық тандемдік күн элементтерінің дамуындағы соңғы мәліметтер мен тенденциялар

Бірнеше өтпелі фотоэлектр элементтердің (ФЭ) пайда болуы бірөтпелі күн элементтерінің Шокли-Квиссер шегін еңсеруге мүмкіндік береді. Соңғы уақытта перовскитті күн батареялары (ПКЭ) және органикалық фотоэлектрлік элементтер (ОФЭ) — бұл энергияны түрлендіру тиімділігінің (ЕРЕ) өте жылдам өсуіне байланысты фотоэлектрлік қоғамдастықтың кең назарын аударған жаңа буынның ең перспективалы екі фотоэлектрлік элементі. ПКЭ және ОФЭ-ді тандемдік құрылымдарда біріктіру абсорбциялық жолақтарды реттеу және мөлдірлікті жақсарту үшін жарық сіңіруші қабаттардың шектік аймақтарын өзгерту мүмкіндігі сияқты көптеген артықшылықтарды ұсынады. Жұқа қабат технологиясын қолдану құрылғылардың жеңілдігі мен икемділігін қамтамасыз етеді, бұл әсіресе кейбір заманауи қолданбалар үшін тиімді. Сонымен қатар, ПКЭ және ОФЭ екеуі де арзан бағасымен ерекшеленеді, бұл оларды болашақта кең ауқымды коммерцияландыру үшін тартымды етеді. Бұл артықшылықтар ПКЭ/ОФЭ тандемдік құрылғыларын дәстүрлі кремний негізіндегі ФЭ-ден тыс қолданбалар үшін перспективалы етеді. Бұл шолуда ПКЭ/ОФЭ тандемдік ФЭ-ның соңғы жетістіктері туралы өзекті ақпарат берілген. ПКЭ және ОФЭ субэлементтерінің қасиеттеріне, сондай-ақ олардың функционалды қабаттарына әсер ететін материалдарды жасаудың заманауи технологиялары мен инженерлік әзірлемелері талқыланған. Сондай-ақ, тандемдік фотоэлектрлік элементтердің осы түрінің дамуына бағыт беру үшін перспективалық нұсқаулық беріледі. Мақала зерттеушілерге бұл технологияны одан әрі дамыту және оның жаңартылатын энергия көздері саласындағы толық әлеуетін ашу үшін бағыт жоспарын ұсына отырып, ПКЭ/ОФЭ тандемдік ФЭ әзірлеу туралы түсінік береді.

Кілт сөздер: перовскиттер, органикалық фотоэлектриктер, тандем күн элементтері, құрылғы инженериясы.

Т. Серикова, Г. Бижанова, Ханлин Ху, Энни Нг

Последние данные и тенденции в развитии перовскитных органических тандемных солнечных элементов

Появление фотоэлектрических элементов (ФЭ) с несколькими переходами предоставило возможность преодолеть предел Шокли–Квиссера однопереходных солнечных элементов. В последнее время перовскитные солнечные элементы (ПСЭ) и органические фотоэлектрические элементы (ОФЭ) являются двумя наиболее перспективными фотоэлектрическими элементами нового поколения, которые привлекли широкое внимание фотоэлектрического сообщества благодаря их исключительно быстрому росту эффективности преобразования энергии (ЭПЭ). Объединение ПСЭ и ОФЭ в тандемных конструкциях дает множество преимуществ, таких как возможность настройки ширины запрещенной зоны поглотителей для регулирования полос поглощения и повышения прозрачности. Использование тонкопленочной технологии обеспечивает легкость и гибкость устройств, что особенно выгодно для некоторых применений. Кроме того, как ПСЭ, так и ОФЭ отличаются низкой стоимостью, что делает их привлекательными их для широкомасштабной коммерциализации в ближайшем будущем. Эти преимущества сделают тандемные устройства ПСЭ/ОФЭ перспективными для применений, выходящих за рамки традиционных ФЭ на основе кремния. В настоящем обзоре представлена актуальная информация о недавнем прогрессе тандемных ФЭ ПСЭ/ОФЭ. Обсуждены современные технологии изготовления и инженерные разработки материалов, влияющие на свойства субэлементов ПСЭ и ОФЭ, а также их функциональных слоев. Кроме того, дано перспективное руководство для направления будущего развития этого типа тандемных фотоэлектрических элементов. Настоящая статья дает представление о разработке тандемных ФЭ ПСЭ/ОФЭ, предоставляя исследователям план действий для дальнейшего развития этой технологии и раскрытия ее полного потенциала в области возобновляемых источников энергии.

Ключевые слова: перовскиты, органические фотоэлектрики, тандемные солнечные элементы, разработка устройств.

DOI 10.31489/2023PH3/16-33

UDC: 628.165

A. Zakharov[1], A. Tukesheva[1,2], Syed Fahad Bin Haque[3], John Ferraris[3], A. Zakhidov[3], T. Tazhibayeva[2], T. Bazarbayeva[2], V. Pavlenko[1,2*]

[1]The Institute of Combustion Problems, Almaty, Kazakhstan;
[2] Al-Farabi Kazakh National University, Almaty, Kazakhstan;
[3]University of Texas, Dallas, USA

(e-mail: Vladimir.Pavlenko@kaznu.edu.kz)

Review of the current state of technology for capacitive deionization of aqueous salt solutions

The availability of clean water at affordable prices is one of the key technological, social, and economic challenges of the 21st century. The increased extraction of groundwater worldwide is leading to the gradual intrusion of salty water into sources and water horizons. In order to use this water for industrial and agricultural purposes, or as drinking water, it needs to be purified and desalinated. Thus, methods of desalinating water of different salinity levels, ranging from brackish to seawater, are becoming more prominent. The overall goal of current research is to make water desalination technologies more energy-efficient and cost-effective. One promising technology that meets these requirements is capacitive deionization (CDI) of water. This technology has been widely known for over 30 years, but significant progress in CDI research has only been achieved in recent years. In this review, we examine the currently developed architectures of CDI cells, advancements in carbon materials, and discuss the prospects and challenges of commercializing this technology.

Keywords: CDI, capacitive deionization, carbon materials, porous carbons, carbon electrodes, Faradaic electrodes.

Introduction

With the growth of population and the development of technological progress, humanity's water needs are increasing. At the same time, some freshwater sources are being polluted due to accidents at industrial facilities, improper waste storage, etc. Currently, almost 98 % of the available water on the earth is seawater or brackish water [1]. To use this water as technical in industries and agriculture or as drinking water, it must be preliminarily purified and desalinated. Various methods are used for desalination, among which multi-stage flash distillation (MSFD), reverse osmosis (RO), and electrodialysis (ED) are worth mentioning. The main method of industrial desalination is reverse osmosis, accounts for about 64 % of the freshwater produced, while 23 % is from multi-stage flash distillation systems, and the rest are other systems [2].

One technology that is currently being actively researched for water purification is capacitive deionization (CDI) systems. The operating principle of such system was firstly described in 1960 [3], but until the mid-2000s, the topic received poor attention by the researchers. Currently, the number of publications is growing exponentially. Compared to classical reverse osmosis, distillation, and even electrodialysis systems, capacitive purification systems have significantly lower energy consumption, lower cost, higher energy efficiency, and eco-friendliness [4–7]. The specific energy consumption for the above-mentioned systems is summarized in Table 1.

Table 1

Values of specific energy consumption for different methods of water demineralization.

Desalination method	Specific energy consumption, kW*h/m^3	Ref
Distillation	10-58	[2, 6]
Reverse osmosis	3,5-6,7	[8, 9]
Electrodialysis	0,4-8,7	[6, 10]
Capacitive deionisation	0,24-0,85	[11, 12]

Currently, CDI systems with various cell architectures and modifications of electrode materials are being actively studied. In this review, we take a look at the progress in the field of CDI systems over the past 5 years.

Various capacitive deionization cell architectures

Up to date two main fundamentally different approaches to cell assembly are proposed. These are the use of the same (symmetrical cells) or different (asymmetric cells) electrodes as the cathode and anode (Fig. 1). Classical cells with carbon electrodes are symmetrical and differ in the principle of liquid flow: through the electrodes (flow-through) or along them (flow-by). Symmetrical cells include systems upgraded with ion-exchange membranes and systems with flowing electrodes. Asymmetric cells have different electrodes, these include hybrid (carbon+faradaic electrodes) and inverse systems (carbon electrodes modified with charged functional groups).

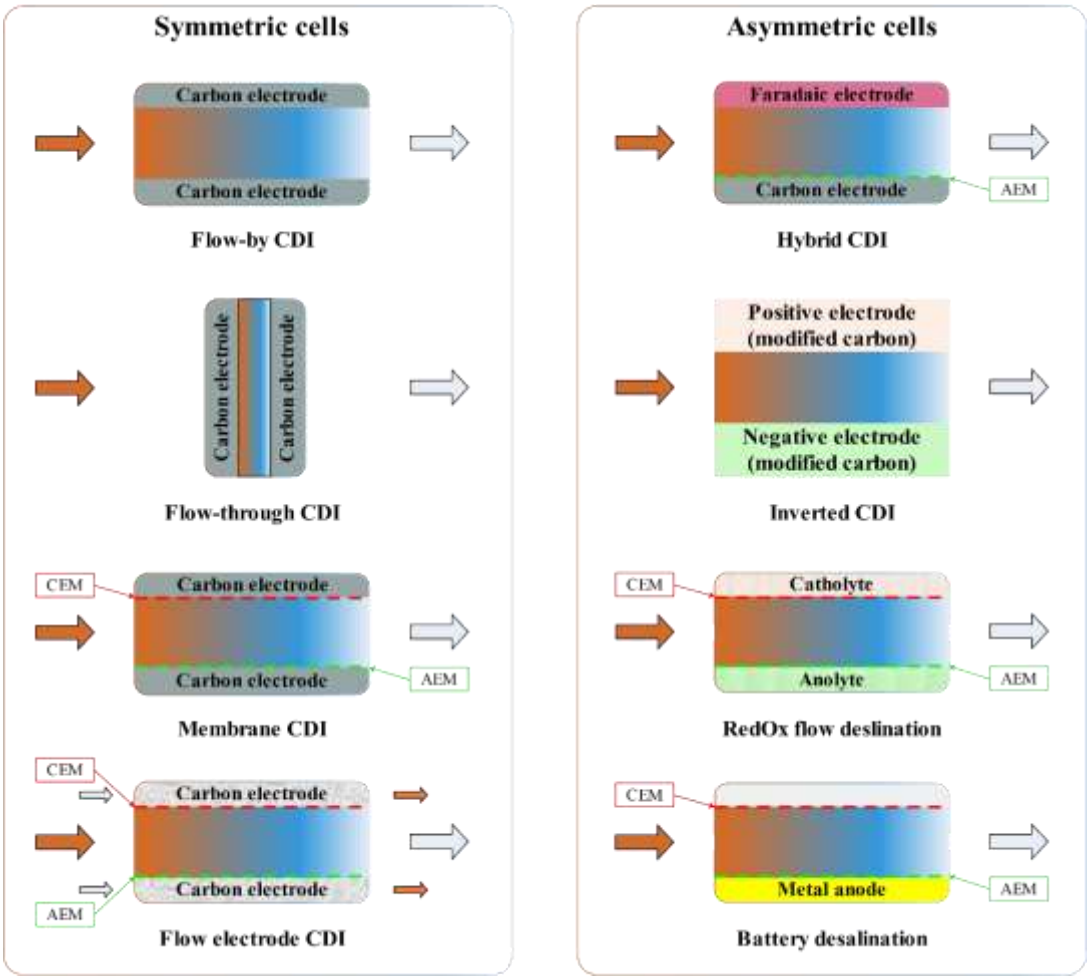

Figure 1. Basic architectures of capacitive deionization cells.

The working principle of a classic capacitive deionization cell is as follows: water is pumped between two electrodes with a potential difference of <1.4 V applied to them. Under the influence of the electric field, positively charged particles migrate to the negative electrode, and negatively charged particles migrate to the positive electrode, resulting in the formation of a double electric layer at the phase boundary. When the free surface is depleted, an inverted or zero voltage is applied to the cell. The double electric layers collapse, and the ions desorb back to the solution [9]. Two cells are required for continuous operation of a system: one cell operating in the adsorption mode and the other in the desorption mode. When the electrode surface is saturated, the cells are swapped [13].

The main problem of the classic CDI system is the secondary sorption of ions during cell regeneration step, when the applied potential is reversed. Some of the ions reach the counter electrode and were sorbed on its surface, which reduces the working capacity in the next cycle. There are two options for solving this problem: regeneration of the cell at zero potential or modernization of the system with ion-selective

membranes. The first option leads to an increase in the desorption time and a decrease in the capacity of the electrodes, since not all ions can desorb under these conditions. The use of membranes is more expensive, but more efficient and makes it possible to completely eliminate cross-sorption. The membrane capacitive deionization (MCDI) cell was first described in [14] in 2006.

Capacitive deionization cells with flow electrodes (FCDI) are the next step in evolution of CDI, developed in 2013 [15]. In such cells, the electrode is not static, and the cell always operates in the adsorption mode [16]. Desorption occurs outside of the cell, through a combination with a second FCDI cell (Fig. 2), reverse osmosis system, or another purification method [9]. Typically, activated carbon suspension in an aqueous electrolyte is used as the electrode material [13]. The major problem of this system is a low charge transfer efficiency of the suspension, as the main component of the electrode is water. An obvious way to overcome this disadvantage is to increase the carbon content of the slurry, however, this leads to an increase in viscosity and a higher probability of clogging the system. The maximum achieved saturation of the slurry is 35 wt.% carbon [17]. Alternative approaches include the addition of conducting additives to the electrolyte, such as acetylene black [18, 19], NaCl [12], CNTs [20, 21].

The hybrid cell (HCDI) was first described in the mid-1960s in [22], but active research on this architecture began only in 2014 [23]. Such system consists of faradaic and capacitive electrodes. The faradaic electrode is usually used to remove sodium ions, while the capacitive electrode is used to sorb chlorine [24]. These systems are described in more detail in section devoted to non-carbon electrode materials.

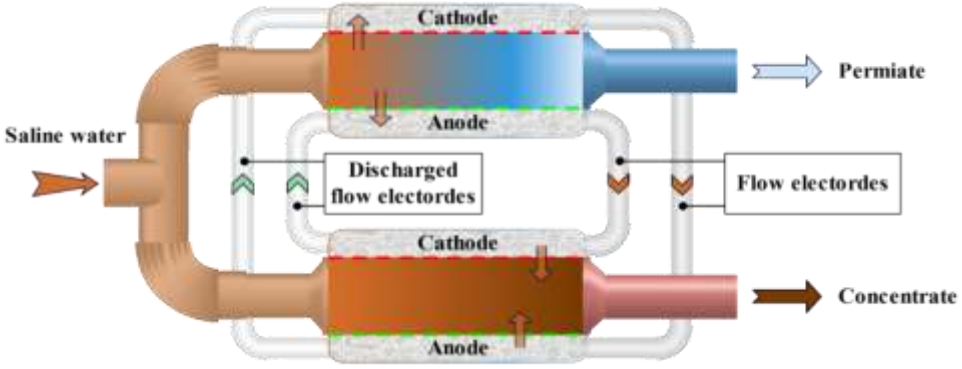

Figure 2. Schematic of the FCDI operation. The upper cell operates continuously in sorption mode, the lower cell in desorption mode.

A common problem of previously described systems is anodic oxidation, the process of formation of oxygen-containing functional compounds on the anode surface, which leads to the displacement of co-ions, and to decrease in the electrode capacity and efficiency [25]. This process is described in detail in the corresponding section below. Possible solution to this problem is to modify the positive electrode with negatively charged functional groups and the negative electrode with positive ones (ICDI). The classic methods for such modification are acid treatment or sulfonation of the positive electrode and amination of the negative. Modified electrodes are charged, so the cell is always polarized and voltage is applied only at the desorption step. Such architecture significantly reduces the total power consumption of the system [26].

Main features of CDI cells of different architectures are summarized in Table 2.

Table 2

Main features of CDI cells of different architectures.

Symmetrical architecture	Assymmetrical architecture
Flow by CDI (FB-CDI) Diffusion is the time determining process for sorption Optimization of cell dimensions is needed to maintain the required flow rate with minimum resistance.	Inverted CDI (ICDI) The cathode and anode are initially charged, so there is no need to apply the potential constantly (only during regeneration), which reduces energy costs
Flow through CDI (FTE-CDI) Less desalting time compared to FB-CDI	Flow electrode CDI (FCDI) No regeneration stage, the process is continuous

Membrane CDI (MCDI) The usage of ion-exchange membranes reduces the capture of ions during regeneration of the electrodes	Hybrid CDI (HCDI) Faradaic material with high specific capacitance Ions storage by intercalation

Carbon materials for CDI

In this review, we will focus on materials for FB-CDI, FTE-CDI, MCDI since materials used for other architectures have specific requirements in each case. For the manufacture of electrodes for cells of the above types, carbon materials are mainly used, which are characterized by a large specific surface area (high capacitance), good chemical and electrochemical stability, bioinertness, low cost, and good electrical conductivity. In many ways, these criteria are similar to the requirements for materials used in supercapacitors. Accordingly, similar mesoporous carbons, carbon fibers and fabrics, carbon nanotubes, aerogels, etc. are used in the case of CDI [27–29]. Carbon materials can be used both in pure form and modified. Modifications include doping with heteroatoms B, N, Si, P, S (individually or in combination); modifications with metal oxides — TiO_2 [30–32], MnO_2 [33, 34], ZnO [35, 36]; activation with alkalis. Various methods for modifying carbon materials are considered in details in a recent review [37].

Activated carbons are the most economically accessible materials, along with fibers and fabrics that are based on them. The surface area of such materials varies from hundreds to thousands of m^2/g, the ratio of macro-micro- and mesopores can be set at the synthesis stage. Different types of pores characterize different processes in the electrode: micropores are important for maximum sorption, mesopores for kinetics, and macropores for electrode permeability and maximization of the flow rate of purified water through the cell [27, 38–40].

Comparative characteristics of electrodes made of various carbon materials are summarized in Table 3. It should be noted that hereinafter we consider both modified and unmodified materials tested in cells for conventional capacitive deionization in the potential range of 1.0–1.4 V.

Table 3

Different carbon electrodes and its performances in CDI cells.

Electrode material type	Electrode material	Specific surface area, m^2/g	Specific capacitance, F/g	Voltage, V	NaCl solution concentration, mg/L	SAC, mg/g	Ref.
Porous carbons	CommercialAC	940	51.8	1.2	100	5.08	[41]
	OMC	844	133	1.2	–	–	[42]
	NKZCs	2566	155,83	1.2	1000	31.30	[43]
	N-HMCS/HGH	337.7	226.5	1.4	500	17.8	[44]
Carbon cloth	ACC-507-15	1339	125	1.2	–	16	[45]
	ACC	1200	–	1.2	100	5.8	[36]
	ACC/ZnO	1300	95	1.2	100	8.5	
	ACC/ZnO	1043	99	1.2	–	8.1	[46]
	ACA	2413	111.89	1.4	500	26.1	[47]
Carbon aerogel	CA	2057	156	1.2	100	29.7	[48]
Carbon nantubes and nanofibers	MO_x/CNTf	~250	50–66	1.2	250	6.5	[49]
	ACF-900	712	228	1.6	–	4.64	[50]
	ACF-900-90	1300	77	1.2	–	4.84	[51]
	CNF-600	481	1.6	1.2	2000	2	[52]
	CNF-800	579	41.8	1.2	2000	6.3	
	CNF-1000	617	52.1	1.2	2000	13.3	
Graphene-based material	RGO/ACF-10	2600	256	1.2	400	7.2	[53]
	Graphene sponge	356	205.20	1.2	500	14.9	[54]

NKZCs — novel nitrogen-rich mesoporous carbons with the zeolitic imidazolate framework-8; *N-HMCS/HGH* — N-doped hollow mesoporous carbon sphere and holey graphene hydrogel with in-plane pores; *OMC* — ordered mesoporous carbon; *ACC-507-15* — commercial activated carbon cloth textiles Kynol-507-15; *ACC* — activated carbon cloth; *ACC/ZnO* — activated carbon cloth material modified

with zinc oxide nanorods; *ACA* –activated carbon aerogel; *CA* — carbon aerogel; *MO_x/CNTf* — a porous metal oxide network interpenetrated into porous fibers of carbon nanotubes; *ACF-900* — activated carbon fiber activated at 900 ˚C; *ACF-900-90* — activated carbon fiber activation processes with N_2/CO_2 at 900 °C for 90 min; *CNF-600* — carbon nanofiber carbonized at 600 °C; *CNF-800* — carbon nanofiber carbonized at 800 °C; *CNF-1000* — carbon nanofiber carbonized at 1000 °C; *RGO/ACF-10* — reduced graphene oxide (RGO) and activated carbon nanofiber composites with varying content of RGO at 10 wt.%.

Mesoporous carbons

Mesoporous carbons (MCs) are widely used as a material for CDI electrodes due to their high specific surface area, good pore size distribution, long-term stability, and low cost [55]. MCs were first applied in CDI in 2008 [42]. The authors showed that, under the same electrochemical conditions, the specific capacitance value of the MC electrode was 1.2 times higher than that of the activated carbon electrode (133 F/g and 107 F/g, respectively). In cell tests at a potential of 1.2 V and a salt solution concentration of 0.5 mg/L, the amount of adsorbed ions on the MC and activated carbon electrodes was 677.9 μg/g and 251.3 μg/g, respectively. The authors of the study attribute the better performance of MCs to the presence of pores with an optimal size (~3 nm) for ion sorption. Modern methods for producing various mesoporous carbons are summarized in recent reviews [56–58].

The main drawbacks of such materials are the need of hydrophobic binders used in the electrode formation process (which reduces the efficiency of charged particle sorption) and low conductivity. To solve the first problem, alternative binders such as PVA [59], PU [60] poly(arylene)sylphone [61], etc. are actively being developed. To solve the second problem, various modifications of the material are applied: heteroatom doping [43, 44], creation of composites with carbon nanotubes [49], modifications with semiconducting oxides [46] or the introduction of conductive additives [62].

A mesoporous carbon material with one of the best performance to date was obtained in 2020 [63], with SAC values of 23.9 mg/g, 46.3 mg/g and 83.0 mg/g for saline solutions of 250 mg/mL, 500 mg/mL and 1000 mg/L, respectively. This result is of great interest not only due to the extremely high SAC value but also because the material does not require any modifications. Thus, the average SAC value for N-modified coals is about 25 mg/g, for undoped coals it is much lower [64]. For example, in a study [43], nitrogen-rich mesoporous carbons (NKZCs) were synthesized using a zeolite imidazolate framework-8. CDI cell testing showed a SAC of 31.30 mg/g for NKZCs electrodes in a 1000 mg/L NaCl solution at 1.2V, which is higher than the carbons made from the ZIF-8/KOH composite. (SAC-20.29 mg/g) and undoped ZIF-8 (SAC-17.18 mg/g). The specific surface area of NKZCs was 2566 m^2/g, the pore volume was 1.65 cm^3/g.

A good cycling stability for mesoporous carbon-based cells is considered to be 100 cycles or more [65]. One of the records of cycling stability is a hierarchical porous carbon synthesized in [66], which has a low SAC of 13.3 mg/g and can cycle for 600 cycles without losing efficiency.

Despite the extremely wide prevalence of mesoporous carbon materials as electrodes for CDI, we have not found any recent reviews dedicated to them, except the work [67]. These materials are partially reviewed in 2017 in work [68] and in the review dedicated to metal-organic framework derived carbon for CDI [69]. We summarized some salt capacity electrosorption of various types of hierarchical carbon materials in Table 4.

Table 4

Comparison of salt capacity electrosorption of various types of hierarchical carbon materials from the literature.

CDI electrode material	Cell voltage, V	NaCl solution concentration, mg/L	SAC, mg/g	Ref.
Activated mesoporous carbon sheets	1.4	1000	3.5	[70]
Hierarchical ordered mesoporous silicon carbide-derived carbon	1.2	290	12.8	[71]
Graphene sponge	1.2	500	14.9	[54]
Hierarchically porous carbon derived from PolyHIPE	1.2	300	17.5	[72]
3D foam-like carbon nanoarchitectures	1.4	300	13.5	[73]
Carbon nanofibers reinforced 3D porous carbon polyhedra network	1.2	500	16.98	[74]

Micro/mesoporoussheets	1.2	300	15.34	[75]
3D porousgraphene	1.4	300	8.97	[76]
Hierarchicalporouscarbon	1.2	580	7.75	[77]
3D Channel-structuredgraphene	1.5	295	9.6	[78]
HierarchicalporouscarbonsHPCs	1.2	292	12.63	[79]
	1.2	292	14.0	

Carbon cloth

The second most accessible and promising material for commercial CDI cells is carbon cloth. The use of this material for electrode fabrication eliminates the need of hydrophobic polymer binders, as well as leads to simplification of the electrode manufacturing process, reducing it to cutting the material. In addition, the use of carbon fabric makes it possible to abandon the use of current collectors by connecting the contact directly to the electrode [39, 80].

Increasing the specific surface area of carbon cloth and the efficiency of salt sorption can be achieved by modifying the surface with semiconductor nanoparticles. In addition, the deposition of a semiconductor enhances the uniformity of the electric field distribution at the electrode-electrolyte interface and reduces resistance, leading to lower losses during device operation [35, 36, 46]. In [46] the authors achieved a 40 % increase in SAC (from 5.7 mg/g to 8.1 mg/g) compared to unmodified carbon cloth electrodes by surface modification with ZnO nanorods. Typical characteristic values of modified carbon cloths compared to conventional ones are presented in Table 5 [81].

Table 5

Various activated carbon cloth (ACC) electrodes and their CDI treatment performance [81].

Carbon electrode	Specific surface area, m^2/g	Cell voltage, V	NaCl solution concentration, mg/L	SAC, mg/g
ACC	984	1.6	1000	5.4
	1043	1.2	100	–
	1980	1.0	5844	1.8
	1200	1.2	100	5.8
	1980	1.2	5844	–
ACC/ZnO	1300	1.2	100	8.5
	637	1.6	1000	8.1
ACC/titania	1180	1.2	5844	8.1
	1890	1.0	5844	4.3
	546	1.2	500	–

Carbon aerogel

Carbon aerogel is one of three most commonly used materials for capacitive deionization (CDI). Aerogels were first used in CDI cells in 1995 [82]. Additional activation of carbon aerogel can improve its characteristics. For example, in the study by [47], this material was synthesized by the sol-gel method from glucose and then activated with KOH. The resulting carbon aerogels showed better characteristics (Table 6) compared to conventional carbon aerogels: the specific surface area and total pore volume increased from 567 m^2/g and 0.300 cm^3/g (activated carbon) to 2413 m^2/g and 1.389 cm^3/g (carbon aerogel), and the specific capacitance increased from 19.70 F/g to 111.89 F/g. The specific adsorption capacity values were determined during desalination of a NaCl solution with a concentration of 100 mg/L and 500 mg/L at a liquid flow rate of 30 ml/min, with a maximum SAC value of 26.1 mg/g.

Table 6

Comparison of NaCl adsorption capability of ACA electrode and other electrode materials [47].

Electrode materials	Adsorption conditions			SAC, mg/g
	Voltage, V	NaCl solution concentration, mg/L	Flow speed, ml/min	
Carbon aerogel	1.2	500	50	15.7
Porous carbons	1.2	500	30	17.2
Activated carbon	1.5	1000	50	14.6

Porous carbon spheres	1.2	500	20	15.8
Porous carbon spheres	1.6	500	50	5.8
Graphene	1.4	500	35	13.7
Graphene	1.8	100	50	4.8
Carbon sponge	1.2	500	80	16.1
Carbon nanofiber	1.2	1000	50	12.8
MoS_2−graphene	1.2	500	50	19.4
Activated carbon aerogel	*1.4*	*500*	*35*	*26.1*

Carbon aerogels possess the capacity to adsorb heavy metals as well. The authors of [48] conducted studies on the adsorption of Cu^{2+} on a carbon aerogel synthesized by the sol-gel method from resorcinol and formaldehyde. A Cu_2SO_4 solution with a concentration of 100 mg/L was used as a model, and the specific adsorption capacity (SAC) was evaluated at different potentials on the cell (0.4-1.5 V). The best result of 29.7 mg/g was obtained at a potential of 1.2 V.

However, despite the fact that aerogels have all the characteristics for CDI processes, their use is limited due to the high cost of production [67, 68].

Carbon nanotubes and nanofibers

Carbon nanotubes are a type of one-dimensional material with a hollow structure, characterized by high conductivity and good mechanical and chemical stability [83]. The high conductivity of CNTs makes it possible to use them as electrode materials and current collectors simultaneously. This also makes it possible to reduce the contact resistance and increase the power density [84]. As electrodes in CDI cells, carbon nanotubes were first used in 2005 [85].

The main problem of usage of a carbon nanotubes is the need for a binder to form the electrode. However, in the case of CNTs, alternative solutions are possible: growing directly on the surface of current collectors [86] or embedding CNTs into the carbon electrode structure [95]. For example, in [49], a CDI cell, including an anode and a cathode made of g-Al_2O_3/CNT and SiO_2/CNT, respectively, showed a SAC of 6.5 mg/g and high performance compared to a number of other materials. The authors attribute the high efficiency to the morphology of the electrodes, in which CNT fibers act simultaneously as a current collector, active material, and metal oxide substrate. This architecture exhibits high capacitance with minimal internal resistance.

Close relatives to carbon nanotubes are carbon nanofibers (CNF), which can be obtained by electrospinning method [87]. The properties of this material can be easily varied: for example, the authors of [50] changed the diameter of the obtained nanofibers within the range of 285-800 nm by varying the activation temperature from 750 to 900 °C. The obtained material had a specific surface area within the range of 335-712 m^2/g and showed a maximum SAC of 4.64 mg/g at a cell voltage of 1.6 V.

The authors of [52] showed a higher value of SAC. In this work, a carbon nanofiber was fabricated by electrospinning followed by one-stage carbonization using phenol resin as a precursor. While testing such electrodes in a CDI cell, SAC value of 50.1 mg/g at a voltage of 1.2 V was achieved, the concentration of the salt solution was 2000 mg/L. Similar values were obtained by the authors of [88]: in their work, the electrodes demonstrated a specific surface area of 3066 m^2/g, a pore volume of 2.23 cm^3/g, and a SAC of 47.22 and 63.83 mg/g in a saline solution with a concentration of 500 mg/l at potentials of 1.2 and 1.6 V, respectively.

It should be noted that despite the good characteristics of electrodes based on carbon nanotubes, their use is associated with the highest risk of developing oncological diseases (compared to other carbon materials) if particles of the material get into the treated drinking water [89].

Graphene-based electrodes

Graphene is a 2D material consisting of a monolayer of sp2-hybridized carbon atoms. Graphene has a number of unique properties, such as high mechanical strength, large specific surface area (2630 m^2/g), high charge carrier mobility, and others [90]. Despite the enormous potential of graphene as a material for electrodes in CDI cells, it is relatively rarely used. This is due to the fact that graphene monolayers can spontaneously agglomerate, which reduces the specific surface area, affects the electrode conductivity and ion transfer rate [91, 92].

One way to solve this problem is to introduce other carbon materials into the graphene matrix. For example, in [53], co-electrospinning of reduced graphene oxide and activated carbon nanofiber was used, followed by activation at 800 °C. The authors noted that the reduced graphene oxide and activated carbon nanofiber electrode exhibited SAC of 7.2 mg/g in 400 mg/L saline. The parameters of the specific surface area and pore size of the electrode made of reduced graphene oxide and activated carbon nanofiber were 621 m^2/g and 0.35 cm^3/g, respectively. Other solutions of the problem can be the doping of graphene with pyrgenic SiO_2 nanoparticles [93], the introduction of conductive polymers [94], or the bonding of graphene sheets using large functional groups [95]. A side effect of using the above methods is a drop in the stability of the composite material. It is also worth highlighting the use of crumpled graphene sheets [96, 97]. The authors of [98] showed that this solution makes it possible to obtain a material with a high specific surface area of 1568 m^2/g and a good SAC of 1.72 mg/g.

Recent advances in the field of graphene-based materials for CDI application are summarized in a number of recent reviews [99–102].

Non-carbon electrode materials

The main alternative to carbon materials in CDI are faradaic materials. These include primarily materials for electrodes in Na-ion and Cl-ion batteries, less commonly materials for Li-ion batteries and conducting polymer materials.

The most utilized materials for CDI are those used in Na-ion batteries. Among them, it is worth highlighting 1D channel structures based on α-, β-, and γ-MnO_2, layered 2D structures based on δ-MnO_2, transition metal dichalcogenides, carbides, nitrides, MXenes, and 3D structures based on λ-MnO_2. Notably, sodium manganese oxide (Na_xMnO_2) deserves separate attention due to its ability to form tunnel, layered, or mixed structures, which is dependent on the quantity of sodium [24].

In 2014, the first cell with a $Na_4Mn_9O_{18}$ anode and a porous carbon cathode separated by anion-exchange membrane was introduced [23]. When cathode was charged by a negative voltage, sodium ions were embedded in the material and released into the solution upon voltage inversion. The material had an SAC of 31.2 mg/g, which was much higher than that of a traditional activated carbon electrode at that time. This work initiated the investigation of a new class of CDI architectures — hybrid CDI.

One-dimensional materials based on manganese oxide allow to obtain a wide range of channel diameters, which can increase the selectivity of sorption for larger cations such as Ca^{2+} or Mg^{2+}. In [103], the authors obtained a material characterized by channels of various sizes, which allowed for the simultaneous accumulation of cations of different radii, such as Na^+, K^+, and Mg^{2+} (Fig. 3).

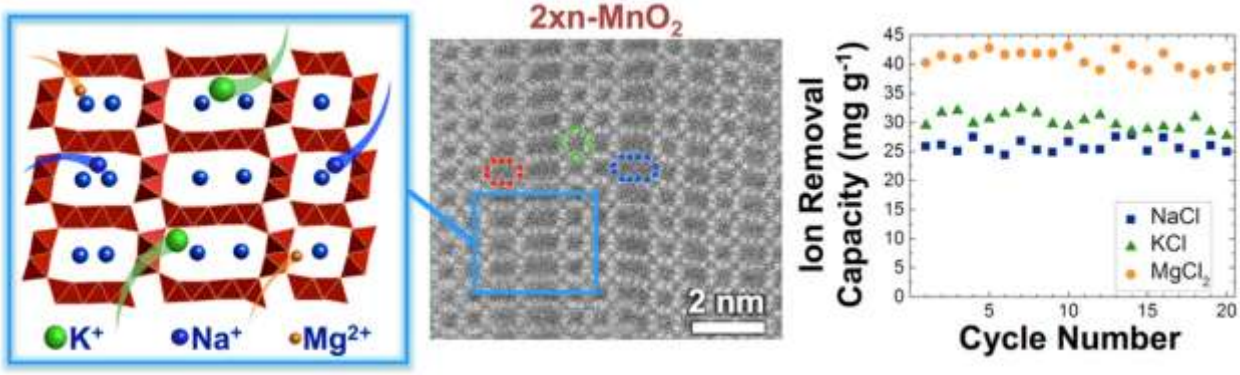

Figure 3. Scheme of available sizes for accumulating ions of various radii in a faradaic material based on MnO_2 structure [103].

Layered two-dimensional materials, such as MoS_2 [104], TiS_2 [105, 106], V_2O_5 [107], MXenes [108], etc, store ions between their layers. Some of these materials exhibit pseudocapacitive behavior and can store both cations and anions, while others show battery-like properties and can store only cations. All these materials have good specific capacitance and SAC, however, they also have a number of drawbacks. Restacking of interlayers and rapid degradation due to volume changes during intercalation-deintercalation processes are common issues [109].

Three-dimensional faradaic materials for CDI are mainly represented by NASICON structural type. Such electrodes are characterized by fantastic SAC values up to 130 mg/g [110, 111], which are unattainable

for carbon materials. The main problems of NASICONs are the high selectivity (intercalation of ions other than sodium is practically impossible) and the significant volume expansion during the operation.

Faradaic materials for CDI are described in detail in a number of recent reviews [24, 64, 112], so we will not consider them. Briefly, the advantages and disadvantages of the considered types of materials for electrodes in CDI cells are summarized in Table 7.

Table 7

Advantages and disadvantages of various adsorption materials for CDI process.

Material	Advantages	Disadvantages
Mesoporous carbons	Good SAC, lowest cost, control of pore size distribution	Small pore size, high degree of pore bending
Carbon fiber and carbon cloth	Low cost, ease of processing, wide availability of commercial samples	Medium SAC, difficult technology to manufacture in the lab
Carbon aerogels	High specific surface area, control of pore size distribution	High costs
Carbon nanotubes and nanofibers	High surface area, great electrical conductivity, high cycling stability	High tendency to aggregate (drop in specific surface area), need for hydrophobic binder, low SAC
Graphene	High surface area, great electrical conductivity	Extreme tendency to aggregation (drop in specific surface area, SAC, etc)
Metal-carbon materials	High specific capacitance, wettability and good electrochemical performance	Complicated production process and high cost
Faradaic materials	Very high specific capacitance and SAC	Complicated production process and high cost Insufficient cyclic stability, high selectivity, significant volumetric expansion of the material

To sum up, there are following trends in the development of carbon materials for CDI: currently, the best results are achieved with classical mesoporous carbons, although the average specific adsorption capacity (SAC) of 25 mg/g for this type of material is still relatively low. Recently, materials with various modifications have been actively studied, including N and B doping, development of composite materials that include both classical carbon and nanoscale materials, and the active exploration of possibilities for transitioning from classical binders (such as PVDF) to more hydrophobic ones. However, there are also harmful trends: when multiple modifications are introduced in pursuit of improving one characteristic, authors often lose ground in others. Therefore, we would like to emphasize the need for a rational approach in the design and development of new materials [113].

The use of faradaic materials as electrodes for CDI seems to be more promising in terms of seawater desalination. Such materials currently allow the desalination of much more concentrated solutions in comparison with classical carbon materials. Nevertheless, this direction has its own peculiarities, among which it is necessary to highlight the extremely high selectivity for the removal of Na^+ and Cl^- ions, which does not allow most materials to be used for water purification from heavy metals and associated ions. The second feature is the presence of a small amount of faradaic materials suitable for capturing Cl^- anions. In fact, currently there are only 3 materials for Cl^- storage in CDI systems: these are MXenes [108], BiOCl [114] and Ag [115]. Adapting other materials used in batteries for Cl^- storage seems to be a promising task. The third feature is that due to the specificity of materials and processes involved, symmetric CDI cells cannot always be created. This leads to the fact that different amounts of electrons may be required to remove ions of opposite charge [114], which means that without additional optimization and synchronization of the processes occurring at the electrodes, such CDI cells will have a reduced desalination efficiency. However, most current research ignores the issue of cell balancing, both in the case of Faraday and carbon electrode materials, focusing solely on the efficiency of the finished system. We highly recommend performing individual ion capture studies for each electrode and optimizing finished cells.

A separate problem is the degradation of electrode materials during operation. And if for faradaic materials this problem is associated with a change in volume during operation and is universal for CDI and batteries, then for carbon materials this problem is unique and does not manifest itself in other applications. We will discuss this issue in details in the next section.

Degradation of electrodes

The most common process of electrode degradation is the process of anodic oxidation, when oxygen-containing functional groups are formed on the surface of the electrode. The reactions describing this process are presented below [64]:

$C + H_2O \rightarrow C{=}O + 2\,H^+ + 2e^-$

$C + H_2O \rightarrow C\text{-}OH + H^+ + e^-$

$C + 2\,H_2O \rightarrow CO_2 + 4\,H^+ + 4e^-$, $E^0 = 0.21$ V/SHE

First, the formation of functional groups disrupts the uniform distribution of potential both on the electrode surfaces and between them, leading to faster cell wear. Second, the formation of new groups reduces the available surface area and pore volume. Finally, this undesirable surface modification leads to an "inversion effect", which is characterized by the displacement of anions from the surface of the charged cell, resulting in a decrease in efficiency [25, 116]. The authors of [117] observed this phenomenon during cycling of a symmetric cell in the +1.2/0 V mode, which led to a decrease in the SAC index from 7.3 to 0.5 mg/g over 70 cycles. Transitioning from a symmetric to an asymmetric cell and optimizing the operating mode (+0.8/-0.4 V) increased cyclability to over 120 cycles without loss of effectiveness while maintaining SAC of 6.3 mg/g. In [118] it is shown that activated carbon tissue undergoes oxidation in Na_2SO_4 or KH_2PO_4/KOH buffer solutions at potentials ranging from -1.5 to 5.0 V. The Table 7 summarizes XPS data, BET surface area determinations, and pH at the point of zero charge for samples subjected to various conditions. It can be seen that the available surface area decreases with increasing applied potential and simultaneous changes in the C and O contents in favor of the formation of oxygen-containing groups on the surface (Table 8). The shift in pH at point of zero charge (pH_{PZC}) from 7.40 to 3.21 also indicates an increase in surface acidity. Based on the research results, the authors propose an optimal range of potentials from -1.5 V to +0.8 V, which is significantly lower than the classical potential values on the cell in the sorption mode (+1.2-1.6 V).

Table 8

Surface textural properties of pristine and polarization treated ACC samples [118].

Sample	S_{BET}, m^2/g	V_{tot}, cm^3/g	C	H	O	pH_{PZC}
ACC	1596	0.697	85.9	1.13	13.0	7.40
ACC + 0.5	1549	0.671	85.1	1.12	13.8	6.83
ACC + 0.8	1541	0.655	81.4	1.15	17.4	6.34
ACC + 1.5	1488	0.652	76.8	1.45	21.8	3.95
ACC + 5.0	1300	0.559	68.3	0.98	30.8	3.21
ACC − 1.5	1518	0.662	84.4	1.14	13.3	7.32

The second undesirable process is cathodic reduction, characterized by the following reactions:

$O_2 + 2\,H^+ + 2e^- \rightarrow H_2O_2$, $E^0 = 0.69$ V/SHE

$H_2O_2 + 2\,H^+ + 2e^- \rightarrow 2\,H_2O$, $E^0 = 1.78$ V/SHE

$O_2 + 4\,H^+ + 4e^- \rightarrow 2\,H_2O$, $E^0 = 1.23$ V/SHE

It can be seen that the main process here is a two-electron transfer with the formation of hydrogen peroxide, which is a strong oxidizing agent. The formation of H_2O_2 in the system further exacerbates the anodic oxidation process. There are several options for solving this problem: modification of the surface of a carbon material [119, 120], the use of membrane technologies [121], which prevent the access of oxygen to the electrode, or the transition to inversion CDI [26]. However, these solutions have their drawbacks: for example, the use of ion-selective membranes and modification of electrodes significantly increase the cost of the device, and iCDI devices cannot compete with classical systems yet.

Regarding non-carbon materials, they are not subjected to oxidation processes during device operation, however, they have their own issues related to the volume change during ion intercalation/deintercalation [24].

Commercial prototypes

Large-scale commercial applications of CDI cells are rarely discussed in major reviews, indicating that the technology is still in its early stages. Nevertheless, the number of patents with the C02F1/4691 code (treatment of water, waste water, or sewage by electrochemical methods; by electrochemical separation, e.g. by electro-osmosis, electrodialysis, electrophoresis; capacitive deionization) has been growing exponentially in the past 25 years (Fig. 4). The leader in the field is China with approximately 40 % of published patents,

followed by South Korea and the US, each with about 19 %. Approximately 9 % of the patents belong to European countries and WIPO, while the remaining countries account for less than 5 % of the patents (Fig. 4). These data collectively indicate the potential of the technology and the interest of the global community in its development.

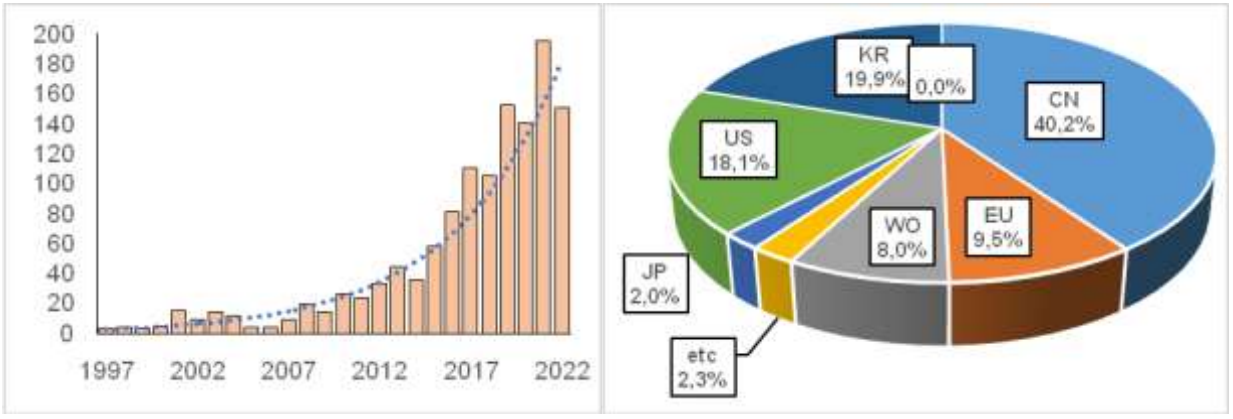

Figure 4. The number of published patents with C02F1/4691 classifier since 1997 till 2022 (left) and the ratio of country codes in these patents (right). CN — China, EU — European countries, WO — WIPO, JP — Japan, US — United States, KR — South Korea, etc. — other countries.

Interestingly, that among the data we analyzed, patents with flow-by cell geometry are rare, in contrast to scientific articles, where such a geometry is used almost universally. As we pointed out at the beginning of the review, the flow-through geometry does not require optimization of the dimensions of the fluid flow channel and separator, which, apparently, simplifies the scaling of the system.

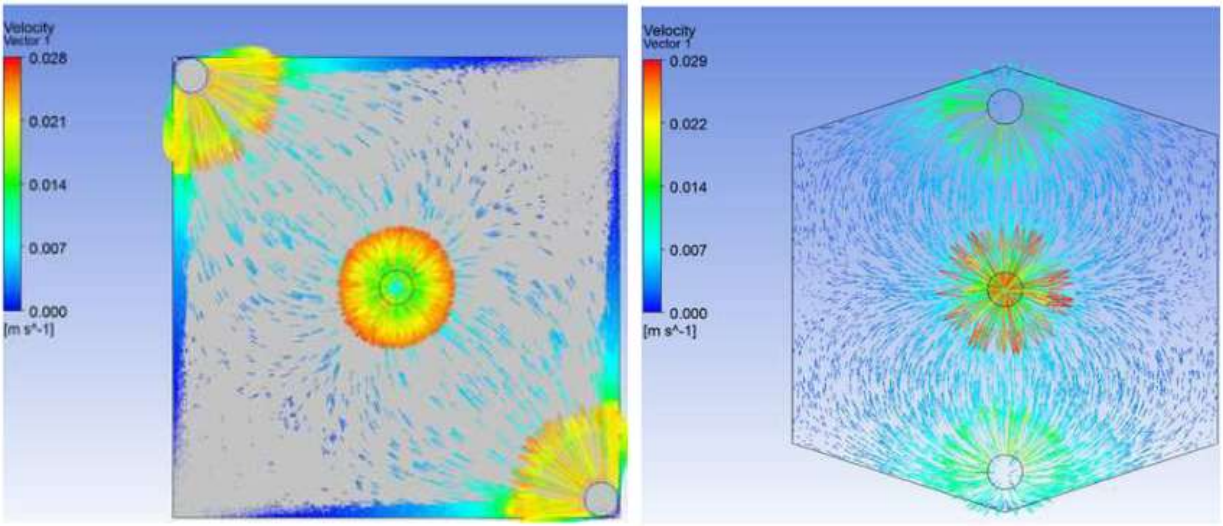

Figure 5. Calculated fluid flow vectors in the square (left) and hexagonal (right) CDI cells [122].

Most of the patents concerning the assembly of the CDI system describe conventional cells [123–125] or MCDI cells [126–128], in recent years FCDI cells [129–131] have also been represented. We have not found any patents for systems with asymmetric electrode geometry. In addition to systems that include only a CDI cell, various combinations of purification systems are also described: ED-CDI [132, 133], FO-CDI [134], RO-CDI [128, 135], PVD-CDI [136], etc.

A lot of patents do not provide any information about any tests of described systems, which makes it difficult to analyze and evaluate the data provided. Nevertheless, we have tried to select a number of works that are interesting from our point of view, concerning configurations and assembly of prototypes. In particular, patent [123] describes the procedure for assembling a conventional CDI cell with an optimized desalination efficiency of 93 %. Liquid inlet is carried out along the plane of the electrodes, outlet from the

center, perpendicular to the plane. We did not find such a cell geometry in scientific articles, but it is not rare in patents [127, 137]. The work [122] describes the optimization of the shape of the flow chamber of the cell, it is shown that the hexagonal shape makes it possible to achieve a much more uniform liquid flow, which increases the purification efficiency (Fig. 5).

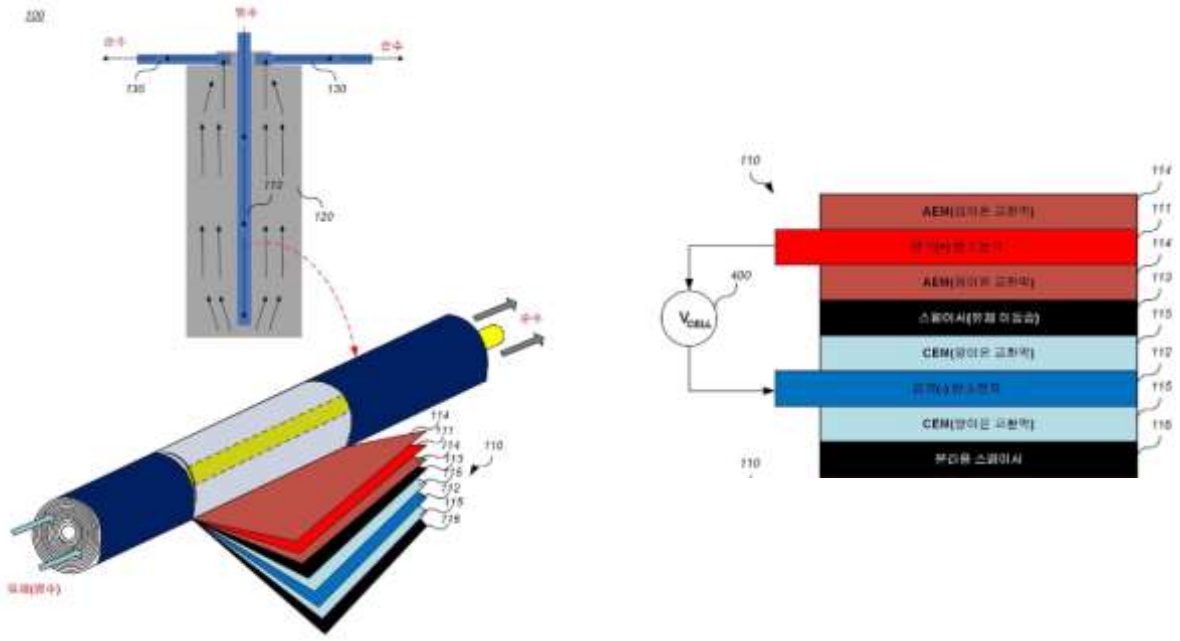

Figure 6. Schematic of a cylindrical CDI module with a winding of a six-layer MCDI [127].

Multilayer cylindrical modules [127] represent another intriguing solution. For this, a six-layer flexible MCDI with two separators (Fig. 6) is assembled, which is wound around the hollow central axis of a cylindrical container. The scheme of fluid flow through the module is shown in Figure 7. Variation of the number of layers makes it easy to control the capacity of the module, the winding process is widely used technologically and does not require the development of additional systems. The procedure for fabricating flexible electrodes for MCDI is described in a patent [129].

Another solution we did not find in the scientific articles is to increase the working area of the electrodes by corrugation [137]. However, this solution seems inefficient, since it entails an increase in the thickness of one module, which leads to an increase in the cost of a full-size installation. FCDI patents mainly describe the general principles for creating such systems, the most interesting prototype is described in [131] with a desalination efficiency of 75 %.

A semi-industrial CDI system available on the international market is the CapDI system manufactured by Voltea [125, 138–140]. System modules are an assembly of several square MCDI cells. Liquid inlet is carried out through 2 holes on opposite square edges, outlet is manufactured through the central hole. The average voltage on the cell is 1 V, the efficiency of desalination is 25-90 %, depending on the characteristics of the source water.

Summary and outlook

Currently, CDI technology is one of the most energy-efficient and cost-effective technologies for desalinating brackish and, in near future, seawater, which makes it extremely attractive for researchers around the world. Ideal materials that can be used as electrodes in CDI systems are various carbon materials similar to those used in supercapacitors. Their comprehensive research has been actively carried out for several decades, and to date there is a huge number of options for various carbon materials suitable for use in CDI systems. The use of well-studied faradaic materials has allowed for further increases in SAC and has shown potential for desalination not only of brackish water but also seawater.

The main methods for improving the characteristics of both carbon and faradaic materials are the methods of modification of bulk material or its surface. However, there are not many studies devoted to the purification of not ideal solutions based on NaCl, but real samples or at least model systems consisting of various ions. This is especially true for works dedicated to faradaic electrodes that have high selectivity for

Na^+ ions. Also, many researchers in the pursuit of improving one characteristic lose in a number of others, which indicates the insufficient use of rational approaches to design and obtaining new materials for electrodes in CDI cells. In addition, it should be noted that there are only a few works devoted to optimizing cell geometries, studying processes occurring in the pre-electrode space, and mechanisms underlying ion sorption/intercalation. Such neglect of fundamental research leads to the underestimation of key indicators of CDI systems, as researchers often conduct tests of unoptimized systems. In articles devoted to the study of hybrid cells based on faradaic and carbon materials, the absence of balancing the cathode and anode is often encountered, although the processes occurring on them are fundamentally different. We urge researchers to conduct their work more carefully and take these aspects into account. We would also like to draw the attention of researchers to the lack of unified protocols for testing CDI cells, the use of different SAC designations and different units for measuring the concentrations of starting salt solutions, which makes it difficult to evaluate and analyze published works.

Commercial use of CDI cells is currently in its early stages. However, there is a certain interest in this direction: the number of patents related to this technology is steadily increasing and in recent years it has been around 200 works per year. In recent years, works [141, 142] have been published on the techno-economic analysis of CDI technology compared to alternative water purification methods, which have shown that there are several challenges on the path to successful commercialization of the technology. The main challenge is electrode degradation caused by anodic oxidation in the case of carbon materials and volume changes during cycling in the case of faradaic materials. To a large extent, this problem can be solved by ion exchange membranes, but this leads to a complication of the system and an increase in its cost. Solving these problems at a fundamental level will make it possible to significantly increase cell cycling, reduce depreciation costs and move CDI technology to a fundamentally new level.

Acknowledgments

V.P. acknowledges the financial support from the Science Committee of the Ministry of Education and Science of the Republic of Kazakhstan (Scientific Research Grant no. AP14872549).

References

1 Fry, L.M., Mihelcic, J.R. & Watkins, D.W. (2008). Water and nonwater-related challenges of achieving global sanitation coverage. *Environ. Sci. Technol., Vol. 42*(12), P. 4298–4304.

2 Borsani, R. & Rebagliati, S. (2005). Fundamentals and costing of MSF desalination plants and comparison with other technologies. *Desalination, Vol. 182,* 1–3, P. 29–37.

3 Murphy, G.W. & Tucker, J.H. (1966). The demineralization behavior of carbon and chemically-modified carbon electrodes. *Desalination, Vol. 1*(3), P. 247–259.

4 Greenlee, L.F. et al. (2009). Reverse osmosis desalination: Water sources, technology, and today's challenges. *Water Research, Vol. 43*(9), P. 2317–2348.

5 Strathmann, H. (2010). Electrodialysis, a mature technology with a multitude of new applications. *Desalination, Vol. 264*(3), P. 268–288.

6 AlMarzooqi, F.A. et al. (2014). Application of Capacitive Deionisation in water desalination: A review. *Desalination, Vol. 342,* P. 3–15.

7 Kang, J. et al. (2014). Comparison of salt adsorption capacity and energy consumption between constant current and constant voltage operation in capacitive deionization. *Desalination, Vol. 352,* P. 52–57.

8 Zhao, R. et al. (2013). Energy consumption in membrane capacitive deionization for different water recoveries and flow rates, and comparison with reverse osmosis. *Desalination, Vol. 330,* P. 35–41.

9 Folaranmi, G. et al. (2020). Towards electrochemical water desalination techniques: a review on capacitive deionization, membrane capacitive deionization and flow capacitive deionization. *Membranes, Vol. 10*(5), P. 96.

10 Turek, M. (2003). Cost effective electrodialytic seawater desalination. *Desalination, Vol. 153,* 1–3, P. 371–376.

11 Ma, J. et al. (2020). Free-standing Ti3C2Tx MXene film as binder-free electrode in capacitive deionization with an ultrahigh desalination capacity. *Chemical Engineering Journal, Vol. 384,* P. 123329.

12 Yang S. et al. (2016). Flow-Electrode Capacitive Deionization Using an Aqueous Electrolyte with a High Salt Concentration. *Environ. Sci. Technol, Vol. 50*(11), P. 5892–5899.

13 Volfkovich, Yu.M. (2020). Capacitive deionization of water (a review). *Russ J Electrochem, Vol. 56*(1), P. 18–51.

14 Lee, J.-B. et al. (2006). Desalination of a thermal power plant wastewater by membrane capacitive deionization. *Desalination, Vol. 196*(1), P. 125–134.

15 Jeon, S. et al. (2013). Desalination via a new membrane capacitive deionization process utilizing flow-electrodes. *Energy Environ. Sci, Vol. 6*(5), P. 1471.

16 Rommerskirchen, A. et al. (2020). Flow-electrode capacitive deionization enables continuous and energy-efficient brine concentration. *Desalination, Vol. 490,* P. 114453.

17 Park, H. et al. (2016). Surface-modified spherical activated carbon for high carbon loading and its desalting performance in flow-electrode capacitive deionization. *RSC Adv, Vol. 6*(74), P. 69720–69727.

18 Hatzell, K.B. et al. (2014). Capacitive deionization concept based on suspension electrodes without ion exchange membranes. *Electrochemistry Communications, Vol. 43,* P. 18–21.

19 Liang, P. et al. (2017). Optimized desalination performance of high voltage flow-electrode capacitive deionization by adding carbon black in flow-electrode. *Desalination, Vol. 420,* P. 63–69.

20 Li, H. et al. (2011). A comparative study on electrosorptive behavior of carbon nanotubes and graphene for capacitive deionization. *Journal of Electroanalytical Chemistry, Vol. 653*(1), P. 40–44.

21 Cho, Y. et al. (2019). Flow-electrode capacitive deionization with highly enhanced salt removal performance utilizing high-aspect ratio functionalized carbon nanotubes. *Water Research, Vol. 151,* P. 252–259.

22 Murphy, G.W. & Caudle, D.D. (1967). Mathematical theory of electrochemical demineralization in flowing systems. *Electrochimica Acta, Vol. 12*(12), P. 1655–1664.

23 Lee, J. et al. (2014). Hybrid capacitive deionization to enhance the desalination performance of capacitive techniques. *Energy Environ. Sci, Vol. 7*(11), P. 3683–3689.

24 Li, Q. et al. (2020). Faradaic Electrodes Open a New Era for Capacitive Deionization. *Adv. Sci, Vol. 7*(22), P. 2002213.

25 Che, X. et al. (2019). Inverted Capacitive Deionization with Highly Enhanced Stability Performance Utilizing Ionic Liquid-Functionalized Carbon Electrodes. *ACS Sustainable Chem. Eng. American Chemical Society, Vol. 7*(18), P. 15715–15722.

26 Gao, X. et al. (2015). Surface charge enhanced carbon electrodes for stable and efficient capacitive deionization using inverted adsorption–desorption behavior. *Energy Environ. Sci, Vol. 8*(3), P. 897–909.

27 S. Bagotsky, V., M. Skundin, A. & M. Volfkovich, Y. (2014). Electrochemical power sources: Batteries, fuel cells, and supercapacitors. *Hoboken, NJ, USA: John Wiley & Sons, Inc.*

28 Porada, S. et al. (2013). Review on the science and technology of water desalination by capacitive deionization. *Progress in Materials Science, Vol. 58*(8), P. 1388–1442.

29 Jia, B. & Zhang, W. (2016). Preparation and application of electrodes in capacitive deionization (CDI): a state-of-art review. *Nanoscale Res Lett, Vol. 11*(1), P. 64.

30 Chang, L.M., Duan, X.Y. & Liu, W. (2011). Preparation and electrosorption desalination performance of activated carbon electrode with titania. *Desalination, Vol. 270,* 1–3, P. 285–290.

31 Ryoo, M.-W. & Seo, G. (2003). Improvement in capacitive deionization function of activated carbon cloth by titania modification. *Water Research, Vol. 37*(7), P. 1527–1534.

32 Ryoo, M.-W., Kim, J.-H. & Seo, G. (2003). Role of titania incorporated on activated carbon cloth for capacitive deionization of NaCl solution. *Journal of Colloid and Interface Science, Vol. 264*(2), P. 414–419.

33 Liu, Y.-H. et al. (2016). Electrodeposited Manganese Dioxide/Activated Carbon Composite As a High-Performance Electrode Material for Capacitive Deionization. A*CS Sustainable Chem. Eng., Vol. 4*(9), P. 4762–4770.

34 Wu, T. et al. (2018). Highly Stable Hybrid Capacitive Deionization with a MnO 2 Anode and a Positively Charged Cathode. *Environ. Sci. Technol. Lett., Vol. 5*(2), P. 98–102.

35 Laxman, K. et al. (2015). Effect of a semiconductor dielectric coating on the salt adsorption capacity of a porous electrode in a capacitive deionization cell. *Electrochimica Acta, Vol. 166,* P. 329–337.

36 Myint, M.T.Z., Al-Harthi, S.H. & Dutta, J. (2014). Brackish water desalination by capacitive deionization using zinc oxide micro/nanostructures grafted on activated carbon cloth electrodes. *Desalination, Vol. 344,* P. 236–242.

37 Cheng, Y. et al. (2019). A review of modification of carbon electrode material in capacitive deionization. *RSC Adv., Vol. 9*(42), P. 24401–24419.

38 Pandolfo, A.G., & Hollenkamp, A.F. (2006). Carbon properties and their role in supercapacitors. *Journal of Power Sources, Vol. 157*(1), P. 11–27.

39 Kim, C. et al. (2017). Influence of pore structure and cell voltage of activated carbon cloth as a versatile electrode material for capacitive deionization. *Carbon, Vol. 122,* P. 329–335.

40 Liu, P.-I. et al. (2015). Effects of activated carbon characteristics on the electrosorption capacity of titanium dioxide/activated carbon composite electrode materials prepared by a microwave-assisted ionothermal synthesis method. *Journal of Colloid and Interface Science, Vol. 446,* P. 352–358.

41 Liu, N.-L., Sun, S.-H., & Hou, C.-H. (2019). Studying the electrosorption performance of activated carbon electrodes in batch-mode and single-pass capacitive deionization. *Separation and Purification Technology, Vol. 215,* P. 403–409.

42 Zou, L. et al. (2008). Using mesoporous carbon electrodes for brackish water desalination. *Water Research, Vol. 42,* 8–9. P. 2340–2348.

43 Zhao, Y. et al. (2019). Nitrogen-rich mesoporous carbons derived from zeolitic imidazolate framework-8 for efficient capacitive deionization. *Electrochimica Acta, Vol. 321,* P. 134665.

44 Mi, M. et al. (2019). Hierarchical composite of N-doped carbon sphere and holey graphene hydrogel for high-performance capacitive deionization. *Desalination, Vol. 464,* P. 18–24.

45 Kim, C. et al. (2017). Influence of pore structure and cell voltage of activated carbon cloth as a versatile electrode material for capacitive deionization. *Carbon, Vol. 122,* P. 329–335.

46 Myint, M.T.Z. & Dutta, J. (2012). Fabrication of zinc oxide nanorods modified activated carbon cloth electrode for desalination of brackish water using capacitive deionization approach. *Desalination, Vol. 305,* P. 24–30.

47 Wang, W. et al. (2022). Activated carbon aerogel as an electrode with high specific capacitance for capacitive deionization. *Processes, Vol. 10*(11), P. 2330.

48 Cao, Z. et al. (2019). Preparation of carbon aerogel electrode for electrosorption of copper ions in aqueous solution. *Materials, Vol. 12*(11), P. 1864.

49 Santos, C. et al. (2018). Interconnected metal oxide CNT fibre hybrid networks for current collector-free asymmetric capacitive deionization. *J. Mater. Chem. A. Vol. 6*(23), P. 10898–10908.

50 Wang, G. et al. (2012). Activated carbon nanofiber webs made by electrospinning for capacitive deionization. *Electrochimica Acta, Vol. 69,* P. 65–70.

51 Liu, N.-L. et al. (2020). Enhanced desalination of electrospun activated carbon fibers with controlled pore structures in the electrosorption process. *Environ. Sci.: Water Res. Technol., Vol. 6*(2), P. 312–320.

52 Chen, Y. et al. (2014). Electrospun carbon nanofiber networks from phenolic resin for capacitive deionization. *Chemical Engineering Journal, Vol. 252,* P. 30–37.

53 Dong, Q. et al. (2014). Electrospun composites made of reduced graphene oxide and activated carbon nanofibers for capacitive deionization. *Electrochimica Acta, Vol. 137,* P. 388–394.

54 Xu, X. et al. (2015). Facile synthesis of novel graphene sponge for high performance capacitive deionization. *Sci Rep., Vol. 5(1),* P. 8458.

55 Lu, P. -J. et al. (2011). Chemical regeneration of activated carbon used for dye adsorption. *Journal of the Taiwan Institute of Chemical Engineers, Vol. 42*(2), P. 305–311.

56 Mehdipour-Ataei, S. & Aram, E. (2023). Mesoporous Carbon-Based Materials: A Review of Synthesis, Modification, and Applications. *Catalysts, Vol. 13*(1).

57 Pavlenko, V. et al. (2022). A comprehensive review of template-assisted porous carbons: Modern preparation methods and advanced applications. *Materials Science and Engineering: R: Reports, Vol. 149,* P. 100682.

58 Weng, J. et al. (2021). A review of metal-organic framework-derived carbon electrode materials for capacitive deionization. *New Carbon Materials, Vol. 36*(1), P. 117–132.

59 Weng, J. et al. (2021). Carbon electrode with cross-linked and charged chitosan binder for enhanced capacitive deionization performance. *Desalination, Vol. 505,* P. 114979.

60 Yen, C.H. et al. (2021). Titanium Dioxide/Activated Carbon Electrode with Polyurethane Binder for the Removal of Indium Ions via Capacitive Deionization. *Processes, Vol. 9*(8), P. 1427.

61 Asquith, B.M., Meier-Haack, J. & Ladewig, B.P. (2015). Poly (arylene ether sulfone) copolymers as binders for capacitive deionization activated carbon electrodes. *Chemical Engineering Research and Design, Vol. 104,* P. 81–91.

62 Park, K.-K. et al. (2007). Development of a carbon sheet electrode for electrosorption desalination. *Desalination, Vol. 206,* 1–3, P. 86–91.

63 Zhang, P., Li, J. & Chan-Park, M.B. (2020). Hierarchical Porous Carbon for High-Performance Capacitive Desalination of Brackish Water. *ACS Sustainable Chem. Eng. American Chemical Society, Vol. 8*(25), P. 9291–9300.

64 Sun, K. et al. (2023). Electrocapacitive Deionization: Mechanisms, Electrodes, and Cell Designs. *Adv Funct Materials.* P. 2213578.

65 Geng, C. et al. (2022). Continuous cycling of carbon-based capacitive deionization systems: An evaluation of the electrode performance and stability. *Journal of Electroanalytical Chemistry, Vol. 914,* P. 116298.

66 Baroud, T.N. & Giannelis, E.P. (2018). High salt capacity and high removal rate capacitive deionization enabled by hierarchical porous carbons. *Carbon. Vol. 139,* P. 614–625.

67 Datar, S.D., Mane, R. & Jha, N. (2022). Recent progress in materials and architectures for capacitive deionization: A comprehensive review. *Water Environment Research, Vol. 94*(3).

68 Huang, Z.-H. et al. (2017). Carbon electrodes for capacitive deionization. *J. Mater. Chem. A. Vol. 5*(2), P. 470–496.

69 Wang, H. et al. (2022). Nanoarchitectonics of Metal–Organic Frameworks for Capacitive Deionization via Controlled Pyrolyzed Approaches. *Small. Vol. 18*(2), P. 2102477.

70 Tsouris, C. et al. (2011). Mesoporous carbon for capacitive deionization of saline water. *Environ. Sci. Technol., Vol. 45*(23), P. 10243–10249.

71 Porada, S. et al. (2013). Direct prediction of the desalination performance of porous carbon electrodes for capacitive deionization. *Energy Environ. Sci., Vol. 6*(12), P. 3700.

72 Xu, X. et al. (2016). Design and fabrication of mesoporous graphene via carbothermal reaction for highly efficient capacitive deionization. *Electrochimica Acta, Vol. 188,* P. 406–413.

73 El-Deen, A.G. et al. (2016). Flexible 3d nanoporous graphene for desalination and bio-decontamination of brackish water via asymmetric capacitive deionization. *ACS Appl. Mater. Interfaces. Vol. 8*(38), P. 25313–25325.

74 Liu, Y. et al. (2016). Electrospun carbon nanofibers reinforced 3D porous carbon polyhedra network derived from metal-organic frameworks for capacitive deionization. *Sci Rep., Vol. 6*(1), P. 32784.

75 Jia, B., & Zou, L. (2012). Graphene nanosheets reduced by a multi-step process as high-performance electrode material for capacitive deionisation. *Carbon, Vol. 50*(6), P. 2315–2321.

76 Hu, W. et al. (2017). Hierarchically porous carbon derived from PolyHIPE for supercapacitor and deionization applications. Langmuir. Vol. *33*(46), P. 13364–13375.

77 Duan, H. et al. (2017). Rapid construction of 3D foam-like carbon nanoarchitectures via a simple photochemical strategy for capacitive deionization. *RSC Adv. Vol. 7*(62), P. 39372–39382.

78 Chang, L. & Hang, Hu.Y. (2019). 3D Channel-structured graphene as efficient electrodes for capacitive deionization. *Journal of Colloid and Interface Science, Vol. 538,* P. 420–425.

79 Baroud, T. & Giannelis, E. (2019). Role of Mesopore Structure of Hierarchical Porous Carbons on the Electrosorption Performance of Capacitive Deionization Electrodes. *ACS Sustainable Chemistry & Engineering, Vol. 7.*

80 Zhao, X. et al. (2020). Electrode materials for capacitive deionization: A review. *Journal of Electroanalytical Chemistry, Vol. 873,* P. 114416.

81 Maddah, H.A. & Shihon, M.A. (2018). Activated carbon cloth for desalination of brackish water using capacitive deionization. Desalination and Water Treatment. Ed. Eyvaz M., Yüksel E. InTech.

82 Farmer, J.C. et al. (1995). The use of capacitive deionization with carbon aerogel electrodes to remove inorganic contaminants from water: UCRL-JC—119844, CONF-950718—1, 80970. P. UCRL-JC—119844, CONF-950718—1, 80970.

83 Pan, H., Li, J. & Feng, Y.P. (2010). Carbon nanotubes for supercapacitor. *Nanoscale Res Lett., Vol. 5*(3), P. 654–668.

84 Frackowiak, E. & Béguin, F. (2001). Carbon materials for the electrochemical storage of energy in capacitors. *Carbon, Vol. 39*(6), P. 937–950.

85 Dai, K. et al. (2005). NaCl adsorption in multi-walled carbon nanotubes. *Materials Letters. Vol. 59*(16), P. 1989–1992.

86 Wang, H. & Na, C. (2014). Binder-Free Carbon Nanotube Electrode for Electrochemical Removal of Chromium. *ACS Appl. Mater. Interfaces. American Chemical Society, Vol. 6*(22), P. 20309–20316.

87 Kim, B.-H. et al. (2011). Solvent-induced porosity control of carbon nanofiber webs for supercapacitor. *Journal of Power Sources.*

88 Zhang, H. et al. (2023). Highly mesoporous carbon nanofiber electrodes with ultrahigh specific surface area for efficient capacitive deionization. *Carbon. Vol. 201,* P. 920–929.

89 Donaldson, K. et al. (2006). Carbon Nanotubes: A Review of Their Properties in Relation to Pulmonary Toxicology and Workplace Safety. *Toxicological Sciences, Vol. 92(1), P. 5–22.*

90 Huang, Y., Liang, J. & Chen, Y. (2012). An Overview of the Applications of Graphene-Based Materials in Supercapacitors. *Small, Vol. 8*(12), P. 1805–1834.

91 Dreyer, D.R., Todd, A.D. & Bielawski, C.W. (2014). Harnessing the chemistry of graphene oxide. *Chem. Soc. Rev, Vol. 43*(15), P. 5288.

92 Li, Z. et al. (2015). 3D porous graphene with ultrahigh surface area for microscale capacitive deionization. *Nano Energy, Vol. 11,* P. 711–718.

93 Kim, D.W., Jung, S.M. & Jung, H.Y. (2020). Long term thermostable supercapacitor using in-situ SnO2 doped porous graphene aerogel. *Journal of Power Sources. Vol. 448,* P. 227422.

94 Zhai, Z. et al. (2022). A review of carbon materials for supercapacitors. *Materials & Design, Vol. 221,* P. 111017.

95 Greenwood, J. et al. (2015). Covalent Modification of Graphene and Graphite Using Diazonium Chemistry: Tunable Grafting and Nanomanipulation. *ACS Nano, Vol. 9*(5), P. 5520–5535.

96 Yan, J. et al. (2012). High-performance supercapacitor electrodes based on highly corrugated graphene sheets. *Carbon, Vol. 50*(6), P. 2179–2188.

97 Wen, Z. et al. (2012). Crumpled Nitrogen-Doped Graphene Nanosheets with Ultrahigh Pore Volume for High-Performance Supercapacitor. *Adv. Mater., Vol. 24*(41), P. 5610–5616.

98 Amiri, A. et al. (2015). Microwave-Assisted Synthesis of Highly-Crumpled, Few-Layered Graphene and Nitrogen-Doped Graphene for Use as High-Performance Electrodes in Capacitive Deionization. *Sci Rep., Vol. 5*(1), P. 17503.

99 Chang, L., Fei, Y. & Hu, Y.H. (2021). Structurally and chemically engineered graphene for capacitive deionization. *J. Mater. Chem. A., Vol. 9*(3), P. 1429–1455.

100 Zhang, M. & Kong, W. (2020). Recent progress in graphene-based and ion-intercalation electrode materials for capacitive *deionization*. *Journal of Electroanalytical Chemistry, Vol. 878,* P. 114703.

101 Liu, Y. et al. (2023). Electrosorption performance on graphene-based materials: a review. *RSC Adv., Vol. 13*(10), P. 6518–6529.

102 Younes, H. et al. (2022). Review on 2D MXene and graphene electrodes in capacitive deionization. *Environmental Technology & Innovation, Vol. 28,* P. 102858.

103 Byles, B.W. et al. (2018). Tunnel structured manganese oxide nanowires as redox active electrodes for hybrid capacitive deionization. *Nano Energy, Vol. 44,* P. 476–488.

104 Peng, W. et al. (2020). Fabrication of 3D flower-like MoS2/graphene composite as high-performance electrode for capacitive deionization. *Desalination, Vol. 473,* P. 114191.

105 Srimuk, P. et al. (2017). Titanium Disulfide: A Promising Low-Dimensional Electrode Material for Sodium Ion Intercalation for Seawater Desalination. Chem. Mater. American Chemical Society, Vol. *29*(23), P. 9964–9973.

106 Srimuk, P. et al. (2018). Potential-Dependent, Switchable Ion Selectivity in Aqueous Media Using Titanium Disulfide. *ChemSusChem., Vol. 11*(13), P. 2091–2100.

107 Lee, J. et al. (2017). Pseudocapacitive Desalination of Brackish Water and Seawater with Vanadium-Pentoxide-Decorated Multiwalled Carbon Nanotubes. *ChemSusChem, Vol. 10*(18), P. 3611–3623.

108 Srimuk, P. et al. (2018). Two-Dimensional Molybdenum Carbide (MXene) with Divacancy Ordering for Brackish and Seawater Desalination via Cation and Anion Intercalation. ACS Sustainable Chem. Eng. American Chemical Society, Vol. *6*(3), P. 3739–3747.

109 Rajagopalan, R. et al. (2020). Advancements and challenges in potassium ion batteries: A comprehensive review. *Adv. Funct. Mater., Vol. 30*(12), P. 1909486.

110 Yue, Z., Gao, T. & Li, H. (2019). Robust synthesis of carbon@Na4Ti9O20 core-shell nanotubes for hybrid capacitive deionization with enhanced performance. Desalination, *Vol. 449*, P. 69–77.

111 Cao, J. et al. (2019). Na3V2(PO4)3@C as Faradaic Electrodes in Capacitive Deionization for High-Performance Desalination. *Nano Lett. American Chemical Society, Vol. 19*(2), P. 823–828.

112 Jiang, Y. et al. (2020). A Review of Battery Materials as CDI Electrodes for Desalination. *Water, Vol. 12*(11), P. 3030.

113 Ntakirutimana, S. et al. (2020). Activated Carbon Electrode Design: Engineering Tradeoff with Respect to Capacitive Deionization Performance. *J. Electrochem. Soc., Vol. 167*(14), P. 143501.

114 Nam, D.-H. & Choi, K.-S. (2017). Bismuth as a New Chloride-Storage Electrode Enabling the Construction of a Practical High Capacity Desalination Battery. *J. Am. Chem. Soc. American Chemical Society, Vol. 139*(32), P. 11055–11063.

115 Pasta, M. et al. (2012). A Desalination Battery. Nano Lett. *American Chemical Society, Vol. 12*(2), P. 839–843.

116 Cohen, I. et al. (2013). Long term stability of capacitive de-ionization processes for water desalination: The challenge of positive electrodes corrosion. *Electrochimica Acta, Vol. 106*, P. 91–100.

117 Lu, D., Cai, W. & Wang, Y. (2017). Optimization of the voltage window for long-term capacitive deionization stability. *Desalination. Vol. 424*, P. 53–61.

118 Bayram, E. & Ayranci, E. (2011). A systematic study on the changes in properties of an activated carbon cloth upon polarization. *Electrochimica Acta, Vol. 56*(5), P. 2184–2189.

119 Srimuk, P. et al. (2017). Enhanced performance stability of carbon/titania hybrid electrodes during capacitive deionization of oxygen saturated saline water. *Electrochimica Acta, Vol. 224*, P. 314–328.

120 Xu, X. et al. (2020). Unprecedented capacitive deionization performance of interconnected iron–nitrogen-doped carbon tubes in oxygenated saline water. *Mater. Horiz, Vol. 7*(5), P. 1404–1412.

121 Tang, W. et al. (2017). Comparison of Faradaic reactions in capacitive deionization (CDI) and membrane capacitive deionization (MCDI) water treatment processes. *Water Research, Vol. 120*, P. 229–237.

122 임지원 et al. (2017). Flow channel design of capacitive deionization unit: pat. KR101721697B1 USA.

123 문형민 et al. (2021). Electro deionization-type water treatment apparatus: pat. KR102220165B1 USA.

124 Juzkow, M. et al. (2020). Liquid treatment using capacitive systems: pat. US10538437B1 USA.

125 Wal, A. van der et al. (2021). Apparatus and method for removal of ions: pat. US11168009B2 USA.

126 Sun, Z. et al. (2016). Membrane enhanced deionization capacitor device: pat. US9272926B2 USA.

127 오현제, 안주석, 정우식. (2021). Capacitive deionization electrode module of roll type, and water treatment apparatus: pat. KR102300797B1 USA.

128 황태문 et al. (2021). Energy self-sufficient system for treating high density salty waste water and side stream using membrane capacitive deionization (mcdi) module: pat. KR102274447B1 USA.

129 Linnartz, C.J., Rommerskirchen, A. & Wessling, M. (2022). Electrochemical module comprising a flexible membrane-electrode assembly: pat. EP3877341B1 USA.

130 Kim, D. et al. (2018). Continuous flow-electrode system, and high-capacity power storage and water treatment method using the same: pat. US9963363B2 USA.

131 Wessling, M., Gendel, Y. & Rommerskirchen, A. (2016). Single module, flow-electrode apparatus and method for continous water desalination and ion separation by capacitive deionization: pat. WO2016113139A1 USA.

132 노현철, 권태옥, 진채현. (2021). Composite electrochemical brackish water desalination system combining electrodialysis and capacitive deionization process: pat. KR102250944B1 USA.

133 柳丽芬, 苑丽新. (2021). Method for removing heavy metals and organic matters through capacitive deionization coupling electrocatalysis cooperation: pat. CN108423776B USA.

134 홍승관, 곽기문, 김인혁. (2020). Membrane Capacitive Deionization-Forward Osmosis Hybrid System for Precious Metal Recover: pat. KR102129493B1 USA.

135 김영오, 최정훈, 이한샘. (2019). Treating apparatus and method for concentrated waste water using ro-cdi process: pat. KR101981019B1 USA.

136 Bordain, Y.C. et al. (2019). Photovoltaic desalination system: pat. US10361329B2 USA.

137 김홍일 et al. (2019). Desalination module apparatus using a fabric electrode: pat. KR102003373B1 USA.

138 Wal, A.V.D. & Dlugolecki, P.E. (2013). A reverse capacitative de-ionisation apparatus and method for generating electricity: pat. EP2607321A1 USA.

139 Wal, A. van der et al. (2014). Apparatus for removal of ions comprising multiple stacks: pat. US20140048418A1 USA.

140 Sullivan, J.P. (2010). Method of Operating A Capacitive Deionization Cell Using Gentle Charge: pat. US20100065438A1 USA.

141 Hasseler, T.D. et al. (2020). Process design tools and techno-economic analysis for capacitive deionization. Water Research. *Vol. 183*, P. 116034.

142 Vineyard, D. et al. (2021). Life cycle assessment of electrodialysis for sidestream nitrogen recovery in municipal wastewater treatment. Cleaner Environmental Systems, *Vol. 2*, P. 100026.

А. Захаров[1], А. Тукешева[1,2], Сайед Фахад Бин Хак[3], Джон Феррарис[3], А. Захидов[3], Т. Тажибаева[2], Т. Базарбаева[2], В. Павленко[1,2*]

Сулы ерітінділерді сыйымдылықты ионсыздандыру технологиясының қазіргі жағдайына шолу

Таза судың қолжетімділігі XXI ғасырдағы басты технологиялық, әлеуметтік және экономикалық міндеттердің бірі. Дүние жүзінде жер асты суларын өндірудің артуы тұзды судың бұлақтар мен сулы горизонттарға біртіндеп енуіне әкеледі. Бұл суды өнеркәсіп пен ауыл шаруашылығында техникалық су ретінде немесе ауыз су ретінде пайдалану үшін алдымен оны тазартып, минералсыздандыру қажет. Осылайша, тұздылығы әртүрлі суларды, әлсіз тұздыдан теңізге дейін тұзсыздандыру әдістері бірінші орынға шығады. Жүргізіліп жатқан зерттеулердің жалпы мақсаты тұзсыздандыру технологияларын, яғни энергияны тиімдірек және үнемді ету. Осы талаптарға жауап беретін перспективті технологиялардың бірі — суды сыйымдылықпен деионизациялау. Бұл технология 30 жылдан астам уақыт бойы кеңінен танымал, бірақ соңғы жылдары ғана суды сыйымдылықпен деионизациялау бойынша зерттеулерде айтарлықтай прогреске қол жеткізілді. Бұл шолуда суды сыйымдылықпен деионизациялау үшін қазіргі уақытта әзірленген жасуша архитектурасын, көміртекті материалдардағы жетістіктер қарастырылған және осы технологияны коммерцияландырудың перспективалары мен қиындықтары талқыланған.

Кілт сөздер: ССД, сыйымдылық деионизациясы, көміртекті материалдар, кеуекті көміртектер, көміртекті электродтар, фарадей электродтары.

А. Захаров, А. Тукешева, Сайед Фахад Бин Хак, Джон Феррарис, А. Захидов, Т. Тажибаева, Т. Базарбаева, В. Павленко

Обзор современного состояния технологии емкостной деионизации водных растворов

Доступность чистой воды является одной из ключевых технологических, социальных и экономических проблем XXI века. Увеличение добычи подземных вод во всем мире приводит к постепенному проникновению соленой воды в источники и водные горизонты. Для использования этой воды в качестве технической в промышленности и сельском хозяйстве или в качестве питьевой воды она должна быть предварительно очищена и обессолена. Таким образом, на передний план выходят методы опреснения вод разной солености: от слабосоленых до морских. Общая цель текущих исследований состоит в том, чтобы сделать технологии опреснения воды более энергоэффективными и рентабельными. Одной из перспективных технологий, отвечающей этим требованиям, является емкостная деионизация воды (ЕДВ). Эта технология широко известна уже более 30 лет, однако только в последние годы был достигнут значительный прогресс в исследованиях ЕДВ. В этом обзоре мы рассмотрели разработанные в настоящее время архитектуры ячеек ЕДВ, достижения в области углеродных материалов, а также перспективы и проблемы коммерциализации этой технологии.

Ключевые слова: ЕДВ, емкостная деионизация, углеродные материалы, пористые угли, угольные электроды, фарадеевские электроды.

DOI 10.31489/2023PH3/34-39

UDC: 538.93

V.G. Kytin[1,2], E.E. Kupriyanov[1], A. Apreleva[1], V.A. Kulbachinskii[1*], I.E. Korsakov[1], T.Yu. Kiseleva[1], Zh.T. Ismailov[3]

[1]Lomonosov Moscow State University, Russia;
[2]VNIIFTRI, Mendeleevo, Moscow region, Russia;
[3]Karaganda University of the name of academician E.A. Buketov, Kazakhstan
([*]E-mail: kulb@mig.phys.msu.ru)

Features of hole transport and density of localized states in $CuCr_{1-x}Mg_xO_2$ and $CuCr_{1-y}Mg_yO_2/(MgCr_2O_4)_{x-y}$ polycrystalline ceramics

Magnesium doped polycrystalline ceramic samples of cooper chromite (I) with 0.6-4.0 at % Mg content have been synthesized. Phase composition of ceramics has been investigated by X-ray diffraction. Temperature dependencies of electrical resistivity and Seebeck coefficient have been measured by four probe method and analyzed in frame of variable range hopping conductivity. The density of localized electronic states and characteristic energy of its variation near Fermi energy have been estimated. It was obtained that the density of localized states at Fermi energy increases with an increase of Mg content, while characteristic energy of variation of localized state density near Fermi energy decreases. Obtained results show that relatively large values of Seebeck coefficient in Mg doped copper chromite (I) can be understood within variable range hopping transport of holes with rapidly increasing density toward valence band maximum.

Keywords: p-type semiconductors, thermal conductivity, electrical conductivity, density of localized states.

Introduction

Copper chromite is a *p*-type semiconductor partially transparent for the visible light [1]. It makes it promising material for transparent electrodes in optoelectronic devices [2-3]. One of the key issues is its relatively large resistivity compared to the best known *n*-type transparent semiconductors as zinc oxide or indium-tin oxide [3-4]. The resistivity of copper chromite (I) can be reduced by several orders of magnitude by doping with group II elements particularly with Mg [5-8]. The mechanism of the hole transport in pure and Mg doped copper chromite remains the subject of research now. Most often copper chromite (I) is synthesized in the form of polyctrystalline ceramic or thin films. Polycrystalline ceramic of magnesium doped copper chromite (I) is usually obtained by heating of the mixture of copper, chromium and magnesium oxides in oxygen poor atmosphere during few tens of hours [6-8]. Such material exhibits up to several hundred microvolts per kelvin Seebeck coefficient together with relatively large electrical conductivity at room temperature [6-7]. Therefore temperature dependencies of resistivity and Seebeck coefficient and their analysis in frame of different models have been reported in several publications [6-8]. Hole transport in polycrystalline ceramic of magnesium doped copper chromite (I) is affected by point defects such as oxygen vacancies, dopant atoms, microstructure and morphology of the material, as well as the presence of additional phases in doped material. The question whether the band or hopping transport of holes dominates in copper chromite (I) remains the subject discussions until now.

In the present work we report the results of the measurements and analysis of the temperature dependencies of electrical resistivity and Seebeck coefficient of polycrystalline copper chromite doped with magnesium using the procedure of chemical homogenization. Magnesium content was taken below and above solubility limit. Measured temperature dependencies have been analyzed in frame variable range hopping transport approach.

Experimental

Polycrystalline Mg doped copper cromite samples were synthesized by solid phase method from a mixture of CuO, Cr_2O_3 and MgO. This mixture was obtained by thermolysis of nitrates in liquid phase solution in NH_4NO_3. Reaction and details of nitrate thermolysis were presented in [9]. According to X-ray diffraction data obtained mixtures were amorphous. The mixtures were annealed at 500-600 ^oC to dissolve the rest of nitrates. Small traces of CuO were detected by X-ray diffraction after this annealing. Then mixtures were pressed in tablets and annealed 24 hours at 1080 ^oC in argon flow for final formation of Mg

doped copper chromite (I) ceramic material and cooled to room temperature. Composition and density of obtained samples are shown in Table.

T a b l e

Mg content, density ρ, an estimated density of hole states at Fermi energy g_0, and characteristic energy of its variation δE.

Sample number	Mg content, at. %	ρ, g/cm^3	g_0, 10^{26} eV^{-1}m^{-3}	δE, eV
1	0.6	2,85	1.2	0,27
2	1,3	3,60	11	0,13
3	4	3,84	212	0,04

Typical XRD pattern of synthesized ceramics are shown in Figure 1. Only delafossite phase was detected in the samples with Mg content up to 1,3 at. %. For 4 at. % Mg content small fraction of spinel phase of $MgCr_2O_4$ was detected. This is consistent with the data of Mg solubility in copper chromite (I) reported earlier [7-10].

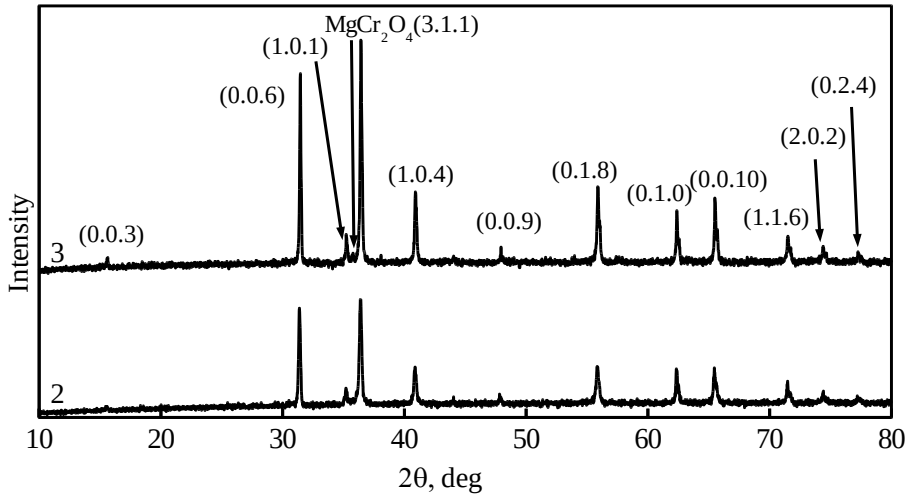

Figure 1 XRD pattern of the ceramics with different Mg content: 1 — 1,3 at %; 2 — 4 at. %

The dependence of lattice parameters on Mg content confirms incorporation of Mg in the delafossite crystalline lattice. No significant dependence of lattice parameters on the duration of synthesis was observed. Density of all samples increases with an increase of Mg content and duration of annealing.

Microstructure of synthesized samples was studied by electron microscopy and reported in previous publication [11]. The larger is the Mg content the better connected look crystallites. Fraction of empty space decreases with an increase of Mg content in accordance with observed increase of density. For the samples with 4 at % Mg formation of micrometer size $MgCr_2O_4$ crystallites is seen in SEM images.

For the measurement of electrical resistivity and Seebeck coefficient samples with rectangular shape and typical dimensions 2x2x5 mm were prepared. Electrical resistivity was measured by 4-probe method at constant current. For the measurement of Seebeck coefficient one end sample was connected to heat drain. Another end of the sample was connected to the heater. The temperature difference between potential contacts at the sample was measured by thermocouple. The voltage between these potential contacts was measured by digital multimeter for several values of temperature difference controlled by the power of the heater. Then the dependence of the voltage on the temperature difference was approximated by linear function and the value of Seebeck coefficient was obtained from the slope of the dependence.

Results and discussion

Temperature dependencies of Seebeck coefficient are shown in Figure 2. For all investigated materials Seebeck coefficient increases when temperature rises. Seebeck coefficient decreases with an increase of Mg content.

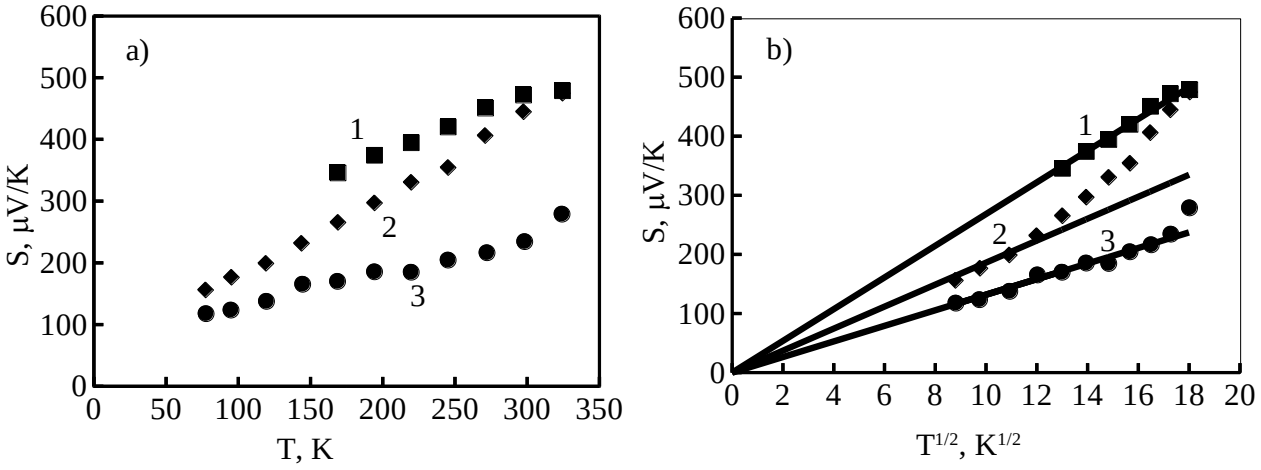

Figure 2 Temperature dependencies of Seebeck coefficient: a) S(T), b) $S(T^{1/2})$ for samples with different Mg content: 1 — 0.6 at. %; 2 — 1.3 at. %; 3 — 4 at. %. Points are experimental data. Solid lines are approximation by proportional dependence for 4 lowest temperature points.

Temperature dependencies of resistivity are plotted in Figure 3. For all samples resistivity increases with lowering of temperature. Resistivity decreases by several orders of magnitude with increase of the magnesium content from 0,6 at % to 4 at %.

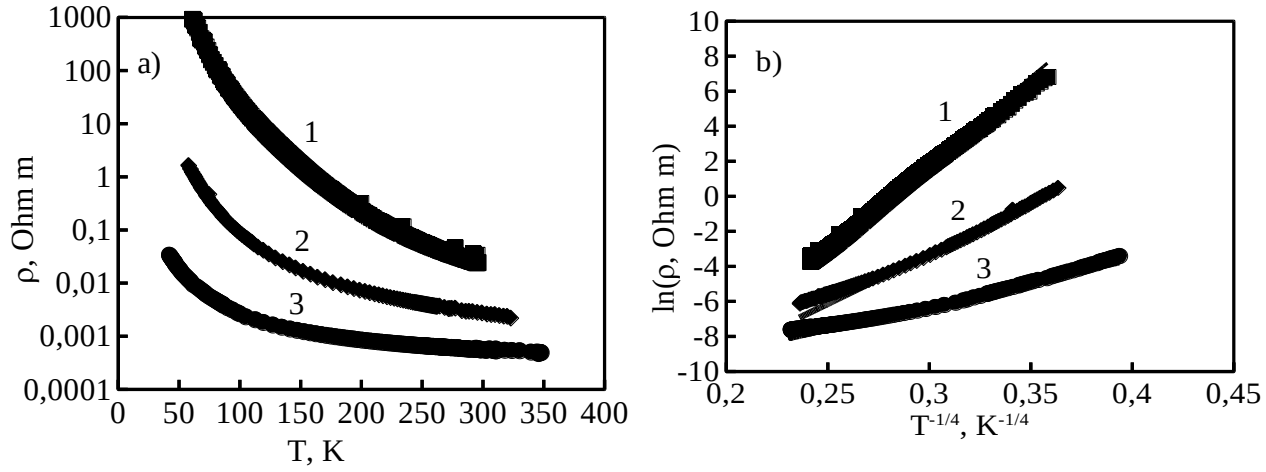

Figure 3. Temperature dependencies of resistivity: a) ρ(T) and b) $\ln(\rho(T^{-1/4}))$ for samples with different Mg content: 1 — 0.6 at. %; 2 — 1.3 at. %; 3 — 4 at. %. Points are experimental data. Solid lines are approximation by linear dependence in the temperature range of 4 lowest temperature points in the temperature dependence of Seebeck coefficient.

At temperatures below 180-300 K temperature dependencies of resistivity can be approximated by Motts law for variable range hopping conductivity [12]:

$$\rho = \rho_0 \exp\left[\left(\frac{T_0}{T}\right)^{1/4}\right], \tag{1}$$

where T_0 is determined by the density of localized states at Fermi energy g_0 and localization length a:

$$T_0 = \frac{21}{k_B g_0 a^3}, \tag{2}$$

where k_B is the Boltzmann constant.

We use the following expression derived for variable range hopping transport to fit temperature dependence of Seebeck coefficient [13]:

$$S = 0{,}1\frac{k_B^2}{e}\frac{(T_0 T)^{1/2}}{\delta E}, \quad (3)$$

where

$\delta E = \left(\frac{d\ln g}{dE}\right)^{-1}_{E=F}$ is the characteristic energy of the variation of the density of states, g is the density of localized states, F is the Fermi energy, e is the elementary charge. Temperature dependencies of Seebeck coefficient were fitted by expression (3) in the temperature range within 4 lowest temperature points. Temperature dependencies of resistivity were fitted by expression (1) in the same temperature range for each sample. The characteristic energy of the variation of the density of states near Fermi energy was estimated from the slopes of fitting lines. Obtained estimates are listed in Table.

To get an estimate of the density of localized states at Fermi energy we estimated localization length using expression for localization length and ionization energy E_a of shallow acceptors:

$$E_a = \frac{me^4}{2(4\pi\varepsilon_0\varepsilon)^2\hbar^2},\ a = \frac{(4\pi\varepsilon_0\varepsilon)\hbar^2}{me^2}, \quad (4)$$

where m is an effective mass of holes, ε_0 is the electric constant, ε is the dielectric constant, ħ is the Planck constant. We assumed that earlier observed activation energy of conductivity of undoped copper chromite (I) equal to 0,28 eV is the energy of ionization localized acceptor state [9]. An estimate of localization length was calculated using expression:

$$a = \frac{e^2}{(4\pi\varepsilon_0\varepsilon)E_a} \quad (5)$$

as an estimation for the dielectric constant we took $\varepsilon = \left(\varepsilon_p^2\varepsilon_l\right)^{1/3}$, where ε_p and ε_l are dielectric constants for in-plane and along c-axis polarization [14]. Obtained estimation value for *a* was equal to 0,29 nm. Obtained results point to a strong localization of holes. Estimated value of localization length is rather small and in general expressions (4) cannot be used for accurate calculation. The estimated density of states at Fermi energy calculated for this value of localization length is listed in Table.

As can be seen from table one density of states at Fermi energy increases by more than 2 orders of magnitude with an increase of Mg content from 0,6 at.% to 4 at. % and by more than 1 order of magnitude with an increase of Mg content from 1,3 at.% to 4 at. %. This fact points to an effective doping of copper chromite by Mg in the range of Mg content close to the solubility limit. The characteristic energy of the variation of the density of states decreases from 0,27 eV to 0,04 eV with an increase of Mg content from 0,6 at. % to 4 at. %. This variation of the density of states at Fermi energy and its derivative can take place because of the creation of localized acceptor states in the bandgap due to substitution of Cr by Mg and shift of the Fermi energy towards the valence band. The reduction of the characteristic energy of the variation of the density of states near Fermi energy with an enhancement of Mg content could point to the significant contribution of magnetic frustration to the energy fluctuations of localized electronic states. Substitution of Cr by Mg suppresses these frustrations [8, 10]. This suppression could make energy distribution of localized states narrower.

Conclusions

Temperature dependencies of electrical resistivity and Seebeck coefficient were measured in Mg doped polycrystalline copper chromite (I) and analyzed in frame of variable range hopping of holes. The estimated density of localized states and the characteristic energy of variation of the density of states near Fermi energy were calculated. Calculated density of states at Fermi energy increases more than 2 orders of magnitude while the characteristic energy of variation of the density of states near Fermi energy decreases several times with and enhancement of Mg content from 0,6 at % to 4 at. %. The obtained results can be explained by creation of localized acceptor states in the band gap and suppression of magnetic frustration due to substitution of Cr by Mg in the crystalline lattice.

Acknowledgments

The authors are grateful to Ministry of science and high education of Russian Federation (project № 075-15-2021-1353). Authors aknowledge Moscow University Program of development for the instrumental support.

References

1 Xiong, D., Xu, Z., Zeng, X., Zhang, W., Chen, W., Xu, X., Wang, M. & Cheng, Y.-B. (2012). Hydrothermal synthesis of ultrasmall CuCrO2 nanocrystal alternatives to NiO nanoparticles in efficient p-type dye-sensitized solar cells. *Journal of Material Chemistry, Vol. 22,* P. 24760. DOI: https://doi.org/10.1039/C2JM35101C.

2 Xiong, D., Zhang, W., Zeng, X., Xu, Z., Chen, W., Cui, J., Wang, M., Sun, L. & Cheng, Y.B. (2013). Enhanced performance of p-type dye-sensitized solar cells based on ultrasmall Mg-doped $CuCrO_2$ nanocrystals. *ChemSusChem, Vol. 6,* P. 1432-1437. DOI: https://doi.org/10.1002/cssc.201300265.

3 Batzill, M. & Diebold, U. (2005). The surface and materials science of tin oxide. *Progress in Surface Science, Vol. 79,* P 47–154. DOI: 10.1016/J.PROGSURF.2005.09.002.

4 Özgür, Ü., Alivov, Ya.I., Liu, C., Teke, A., Reshchikov, M.A., Doğan, S., Avrutin, V., Cho, S.-J. & H. Morkoç J. (2005). A Comprehensive Review of ZnO Materials and Devices. *Journal of Applied Physics, Vol. 98*(4), P. 041301-041301-103. DOI: 10.1063/1.1992666.

5 Sinnarasa, I., Thimont, Y., Presmanes, L., Barnabé, A. & Tailhades, Ph. (2017). Thermoelectric and Transport Properties of Delafossite $CuCrO_2$: Mg Thin Films Prepared by RF Magnetron Sputtering. *Nanomaterials, Vol. 7,* P. 157. DOI: 10.3390/nano7070157.

6 Moreira, M., Afonso, J., Crepelliere, J., Lenoble, D. & Lunca-Popa, P. (2022). A review on the p-type transparent Cu–Cr–O delafossite materials. *Vol. 57,* P. 3114–3142. DOI: https://doi.org/10.1007/s10853-021-06815-z.

7 Guilmeau, E., Poienar, M., Kremer, S., Marinel, S., Hébert, S., Frésard, R. & Maignan, A. (2011). Mg substitution in $CuCrO_2$ delafossite compounds. *Solid State Communications. Vol. 151,* P. 1798–1801. DOI: https://doi.org/10.1016/j.ssc.2011.08.023.

8 Okuda, T., Jufuku, N., Hidaka, S. & Terada, N. (2005). Magnetic, transport, and thermoelectric properties of the delafossite oxides $CuCr_{1-x}Mg_xO_2$ (0<x<0.04)>. *Physical Review B., Vol. 72,* P. 144403. DOI: https://doi.org/10.1103/PhysRevB.72.144403.

9 Kulbachinskii, V.A., Kondratieva, D.Yu., Konstantinova, E.A., Pavlikov, A.V., Grigoriev, A.N., Mankevich, A.S. & Korsakov, I.E. (2019). Electrical conductivity, thermoelectrical properties, and EPR spectroscopy of copper chromite ceramic samples doped with magnesium. *Low Temperature Physics, Vol. 45,* P. 194-200. DOI: https://doi.org/10.1063/1.5086413.

10 Maignan, A., Martin, C., Frésard, R., Eyert, V., Guilmeau, E., Hébert, S. & M. Poienar, D. (2009). On the strong impact of doping in the triangular antiferromagnet $CuCrO_2$. *Pelloquin Solid State Communications, Vol. 149,* P. 962-967. DOI: 10.1016/j.ssc.2009.02.026.

11 Kulbachinskii1, V.A., Kytin, V.G., Korsakov, I.E., Kupriyanov, E.E. & Ismailov, Zh.T. (2022). Effect of synthesis duration on heat and charge transport in polycrystalline CuCr1-xMgxO2. *Bulletin of the University of Karaganda –Physics, Vol. 107,* P. 6-11. DOI: 10.31489/2022PH3/6-11.

12 Shklovskii, B.I. & Efros, A.L. (2013). Electronic Properties of Doped Semiconductors. *Springer Verlag Berlin Heidelberg.* 388 P. ISBN 978-3-662-03405-8 DOI: 10.1007/979-3-662-02473-4.

13 Zvyagin, I.P. (1973). On the Theory of Hopping Transport in Disordered Semiconductors. *Physica status solidi (b), Vol. 58,* P. 443-449. DOI: 10.1002/pssb.2220580203.

14 Poienar, M. (2012). Revisiting thepropertiesofdelafossite$CuCrO_2$: A single crystal study. *Journal of Solid State Chemistry, Vol. 185,* P. 56–61 DOI: 10.1016/j.jssc.2011.10.047.

В.Г. Кутин, Е.Е. Куприянов, А. Апрелева, В.А. Кульбачинский, И.Е. Корсаков, Т.Ю. Киселева, Ж.Т. Исмаилов

$CuCr_{1-x}Mg_xO_2$ және $CuCr_{1-y}Mg_yO_2/(MgCr_2O_4)_{x-y}$ поликристалды керамикадағы кемтіктердің тасымалдануларының және локализацияланған күйлердің тығыздықтарының ерекшеліктері

Поликристалдық керамикалық Mg мөлшері 0,6-4,0 ат. % тең қоспаланған мыс (I) хромитінің үлгілері синтезделді. Керамиканың фазалық құрамы рентгендік фазалық талдау арқылы зерттелді. Электр кедергісінің және Зеебек коэффициентінің температураға тәуелділіктері төрт зондты әдіспен өлшенді және ауыспалы секіру өткізгіштігі тұрғысынан талданды. Локализацияланған электрондық күйлердің тығыздығы және оның Ферми энергиясының жанындағы өзгеруінің сипаттамалық энергиясы бағаланған. Ферми энергиясының жанында орналасқан локализацияланған күйлердің тығыздығы Mg мөлшерінің жоғарылауымен жоғарылайтыны, ал Ферми энергиясының жанындағы локализацияланған

күйлердің тығыздығының өзгеруінің сипаттамалық энергиясы төмендейтіні анықталды. Алынған нәтижелер Mg қоспаланған мыс (I) хромитіндегі Зеебек коэффициентінің салыстырмалы түрде үлкен мәндерін валенттік диапазонның максимумына қарай тығыздығы тез өсетін кемтіктердің ауыспалы диапазонда секіріп тасымалдануымен түсіндіруге болатынын көрсетеді.

Кілт сөздер: р-типті жартылай өткізгіштер, жылуөткізгіштік, электрөткізгіштік, локализацияланған күйлердің тығыздығы.

В.Г. Кутин, Е.Е. Куприянов, А. Апрелева, В.А. Кульбачинский, И.Е. Корсаков, Т.Ю. Киселева, Ж.Т. Исмаилов

Особенности транспорта дырок и плотность локализованных состояний в $CuCr_{1-x}Mg_xO_2$ и в поликристаллической керамике $CuCr_{1-y}Mg_yO_2/(MgCr_2O_4)_{x-y}$

Синтезированы легированные магнием поликристаллические керамические образцы хромита меди (I) с содержанием Mg 0,6–4,0 ат. %. Методом рентгенофазового анализа исследован фазовый состав керамики. Температурные зависимости удельного электрического сопротивления и коэффициента Зеебека измерены четырехзондовым методом и проанализированы в рамках переменной прыжковой проводимости. Оценены плотность локализованных электронных состояний и характерная энергия ее изменения вблизи энергии Ферми. Получено, что плотность локализованных состояний вблизи энергии Ферми увеличивается с повышением содержания Mg, а характерная энергия изменения плотности локализованных состояний вблизи энергии Ферми уменьшается. Полученные результаты показывают, что относительно большие значения коэффициента Зеебека в хромите меди (I), легированном Mg, можно объяснить прыжковым переносом дырок с переменным диапазоном с быстро увеличивающейся плотностью к максимуму валентной зоны.

Ключевые слова: полупроводники р-типа, теплопроводность, электропроводность, плотность локализованных состояний.

DOI 10.31489/2023PH3/40-49

UDC 621.793.09

B.K. Rakhadilov [1], D.N. Kakimzhanov [1,2*], Yu.N. Tyurin[3], O.V. Kolisnichenko[3], O.A. Stepanova[4], A.K. Seitkhanova[5]

[1]*PlasmaScience LLP, Ust-Kamenogorsk, Kazakhstan;*
[2]*D. Serikbayev East Kazakhstan Technical University, Ust-Kamenogorsk, Kazakhstan;*
[3]*E.O. Paton Electric Welding Institute, Kiev, Ukraine;*
[4]*Shakarim University, Semey, Kazakhstan;*
[5]*Pavlodar Pedagogical University, Kazakhstan*
*(*E-mail: dauir_97@mail.ru)*

Structure and tribological properties of detonation coatings based on Cr_3C_2-NiCr after pulse-plasmaine treatment

Cr_3C_2-NiCr metal-ceramic coatings have found wide application in the protection of machine parts and equipment operating under extreme conditions. In this study, Cr_3C_2-NiCr based detonation coatings which have been subjected to pulse-plasma treatment were studied. The study showed that IPO reduced the surface roughness by 48 %, reduced the coating friction coefficient by about 2 times, increased the hardness of the coatings from the original 12 GPa to 16.2 GPa and improved their wear resistance by 2 times compared to untreated coatings. Pulse-plasma treatment provides qualitative formation of coatings from metal-ceramic material of Cr_3C_2-NiCr system with complex heterogeneous structure-phase state, where the layered structure of areas of carbide particles and matrix metal in immediate proximity from "carbide-matrix" border with selections in matrix of dispersed secondary carbides is revealed.

Keywords: ceramic metal coatings, detonation spraying, pulse-plasma treatment, coating modification, hardness, wear resistance.

Introduction

Metalloceramic chromium carbide-nickel-chromium alloys are used as acid-resistant materials in the chemical industry and for the manufacture of wear-resistant parts. They compete in this respect with WC-Ni-Cr and TiC- Ni(Co)-Cr alloys. Due to the high melting point, hardness and chemical resistance the highest Cr_3C_2 chromium carbide is used as a component of cladding alloys, as well as alloys used for manufacturing nozzles, stamps, high-temperature bearings, press molds for pressing brass profiles, sandblaster tips, inserts in large-sized matrices for pipe broaching [1-4].

Cr_3C_2-NiCr based coatings are used for corrosion and wear protection of component surfaces working at high temperatures and in aggressive environments [5], which is provided by the possibility to bind a solid phase of Cr_3C_2 carbide with a NiCr matrix and create a high density coating material [6]. Various spraying technologies are used for coating deposition: atmospheric plasma spraying (APS), high-velocity oxy-fuel spraying, air-fuel spraying (HVOF, HVAF) and detonation spraying.

In the process of coating materials made of Cr_3C_2-NiCr powder by HVOF and HVAF methods, a change in the chemical composition of the material is observed due to a decrease in the carbide content in the coating due to elastic rebound [7] and also due to oxidation [8, 9] caused by the presence of oxygen and superheated water vapor in the combustion products [9, 10].

The coating materials obtained by detonation spraying are characterized by increased hardness and wear resistance compared to HVOF and atmospheric plasma spraying [11-13]. Detonation spraying does not cause a large change in the chemical composition of the material and it is possible to regulate the chemical composition of the coating by changing the technological regimes [14, 15].

The specifics of gas-thermal spraying methods of ceramic-metal materials on a carbide base is that under the influence of high temperature (several thousand degrees) and oxidizing atmosphere of gaseous combustion products of a combustible mixture the depletion of higher carbides to lower carbides, oxidation of carbide particles, as well as migration of products of carbide particles dissociation into the metal matrix takes place [16, 17]. Since the highest carbide Cr_3C_2 has the highest performance characteristics, the processes of significant decarbonization of carbide particles are undesirable.

Further improvement of the qualitative characteristics of carbide-based metal-ceramic coatings is possible by external high-energy impact [18, 19]. The most effective technology is a complex pulse-plasma treatment, including surface modification by: magnetic field, electric current (flow of charged elementary

particles), high gradient thermal stream (plasma), containing metallic and nonmetallic alloying elements [20].

Pulse-plasma treatment (PPT) provides a rapid heating (heating time 10^{-3} — 10^{-4} s) of a surface layer followed by its intense cooling by heat removal into the volume of a product. High speed (up to 10^7 K/s) of melting and crystallization of surface layers contribute to formation of nanodisperse crystal structure and high density of dislocations. Impulse heat influence, elastoplastic deformation of processed material structure in combination with electromagnetic influence are carried out. Due to pulse current (up to 10 kA/cm^2) flowing through the surface layers of the coating, physical and chemical processes as well as heat and mass transfer are intensified.

The purpose of this work is to study the possibility of increasing the complex of physical and mechanical properties of the coating material made of Cr_3C_2-NiCr powder with the use of modern methods of cumulative-detonation coating deposition and subsequent pulse-plasma treatment.

Materials and methods of research.

Powder of Cr3C2-NiCr (75/25) (H.C. Starck: AMPERIT® 584.054) with a dispersion of 10-45 μm was used as the spraying material. The coatings were applied to 12Cr1MF steel samples by detonation spraying (DS) on a multichamber detonation apparatus [21]. To create high parameters (pressure, velocity) of the combustion products, a multichamber device design was used in which the detonation combustion regime of the gas mixture in specially profiled chambers and the subsequent accumulation of combustion energy from these chambers in a cylindrical bore are implemented [21]. The device provides formation of a jet of combustion products to accelerate and heat the sprayed powder and to apply high-quality metal and ceramic coatings [21, 24].

Figure 1 shows a general view of a multichamber detonation device [21, 24], which was developed at the E.O. Paton Institute of Electric Welding, National Academy of Sciences of Ukraine. The device has three chambers: 1 — prechamber for initiation of the detonation process; 2 — the main cylindrical chamber, where the detonation mode of combustion occurs; 3 — an annular hemispherical chamber with a slotted exit to the conoid chamber coaxial with the barrel. The powder dosage is accelerated and heated in the cylindrical barrel 4. The powder is metered and fed through an annular slot 5. Detonation is initiated by a spark plug 6. The pressure and velocity of the combustion products are measured by pressure sensors 7 and 8 mounted at the ends of the barrel. In the hemispherical chamber, the detonation mode in the corner concentrators is implemented, which significantly increases the rate and completeness of combustion of the combustible mixture components. The combustion products from the chambers are accumulated and provide them with high pressure and temperature. In the final result, this is realized in high velocity and sufficiently high temperature, providing the possibility of spraying ceramic coatings [25].

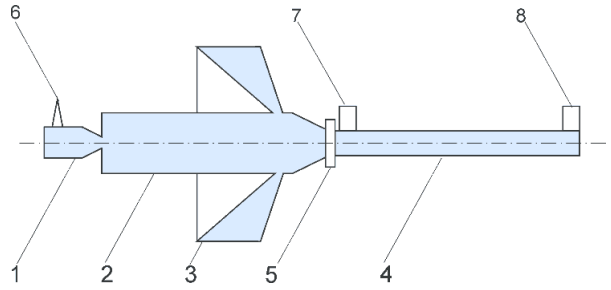

Figure 1. Scheme of the detonation apparatus. 1 — prechamber; 2 — cylindrical chamber; 3 — annular hemispherical chamber; 4 — barrel; 5 — annular slot; 6 — spark plug for initiation of detonation; 7, 8 — pressure sensors.

The design features of the multichamber detonation device provide the possibility of detonation combustion of poor combustible mixtures, which reduces the temperature of the combustion products, almost without reducing their velocity. For acceleration and heating, a dose of powder is fed into the barrel. The internal diameter of the barrel is 16/18 mm and its length is 300/500 mm, depending on the material properties of the sprayed powder. As a result of collapse of combustion products in front of the nozzle barrel from the annular hemispherical and cylindrical chambers, the pressure (up to 40 atm.) and their density increase significantly, which ensures effective acceleration and heating of the powder dose fed through the annular slot of a special gas dynamic dosing and pulse delivery unit of a compact dose of gas-powder

mixture. The detonation regime of combustion of the combustible mixture is initiated by an automotive spark plug.

The detonation repetition frequency is 20 Hz or higher. The supply of gases and powder to the detonation device is carried out continuously, from a standard powder feeder. Powder flow rate is 0.9 kg/hour and higher. Dosing of gases and powder and their release into the device is carried out by gas dynamic devices at the expense of the energy of combustion products. The flow rate of combustible mixture components of this device is shown in Table 1.

Table 1

Consumption of combustible mixture components of the detonation apparatus

The components of the mixture:		Flow rate, m^3/hour
	O_2	2.92
Chamber 1	Air	1.33
	C_3H_8	0.66
	O_2	2.93
Chamber 2	Air	1.43
	C_3H_8	0.66
Transporting gas:		0.9

To modify the resulting detonation coating on the surface of the product, a pulsed plasma technology (PPT) was used. Pulsed plasma generation was carried out at the "Impulse-6" unit developed at the Institute of Electric Welding named after E.O. Paton of the National Academy of Sciences of Ukraine [21]. Paton Institute of Electric Welding of NAS of Ukraine [22]. The peculiarity of the technology is the possibility to commutate electric current up to 15 kA by ionized gas region behind the detonation wave front [23].

The pulsed electric current releases thermal energy on the weakened areas of the coating material that have an increased resistivity. It heats them, up to melting, activates diffusion processes and, eventually, "heals" defects (microcracks, pores), increasing the adhesion and cohesion characteristics [26, 27].

Pulse-plasma generator (Fig. 2) consists of a detonation chamber — 1, where the initiation of combustion of combustible gas mixture (C_3H_8, O_2, air) and coaxial electrodes — 2, 3. If it is necessary to introduce dopant elements into plasma in the form of vapor phase, erodible electrode — 4 is used. When electric current flows behind the detonation wave — 5 in the interelectrode gap, joule heat is released, thereby increasing the electromagnetic and gas dynamic components of the force, which accelerates the plasma flowing on the surface on the products -6. The energy characteristics of plasma jets at the outlet of the pulse-plasma device depend on the geometry of the coaxial electrodes and the electric field strength in the interelectrode gap.

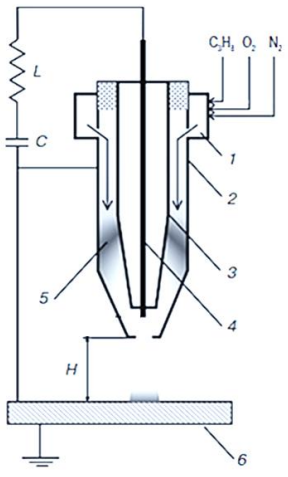

Figure2. Schematic diagram of the pulse-plasma device. 1 — detonation chamber; 2,3 — coaxial electrodes; 4 — eroding electrode; 5 — interelectrode gap; 6 — product; H — distance to product surface.

The parameters of the pulse-plasma treatment are shown in Table 2.

Table 2

Consumption of combustible mixture components of the detonation device

Parameter	Value
Capacitor battery voltage (V)	3200
Capacitor bank capacity (μF)	960
Discharge circuit inductance (μH)	30
Plasma pulse frequency (Hz)	1.2
Displacement speed (mm/s)	5
Distance to surface (mm)	50

At electric field strength between the electrodes 3.5×10^5 V/m the plasma velocity at the exit from the plasma torch reaches 4 km/s, and the temperature is 12000 K. At the moment of interaction of the plasma pulse with the surface of the product — 6 an area of shock-compressed plasma layer is formed in the contact zone.

The electric circuit between the electrode being eroded and the item is closed. The current density reaches 10 kA/cm^2. As a result, the surface is subjected to multiple pulses of electric current, magnetic field and plasma heat. Heat flux power density is 10^4-10^6 W/cm^2. It is possible to generate pulsed plasma with a frequency of 1-4 Hz and energy up to 7 kJ.

The phase composition of DS and DS/PPT coatings was studied using X-ray diffractometer X'PertPRO with Cu-Kα radiation (λ = 2.2897 Å), voltage 40 kV and current 30 mA. The diffractograms were interpreted using HighScore software, and measurements were made in the 2θ range equal to 20°-90° with a step of 0.02 and a counting time of 0.5 s/step. The surface morphology was investigated by scanning electron microscopy (SEM) using backscattered electrons (BSE) on a JSM-6390LV scanning electron microscope. Micrographs of the coating surface were obtained using an Altami MET 5S metallographic microscope. The surface roughness of the coatings Ra was evaluated using a profilometer model 130. Microhardness of cross-section of samples was measured according to GOST 9450-76 (ASTM E384-11) on Metolab 502 microtest meter at loads on indenter P=1 N and exposure time 10 s.

Tribological tests for sliding friction were performed on a TRB^3 Anton PaarSrl tribometer, using the standard "ball-on-disk" technique (international standards ASTM G 133-95 and ASTM G99), where a ball 6.0 mm in diameter, SiC coated steel, with a load of 6 N and a linear speed of 15 cm/s, a curvature radius of 5 mm, a friction path of 1200 m was used as a counterbody.

Results and discussion.

Figure 3 shows the results of measuring the surface roughness of the Cr_3C_2-NiCrbased coating material, according to which it was found that the surface has a non-uniform structure with the presence of pores. The Ra value, which is the arithmetic mean deviation of the profile, was chosen as the main parameter for assessing the surface roughness of the coatings. The roughness parameter of the coatings obtained before the PPT has a value of Ra = 11.2 (Fig. 3a), and after the PPT has a value of Ra = 5.31 (Fig. 3b). The twofold decrease in the roughness parameter is caused by pulse plasma melting of the protruding fragments and pores of the coating roughness, which contributed to a decrease in the surface roughness value by ≈ 48 % as compared to the coating roughness parameters before PPT.

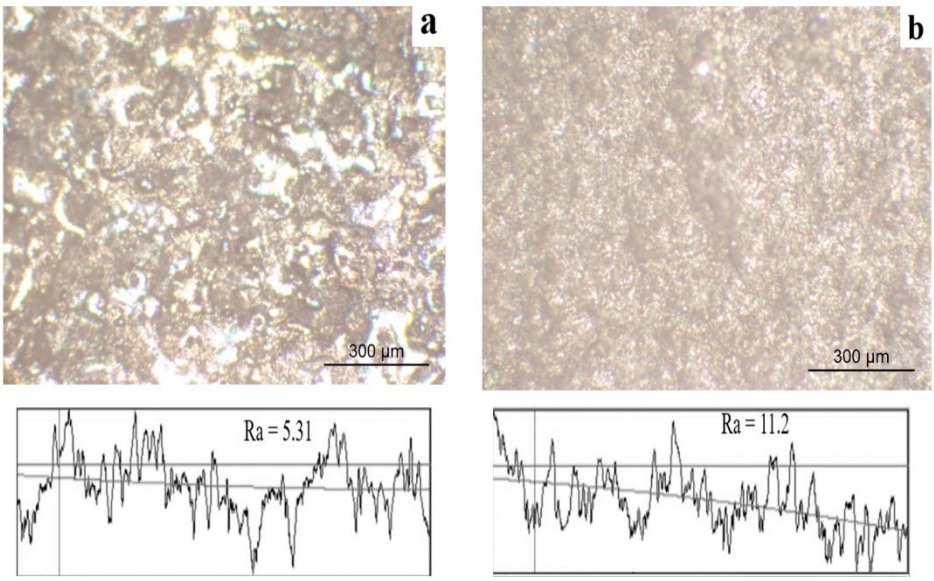

Figure 3. Micrograph of topography and surface roughness of Cr_3C_2 coatings before (a) and after the PPT

Figure 4 shows the diffractograms of the coating surface before and after the pulsed plasma treatment (PPT). The following phase components were detected in the coatings before the pulse-plasma treatment: Ni-Cr-Fe, Cr_3C_2, Ni-Cr-Fe/ Cr_7C_3 and Cr_7C_3 phases (Fig. 4a). Cr_2O_3 chromium oxide phases were found on the surface after PPT (Fig. 4b). Thus, after an PPT on the diffractogram it is observed growth of intensity of peaks of chrome carbide Cr_3C_2, (Fig. 4b), the reason for which is short-term activization of a surface of a covering from behind a pulse plasma where the plasma containing active carbon and oxygen causes course of two mutually exclusive chemically thermal processes of oxidation and carburization. The combination of solid phases of chromium oxide and carbide in the hardened metal matrix significantly increases the durability of the resulting material in conditions of abrasive wear.

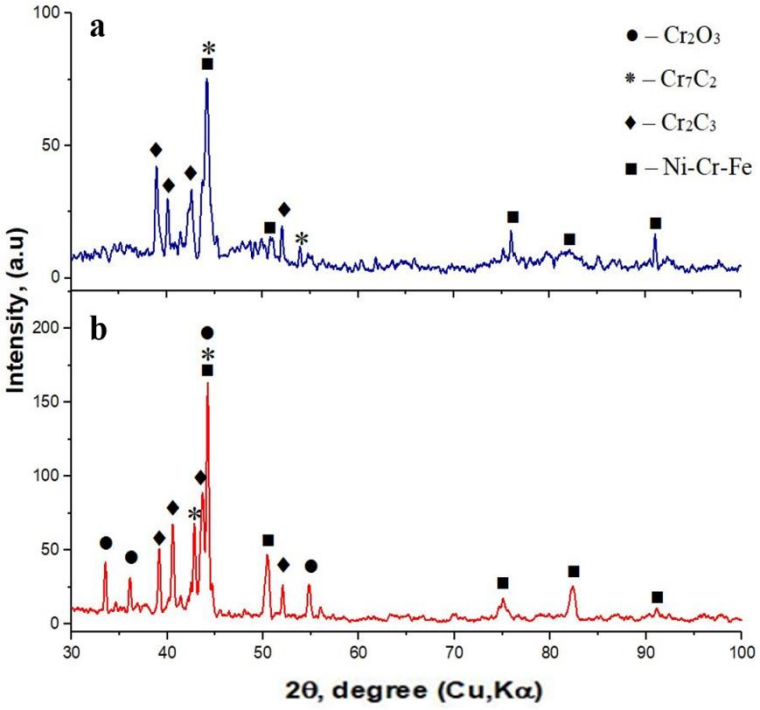

Figure 4. Surface diffractograms of Cr_3C_2-NiCr coating material before (a) and after (b) pulse plasma treatment

Figure 5 shows SEM images of the cross section of the coating material before (Fig. 5a) and after the pulse-plasma treatment (Fig. 5b). According to the image obtained with SEM before the pulse-plasma treatment (Fig. 5a), one can observe the porous structure characteristic of detonation spraying with large open defects of medium size localized closer to the surface layer of the coating. After pulse-plasma treatment in a subsurface layer of the coating pores are reduced to the minimum indicators, see Fig. 5b., which is associated with melting of the boundaries of large defects, as well as melting by pulse plasma of the protruding fragments and pores of coating that is caused by subsequent "healing" of defects during the passage of pulses of electric current.

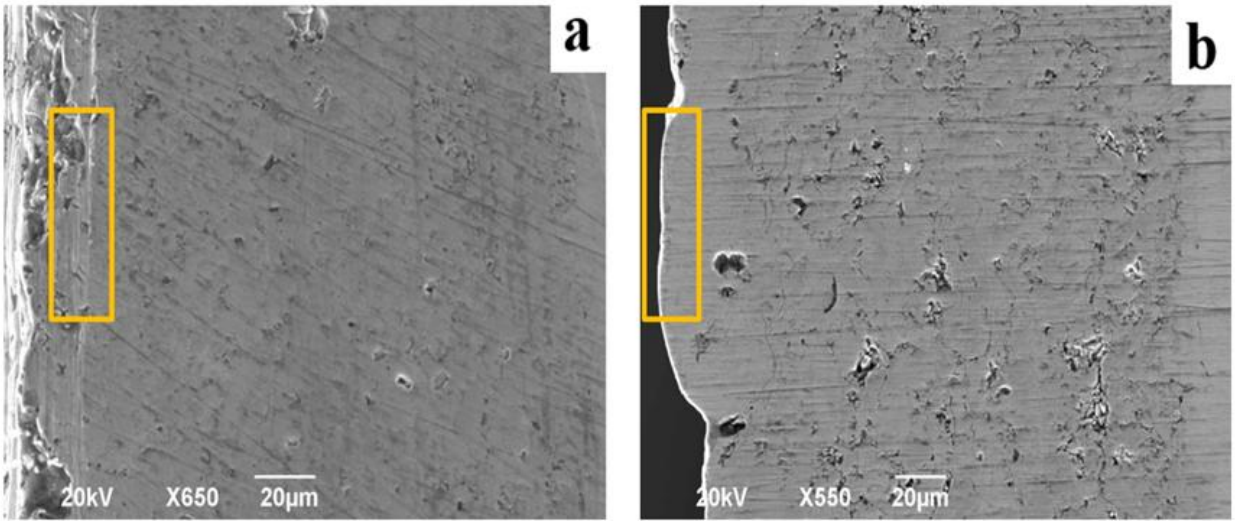

Figure 5. SEM image of the coating material before (a) and after PPT (b).

Figure 6 shows the plots of microhardness distribution by coating thickness before and after pulse-plasma treatment. The graph of dependence of microhardness on thickness of the Cr_3C_2-NiCr coating material (Fig. 6) shows non-uniform distribution of hardness: the coating material near the transition layer to the part base has a lower value of microhardness in contrast to the near-surface layers. The microhardness of the coating material deposited after the PPT (Fig. 6b) is rather higher than before the pulsed plasma treatment (Fig. 6a).

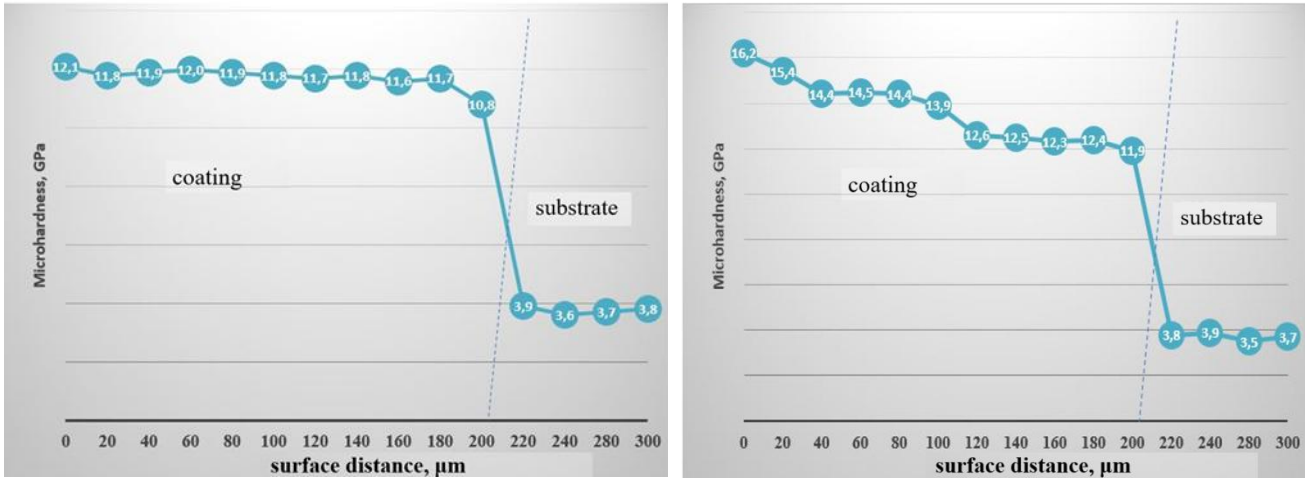

a) b)

Figure 6. Graph of the depth hardness distribution of Cr_3C_2-NiCr coatings before (a) and after the PPT (b)

One of the main properties responsible for the durability of products is the tribological parameters, which in this work were evaluated by the value of the wear volume of coatings before and after the PPT according to the scheme "ball-on-disk" (Fig. 7a). Profilograms were built using the obtained values of the

profilometer, and values for calculating the wear volume before and after the PPT were obtained using a special program. The test results showed that after PPT the coating has increased wear resistance according to the confirmation of the XRD this is most likely due to the increased proportion of Cr_3C_2 carbide phase, which has a high resistance to wear. According to the study of tribological characteristics of the coating surface it was found that the pulsed plasma treatment had a significant impact on the friction coefficient of the coating surface (decreased by 2 times) and wear resistance (increased by 2 times compared with the values before the PPT).

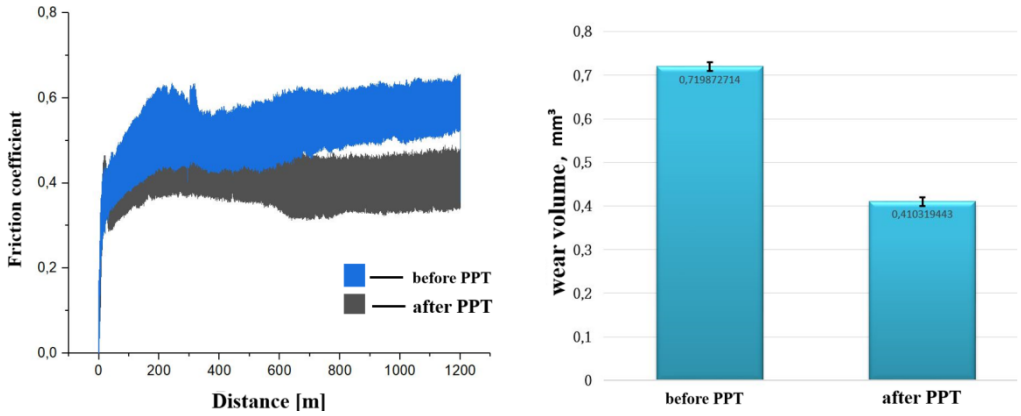

Figure 7. Graph of the depth hardness distribution of Cr_3C_2-NiCr coatings before (a) and after PPT (b)

Conclusion

According to the evaluation and analysis of all obtained results, we can draw the following main conclusions on the present research work:

- Detonation coating technology and subsequent pulse-plasma processing provide formation of quality coatings from ceramic-metal powder on the basis of Cr_3C_2-NiCr with complex heterogeneous structural-phase state, where the layered structure of carbide particles and matrix metal areas in the immediate vicinity of the "carbide-matrix" border with allocation of dispersed secondary carbides in the matrix is revealed;

- Pulse-plasma treatment of coatings provides increase of hardness of matrix without significant degradation of primary carbide particles and formation of high values of local internal stresses that is caused by healing of defects, as well as accelerated mass transfer of carbon, oxygen, increase of carbide particles quantity and creation of chrome oxides in near-surface layer;

- Pulse-plasma treatment contributes to a 48 % decrease in surface roughness value and coating friction coefficient, an increase in material microhardness of Cr_3C_2-NiCr coatings from ~12 GPa (initial) to ~16.2 GPa and a 2-fold increase in wear resistance compared to untreated coating;

Detonation spraying and subsequent pulse-plasma treatment, can be recommended as an optimal way to protect the surfaces of parts operating in extreme wear conditions.

Acknowledgment

This research is funded by the Science Committee of the Ministry of Science and Higher Education of the Republic of Kazakhstan (Grant No. AP09261164).

References

1 Корнилов В.И. Турбулентный пограничный слой на теле вращения при периодическом вдуве/отсосе / В.И. Корнилов // Теплофизика и аэромеханика. — 2006. — № 13(3). — С. 369–385.

2 Lu H. Erosion and corrosion behavior of shrouded plasma sprayed Cr3C2-NiCr coating / H. Lu, J. Shang, X. Jia, Y. Li, F. Li, J. Li, Y. Nie // Surface and Coatings Technology. — 2020. — 388. — P. 125534.

3 Pogrebnyak A.D. Modification of material properties and coating deposition using plasma jets / A.D. Pogrebnyak, Y.N. Tyurin // Physics-Uspekhi. — 2005. — 48. — 5. — P. 487.

4 Li C.J. Dominant effect of carbide rebounding on the carbon loss during high velocity oxy-fuel spraying of Cr3C2–NiCr / C.J. Li, G.C. Ji, Y.Y. Wang, K. Sonoya // Thin Solid Film. — 2002. — 419. — 1-2. — P. 137-143.

5 Janka L. Influence of heat treatment on the abrasive wear resistance of a Cr3C2NiCr coating deposited by an ethene-fuelled HVOF spray process / L. Janka, J. Norpoth, R. Trache, L.M. Berger // Surface and Coatings Technology. — 2016. — No. 291. —P. 444-451.

6 Matikainen V. A study of Cr3C2-based HVOF-and HVAF-sprayed coatings: abrasion, dry particle erosion and cavitation erosion resistance / V. Matikainen, H. Koivuluoto, P. Vuoristo // Wear. — 2020. — 446. — P. 203188.

7 Korpiola K. High temperature oxidation of metal, alloy and cermet powders in HVOF spraying process / K. Korpiola. — Helsinki University of Technology. — 2004.

8 Nenashev M.V. Technology and properties of nanostructured detonation coatings / M.V. Nenashev, D.A. Demoretsky, I.D. Ibatullin, I.V. Nechaev, S.Y. Ganigin, A.Y. Murzin, R.R. Neyaglova // Izv. RAS SamSC. — 2011. — No. 13. — P. 390-393.

9 Kakimzhanov, D.N. Influence of pulsed plasma treatment on phase composition and hardness of Cr3C2-NiCr coati ngs. / D.N. Kakimzhanov, B.K. Rakhadilov, Y.N. Tyurin, O.V. Kolisnichenko, L.G. Zhurerova, M.K. Dautbekov // Eurasian Journal of Physics and Functional Materials, 2021. Vol. 5, No 1. — P. 45-51.

10 Ulianitsky V.Y. The experience of research and application of technology for applying detonation coatings / V.Y. Ulianitsky, M.V. Nenashev, V.V. Kalashnikov, I.D. Ibatullin, S.Y. Ganigin, K.P. Yakunin, A.A. Shterzer // Izv. RAS SamSC. — 2010. — No. 12. — P. 569-575.

11 Sydorets V. Modern techniques for automated acquiring and processing data of diffraction electron microscopy for nano-materials and single-crystals / V. Sydorets, O. Berdnikova, Y. Polovetskyi, Y. Titkov, A. Bernatskyi // Materials Science Forum. Trans Tech Publications Ltd. — 2020. — 992. — P. 907-915.

12 Roy M. Abrasive wear behaviour of detonation sprayed WC–Co coatings on mild steel / M. Roy, C.V.S. Rao, D.S. Rao, G. Sundararajan // Surface Engineering. — 1999. — 15. — 2. — P. 129-136.

13 Roy M. Dynamic hardness of detonation sprayed WC-Co coatings / M. Roy // Journal of thermal spray technology. — 2002. — 11.— 393-399.

14 Ulianitsky V.Y. Detonation spraying behaviour of refractory metals: Case studies for Mo and Ta-based powders / V.Y. Ulianitsky, I.S. Batraev, A. A. Shtertser, D.V. Dudina, N.V. Bulina, I. Smurov // Advanced Powder Technology. — 2018. — 29. — 8. — P. 1859-1864.

15 Rakhadilov B. Structure and tribological properties of Ni–Cr–Al-based gradient coating prepared by detonation spraying / B. Rakhadilov, M. Maulet, M. Abilev, Z. Sagdoldina, R. Kozhanova // Coatings. — 2021. — 11. — 2. — P. 218.

16 Rakhadilov B. Structural features and tribological properties of detonation gun sprayed Ti–Si–C coating / B. Rakhadilov, D. Buitkenov, Z. Sagdoldina, B. Seitov, S. Kurbanbekov, M. Adilkanova // Coatings. — 2021. — 11. — 2. — P. 141.

17 Ji G.C. Microstructural characterization and abrasive wear performance of HVOF sprayed Cr3C2–NiCr coating. / G.C, Ji, C.J. Li, Y.Y. Wang, W.Y. Li // Surface and Coatings Technology. — 2006. — 200. — 24. — P. 6749-6757.

18 Chatha S.S. Characterisation and corrosion-erosion behaviour of carbide based thermal spray coatings / S.S. Chatha, H.S. Sidhu, B.S. Sidhu // Journal of Minerals and Materials Characterization and Engineering. — 2012. — 11. — P. 569.

19 Rakhadilov B. Structural Phase Transformations in Detonation Coatings Based on Ti3SiC2 after Pulse-Plasma Effect / B. Rakhadilov, D. Kakimzhanov, D. Buitkenov, S. Abdulina, L. Zhurerova, Z. Sagdoldina // Crystals. — 2022. — 12. — 10. —P. 1388.

20 Akamatsu H. Surface treatment of steel by short pulsed injection of high-power ion beam / H. Akamatsu, T. Ikeda, K. Azuma, E. Fujiwara, M. Yatsuzuka // Surface and coatings technology. — 2001. — 136. — 1-3. — P. 269-272.

21 Tyurin Y.N. Plasma Strengthening Technologies / Y.N. Tyurin, M.L. Zhadkevich. — Naukova Dumka, Kiev, 2008. — 218 p.

22 Ilyuschenko A.P. Friction and wear of powder coatings produced by using high-energy pulsed flows / A.P. Ilyuschenko, A.I. Shevtsov, V.M. Astashynski, A.M. Kuzmitski, G.F. Gromyko, A.N. Chumakov, K.V. Buikus // High Temperature Material Processes: An International Quarterly of High-Technology Plasma Processes. — 2015. — 19. — 2.

23 Рахадилов Б.К. Способ получения износостойкого покрытия / Б.К. Рахадилов, Ж.Б. Сагдолдина, М.К. Кылышканов, Д.Б. Буйткенов // Патент KZ на полезную модель. — № 6659. — Заявка № 03.08.21 г. — Опубл. 12.11.21 г.

24 Маркашова Л.И. Автоматическая сварка. — 2017. — № 09. Автоматическая сварка, (09), 06 / Л.И. Маркашова, Ю.Н. Тюрин, О.В. Колисниченко, Е.Н. Бердникова, О.С. Кушнарева, Е.В. Половецкий, Е.П. Титков.

25 Колисниченко О.В. Эффективность процесса напыления покрытий с использованием многокамерного детонационного устройства / О.В. Колисниченко, Ю.Н. Тюрин, Р. Товбин. — 2017. — Автоматическая сварка.

26 Girolamo Di Microstructure and mechanical properties of plasma sprayed alumina-based coatings / Di Girolamo, G., Brentari, A., Blasi, C., Serra, E. // Ceramics International. — 2014. — 40(8), 12861-12867.

27 Кукуджанов К.В. Процессы залечивания микротрещин в металле под действием импульсов тока высокой плотности / К.В. Кукуджанов // Проблемы прочности и пластичности. — 2016. — № 78 (3). — С. 300–310.

Б.К. Рахадилов, Д.Н. Кәкімжанов, Ю.Н. Тюрин, О.В. Колисниченко,
О.А. Степанова, А.К. Сейтханова

Импульсті-плазмалық өңдеуден кейін Cr_3C_2-NiCr негізіндегі детонациялық жабынның құрылымы мен трибологиялық қасиеттері

Cr_3C_2-NiCr металл керамикалық жабындары экстремалды жағдайларда жұмыс істейтін машина бөлшектері мен жабдықтарын қорғауда кеңінен қолданылады. Бұл зерттеу импульсті-плазмалық өңдеуден өткен Cr_3C_2-NiCr негізіндегі детонациялық жабындарды зерттеуге арналған. Зерттеу нәтижелері көрсеткендей, импульсті-плазмалық өңдеу (ИПӨ) бетінің кедір-бұдырлығын 48 %–ға төмендетеді, жабынның үйкеліс коэффициентін шамамен 2 есе азайтады, жабындардың қаттылығын бастапқы 12 ГПа-дан 16,2 ГПа-ға дейін арттырады және өңделмеген жабындармен салыстырғанда олардың тозуға төзімділігін 2 есе жақсартады. Импульстік-плазмалық өңдеу күрделі гетерогенді құрылымдық-фазалық күйі бар Cr_3C_2-NiCr жүйесінің металл-керамикалық материалынан жасалған жабындардың сапалы қалыптасуын қамтамасыз етеді, мұнда дисперсті қайталама карбидтер матрицасындағы секрециялармен «карбид-матрица» шекарасына жақын карбид бөлшектері мен матрицалық металл аймақтарының қабатты құрылымы анықталады.

Кілт сөздер: металл-керамикалық жабындар, детонациялық бүрку, импульсті-плазмалық өңдеу, жабынды өзгерту, қаттылық, тозуға төзімділік.

Б.К. Рахадилов, Д.Н. Какимжанов, Ю.Н. Тюрин, О.В. Колисниченко,
О.А. Степанова, А.К. Сейтханова

Структура и трибологические свойства детонационного покрытия на основе Cr_3C_2–NiCr после импульсно-плазменной обработки

Металлокерамические покрытия Cr_3C_2–NiCr нашли широкое применение в защите машинных деталей и оборудования, работающих в экстремальных условиях. В данном исследовании были изучены детонационные покрытия на основе Cr_3C_2–NiCr, которые были подвергнуты импульсно-плазменной обработке. Исследование показало, что ИПО снижает шероховатость поверхности на 48 %, уменьшает коэффициент трения покрытия примерно в 2 раза, увеличивает твердость покрытий от исходных 12 до 16,2 ГПа и улучшает их износостойкость в 2 раза по сравнению с необработанными покрытиями. Также было выявлено, что после ИПО повышается стойкость покрытий Cr_3C_2–NiCr к абразивному износу и эрозии. Импульсно-плазменная обработка обеспечивает качественное формирование покрытий из металлокерамического материала системы Cr_3C_2–NiCr со сложным гетерогенным структурно-фазовым состоянием, где обнаруживается слоистая структура областей карбидных частиц и матричного металла в непосредственной близости от границы «карбид–матрица» с выделениями в матрице дисперсных вторичных карбидов.

Ключевые слова: металлокерамические покрытия, детонационное напыление, импульсно-плазменная обработка, модифицирование покрытия, твердость, износостойкость.

References

1 Kornilov, V.I. (2006). Turbulentnyi pogranichnyi sloi na tele vrashcheniia pri periodicheskom vduve/otsose [Turbulent Boundary Layer on a Body of Revolution with Periodic Injection/Suction]. *Teplofizika i aeromekhanika — Thermophysics and Aeromechanics*, *13*(3), 369–385 [in Russian].

2 Lu, H., Shang, J., Jia, X., Li, Y., Li, F., Li, J. & Nie, Y. (2020). Erosion and corrosion behavior of shrouded plasma sprayed Cr3C2-NiCr coating. *Surface and Coatings Technology*, *388*, 125534.

3 Pogrebnyak, A.D. & Tyurin, Y.N. (2005). Modification of material properties and coating deposition using plasma jets. *Physics-Uspekhi — Physics-progress*, *48*(5), 487.

4 Li, C.J., Ji, G.C., Wang, Y.Y. & Sonoya, K. (2002). Dominant effect of carbide rebounding on the carbon loss during high velocity oxy-fuel spraying of Cr3C2–NiCr. *Thin Solid Film, 419*, 1-2, 137-143.

5 Janka, L., Norpoth, J., Trache, R. & Berger, L.M. (2016). Influence of heat treatment on the abrasive wear resistance of a Cr3C2NiCr coating deposited by an ethene-fuelled HVOF spray process. *Surface and Coatings Technology*, 291, 444-451.

6 Matikainen, V., Koivuluoto, H. & Vuoristo, P. (2020). A study of Cr3C2-based HVOF-and HVAF-sprayed coatings: abrasion, dry particle erosion and cavitation erosion resistance. *Wear*, 446, 203188.

7 Korpiola, K. (2004). High temperature oxidation of metal, alloy and cermet powders in HVOF spraying process. Helsinki University of Technology.

8 Nenashev, M.V., Demoretsky, D.A., Ibatullin, I.D., Nechaev, I.V., Ganigin, S.Y., Murzin, A.Y. & Neyaglova, R.R. (2011). Technology and properties of nanostructured detonation coatings. *Izv. RAS SamSC, 13*, 390-393.

9 Kakimzhanov, D.N., Rakhadilov, B.K., Tyurin, Y.N., Kolisnichenko, O.V., Zhurerova, L.G. & Dautbekov, M.K. (2021). Influence of pulsed plasma treatment on phase composition and hardness of Cr3C2-NiCr coatings. *Eurasian Journal of Physics and Functional Materials, 5*(1), 45-51.

10 Ulianitsky, V.Y., Nenashev, M.V., Kalashnikov, V.V., Ibatullin, I.D., Ganigin, S.Y., Yakunin, K.P. & Shterzer, A.A (2010). The experience of research and application of technology for applying detonation coatings. *Izv. RAS SamSC, 12*, 569-575.

11 Sydorets, V., Berdnikova, O., Polovetskyi, Y., Titkov, Y. & Bernatskyi, A. (2020). Modern techniques for automated acquiring and processing data of diffraction electron microscopy for nano-materials and single-crystals. *Materials Science Forum.* Trans Tech Publications Ltd, 992, 907-915.

12 Roy, M., Rao, C.V.S., Rao, D.S., Sundararajan, G. (1999). Abrasive wear behaviour of detonation sprayed WC–Co coatings on mild steel. *Surface Engineering, 15*, 2, 129-136.

13 Roy, M. (2002). Dynamic hardness of detonation sprayed WC-Co coatings. *Journal of thermal spray technology, 11*, 393-399.

14 Ulianitsky, V.Y., Batraev, I.S., Shtertser, A.A., Dudina, D.V., Bulina, N.V. & Smurov, I. (2018). Detonation spraying behaviour of refractory metals: Case studies for Mo and Ta-based powders. *Advanced Powder Technology, 29*, 8, 1859-1864.

15 Rakhadilov, B., Maulet, M., Abilev, M., Sagdoldina, Z. & Kozhanova, R. (2021). Structure and tribological properties of Ni–Cr–Al-based gradient coating prepared by detonation spraying. *Coatings, 11*, 2, 218.

16 Rakhadilov, B., Buitkenov, D., Sagdoldina, Z., Seitov, B., Kurbanbekov, S. & Adilkanova, M. (2021). Structural features and tribological properties of detonation gun sprayed Ti–Si–C coating. *Coatings, 11*, 2. 141.

17 Ji, G.C., Li, C.J., Wang, Y.Y. & Li, W.Y. (2006). Microstructural characterization and abrasive wear performance of HVOF sprayed Cr3C2–NiCr coating. *Surface and Coatings Technology, 200*, 24, 6749-6757.

18 Chatha, S.S., Sidhu, H. S. & Sidhu, B. S. (2012). Characterisation and corrosion-erosion behaviour of carbide based thermal spray coatings. *Journal of Minerals and Materials Characterization and Engineering*, *11*, 569.

19 Rakhadilov, B., Kakimzhanov, D., Buitkenov, D., Abdulina, S., Zhurerova, L. & Sagdoldina, Z (2022). Structural Phase Transformations in Detonation Coatings Based on Ti3SiC2 after Pulse-Plasma Effect. *Crystals*, *12*, 10, 1388.

20 Akamatsu, H. Ikeda, T., Azuma, K., Fujiwara, E. & Yatsuzuka, M (2001). Surface treatment of steel by short pulsed injection of high-power ion beam. *Surface and coatings technology*, *136*, 1-3, 269-272.

21 Tyurin, Y.N. & Zhadkevich, M.L. (2008). Plasma Strengthening Technologies. Naukova Dumka, Kiev, 218.

22 Ilyuschenko A.P., Shevtsov, A.I., Astashynski, V.M., Kuzmitski, A.M., Gromyko, G.F., Chumakov, A.N. & Buikus, K.V. (2015). Friction and wear of powder coatings produced by using high-energy pulsed flows. *High Temperature Material Processes: An International Quarterly of High-Technology Plasma Processes*, 19, 2.

23 Rakhadilov, B.K., Sagdoldina, Zh.B., Kylyshkanov, M.K. & Buytkenov, D.B. Sposob polucheniia iznosostoikogo pokrytiia [Method for obtaining a wear-resistant coating]. *Patent KZ na poleznuiu model № 6659, zaiavka № 03.08.21 g.; opubl. 12.11.21 g. — KZ patent for utility model No. 6659. Application No. 03.08.21. Publ. 12.11.21* [in Russian].

24 Markashova, L.I., Tyurin, Yu.N., Kolisnichenko, O.V., Berdnikova, E.N., Kushnareva, O.S., Polovetskiy, E.V.& Titkov, E.P. (2017). Avtomaticheskaia svarka *№*.09 — *Automatic welding №09*, (09), 06 [in Russian].

25 Kolisnichenko, O.V., Tyurin, Yu.N. & Tovbin, R. (2017). Effektivnost protsessa napyleniia pokrytii s ispolzovaniem mnogokamernogo detonatsionnogo ustroistva [Efficiency of the coating deposition process using a multi-chamber detonation device]. *Avtomaticheskaia svarka — Automatic welding* [in Russian].

26 Di Girolamo, G., Brentari, A., Blasi, C. & Serra, E. (2014). Microstructure and mechanical properties of plasma sprayed alumina-based coatings. *Ceramics International*, *40*(8), 12861-12867.

27 Kukudzhanov, K.V. (2016). Protsessy zalechivaniia mikrotreshchin v metalle pod deistviem impulsov toka vysokoi plotnosti [Healing of microcracks in metal under the action of high-density current pulses]. *Problemy prochnosti i plastichnosti — Problems of Strength and Plasticity*, *78*(3), 300–310 [in Russian].

DOI 10.31489/2023PH3/50-57

UDC 537.533, 13.1:13.2:13.3

B.D. Igamov[1], G.T. Imanova[2*], A.I. Kamardin[1], I.R. Bekpulatov[3]

[1]Scientific and technical center with a design bureau and pilot production of the Academy of Sciences of the Republic of Uzbekistan, Tashkent, Uzbekistan;
*[*2]Ministry of Science and Education of the Republic of Azerbaijan, Institute of Radiation Problems, Baku, Azerbaijan;*
[3]Tashkent State Technical University, 100095, Uzbekistan
*(*E-mail: gunel_imanova55@mail.ru)*

Formation of targets and investigation of Mn_4Si_7 coatings produced by magnetron sputtering

The morphology, composition, electrical and optical properties of bulk samples and vacuum coatings of Mn_4Si_7 obtained by magnetron sputtering on a SiO_2/Si structure were studied. It is shown that manganese silicide coatings with a thickness of about 150 nm are close in properties to bulk Mn_4Si_7, have a uniform fine-grained structure of a semiconductor nature, which is characterized by thermal sensitivity up to 20-30 μV per degree. In addition, this article presents the electrophysical properties of high manganese silicide films produced by the authors by magnetron sputtering method. Heated films Mn_4Si_7 -146 nm coating has a uniform structure with fine grains, due to sufficient coating density. Since Mn_4Si_7 nanoclusters are semiconductor materials, it can be assumed that there will be energy barriers for charge carriers at the nanocluster–amorphous phase interface separating this phase. An increase in thermal sensitivity from 0 μV/K to 20 μV/K up to 800 K is explained by the disappearance of energy barriers for charge carriers at the nanocluster–amorphous phase interface due to the ordering of nanoclusters. The change from 20 μV/K to 28 μV/K upon cooling is explained by the appearance of structural relaxation in the amorphous phase.

Keywords: Hall constant, Mn_4Si_7, thin coating, nanocluster, electrical conductivity, nanostructure, resistivity, volume concentration.

Introduction

The main task facing scientists all over the world today is to search for environmentally friendly types of energy and increase the utilization rate of identified types. The main goal at the same time is to receive energy without harming the environment. Unfortunately, the efficiency of currently produced thermo- and photo batteries is very low. A key role in solving this problem is played by the creation of new materials and structures or the replacement of existing ones with cheap and high-quality ones.

Receiving and converting energy is one of the most important activities of modern civilization [1-7]. In this regard, much attention is paid to solid-state thermoelectric converters that do not have moving parts, operate silently, have high reliability and small size. An increase in the efficiency of using thermoelectric materials is associated with the formation of high quality layers [8-23]. Of all silicon compounds of thermoelectric interest, one can choose compounds representing a certain class of materials. These are, for example, solid solutions based on cobalt monosilicide (CoSi), high manganese silicide ($MnSi_{1.7}$), and Mn_2X (X=Si, Ge, Sn). Highmanganese silicide (HMS-$MnSi_{1.7\text{-}1.75}$), even in the unalloyed state, has a high thermoelectric efficiency and is a good basis for creating an efficient *p*-type thermoelectric. Therefore, thin vacuum coatings of Mn_4Si_7 were chosen as objects of study.

Experimental

To obtain thin-film samples of Mn_4Si_7, a disk target was first formed. Pure monocrystalline silicon and manganese were first pulverized in a mill (HERZOG HSM-100P), then 52.9 % Mn and 47.1 % Si (by mass) were mixed and sintered using electric spark plasma welding (SPS). The Mn_4Si_7 disk target was pressed in a setup under vacuum conditions with a residual gas pressure of 10^{-2} Torr at a temperature of 1050 °C, with a pressing force of $6.5 \cdot 10^4$ N for 2 hours (Fig. 1).

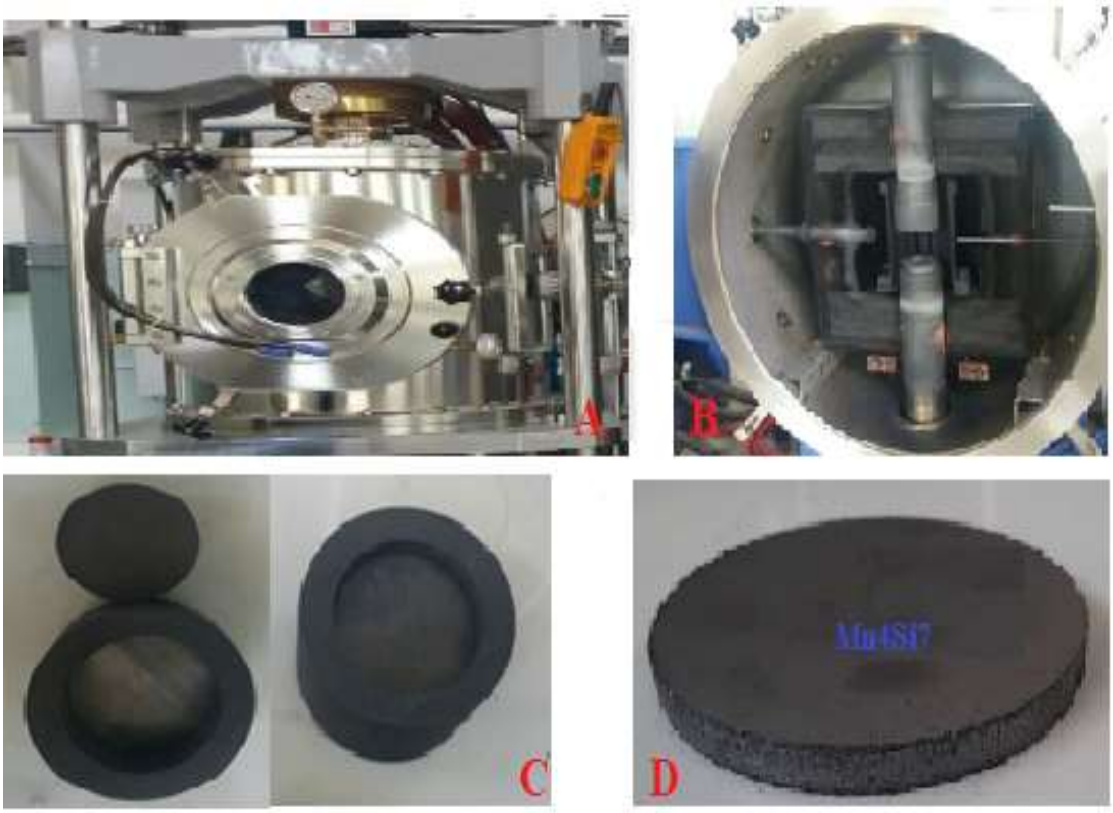

Figure 1. Preparation of the Mn_4Si_7 target by the (SPS) method

Polished silicon wafers of the Si(111) type with a diameter of 60 mm were used as a base (substrate) for deposition of thermally sensitive coatings. A group of plates after preliminary chemical cleaning in an ammonium peroxide solution, washing and drying were subjected to high-temperature treatment to create an oxide layer. Silicon dioxide layers of various thicknesses were grown on plates in an environment of dry oxygen at a temperature of 1200 ±5 °C in a diffusion furnace of the SDO-125 type. The SiO_2/Si structures prepared in this way were processed in a vacuum working chamber. The surface of the Si(111) substrate was cleaned with an Ar plasma flow for 1 minute. The device and the process of processing plates is shown in Figure 2.

The SiO_2/Si structures were placed in a modified (EPOS-PVD-DESK-PRO) installation for magnetron sputtering of the Mn_4Si_7 target and coating formation. The coating formation process was carried out after reaching the starting vacuum degree of about 10^{-5}Torr. The SiO_2/Si structures were treated individually with heating up to 150 °C. The pressure of the working gas (pure argon) during spraying was $(2\text{-}4)\cdot10^{-3}$Torr. The discharge current was 200–300 mA at voltages of 450–550 V. The coating deposition time was 2–10 minutes. In one vacuum cycle, 3 structures were sequentially processed. The morphology, microstructure, and chemical composition of the coated samples were determined by scanning electron microscopy and energy-dispersive X-ray spectroscopy (Scios FEI; Quanta 200 3D setups). The electrical properties of the Mn_4Si_7 coating were studied by a four-probe method (JANDEL RM3000 setup), and the Hall constant was determined using an ECOPIA setup (HMS-3000 VER3.53).

Mn_4Si_7 samples obtained by sintering (SPS) and coated samples obtained by magnetron sputtering on the EPOS-PVD-DESK-PRO facility were studied.

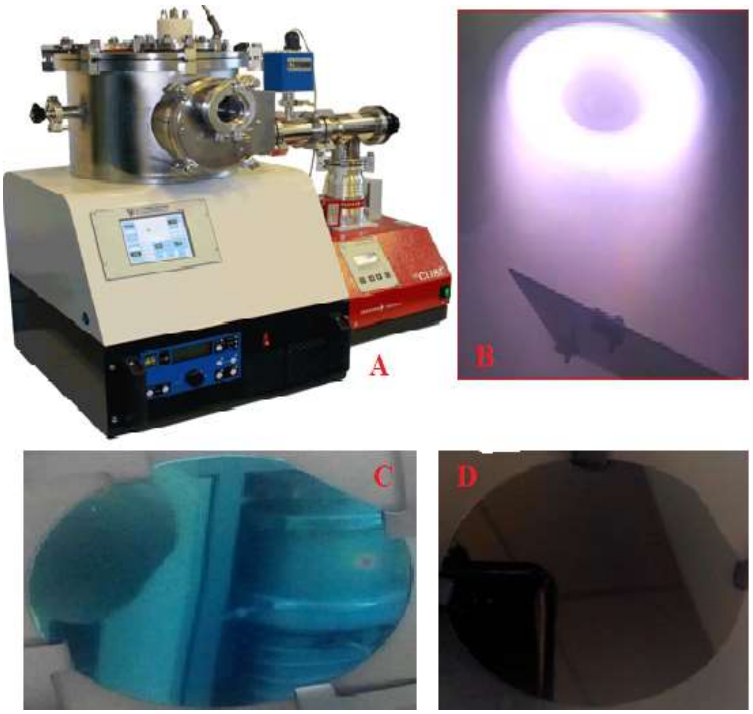

Figure 2. The process of forming the Mn_4Si_7 coating by the method of magnetron sputtering

Results and Discussion

Figure 3a, b shows images of the surface of the samples and the results of energy dispersive analysis: (a) — sample prepared by the (SPS) method, (b) — sample obtained by magnetron sputtering.

Figure 4 shows an electron microscope photograph of a cut of the Mn_4Si_7 coating on the SiO_2/Si(111) structure. The measurements show a thickness of the silicon dioxide coating of about 249 nm, and the thickness of the Mn_4Si_7 coating is about 146 nm.

The results of averaged measurements by the four-probe method of the conductivity of Mn_4Si_7 (SPS) samples and the conductivity of Mn_4Si_7 coatings obtained by magnetron sputtering are shown in Table 1.

Table 1

Layer resistances of bulk samples Mn4Si7 and Mn4Si7 coatings on the SiO2/Si structure

Sample type	Sheet resistance values, Ohm/square	Average value of sheet resistance, Ohm/square
Volume	508-602	556
Coating	4380-4460	4401

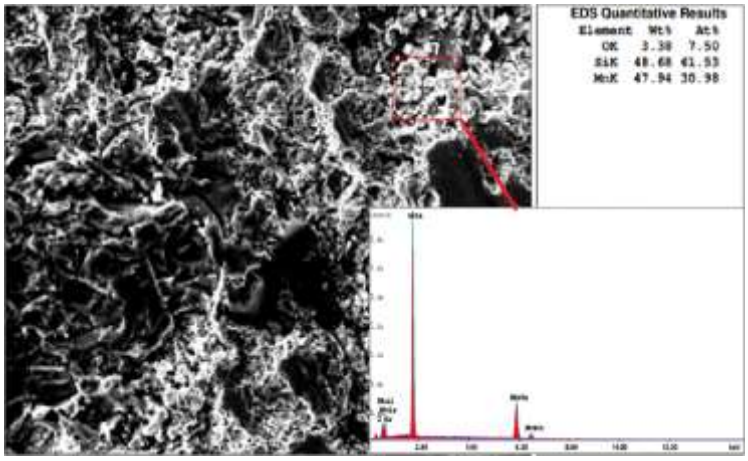

a

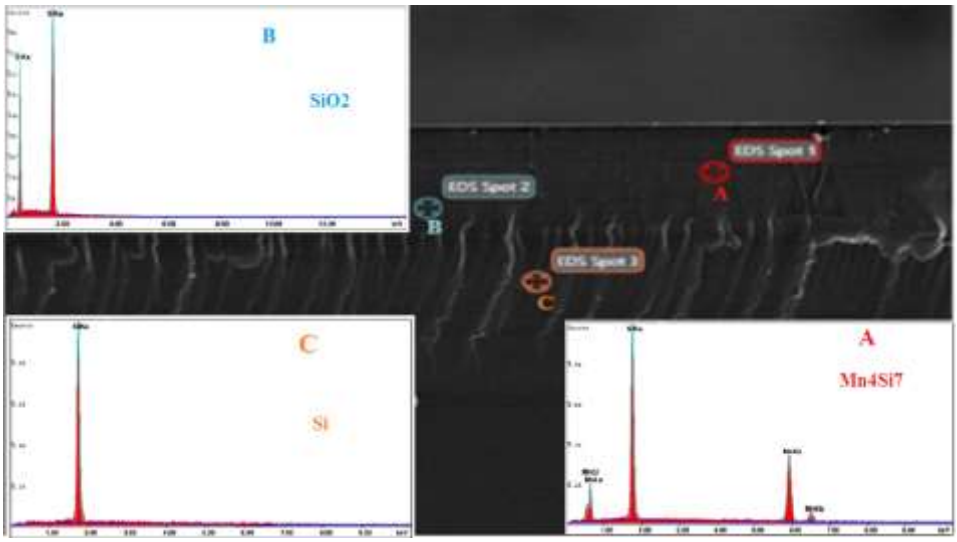

b

Figure 3. Image of Mn_4Si_7 sample (Scios FEI; Quanta 200 3D)

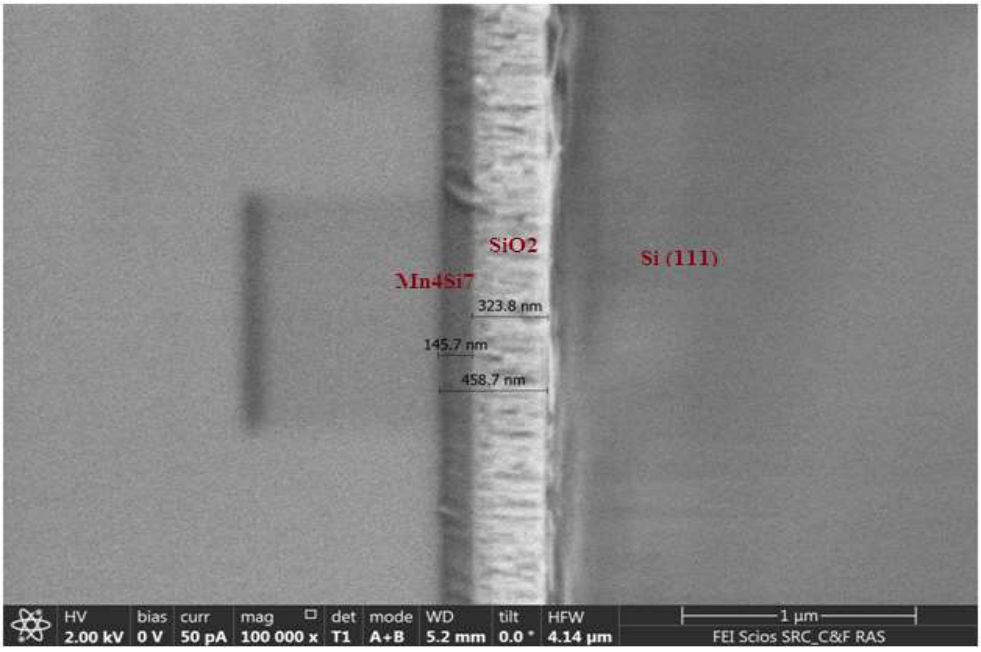

Figure 4. Image of nanosized Mn_4Si_7 coating on SiO_2/Si structure

The measurement results show that the resistance of the samples (SPS) is different, which is possibly due to the different concentrations of Mn and Si in different zones of the samples. In Mn_4Si_7vacuum coatings, the uniformity of the formed layer is higher, which indicates the same coating thickness.To determine the Hall constant on an ECOPIA(HMS-3000 VER3.53) instrument, a (SPS) Mn_4Si_7 sample with an area of 1 cm^2 and a thickness of 1 mm and a sample with a vacuum coating of Mn_4Si_7 with a thickness of 146 nm were used. In all measurements, the current strength was 100 μA, the magnetic field induction was 0.54 T, and the temperature was 27 °C.

The results of measurements obtained for these samples (Table 2), the dependences of the samples (VAX) and resistance on current (Fig. 5) are presented. There are the results of Hall measurements of bulk samples of Mn_4Si_7 and Mn_4Si_7 in the SiO_2/Si structure in Table 2.

Table 2

Electrophysical properties of high manganese silicide structure formed by two different methods

Options	Volume Mn_4Si_7	Coating Mn_4Si_7
Resistivity, Ohm·cm	$7.826 \cdot 10^{-4}$	$6.409 \cdot 10^{-4}$
Hall constant, cm^3/C	$1.285 \cdot 10^{-3}$	$1.597 \cdot 10^{-3}$
Conductivity, 1/Ohm·cm	$1.278 \cdot 10^{3}$	$1.560 \cdot 10^{3}$
Surface concentration, cm^{-2}	$1.215 \cdot 10^{17}$	$9.770 \cdot 10^{16}$
Volume concentration, cm^{-3}	$4.859 \cdot 10^{21}$	$3.908 \cdot 10^{21}$
Carrier mobility, $cm^2/V \cdot s$	1.642	2.492

From the results obtained with the ECOPIA instrument (HMS-3000 VER3.53), it can be seen that the bulk sample (SPS) and the coating sample (EPOS-PVD-DESK-PRO) are close to each other.

Figure 6 shows the optical absorption and transmission spectra of the samples obtained on an IR Tracer-100-SHIMADZU instrument.

The measurement results show that the nanoscale Mn_4Si_7 coating (a) has an IR transmission of 35 %, (b) an IR absorption of about 1 %, from which it can be seen that the Mn_4Si_7 coating has a low IR absorption of the rays. Figure 6 shows the results of measurements of the Seebeck coefficient (*S*) and resistance (*R*) of the Mn_4Si_7 -146 nm coating during heating and cooling.

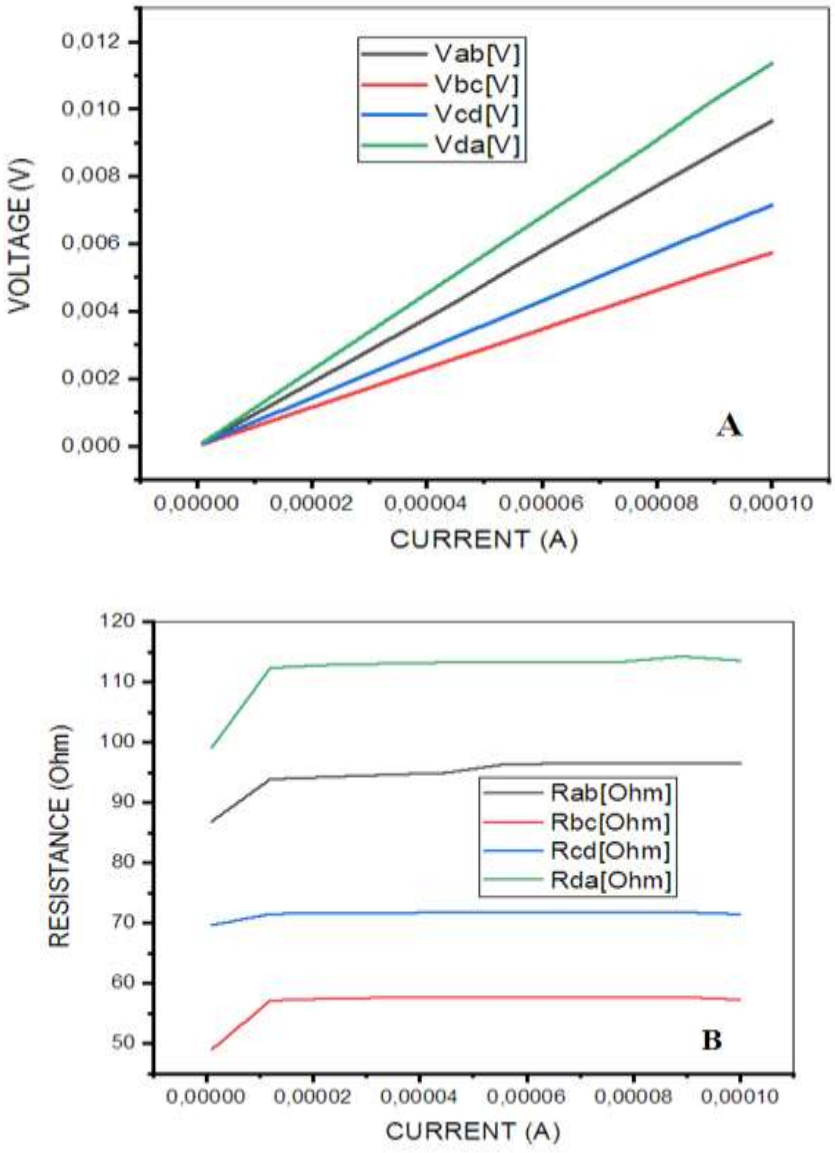

Figure 5. a) samples (I-V), b) relationship between (I-R)

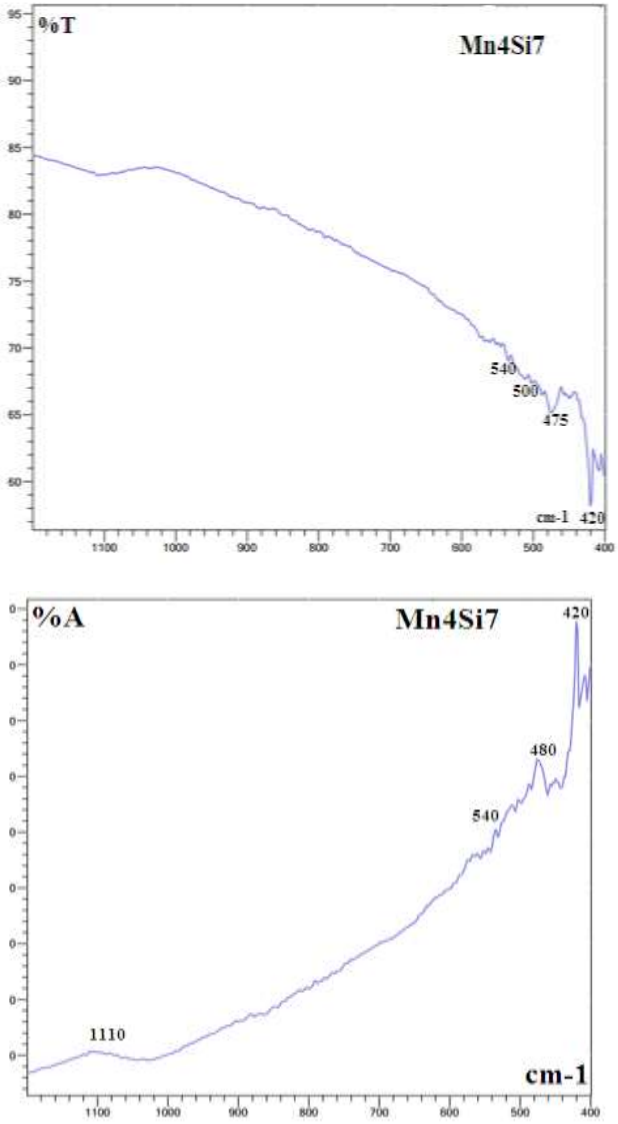

Figure6. Spectra obtained with the IRTracer-100 — SHIMADZU instrument

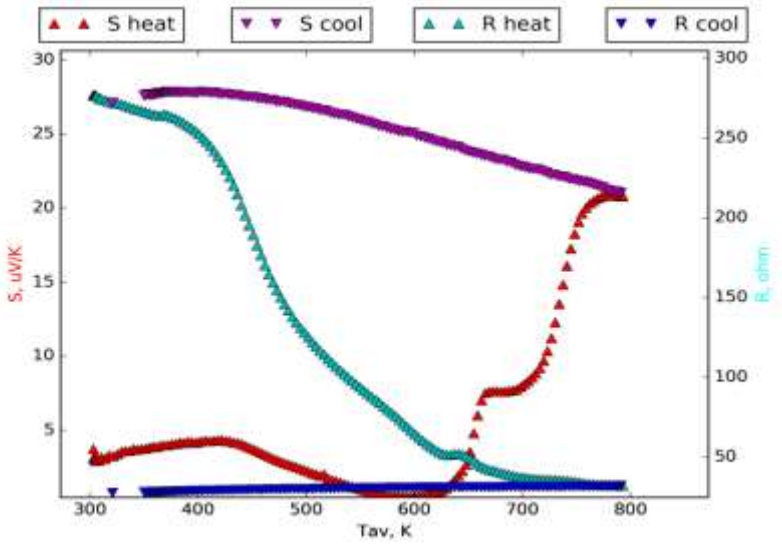

Figure 7. Temperature dependence of the Seebeck coefficient (*S*) and resistance (*R*) of a thin Mn_4Si_7 coating

When heated, Mn_4Si_7 -146 nm coating has a uniform structure with fine grains, due to sufficient coating density. With an increase in temperature from room temperature to 800 K, a decrease in resistance is observed from 250 Ohms to 25 Ohms, which in turn indicates a change in the characteristics of this material. The Seebeck coefficient decreases upon heating from room temperature from 300 K to 620 K. Since Mn_4Si_7 nanoclusters are semiconductor materials, it can be assumed that there will be energy barriers for charge carriers at the nanocluster–amorphous phase interface separating this phase (Fig. 7).

An increase in thermal sensitivity from 0 μV/K to 20 μV/K up to 800 K is explained by the disappearance of energy barriers for charge carriers at the nanocluster–amorphous phase interface due to the ordering of nanoclusters. The change from 20 μV/K to 28 μV/K upon cooling is explained by the appearance of structural relaxation in the amorphous phase. Seebeck coefficient (*S*) and resistance (*R*) vary with coating thickness.

Conclusions

Studies of the parameters of thin coatings of manganese silicide deposited on the SiO_2/Si structure by magnetron sputtering of a silicide target show that manganese silicide layers have a uniform fine-grained structure of a semiconductor nature, which is characterized by thermal sensitivity up to 20-30 μV per degree.

Heated films Mn_4Si_7 -146 nm coating has a uniform structure with fine grains, due to sufficient coating density. With an increase in temperature from room temperature to 800 K, a decrease in resistance is observed from 250 Ohms to 25 Ohms, which in turn indicates a change in the characteristics of this material. The Seebeck coefficient decreases upon heating from room temperature from 300 K to 620 K. Since Mn_4Si_7 nanoclusters are semiconductor materials, it can be assumed that there will be energy barriers for charge carriers at the nanocluster–amorphous phase interface separating this phase.

An increase in thermal sensitivity from 0 μV/K to 20 μV/K up to 800 K is explained by the disappearance of energy barriers for charge carriers at the nanocluster–amorphous phase interface due to the ordering of nanoclusters. The change from 20 μV/K to 28 μV/K upon cooling is explained by the appearance of structural relaxation in the amorphous phase.

References

1 Markov, V.F. (2014). Materials of modern electronics. Ministry of Education and Science Ros. Federation. P. 272.

2 Bekpulatov, I.R., Imanova, G.T., Kamilov, T.S., Igamov, B.D. & Turapov, I.K. (2022). Formation of n — type CoSimonosilicide film which can be used in instrumentation. *International Journal of Modern Physics B., 2350164.* DOI: 10.1142/S0217979223501643.

3 Umirzakov, B.E., Bekpulatov, I.R., Turapov, I.Kh. & Igamov, B.D. (2022). Effect of Deposition of Submonolayer Cs Coatings on the Density of Electronic States and Energy Band Parameters of CoSi2/Si(111). *Journal of Nano- and Electronic Physics, Vol. 14, 2, P. 02026.* DOI: 10.21272/jnep.14(2).02026.

4 Normurodov, M.T., Rysbaev, A.S., Bekpulatov, I.R., Normurodov, D.A. & Tursunmetova, Z.A. (2021). Formation and Electronic Structure of Barium-Monosilicide- and Barium-Disilicide Films. *Journal of Surface Investigation, Vol. 15,* P. S211-S215. DOI: 10.1134/S1027451022020318.

5 Isakhanov, Z.A., Umirzakov, Y.E., Ruzibaeva, M.K. & Donaev, S.B. (2015). Effect of the O2+-ion bombardment on the TiN composition and structure. *Technical Physics, Vol. 60, 2,* P. 313-315. DOI: 10.1134/S1063784215020097.

6 Umirzakov. B.E., Donaev, S.B. & Mustafaeva, N.M. (2019). Electronic and Optical Properties of GaAlAs/GaAs Thin Films. *Technical Physics, Vol. 64, 10,* P. 1506-1508. DOI: 10.1134/S1063784219100220.

7 Donaev, S.B., Umirzakov, B.E. & Mustafaeva, N.M. (2019). Emissivity of Laser-Activated Pd–Ba Alloy. *Technical Physics, Vol. 64, 10, P. 1541-1543.* DOI: 10.1134/S1063784219100074

8 Weissmuller, J. (1996). Synthesis and Processing of Nanocrystalline Powder / TMS.

9 Hicks, L.D. & Dresselhaus, M.S. (1993). Effect of quantum-well structures on thethermoelectric figure of merit. *Physical Review B., Vol. 47,* P. 12727–12731.

10 Allon, I. (2008). Enhanced thermoelectric performance of rough silicon nanowires. *NAT, Vol. 451, 7175,* P.163–167.

11 Burkov, A.T., Novikov, S.V., & Schumann J. (2012). Nanocrystallization of AmorphousM-Si Thin Film Composites (M=Cr, Mn) and Their Thermoelectric Properties. *AIP Conference Proceedings, 9th European Conference on Thermoelectric, Vol. 1449,* P. 219-222.

12 Novikov, S.V., Burkov, A.T. & Schumann, J. (2013). Enhancement of thermoelectricproperties in nanocrystalline M–Si thin film composites (M = Cr, Mn). *Journal of Alloys and Compounds, Vol. 557,* P. 239–243.

13 Orekhov, A.S. & Klechkovskaya, V.V. (2017). Establishment of the relationship between the microstructure and thermoelectric properties of crystals of higher manganese silicide, doped with germanium. *Physics and technology of semiconductors, Vol. 51, 7,* P. 925-928.

14 Adachi K., Ito, K., Zhang, L.T. & Yamaguchi, M. (2003). Material Science. P. 3445–3450.

15 Maex, K. (2003). Properties of Metal Silicides. INSPEC, Stevenage.

16 Yoneyama, T. & Okada, A. (2013). Formation of polycrystalline BaSi2 films by radio-frequency magnetron sputtering for thin-film solar cell applications. *Thin Solid Films, Vol. 534,* P. 116-119. DOI: 10.1016/j.tsf.2013.02.003.

17 Dubov, V.L. (2008). Formation, structure, optical and photoelectric properties of textured BaSi2 films on Si(111) and heterostructures based on them. *Dissertation. Blagoveshchensk. Vol. 124,* P. 67-70.

18 Egerton, R.F. (2008). Electron energy-loss spectroscopy in the TEM. *Reports on Progress in Physics. Vol. 72, 1,* P. 016502.

19 Pani, M. & Palenzona, A. (2008). The phase diagram of the Ba–Si system. *Journal of Alloys and Compounds, Vol. 454, 1-2,* P. L1-L2.

20 Miyazaki, Y., Igarashi, D., Hayashi, K. & Kajitani, T. (2008). *Physical Review B., Vol. 78,* P. 214104.

21 Kajitani, T. (2010). *Journal of Electronic Materials, Vol. 39, P.* 1482-1487.

22 Migas, D.B. (2008). *Physical Review B., Vol. 77,* P. 075205.

23 Kamilov, T.S., Rysbaev, A.S., Klechkovskaya, V.V., Orekhov, A.S., Igamov, B.D. & Bekpulatov, I.R. (2019). The Influence of Structural Defects in Silicon on the Formation of Photosensitive Mn4Si7–Si(Mn)–Mn4Si7 and Mn4Si7–Si(Mn)–M Heterostructures. *Applied Solar Energy, Vol. 55,* P. 380-384.

Б.Д. Игамов, Г.Т. Иманова, А.И. Камардин, И.Р. Бекпулатов

Нысанды қалыптастыру және магнетронды шашырату арқылы алынған Mn_4Si_7 жабындарын зерттеу

SiO_2/Si құрылымында магнетронды шашырату арқылы алынған Mn_4Si_7 көлемді үлгілері мен вакуумдық жабындарының морфологиясы, құрамы және электрлік және оптикалық қасиеттері зерттелді. Қалыңдығы шамамен 150 нм болатын марганецті силицидті жабындар қасиеттері бойынша массалық Mn_4Si_7-ге жақын, жартылай өткізгіш сипаттағы біркелкі ұсақ түйіршікті құрылымы бар, ол бір градусқа 20-30 мкВ-қа дейінгі термиялық сезімталдықпен сипатталады. Сонымен қатар мақалада авторлар магнетронды шашырату әдісімен шығарған жоғары марганецті силицидті қабыршақтардың электрофизикалық қасиеттерін ұсынған. Қыздырылған пленкалар Mn_4Si_7-146 нм жабынның жеткілікті тығыздығына байланысты ұсақ түйіршіктері бар біркелкі құрылымға ие. Mn_4Si_7 нанокластерлері жартылай өткізгіш материалдар болғандықтан, осы фазаны бөлетін нанокластер-аморфты фаза интерфейсінде заряд тасымалдаушылар үшін энергетикалық кедергілер болады деп болжауға болады. Термиялық сезімталдықтың 0 мкВ/К-ден 20 мкВ/К-ден 800 К-ге дейін жоғарылауына нанокластерлердің реттелгеніне байланысты нанокластер-аморфты фаза интерфейсіндегі заряд тасымалдаушыларға арналған энергетикалық кедергілердің жойылуымен түсіндіріледі. Салқындату кезінде 20 мкВ/К-ден 28 мкВ/К-ге дейін өзгеруі аморфты фазадағы құрылымдық релаксацияның пайда болуымен түсіндіріледі.

Кілт сөздер: Холл тұрақтысы, Mn_4Si_7, жұқа жабын, нанокластер, электрөткізгіштік, наноқұрылым, меншікті кедергі, көлемді концентрациясы.

Б.Д. Игамов, Г.Т. Иманова, А.И. Камардин, И.Р. Бекпулатов

Формирование мишеней и исследование покрытий Mn_4Si_7, полученных методом магнетронного распыления

Исследованы морфология, состав, электрические и оптические свойства объемных образцов и вакуумных покрытий Mn_4Si_7, полученных методом магнетронного напыления на структуру SiO_2/Si. Показано, что покрытия из силицида марганца толщиной около 150 нм близки по свойствам к объемному Mn_4Si_7, имеют однородную мелкозернистую структуру полупроводниковой природы, которая характеризуется термочувствительностью до 20–30 мкВ на градус. Кроме того, в настоящей статье представлены электрофизические свойства пленок высокомарганцевого силицида, полученных авторами методом магнетронного распыления. Нагретые пленки Mn_4Si_7 —146 нм. Покрытие имеет однородную структуру с мелкими зернами, что обусловлено достаточной плотностью покрытия. Поскольку нанокластеры Mn_4 Si_7 являются полупроводниковыми материалами, можно предположить, что на границе раздела «нанокластер–аморфная фаза», разделяющей эту фазу, будут существовать энергетические барьеры для носителей заряда. Увеличение термочувствительности от 0 до 20 мкВ/К вплоть до 800 К объясняется исчезновением энергетических барьеров для носителей заряда на границе «нанокластер–аморфная фаза» за счет упорядочения нанокластеров. Изменение от 20 до 28 мкВ/К при охлаждении объясняется появлением структурной релаксации в аморфной фазе.

Ключевые слова: постоянная Холла, Mn4Si7, тонкое покрытие, нанокластер, электропроводность, наноструктура, удельное сопротивление, объемная концентрация.

DOI 10.31489/2023PH3/58-64

UDC 544.6.076.324.4

D. Suleimenova[1,2], Ye. Tashenov[1,2], Mannix P. Balanay[3], B. Baptayev[1*]

[1]National Laboratory Astana, Nazarbayev University, 53 Kabanbay Batyr Ave., Astana, 010000 Kazakhstan;
[2]Department of Chemistry, L.N. Gumilyov Eurasian National University, 2 Satpayev St., Astana, 010008 Kazakhstan;
[3]Chemistry Department, Nazarbayev University, 53 Kabanbay Batyr Ave., Astana, 010000 Kazakhstan
*(*Email: bbaptayev@nu.edu.kz)*

Unveiling the Potential of $Mn_xCo_{3-x}S_4$ Electrocatalyst in Triiodide Reduction for Dye-sensitized Solar Cells

The development of a low-cost and high-efficiency Pt-free counter electrode is an important goal to improve the performance of dye-sensitized solar cells. In this study, we successfully synthesized a $Mn_xCo_{3-x}S_4$-based counter electrode by a facile solvothermal synthesis technique. The electrocatalyst was directly deposited on a fluorine doped titanium oxide (FTO) coated glass substrate. Various characterization techniques such as X-ray diffraction, scanning electron microscopy, energy dispersive X-ray spectroscopy and X-ray photoelectron spectroscopy were employed to analyze the obtained $Mn_xCo_{3-x}S_4$ counter electrode material. The photovoltaic measurements performed on the dye-sensitized solar cells showed a remarkable improvement in energy conversion efficiency with the $Mn_xCo_{3-x}S_4$counter electrode (8.60 %) compared to the conventional Pt (8.11 %). Moreover, the $Mn_xCo_{3-x}S_4$counter electrode exhibited excellent stability, further highlighting its potential as an efficient and durable alternative to Pt in dye-sensitized solar cells. Overall, our results contribute to the further development of Pt-free counter electrode materials for sustainable solar energy applications.

Keywords: $MnCo_2S_4$; ternary sulfide; solvothermal synthesis; Pt-free counter electrodes, dye-sensitized solar cells.

Introduction

The demand for photovoltaic technology continues to increase as the world's population grows and environmental concerns increase. Among the various types of photovoltaic technologies, dye-sensitized solar cells (DSSCs) have emerged as a promising third-generation solution due to their low cost, high efficiency, and ease of fabrication. These characteristics make DSSCs a potential replacement for expensive silicon-based solar cells [1]. However, the commercialization of DSSCs faces challenges such as relatively low efficiency, poor stability, and non-competitive prices. Another hurdle is the use of platinum (Pt) as a counter electrode in DSSCs, which is problematic due to high cost, limited availability, and stability-related issues [2-4]. Consequently, there is an urgent need to develop low-cost and high-efficiency Pt-free counter electrodes to improve the overall affordability of solar cells [5].

Transition metal compounds, especially ternary compounds such as oxides, sulfides, and selenides, have emerged as promising alternatives to Pt due to their excellent electrocatalytic activity, long-term stability, and abundance [6-8]. In this study, we focused on the development of a $MnCo_3S_4$ electrocatalyst as a Pt-free counter electrode for DSSC applications. $MnCo_2S_4$ is a ternary compound derived from Co_3S_4 with one Co atom replaced by Mn. To achieve this, we synthesized a $Mn_xCo_{3-x}S_4$ counter electrode directly on a fluorine-doped titanium oxide (FTO) coated glass substrate using a simple one-step solvothermal method. The resulting $Mn_xCo_{3-x}S_4$/FTO counter electrode was extensively characterized by various spectroscopic and microscopic techniques and then integrated into a DSSC device to evaluate its performance.

Remarkably, the DSSC with the $Mn_xCo_{3-x}S_4$composite counter electrode achieved a higher efficiency (PCE) of 8.60 % compared to the device with a conventional Pt counter electrode (PCE of 8.11 %). These results demonstrate the potential of $Mn_xCo_{3-x}S_4$ counter electrodes as a promising alternative to Pt in DSSCs, offering advantages such as lower cost and higher efficiency. With this research, we contribute to the further development of Pt-free counter electrode materials and pave the way for more affordable and sustainable photovoltaic technologies.

2. Experimental

2.1. Materials

Chemicals and materials were obtained from commercial sources and utilized as received, unless specifically stated otherwise.

2.2. Synthesis of $Mn_xCo_{3-x}S_4$ counter electrode

A composite material, $Mn_xCo_{3-x}S_4$, was synthesized by the solvothermal method. In this method, the precursors $Mn(NO_3)_2$, $Co(NO_3)_2$, and thiourea were dissolved in ethanol in an ultrasonic bath. The resulting solution, together with the FTO glass, was then transferred to a 50-mL stainless steel autoclave lined with Teflon and kept at a temperature of 180 °C for 14 hours. The stoichiometric ratio of manganese and cobalt nitrates to thiourea was 1:2:10, respectively. Subsequently, the electrocatalyst-coated FTO substrates were washed with water and ethanol and dried at 70 °C for 12 hours in a vacuum oven.

2.3. Fabrication of dye-sensitized solar cells

Preparation of the working electrode (WE) included the following steps: First, the FTO glass slides (2.2 mm thick, surface resistivity 7 Ω/sq, Sigma-Aldrich) were cleaned with ethanol and ultrasound and then air dried. A compact TiO_2 layer was formed by soaking the FTO in a 50 mM titanium (IV) isopropoxide solution in 2M HCl at 70ºC for 30 minutes and sintering at 500ºC for 30 minutes. A transparent TiO_2 paste (particle size: 18-20 nm, DN -EP03, Dyenamo) was doctor bladed the compact TiO_2 layer. After the transparent TiO_2 layer was air dried for 30 minutes, the electrodes were sintered in an oven at different temperatures: 125ºC for 5 minutes, 325ºC for 10 minutes, 425ºC for 15 minutes, and 500ºC for 30 minutes. Once the electrodes were cooled to 70ºC, a light-scattering TiO_2 layer (particle size: 150-250 nm, Greatcell Solar WER2-O, Sigma-Aldrich) was doctor bladed over the transparent TiO_2 film and air dried for 1 hour before sintering as described above. After cooling, the electrodes were immersed in a dye solution containing 0.25 mM of ruthenium-based standard dye N719 (Sigma-Aldrich) and 0.75 mM chenodeoxycholic acid (CDCA, Sigma-Aldrich) in an acetonitrile: tert-butanol mixture (1:1) for 24 hours. After loading the dye, the electrodes were rinsed with ethanol to remove unbound dye molecules from the surface of the TiO_2 film and then dried.

The counter electrode (CE) was prepared using a Pt-based approach. A commercial Pt paste (containing terpineol and hexachloroplatinic acid, Sigma-Aldrich) was doctor bladed onto a clean and dry FTO glass substrate and then sintered at 500ºC for 30 minutes.

To construct the dye-sensitized solar cell, an MPN-based iodine/iodide redox electrolyte (DN-OD03 S104, Dyenamo) was applied to the dye-loaded TiO_2 photoanode and the CE (either Pt or $Mn_xCo_{3-x}S_4$) was placed on top. The two electrodes were separated with double-sided adhesive tape.

2.4. Characterization

The electrocatalyst was subjected to various characterization techniques to evaluate its properties. X-ray diffraction (XRD) patterns were obtained using a Rigaku SmartLab system. The structure and morphology were analyzed using a Zeiss Crossbeam 540 scanning electron microscope (SEM). Energy dispersive X-ray spectroscopy (EDS) and NEXSA Thermoscientific X-ray photoelectron spectroscopy (XPS) were used to determine material composition.

The photovoltaic analysis of the solar cells was performed using Dyenamo Toolbox (DN -AE01). Electrochemical analysis, on the other hand, was performed in the dark using the IM6 electrochemical station from Zahner Elektrik. The measurements were performed with a bias voltage of -0.72 V, an amplitude of 10 mV and a frequency range of 0.1 — 100000 Hz. The obtained data were further processed and fitted using the EIS Spectrum Analyzer.

3. Results and Discussion

3.1. Characterization of $Mn_xCo_{3-x}S_4$ electrocatalyst

Figure 1 shows the XRD patterns of $Mn_xCo_{3-x}S_4$. In addition to the prominent peaks originating from the FTO substrate, specific diffraction peaks can be observed at 32.09°, 36.73°, 48.36°, and 55.83° corresponding to the (311), (400), (511), and (440) crystal planes of Co_3S_4, respectively (PDF42-1448) [9]. It is noteworthy that the XRD diffraction peaks of $Mn_xCo_{3-x}S_4$ are very similar to those of Co_3S_4, indicating the substitution of a single Co atom by Mn and the similarity of crystal structure between the two[10]. Therefore, we can conclude that the doping process led to the formation of $MnCo_2S_4$.

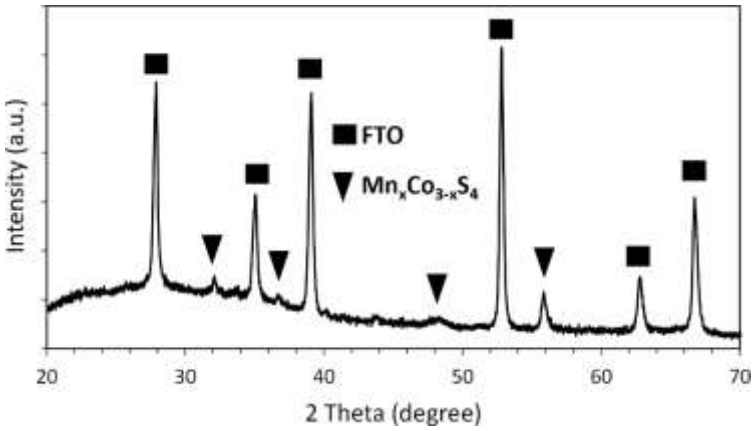

Figure 1: X-ray diffraction pattern of a thin film of $Mn_xCo_{3-x}S_4$on an FTO substrate.

The elemental composition and valence states were analyzed by X-ray photoelectron spectroscopy, and the corresponding spectra are shown in Figure 2. The full XPS spectrum of the $Mn_xCo_{3-x}S_4$ composites shows distinct peaks attributable to Mn, Co, and S, confirming the presence of these elements and their corresponding valence states in the sample. It is worth noting that the elements C, N and O are normally present in air.

The Co 2p spectrum shows two spin-orbit doublet peaks. The dominant peaks at 781.8 and 797.0 eV correspond to the 2p3/2 and 2p1/2 spin-orbit states of Co^{2+}, respectively, while the weaker peaks at 777.6 and 792.8 eV are associated with Co^{3+}[10]. The presence of Co^{3+} peaks in the spectrum indicates possible oxidation of the surface when exposed to air. As can be seen in Figure 2, the Mn 2p orbitals show spin splitting leading to two singlet pairs: Mn 2p3/2 (642.8 eV) and Mn 2p1/2 (654.6 eV), which can be attributed to the Mn^{2+} binding energy[11]. In the S 2p XPS spectra, a satellite peak at 168.7 eV and three peaks representing different sulfur species are observed. The peaks at 162.3 and 163.5 eV correspond to S 2p3/2 and S 2p1/2, respectively. In addition, the peak at 164.6 eV indicates metal-bonded sulfur (S-M) [12].

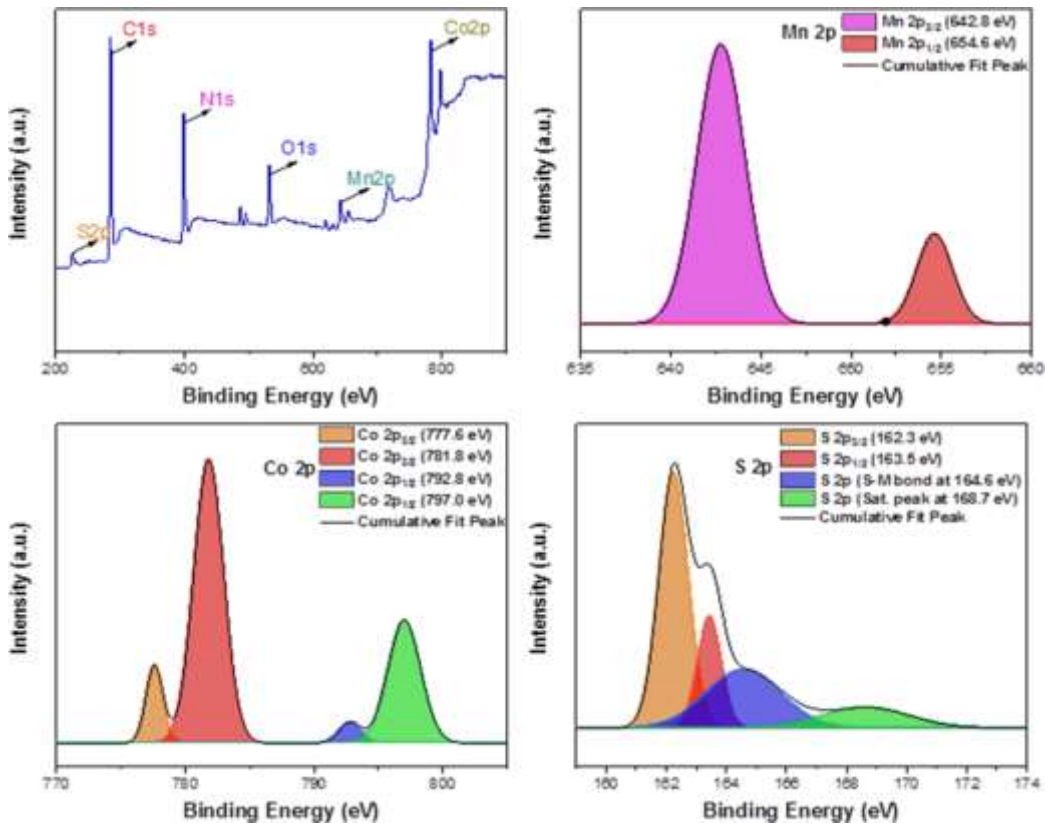

Figure 2. XPS spectra of the $Mn_xCo_{3-x}S_4$ electrocatalyst.

Uniformly grown $Mn_xCo_{3-x}S_4$ nanoflakes were prepared on the surface of FTO glass by a solvothermal reaction. The resulting electrocatalyst had nanoflakes with an average diameter of about 260 nm and a plate thickness of 36.5 nm, as shown in the upper part of Figure 3. The lower part of Figure 3 shows the spectrum of energy dispersive X-ray spectroscopy of the synthesized $Mn_xCo_{3-x}S_4$ composite, which confirms the presence of elements Mn, Co and S in the prepared material.

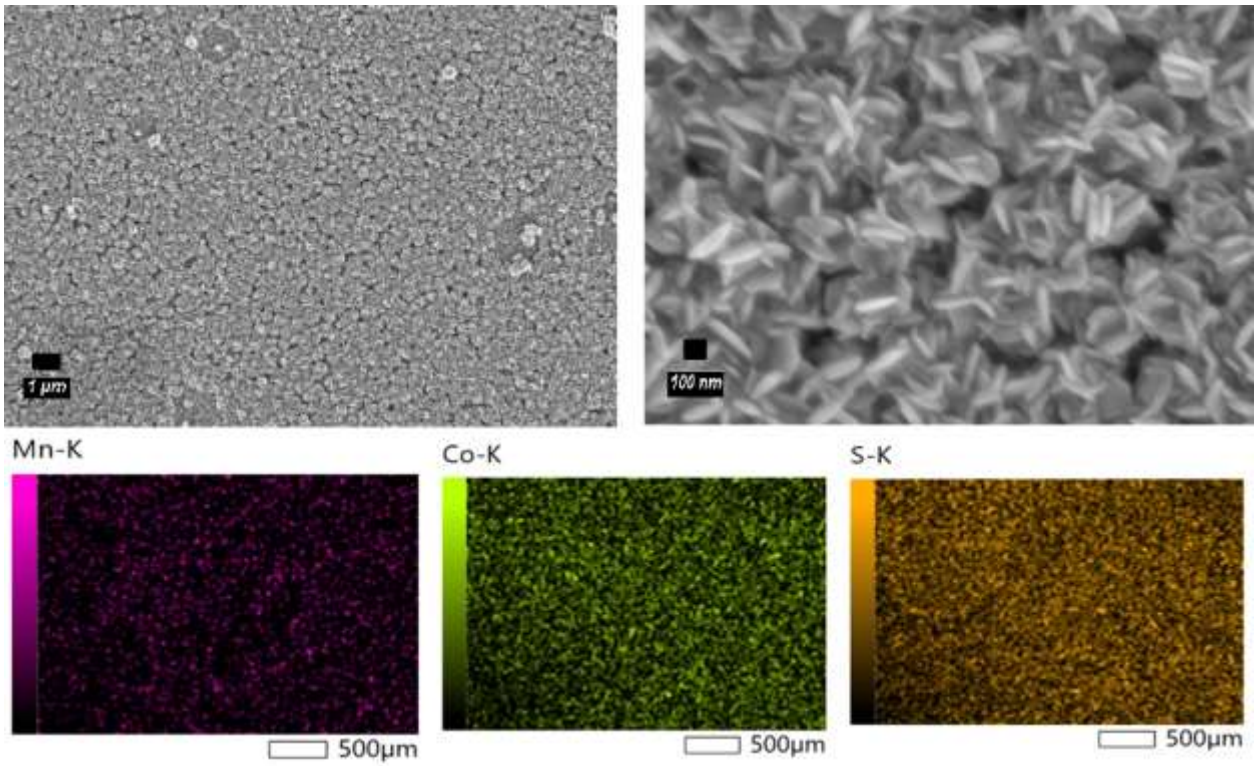

Figure 3. Top: FE-SEM images of the $Mn_xCo_{3-x}S_4$ coated FTO electrode showing magnifications of 5000 (left) and 40000 (right). Bottom: EDS mapping of the electrocatalyst.

3.2. Photovoltaic and electrochemical performance of $Mn_xCo_{3-x}S_4$ electrocatalyst

To investigate the photovoltaic and electrochemical performances of an electrocatalyst, dye-sensitized solar cells were constructed using $Mn_xCo_{3-x}S_4$ and Pt as counter electrodes. The photovoltaic measurements were performed under the standard solar conditions AM 1.5 and an illuminance of 1000 W/cm^2. The obtained results are summarized in Table. Figure 4a shows the current-voltage (J-V) curve of the solar cells, while Figure 4b presents the Nyquist diagrams. It is worth noting that the $Mn_xCo_{3-x}S_4$ composite cell has an excellent performance with a power conversion efficiency (PCE) of 8.60 %, slightly exceeding the Pt cell efficiency of 8.11 %. The main factor contributing to the increase in PCE efficiency is the short circuit current (J_{SC}), which was 16.60 mA/cm^2 for the $Mn_xCo_{3-x}S_4$ cell and 15.87 mA/cm^2 for the Pt control device. This higher J_{SC} indicates better electrocatalytic activity of the $Mn_xCo_{3-x}S_4$ electrocatalyst compared to Pt. The electrochemical impedance spectroscopy measurements confirm this result (Fig. 4b). The Nyquist diagrams of the solar cells consist of two semicircles: The smaller arc represents the charge transfer resistance at the interface between the counter electrode and the electrolyte (R_{CT}), while the larger arc corresponds to the charge transfer resistance at the interface between the semiconductor and the electrolyte (R_{TiO_2}). The intersection of the graph with the x-axis indicates the series resistance of the device (R_S). It is worth noting that the $Mn_xCo_{3-x}S_4$ cell has a lower series resistance (19.2 Ω) compared to Pt (22.6 Ω), indicating better contact between $Mn_xCo_{3-x}S_4$ and FTO. In addition, the R_{CT} of the $Mn_xCo_{3-x}S_4$cell was also lower than that of the Pt solar cell, indicating improved electrocatalytic activity of the novel Pt-free counter electrode and improved electron flow at the counter electrode-electrolyte interface. This electron flow, referred to as the exchange current (J_o), is indirectly proportional to the charge transfer resistance R_{CT} and can be expressed as

$$J_o = \frac{RT}{nFR_{CT}},$$

where R is the universal gas constant, T is the absolute temperature, n is the number of electrons involved in the triiodide reduction process, and F is Faraday's constant. The superior electrocatalytic activity of $Mn_xCo_{3-x}S_4$ provides an explanation for the improved J_{SC} in the DSSCs compared to Pt.

T a b l e

Photovoltaic parameters comparison between DSSCs with $Mn_xCo_{3-x}S_4$ composites and Pt counter electrodes.

DSSCs	PCE (%)	V_{OC}(V)	J_{SC} (mA/cm^2)	FF	R_S (Ω)	R_{CT} (Ω)	R_{TiO_2} (Ω)
$Mn_xCo_{3-x}S_4$	8.60	0.73	16.60	0.71	19.2	12.9	47.9
Pt	8.11	0.73	15.87	0.70	22.6	13.1	54.6

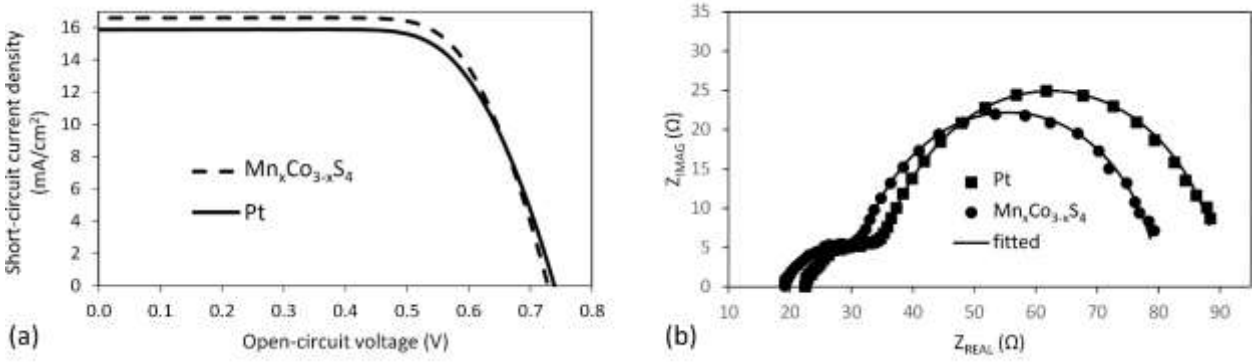

Figure 4. (a) Current-voltage curves and (b) Nyquist plots depicting the performance of dye-sensitized solar cells.

4. Conclusions

In this study, Pt-free counter electrodes based on $Mn_xCo_{3-x}S_4$ were successfully synthesized by a one-pot solvothermal method. The electrocatalytic activity of $Mn_xCo_{3-x}S_4$ proved to be excellent and exceeded that of Pt, as further measurements showed. In particular, the dye-sensitized solar cell with $Mn_xCo_{3-x}S_4$ composites as the counter electrode achieved an efficiency of 8.60 %, slightly outperforming the DSSC with Pt counter electrode (PCE: 8.11 %). These results highlight the potential of $Mn_xCo_{3-x}S_4$ composites as a promising alternative to Pt for DSSC counter electrodes due to their improved electrocatalytic performance and cost efficiency. Moreover, this research introduces a novel idea and strategy for fabricating efficient base metal counter electrode materials for DSSCs. The convenient solvothermal method used in this study provides a practical and scalable approach to fabricate $Mn_xCo_{3-x}S_4$ composites. This technique can potentially be extended to other metal sulfide materials, allowing the development of a broader range of base metal counter electrodes. The successful implementation of $Mn_xCo_{3-x}S_4$ composites as Pt-free counter electrodes not only solves the problem of scarcity and high cost of Pt, but also provides a sustainable and environmentally friendly solution for DSSC technology. Future studies can address the optimization of the composition and morphology of $Mn_xCo_{3-x}S_4$ composites to further improve their performance in DSSCs and ultimately advance the field of renewable energy.

5. Author contributions

Diana Suleimenova was responsible for the conception and design of the analysis and for performing the synthesis, characterization, and electrochemical and photovoltaic measurements. She was also involved in writing the first draft of the manuscript. Yerbolat Tashenov played a key role in the analysis of the data. Bakhytzhan Baptayev contributed to the conception and design of the analysis, performed an overall analysis of the data, and provided the necessary funding. Mannix P. Balanay contributed to the conception and design of the analysis and provided critical revisions to the overall manuscript.

6. Conflicts of interest

There are no conflicts to declare.

7. Acknowledgements

This research was funded by the Science Committee of the Ministry of Education and Science of the Republic of Kazakhstan (Grant No. AP13068358 “Low-cost solid-state dye-sensitized solar cells — a new strategy of the development of the field”, project PI — B.B.).

References

1 O'Regan, B. & Grätzel, M. (1991). A low-cost, high-efficiency solar cell based on dye-sensitized colloidal TiO2 films. *Nature, 353*(6346), 737-740.

2 Olsen, E., Hagen, G. & Eric Lindquist, S. (2000). Dissolution of platinum in methoxy propionitrile containing LiI/I2. *Sol. Energy Mater. Sol. Cells, 63*(3), 267-273.

3 Shu, Z. X. & Bruckenstein, S. (1991). Iodine adsorption studies at platinum. J. Electroanal. *Chem. Interfacial Electrochem, 317*(1-2), 263-277.

4 Kay, A. & Grätzel, M. (1996). Low cost photovoltaic modules based on dye sensitized nanocrystalline titanium dioxide and carbon powder. *Sol. Energy Mater. Sol. Cells, 44*(1), 99-117.

5 Ahmed, U., Alizadeh, M., Rahim, N.A., Shahabuddin, S., Ahmed, M.S. & Pandey, A.K. (2018). A comprehensive review on counter electrodes for dye sensitized solar cells: A special focus on Pt-TCO free counter electrodes. *Sol. Energy, 174,* 1097-1125.

6 Liu, K., Wei, A., Liu, J., Liu, Z., Xiao, Z. & Zhao, Y. (2018). NiCo2S4 nanosheet thin film counter electrodes prepared by a two-step approach for dye-sensitized solar cells. *Mater. Lett. 217,* 185-188.

7 Theerthagiri, J., Senthil, R.A., Buraidah, M.H., Madhavan, J., Arof, A.K. & Ashokkumar, M. (2016). One-step electrochemical deposition of Ni1−xMoxS ternary sulfides as an efficient counter electrode for dye-sensitized solar cells. *J. Mater. Chem. A, 4*(41), 16119-16127.

8 Hou, W., Xiao, Y. & Han, G. (2017). An interconnected ternary MIn2S4 (M=Fe, Co, Ni) thiospinel nanosheet array: A type of efficient platinum-free counter electrode for dye-sensitized solar cells. *Angew. Chem., 129*(31), 9274-9278.

9 Li, Y., Wang, N., Xu, J., Liu, Z. & Yu, H. (2019). Significant effect of advanced catalysts Co3S4 modified CuWO4·2H2O under visible light condition photocatalytic hydrogen production. *J. Nanopart. Res., 21*(4), 80.

10 Dai, Z., Feng, X., Li, Q., Su, P., Shen, X., Zheng, Y., Jiao, Q., Zhao, Y., Li, H. & Feng, C. (2021). Construction of porous core-shell MnCo2S4 microrugby balls for efficient oxygen evolution reaction. *J. Alloys Compd., 872.*

11 Raghavendra, K.V.G., Gopi, C.V. V. M., Vinodh, R., Rao, S.S., Obaidat, I.M. & Kim, H.-J. (2020). Facile synthesis of nanoparticles anchored on honeycomb-like MnCo2S4 nanostructures as a binder-free electroactive material for supercapacitors. *J. Energy Storage, 27.*

12 Wang, H., Zhang, K., Song, Y., Qiu, J., Wu, J. & Yan, L. (2019). MnCo2S4 nanoparticles anchored to N- and S-codoped 3D graphene as a prominent electrode for asymmetric supercapacitors. *Carbon, 146,* 420-429.

Д. Сүлейменова, Е. Ташенов, Маникс П. Баланэй, Б. Баптаев

Бояғышқа сезімтал күн батареялары үшін триодидтерді тотықсыздану кезінде $Mn_xCo_{3-x}S_4$ электрокатализаторының әлеуетін ашу

Қымбат емес және жоғары тиімді, құрамында платинасы жоқ қарсыэлектродты жасау бояғышқа сезімтал күн батареяларының өнімділігін жақсартудың маңызды міндеті болып табылады. Бұл зерттеуде біз қарапайым солвотермиялық синтез әдісін қолдана отырып, MnxCo3-xS4 қарсы электродты сәтті синтездедік. Электрокатализатор тікелей фтор легирленген титан оксидімен (FTO) қапталған шыны төсенішке қолданылды. Алынған $Mn_xCo_{3-x}S_4$ қарсыэлектрод материалын талдау үшін рентгендік дифракциялық спектроскопия, сканерлеуші электрондық микроскопия, энергиялық дисперсиялық рентгендік спектроскопия және рентгендік фотоэлектрондық спектроскопия сияқты әртүрлі сипаттама әдістері пайдаланылды. Бояғышқа сезімтал күн батареяларында жүргізілген фотоэлектрлік өлшеулер әдеттегі Pt (8,11 %) салыстырғанда $Mn_xCo_{3-x}S_4$ есептегіш электродпен (8,60 %) қуатты түрлендіру тиімділігінің айтарлықтай жақсарғанын көрсетті. Сонымен қатар, $Mn_xCo_{3-x}S_4$ қарсыэлектроды тамаша тұрақтылықты көрсетті, бұл оның әлеуетін одан әрі бояғышқа сезімтал күн батареяларында Pt-ге тиімді және берік балама ретінде әлеуетін одан әрі көрсетеді. Тұтастай алғанда, біздің нәтижелеріміз күн энергиясын тұрақты пайдалану үшін Pt-сіз контрэлектродтық материалдарды одан әрі дамытуға ықпал етеді.

Кілт сөздер: $MnCo_2S_4$, үштік сульфид, солвотермиялық синтез, Pt жоқ қарсы электродтар, бояғышқа сезімтал күн батареялары.

Д. Сулейменова, Е. Ташенов, Маникс П. Баланэй, Б. Баптаев

Раскрытие потенциала электрокатализатора $Mn_xCo_{3-x}S_4$ в восстановлении трийодидов для солнечных элементов, сенсибилизированных красителем

Разработка недорогого и высокоэффективного противоэлектрода, не содержащего платины, является важной задачей для улучшения характеристик солнечных элементов, сенсибилизированных красителем. В этом исследовании мы успешно синтезировали противоэлектрод на основе $Mn_xCo_{3-x}S_4$ с помощью простого метода сольвотермического синтеза. Электрокатализатор наносили непосредственно на стеклянную подложку с покрытием из легированного фтором оксида титана (FTO). Для анализа полученного материала противоэлектрода $Mn_xCo_{3-x}S_4$ использовались различные методы характеризации, такие как рентгеновская дифракционная спектроскопия, сканирующая электронная микроскопия, энергодисперсионная рентгеновская спектроскопия и рентгеновская фотоэлектронная спектроскопия. Фотогальванические измерения, выполненные на солнечных элементах, сенсибилизированных красителем, показали заметное улучшение эффективности преобразования энергии с противоэлектродом $Mn_xCo_{3-x}S_4$ (8,60 %) по сравнению с обычным Pt (8,11 %). Кроме того, противоэлектрод $Mn_xCo_{3-x}S_4$ продемонстрировал превосходную стабильность, что еще больше подчеркивает его потенциал в качестве эффективной и долговечной альтернативы Pt в солнечных элементах, сенсибилизированных красителем. В целом, наши результаты способствуют дальнейшему развитию материалов противоэлектродов, не содержащих Pt, для устойчивого использования солнечной энергии.

Ключевые слова: $MnCo_2S_4$, тройной сульфид, сольвотермальный синтез, бесплатиновые противоэлектроды, солнечный элемент, сенсибилизированный краситель.

DOI 10.31489/2023PH3/65-74

UDC 620.171

L.B. Bayatanova[1,2], A.Zh. Zhassulankyzy[3], N.M. Magazov[2,3], B.K. Rakhadilov[1,3], N. Muktanova[1,2]*, G.K. Uazyrkhanova[2]

[1]PlasmaScience LLP, Ust-Kamenogorsk, Kazakhstan;
[2]D. Serikbayev East Kazakhstan Technical University, Ust-Kamenogorsk, Kazakhstan;
[3]Shakarim University of Semey, Kazakhstan
*(*E-mail: nmuktanova@bk.ru)*

Effect of plasma-electrolytic oxidation on mechanical properties of titanium coatings

The process of plasma electrolytic oxidation (PEO) allows to obtain multifunctional coatings with unique properties, including wear-resistant, corrosion-resistant, heat-resistant, electrical insulating and decorative. Therefore, the field of application of these coatings is quite wide: medicine, aircraft construction, shipbuilding, instrumentation, automotive and other industries. The technology is based on the phenomenon of micro-arc discharges promoting the formation of oxide layers on metal surfaces. In this review the technologies of obtaining coatings by plasma electrolytic oxidation on titanium are considered. The experiment on PEO of VT1-0 titanium substrate under anodic treatment with the addition of TiO_2 nanoparticles to the electrolyte was carried out. Dense, uniform oxide coatings that do not require additional surface grinding were obtained. The coating thickness values were 18.5-62.4 μm. The influence of PEO on the microhardness of calcium-phosphate coatings formed as a result of this treatment was studied. With a satisfactory thickness of the formed layer (62.4 μm), the surface microhardness value (4.04 GPa) was found to be the highest among all the treatment modes compared, simultaneously with a high elastic modulus value (348 GPa) and a small value of the indenter penetration depth on the coating (968.99 nm). These coatings were formed in an electrolyte containing calcium phosphate with the addition of 0.75g of titanium oxide nanoparticles. The increase of microhardness in comparison with the sample without coating is in 2,5 times. As a result of the carried out researches optimum modes and parameters of calcium-phosphate coatings receiving have been established and defined. It is shown that by changing the composition of the electrolyte of the micro-arc treatment process it is possible to influence significantly the structure, thickness and surface properties of the obtained coatings.

Keywords: plasma-electrolytic oxidation (PEO), electrolyte, nanoparticles, coating, structure, microhardness, titanium, titanium oxide.

Introduction

Plasma electrolytic methods of material treatment are a very promising area of research to create new materials with unique properties [1]. Plasma electrolytic oxidation refers to an electrochemical process which has proven effective in altering the surface properties of metals and alloys, offering a number of potential advantages in various applications [2, 3]. This process is carried out at higher voltages, up to 1000 V, with AC and pulsed currents being used more frequently than DC currents. The PEO process is most fully investigated for valve metals and their alloys (aluminium, magnesium, titanium, tantalum, niobium, zirconium, etc.) [4, 5]. The process of PEO allows to receive multifunctional coatings with unique complex of properties, including wear-resistant, corrosion-resistant, heat-resistant, electrical insulating and decorative. Therefore, the field of application of these coatings is quite wide: medicine, aviation, ship, instrumentation, automotive and other industries. One of the applications of electrolytic-plasma treatment is surface modification of medical implants and this process can make them more compatible with the human body, reducing the risk of rejection and improving their overall performance [6-8]. In this paper, technologies for producing coatings on titanium by plasma electrolytic oxidation are discussed. The methods are classified according to the properties of the coatings obtained, but it should be noted that this division is arbitrary, since coatings are often multifunctional. Titanium and its alloys are widely used in medicine, because of their good biocompatibility and high strength, but the improvement of biocompatibility requires the deposition of special coatings on the titanium material. For this purpose, calcium phosphate and hydroxyapatite coatings are applied to the surface using the PEO method. The chemical composition of hydroxyapatite $Ca_{10}(PO_4)_6(OH)_2$ is similar to that of bone tissue, so that bone tissue can form a strong chemical bond with the implant and not cause rejection. When titanium oxide nanoparticles are added to the solution, coatings with strong mechanical properties are obtained [9-11].

The aim of this work was to investigate the formation of calcium-phosphate coatings on titanium VT1-0 under anodic PEO in phosphoric acid electrolytes with the addition of TiO_2 nanoparticles, study the cross-sectional microstructure and microhardness of these coatings.

Experimental

Technically pure titanium material VT1-0, often used in medicine, was used as a substrate [12]. Samples of technical titanium VT1-0 for research were cut from rods in the state of delivery in the form of parallelepipeds. The samples were PEO-sanded to remove the oxide film and scratches.

Table 1 shows the chemical composition of technically pure titanium VT1-0.

Table 1

Chemical composition of commercially available pure titanium VT1-0 (wt.)

Fe	C	Si	N	Ti	O	H
0,25	0,07	0,1	0,04	99,7	0,2	0,01

For the production of calcium-phosphate coatings using the PEO method a pilot plant MAO was used, which consists of a power supply, an electrolytic bath with a cooling system and electrodes.

Pilot plant for PEO is designed and manufactured by scientific-production company "PlasmaScience" (Kazakhstan, Ust-Kamenogorsk) [13]. It is equipped with an AC power unit APS-77300. This equipment enables to apply calcium phosphate coating on medical implants, thus allowing to conduct researches. By controlling the parameters of the MAO, the unit enables several products (total area over 200 cm^2) to be coated simultaneously due to the high power in a single cycle.

APS-77300 power supply with output power: 3000 VA, voltage: up to 600 V, current: up to 25.2 A. Wide range of output voltage settings (amplitude, frequency, start and end phase). Frequency range: 999.9 Hz. Discontinuous adjustment of output parameters in 0.01 V / 0.01 Hz steps. Low harmonic coefficient (0.5 %).

Calcium-phosphate coating was performed in anodic-potentiostatic mode. PEO process parameters included the following limits: pulse duration — 100-500 μs, pulse frequency — 50-100 Hz, initial current density — 0.13-0.35 A/cm^2, process duration — 5-20 min, electric voltage — 50-100 V. A schematic of the MAO device is shown in Figure 1.

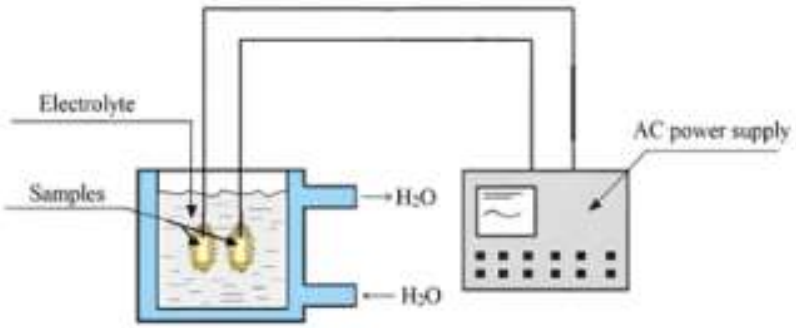

Figure 1. Schematic diagram of the MAO device

Various acid, salt and alkaline electrolytes can be used for the micro-arc treatment of titanium and titanium alloy parts. The most common electrolyte used for MAO titanium is a mixed phosphate-alkaline electrolyte of the KOH-Na_3PO_4 type. In this formulation, KOH is an activator affecting the enrichment capacity, which allows a hardening layer to be formed on the oxidized surface relative to the nominal amount of the part, this results in a significant increase in the adhesion strength of the coatings [9].

The parameters of MAO process in operation include the following limits: pulse duration — 100 μs, pulse frequency — 100 Hz, electric voltage — 100 V, initial current density — 0,15-0,35 A/cm^2, process duration — 10 min. During the calcium-phosphate coating with nanoparticles of titanium oxide the titanium samples attached to suspension were immersed into the electrolyte in the bath. The MAO was carried out in anodic mode at an AC voltage of 100 V for 10 minutes. As a result of the experiment local microplasma discharges appeared on the surface of samples and in their area the coating was synthesized. To obtain

calcium-phosphate coating on samples of technical titanium of VT1-0 grade, which underwent PEO process, three different amounts of titanium oxide were added into electrolyte composition.

The thickness and cross-sectional microstructure of calcium-phosphate coatings with the addition of titanium oxide nanoparticles obtained in the MAO process were studied using an ALTAMI-MET-5C optical microscope. To improve the image quality of the microscope, an advanced illumination system with a high-power lamp (12 V, 50 W) is used as the light source. Basic equipment of ALTAMI-MET-5C is equipped with digital USB-camera with 3 MPix resolution and Altami Studio software. To measure the transverse thickness of the calcium-phosphate coatings obtained in the process of MAO, cut to a scale of 1/10 with a preliminary application of glue, epoxy paint and hardener, and a procedure of cryopreservation. The cured specimens were cleaned and wiped with diamond paste, after seating with 100-2000 welding paper.

Cross-section microhardness of coatings on VT1-0 alloy was investigated with nanosensor "NanoScan-4D Compact". NanoScan-4D Compact uses a diamond pyramid of Berkovich type as an indenter. The Berkowitz-type indenter is a triangular pyramid with an angle of 65.3° between the pyramid's axis and the surface. The equivalent angle of the cone is 70.32°. The radius of curvature of the indenter tip is less than 100 nm. Ten measurements of the micro-hardness values of the coatings for each sample were made. The arithmetic mean values are used in this work.

The values of microhardness and modulus of elasticity of the material were automatically calculated using a special programme "NanoScan Viewer" in the form of a table. The results were obtained in the form of a graph showing the depth of penetration of the indenter into the sample as a function of the applied force.

Results and Discussion

To find out the effect of the electrolytes on the calcium-phosphate coating with titanium oxide nanoparticles, an electrolyte of three different compositions was prepared (Table 2). Calcium phosphate coating with titanium oxide nanoparticles was prepared using distilled water, orthophosphoric acid, hydroxyapatite and three different grams of titanium oxide.

Table 2

MDO process limits for each electrolyte

Electrolyte	No.1 0.5 g TiO_2 + 500 g dist.water + 10 g H_3PO_4 + 5 g HA: No. 1	No.2 0.75 g TiO_2 + 500 g dist.water + 10 g H_3PO_4 + 5 g HA: No. 2	No.3 1 g TiO_2 + 500 g dist.water + 10 g H_3PO_4 + 5 g HA: #3
Frequency (Hz)	100 Hz	100 Hz	100 Hz
Voltage (V)	100 V	100 V	100 V
Pulse (μs)	100 μs	100 μs	100 μs
Time (min)	10 min	10 min	10 min

The process of surface modification of titanium alloy VT1-0 by plasma electrolytic oxidation was investigated. PEO allows to obtain dense, uniform, not requiring additional surface grinding oxide coatings. The coating thickness values were 18.5-62.4 μm.

Figure 2 shows the cross-sectional thickness of calcium-phosphate-coated titanium VT1-0 when 0.5 g titanium oxide is added to the electrolyte.

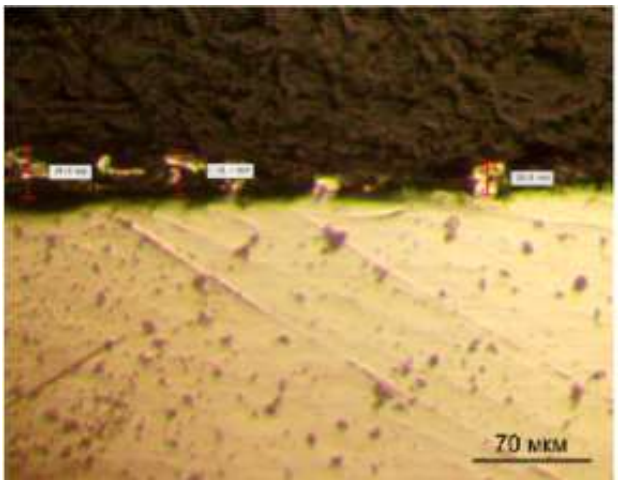

Figure 2.Cross-sectional thickness of calcium-phosphate-coated titanium VT1-0 when 0.5 g titanium oxide is added to the electrolyte composition

In most cases, the main quality parameter for a coating that meets technical and economic requirements is its thickness. In addition, the determination of coating thickness is the basis for quality assurance.

Studies of the cross-sectional structure of MAO coatings have shown that they have a three-layer structure regardless of the base material. The elements contained in the electrolyte must reside mainly in the porous outer layer of the MAO coatings (Fig. 1), which for different alloys is 20 % or more of the total coating thickness (Fig. 2). Thin barrier (transitional layer between the MAO coating and the substrate) layer located in close proximity to the base material must contain polycrystalline titanium oxide [14, 15]. In between is an intermediate layer (Fig. 2-4) consisting mainly of the TiO_2 phase. In this case the total thickness of MAO-coatings exceeds the thickness of the pro-oxidized titanium layer by about 20 %.

The cross-sectional thicknesses of VT1-0 titanium obtained by the MAO method when 0.5 g of titanium oxide nanoparticles were added to the electrolyte were 29.3 μm, 25.4 μm, 18.5 μm.

Figure 3 shows the cross-sectional thickness of calcium-phosphate-coated titanium VT1-0 when 0.75 g titanium oxide is added to the electrolyte.

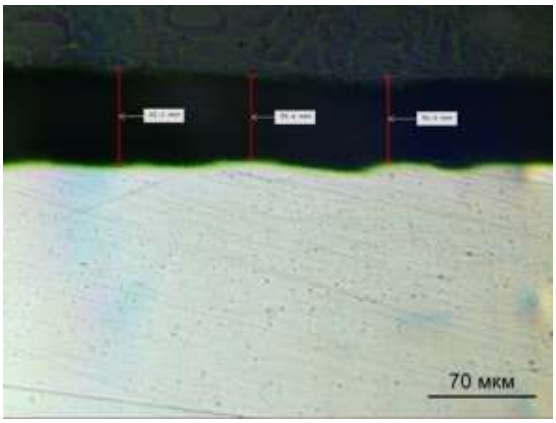

Figure 3. Cross-sectional thickness of calcium-phosphate-coated titanium VT1-0 when 0.75 g titanium oxide is added to the electrolyte composition

The cross-sectional thicknesses of VT1-0 titanium obtained by the MAO method with the addition of 0.75 g of titanium oxide nanoparticles to the electrolyte were 62.4 μm, 55.6 μm, 56.6 μm.

Thus, three different layers can be distinguished in the coating structure: an agglomerated layer (at the coating surface), an intermediate layer and a barrier layer (at the interface with the titanium substrate).

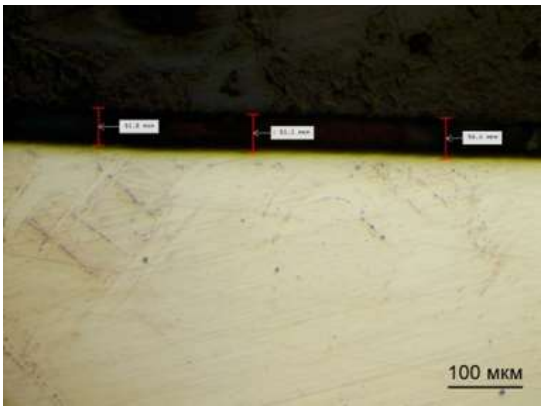

Figure 4.Cross-sectional thickness of calcium-phosphate-coated titanium VT1-0 when 1 g of titanium oxide is added to the electrolyte

The cross-sectional thicknesses of VT1-0 titanium obtained by MAO with calcium-phosphate coating when 1 g of titanium oxide nanoparticles were added to the electrolyte were 51.8 μm, 51.1 μm, 56.4 μm.

The process of oxide coating formation in plasma electrolytic oxidation or micro-arc oxidation is presented in several successive stages: Salt dissociation into ions; ion delivery to the electrode surface; electrochemical reaction and accompanying microplasma process; oxide or ceramic coating formation; subsequent chemical reaction, removal of gaseous reaction products [8]. As a result of local high-energy impact on the surface of the products layers are formed which include both elements of the matrix (oxidized metal) and elements of the electrolyte [9]. With a PEO treatment duration of 10 min, dense uniform oxide coatings are formed in all electrolyte solutions.

The highest micro-hardness of the coating was obtained in electrolyte No. 2 and is 2.84 GPa (Table 4), and the increase compared to the uncoated sample is 2.5 times.

The results of microhardness measurements of all calcium-phosphate coatings of VT1-0 titanium with titanium oxide nanoparticles, showed significant increases compared to the microhardness of pure uncoated titanium (1.7 GPa).

Figure 5 shows a graph of the depth of penetration of an indenter into the sample as a function of the applied force for calcium-phosphate-coated titanium VT1-0 obtained by adding 0.5 g of titanium oxide to the electrolyte.

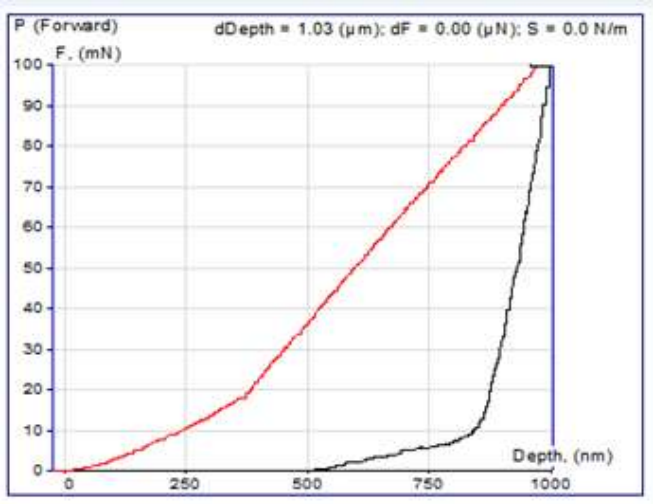

Figure 5. Dependence plot of indenter penetration depth on applied force in calcium-phosphate-coated titanium VT1-0 sample when 0.5 g titanium oxide is added to the electrolyte

Nano-hardness tester data for calcium-phosphate-coated titanium VT1-0 obtained by adding 0.5 g of oxide to the electrolyte is shown in Table 3.

Table 3

Values measured on a calcium phosphate nanohardness tester for calcium phosphate coatings obtained by adding 0.5 g titanium oxide to the electrolyte

	h_{max}, нм	h_c, нм	Force, mN	H, GPa	E, GPa	r,%	W_p	W_e
Average value	1382.77	1266.21	99.59	2.84	128.92	45.93	41.55	14.41
Standard deviation	311.10	263.10	0.29	1.18	114.11	33.23	8.06	8.02

Figure 6 shows a plot of the indenter penetration depth versus applied force in a calcium-phosphate-coated VT1-0 titanium sample when 0.75 g of titanium oxide is added to the electrolyte.

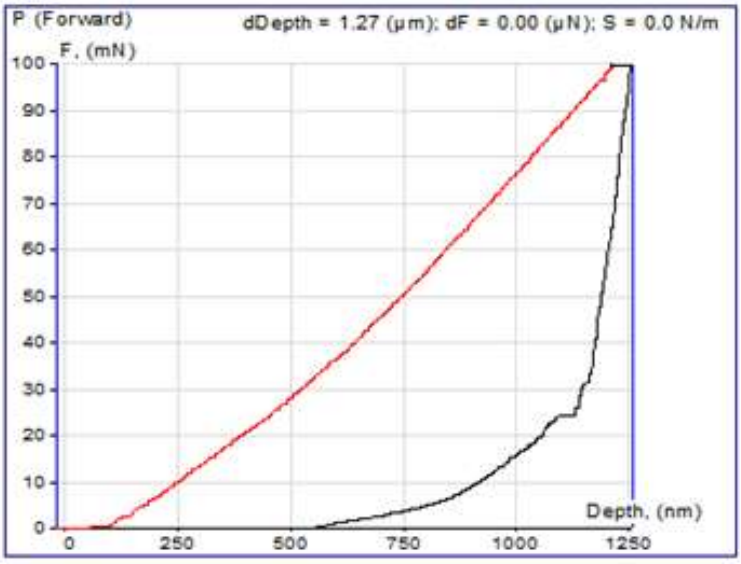

Figure 6. Dependence plot of indenter penetration depth on applied force in calcium-phosphate-coated titanium VT1-0 sample when 0.75 g titanium oxide is added to the electrolyte

The values obtained on the nanohardness tester for the electrolyte composition with the addition of 0.75 g of titanium oxide are shown in Table 4.

Table 4

Values measured on a calcium phosphate nanohardness tester for calcium phosphate coatings obtained by adding 0.75 g titanium oxide to the electrolyte

	h_{max}, nm	h_c, nm	Force, mN	H, GPa	E, GPa	r,%	W_p	W_e
Average value	1019.17	968.99	99.29	4.04	348.52	19.55	30.23	5.39
Standard deviation	58.94	61.38	0.92	0.41	82.05	15.26	3.48	0.96

Figure 7 shows a plot of the indenter penetration depth versus applied force in a calcium-phosphate-coated VT1-0 titanium sample when 1 g of titanium oxide is added to the electrolyte.

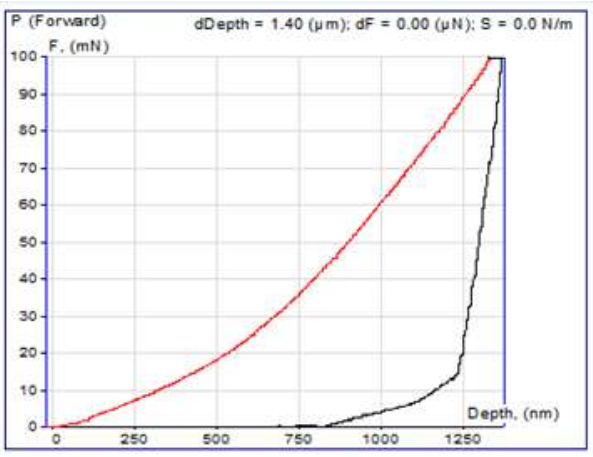

Figure 7.Dependence of indenter penetration depth on applied force in calcium-phosphate-coated titanium VT1-0 sample when 1 g titanium oxide is added to the electrolyte

The values obtained on the nanohardness tester for the composition of the electrolyte with the addition of 1g of titanium oxide are shown in Table 5.

Table 5

Values measured on a calcium phosphate nanohardness tester for calcium phosphate coatings obtained by adding 1 g of titanium oxide to the electrolyte

	h_{max}, nm	h_c, nm	Force, mN	H, GPa	E, Gpa	r,%	W_p	W_e
Average value	1147.75	1083.53	99.75	3.44	235.06	13.03	36.79	6.71
Standard deviation	114.66	115.25	0.17	0.57	25.96	1.46	3.89	1.18

Tables 3-5 show that the mechanical properties of the samples as well as the thickness of the MAO layer depend on the concentration of titanium oxide nanoparticles. When evaluating all the considered parameters of the obtained layer, the best performance was and obtained with the composition of electrolyte No. 2 (see Table 2). With a satisfactory thickness of the formed MAO layer (62.4 µm), the surface microhardness value (4.04 GPa) was found to be the highest among all compared processing modes, simultaneously with a high modulus of elasticity (348 GPa) and a low indentation depth (Fig. 5-7) in the coating (968.99 nm).

Conclusions

The process of plasma electrolytic oxidation of VT1-0 titanium with different composition of electrolyte was investigated. PEO allows to obtain dense, uniform, not requiring additional surface grinding oxide coatings. Three different layers can be distinguished in the coating structure: agglomerated (at the coating surface), intermediate and barrier (at the boundary with the titanium base). The coating thickness values were 18.5-62.4 µm. The obtained coatings are distinguished by high surface microhardness. The oxide coating microhardness of which is 4,04 GPa at covering thickness of 62,4 microns is received. These coatings were formed in an electrolyte containing calcium phosphate with the addition of titanium oxide nanoparticles. The increase compared to the uncoated sample is 2.5 times.

Acknowledgements

This research is funded by the Science Committee of the Ministry of Science and Higher Education of the Republic of Kazakhstan (Grant No. AP13068451).

This work was carried out under grant AR13068451 of the Ministry of National Economy of the Republic of Kazakhstan “Obtaining multifunctional calcium-phosphate coatings with titanium dioxide nanoparticles by plasma-electrolytic oxidation”.

References

1 Каблов Е.Н. Конструкционные и функциональные материалы — основа экономического и научно-технического развития России / Е.Н. Каблов // Вопросы материаловедения. — 2006. — № 1. — С. 64–67.

2 Суминов И.В. Плазменно-электролитическое модифицирование поверхности металлов и сплавов / И.В. Суминов, П.Н. Белкин, А.В. Эпельфельд. — М.: Техносфера, 2011. — 512 с.

3 Rakhadilov B. Method of electrolyte-plasma surface hardening of 65G and 20GL low-alloy steels samples / B. Rakhadilov, L. Zhurerova, A. Pavlov // Paper presented at the IOP Conference Series: Materials Science and Engineering. ― 2016. ― 142(1). DOI:10.1088/1757-899X/142/1/012028.

4 Козлов И.А. Влияние наполнения в растворе натриевого жидкого стекла на электрохимические свойства плазменного электролитического покрытия на сплаве ВМЛ20 / И.А. Козлов, В.А. Дуюнова // Авиационные материалы и технологии. — 2015. — № 4 (37). — С. 61–66. DOI: 10.18577/2071-9140-2015-0-4-61-66.

5 Гнеденков С.В. Строение и свойства покрытий, полученных методом плазменного электролитического оксидирования на авиационных магниевых сплавах / С.В. Гнеденков, М.В. Сидорова, С.Л. Синебрюхов, В.В. Антипов, В.М. Бузник, Е.Ф. Волкова, В.И. Сергиенко // Авиационные материалы и технологии. — 2013. — № 2. — С. 36–45.

6 S. Ferraris, S., Spriano, S. Antibacterial titanium surfaces for medical implants / S. Ferraris, S. Spriano // Mater. Sci. Eng. C Mater. Biol. Appl. — 2016. — 61. — 965–978.

7 Rakhadilov B.K. Phase composition and structure of composite Ti/HA coatings synthesized by detonation spraying / B.K. Rakhadilov, D.R. Baizhan, Z.B. Sagdoldina, D.B. Buitkenov, M. Maulet // Paper presented at the AIP Conference Proceedings. ― 2020. ― 2297. DOI:10.1063/5.0029754.

8 Wang Yi. Review of the biocompatibilityofmicro-arc oxidation coated titanium alloys / Yi. Wang, Yu. Huijun, Chen Chuanzhong, Zhao Zhihuan // Mater. Des. ― 2015. ― 85. ― 640–652.

9 Wang P. Effect of Al2O3 particle concentration on the characteristics of microarc oxidation coatings formed on pure titanium / P. Wang, J. Pu, J.H. Zhou, W.J. Cao, Y.T. Xiao, Z.Y. Gong, J. Hu, J. // Int. Electrochem. Sci., 2018. ―13. ― 8995–9006. https://doi.org/.

10 Lee K.M. Electrochemical response of ZrO2 in-corporated titanium oxide film / K.M. Lee, B.K. Jung, Y.G. Ko, D.H. Shin. // Mater. Res. Innov. 2014. — 18. — S2407-S2411. https://doi.org/10.1179/1432891714Z.000000000440 https://doi.org/.

11 Toorani M. Microstructural, protective, inhibitory and semiconducting properties of PEO coatings containing CeO2 nanoparticles formed on AZ31 Mg alloy / M. Toorani, M. Aliofkhazraei, A. Sabour Rouhaghdam // Surface and Coatings Technology, 2018. ― Volume 352. ― 25 October. ― P. 561-580.

12 Колобов Ю.Р. Технологии формирования структуры и свойств титановых сплавов для медицинских имплантов с биоактивными покрытиями / Ю.Р. Колобов // Российские нанотехнологии. — 2009. — Т. 4. — № 11, 12. — С. 19–31.

13 Рахадилов Б.К. Патент № 35998 на изобретение Республики Казахстан: 2021/0608.1 / Способ микродугового оксидирования / Б.К. Рахадилов, Ю.Н. Тюрин, Д.Р. Байжан. Опубл. 15.12.2022.

14 Preparation method and application of magnesium doped porous nano titanium oxide coating: pat. 101928974 CN; publ. 29.12.10.

15 Method of preparing magnesium-doped hydroxyapatite/ titania active film on surface of medical titanium alloy: pat. 102747403 CN; publ. 24.10.12.

Л.Б. Баятанова, А.Ж. Жасұланқызы, Н.М. Магазов, Б.К. Рахадилов,
Н. Мұқтанова, Г.К.Уазырханова

Титан жабындарының механикалық қасиеттеріне плазма-электролиттік тотығудың әсері

Плазма-электролиттік тотығу процесі (ПЭТ) тозуғатөзімді, коррозияғатөзімді, ыстыққатөзімді, электр оқшаулағыш және сәндік қасиеттерін қоса алғанда, бірегей қасиеттері бар көп функционалды жабындарды алуға мүмкіндік береді. Сондықтан бұл жабындардың қолданылу аясы айтарлықтай кең. Атап айтсақ: медицина, авиация, кеме жасау, аспап жасау, автомобиль жасау және басқа салалар. Технология металдардың бетінде оксид қабаттарының пайда болуына ықпал ететін микродоғалық разрядтарының құбылысына негізделген. Бұл жұмыста титанға плазмалық электролиттік тотығу арқылы жабындарды алу технологиялары қарастырылған. TiO_2 нанобөлшектерін электролитке қоса отырып, анодты өңдеу жағдайында ВТ1-0 маркалы титаннан жасалған субстратқа плазмалық-электролиттік тотықтыру (ПЭТ) бойынша эксперимент жүргізілді. Бетті қосымша тегістеуді қажет етпейтін тығыз, біркелкі оксидті жабындар алынды. Жабынның қалыңдығы 18,5–62,4 мкм болды. Осы өңдеу нәтижесінде алынған кальций-фосфат жабындарының микроқаттылығына ПЭТ-дың әсері зерттелді. Түзілген қабаттың орташа қалыңдығымен (62,4 мкм) барлық салыстырылған өңдеу режимдерінің ішінде бетінің микроқаттылығының ең үлкен мәні (4,04 ГПа) жоғары серпімділік модулімен (348 ГПа) және индентордың жабынға (968,99 нм) ену тереңдігінің аз мәнімен анықталды.

Бұл жабындар кальций фосфаты бар электролитке 0,75г титан оксиді нанобөлшектерін қосу арқылы түзілді. Жабынның микроқаттылығы жабынсыз үлгінің микроқаттылығымен салыстырғанда 2,5 есе жоғары болды. Жүргізілген зерттеулер нәтижесінде кальций-фосфат жабындарын алудың оңтайлы режимдері мен параметрлері анықталып, дәлелденді. Алынған жабындардың құрылымына, қалыңдығына және беткі қасиеттеріне микродоғалық өңдеу процесінің электролит құрамын өзгерту арқылы айтарлықтай әсер етуге болатындығы көрсетілген.

Кілт сөздер: плазма-электролиттік тотығу (ПЭТ), электролит, нанобөлшектер, жабын, құрылым, микроқаттылық, титан, титан оксиді.

Л.Б. Баятанова, А.Ж. Жасұланқызы, Н.М. Магазов, Б.К. Рахадилов, Н. Мұқтанова, Г.К. Уазырханова

Влияние плазменно-электролитического оксидирования на механические свойства титановых покрытий

Процесс плазменно-электролитического оксидирования (ПЭО) позволяет получать многофункциональные покрытия с уникальным комплексом свойств, в том числе износостойкие, коррозионностойкие, теплостойкие, электроизоляционные и декоративные. Поэтому область применения данных покрытий достаточно широка: медицина, авиа-, судо-, приборо-, автомобилестроение и другие отрасли промышленности. В основу технологии положено явление микродуговых разрядов, способствующих образованию оксидных слоев на поверхности металлов. В данной работе был проведен эксперимент по плазменно-электролитическому оксидированию подложки из титана марки ВТ1–0 в условиях анодной обработки с добавлением в электролит наночастиц TiO_2. Были получены плотные, равномерные, не требующие дополнительной шлифовки поверхности оксидные покрытия. Значения толщины покрытий составили 18,5–62,4 мкм. Исследовано влияние ПЭО на микротвердость кальций-фосфатных покрытий, образующихся в результате данной обработки. При удовлетворительной толщине сформированного слоя (62,4 мкм) было выявлено наибольшее среди всех сравниваемых режимов обработки значение микротвердости поверхности (4,04 ГПа) одновременно с высоким показателем модуля упругости (348 ГПа) и малым значением глубины проникновения индентора на покрытие (968,99 нм). Данные покрытия сформированы в электролите, содержащем кальций-фосфат, с добавлением 0,75 г наночастиц оксида титана. Увеличение микротвердости по сравнению с образцом без покрытия происходит в 2,5 раза. В результате проведенных исследований установлены и определены оптимальные режимы и параметры получения кальций-фосфатных покрытий. Показано, что, меняя состав электролита, возможно существенно воздействовать на структуру, толщину и поверхностные свойства получаемых покрытий.

Ключевые слова: плазменно-электролитическое оксидирование, электролит, наночастицы, покрытие, структура, микротвердость, титан, оксид титана.

References

1 Kablov, Ye.N. (2006). Konstruktsionnye i funktsionalnye materialy — osnovy ekonomicheskogo i nauchno-tekhnicheskogo razvitiia Rossii [Structural and functional materials — the basis of economic and scientific and technical development of Russia]. *Voprosy materialovedeniia — Matters of materials science, 1,* 64–67 [in Russian].

2 Suminov, I.V., Belkin, P.N. & Epelfeld, A.V. (2011). Plazmenno-elektroliticheskoe modifitsirovanie poverkhnosti metallov i splavov [Plasma electrolytic surface modification of metals and alloys]. Moscow: Tekhnosfera [in Russian].

3 Rakhadilov, B., Zhurerova, L. & Pavlov, A. (2016). Method of electrolyte-plasma surface hardening of 65G and 20GL low-alloy steels samples. *Paper presented at the IOP Conference Series: Materials Science and Engineering, 142*(1). DOI:10.1088/1757-899X/142/1/012028.

4 Kozlov, I.A. & Duyunova, V.A. (2015). Vliianie napolneniia v rastvore natrievogo zhidkogo stekle na elektrokhimicheskie svoistva plazmennogo elektroliticheskogo pokrytiia na splave VML20 [Influence of filling in a solution of sodium liquid glass on the electrochemical properties of a plasma electrolytic coating on the VML20 alloy]. *Aviatsionnye materialy i tekhnologii — Aviation materials and technologies, 4*(37), 61–66. DOI: 10.18577/2071-9140-2015-0-4-61-66 [in Russian].

5 Gnedenkov, S.V., Sidorova, M.V., Sinebryukhov, S.L., Antipov, V.V., Buznik, V.M., Volkova, Ye.F. & Sergiyenko V.I. (2013). Stroenie i svoistva pokrytii, poluchennykh metodom plazmennogo elektroliticheskogo oksidirovaniia na aviatsionnykh magnievykh splavakh [Structure and properties of coatings obtained by plasma electrolytic oxidation on aviation magnesium alloys]. *Aviatsionnye materialy i tekhnologii — Aviation materials and technologies, S2,* 36–45 [in Russian].

6 S. Ferraris & S. Spriano (2016). Antibacterial titanium surfaces for medical implants. *Mater. Sci. Eng. C Mater. Biol. Appl. 61,* 965–978.

7 Rakhadilov, B. K., Baizhan, D. R., Sagdoldina, Z. B., Buitkenov, D. B. & Maulet, M. (2020). Phase composition and structure of composite Ti/HA coatings synthesized by detonation spraying. *Paper presented at the AIP Conference Proceedings, 2297* DOI:10.1063/5.0029754.

8 Wang, Yi., Huijun, Yu., Chuanzhong, Chen & Zhihuan, Zhao. (2015). Review of the biocompatibilityofmicro-arc oxidation coated titanium alloys. *Mater. Des., 85*, 640–652.

9 Wang, P., Pu, J., Zhou, J.H., Cao, W.J., Xiao, Y.T., Gong, Z.Y. & Hu, J. (2018). Effect of Al2O3 particle concentration on the characteristics of microarc oxidation coatings formed on pure titanium, *Int. Electrochem. Sci. 13*, 8995–9006. https://doi.org/

10 Lee, K.M., Jung, B.K., Ko, Y.G. & Shin, D.H. (2014). Electrochemical response of ZrO2 in- corporated titanium oxide film. *Mater. Res. Innov., 18*, S2407-S2411, https://doi.org/10.1179/1432891714Z.000000000440 https://doi.org/.

11 Toorani, M., Aliofkhazraei, M. & Sabour Rouhaghdam, A. (2018). Microstructural, protective, inhibitory and semiconducting properties of PEO coatings containing CeO2 nanoparticles formed on AZ31 Mg alloy. *Surface and Coatings Technology, Vol. 352*, 561-580.

12 Kolobov, Yu.R. (2009). Tekhnologii formirovaniia struktury i svoistv titanovykh splavov dlia meditsinskikh implantatov s bioaktivnymi pokrytiiami [Technologies for forming the structure and properties of titanium alloys for medical implants with bioactive coatings]. *Rossiiskie nanotekhnologii — Russian nanotechnologies, Vol. 4,* 11–12, 19–31 [in Russian].

13 Rakhadilov, B.K., Tyurin, Yu.N. & Bayzhan, D.R. (2022). Patent № 35998 na izobretenie Respubliki Kazakhstan: 2021/0608.1. Sposob mikrodugovogo oksidirovaniia [Patent No. 35998 for the invention of the Republic of Kazakhstan: 2021/0608.1. Microarc oxidation method] [in Russian].

14 Preparation method and application of magnesium doped porous nano titanium oxide coating: pat. 101928974 CN; publ. 29.12.10.

15 Method of preparing magnesium-doped hydroxyapatite/ titania active film on surface of medical titanium alloy: pat. 102747403 CN; publ. 24.10.12.

DOI 10.31489/2023PH3/75-85

UDC 55.23.13

Z. Berkinova, B. Golman*

School of Engineering and Digital Sciences, Nazarbayev University, Kabanbay Batyr ave. 53, Astana, 010000, Kazakhstan
*(*E-mail: boris.golman@nu.edu.kz)*

Flow Behavior of Complex-Shaped Particle Mixtures in Rotary Drums: A DEM Study

Metal matrix composites hold great potential as functional materials for energy conservation applications. These composites are manufactured using powder metallurgy, which involves the incorporation of fine particles with diverse shapes. Understanding the flowability of particle mixtures with varying shapes is crucial for optimizing industrial processes. This study focuses on analyzing the flowability and flow behavior of mixtures composed of alumina and aluminum alloy particles using the discrete element method. The particle shapes are modeled to closely resemble actual particles, and their flow behavior in a rotating drum is simulated. The upper and lower dynamic angles of repose, outlines of particle bed surface, particle displacements, and particle velocity distributions were analyzed to understand the flow characteristics of complex-shaped particles. The results reveal the influence of particle shape on the flow behavior of powder mixtures, providing valuable insights for process optimization and design.

Keywords: Complex shaped particles, powder mixtures, metal matrix composites, rotary drum, discrete element method, flowability, dynamic angle of repose, flow behavior.

Introduction

Granular materials have a wide range of applications in various industrial processes, such as additive manufacturing, powder metallurgy, pharmaceuticals, agriculture, and food engineering. Advanced functional materials, such as metal matrix composites, are commonly manufactured using powder metallurgy techniques [1]. Ceramic-reinforced metal matrix composites, in particular, hold great promise for energy applications owing to their lightweight nature and high strength [2]. The raw powder comes in different shapes, from simple spherical particles to complex elongated, bulky, and flaky particles. The shape of particles significantly affects various aspects of powder behavior, including powder flow dynamics [3], mixing rate [4], flow patterns [5], and particle breakage [6].

Flowability is a crucial property of bulk materials that can greatly impact both the production process and the functionality of various products. Powder flowability depends on several factors, such as particle shape and size distribution, the composition of the powder mixture, and environmental conditions. Various experimental techniques exist for measuring powder flowability, and their choice depends on the specific application. One effective method involves using a drum filled with powder that continuously rotates at low speeds, such as 4 rpm [7], 0-65 rpm [8], 5-20 rpm [9], and 6, 9, and 12 rpm [10], to measure the dynamic angle of repose of the powder.

The Discrete Element Method (DEM) has recently gained extensive use in studying the flow behavior of granular materials. However, many researchers rely on simplified models of particle shapes, such as spherical or ellipsoidal particles [11]. Unfortunately, these models may not accurately represent the shape of actual particles. Simulating the motion of irregular-shaped particles is computationally expensive and requires significant computational resources. Despite these challenges, a few studies have focused on complex-shaped particles. For example, Norouzi et al. [10] conducted research on the flow behavior of oval, oblong, and biconvex-shaped particles using a rotary drum. Their investigation revealed that the transition from a rolling to a cascading flow regime depends not only on the size and filling level of the particles but also on their shape.

Despite the significance of understanding the flow behavior of particle mixtures in rotary drums, there remains a gap in research concerning the analysis of mixtures consisting of particles of varying shapes. Therefore, the present study aims to analyze the flowability and flow behavior of mixtures of two materials with varying particle shapes using DEM. The shape of particles is modeled to closely resemble the actual particles.We investigated the flowability of alumina and aluminum alloy particle mixtures. The upper and lower dynamic angles of repose were measured using a rotary drum. Furthermore, we analyzed the impact of

the composition of complex-shaped particle mixtures on the particle bed surface, particle displacements, and particle velocities.

Materials and Methods

Materials

The AlSi10Mg alloy powder was procured from Avimetal, China, while the aluminum oxide was obtained from Sigma-Aldrich, Switzerland. For this study, we utilized mixtures of alumina and alloy powders containing alumina weight percentages of 2 %, 6 % and 10 %.

Particle size distribution

The size distributions of alumina and aluminum alloy powders were measured using the laser diffraction particle analyzer, Mastersizer 3000 by Malvern Panalytical. The analyzer was used in combination with the Aero S dry disperser. The disperser was operated under a pressure of 0.5 bar and 1 bar for alumina and aluminum alloy, respectively. The volume-based size distributions of alumina and aluminum alloy powders are illustrated in Figure 1. The characteristic diameters and span of size distributions are listed in Table 1. The diameters d10, d50, and d90 represent the particle sizes at which 10 %, 50 %, and 90 % of the cumulative undersize distribution are achieved. The span value is calculated as follows:

$$Span = \frac{d_{90}-d_{10}}{d_{50}}. \quad (1)$$

The alumina powder has a significantly larger size than the aluminum alloy powder, although its size distribution is slightly narrower.

Table 1

Characteristic diameters and span of particle size distributions

Property	Al_2O_3	AlSi10Mg
d_{10}(μm)	64.4	27
d_{50}(μm)	99.1	44
d_{90}(μm)	149	70.1
Span	0.854	0.980

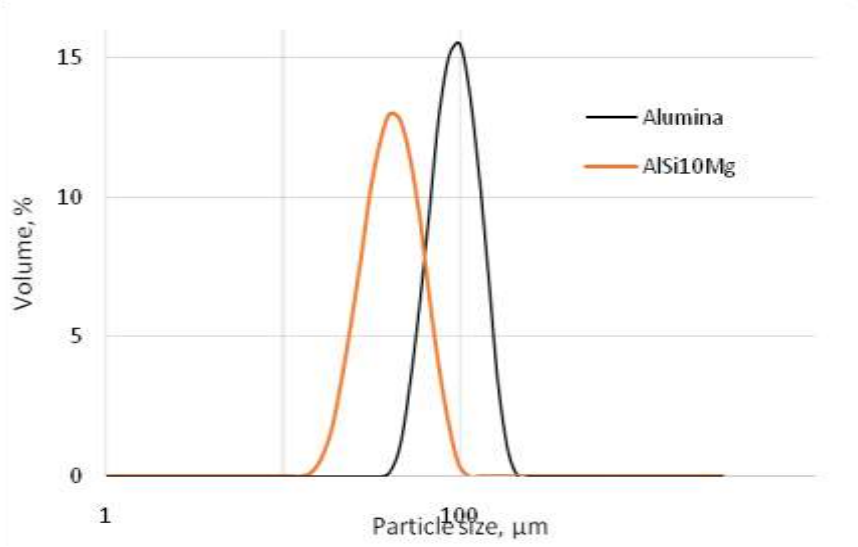

Figure 1. Size distribution of aluminum alloy and alumina particles

Particle morphology

The morphology of aluminum alloy and alumina particles was observed using a scanning electron microscope (SEM) provided by Zeiss Crossbeam 540, Switzerland. First, the samples were coated with carbon to protect the surface. Afterward, aluminum alloy particles were sputter coated with gold in a

Quorum Q150T ES to decrease charging during imaging. The SEM images of particles are illustrated in Figure 2.

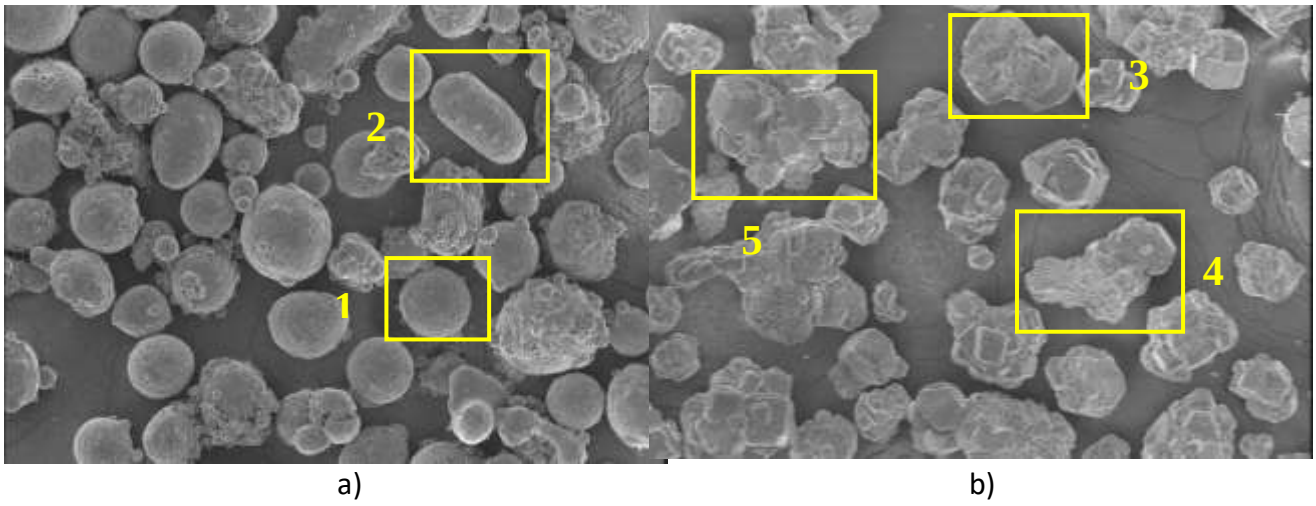

Figure 2. SEM images indicting outlined particle types of a) aluminum alloy and b) alumina particles

DEM contact model

The particle flow within the rotating drum was simulated numerically using DEM, initially proposed by Cundall and Strack [12]. DEM tracks the displacement and rotation of individual particles based on Newton's second law. Particle movement is described through translational and rotational motions as follows:

$$m_i \frac{dv_i}{dt} = \sum F_{c,i} + m_i\, g, \tag{2}$$

$$\frac{d(I_i \omega_i)}{dt} = R_i\left(\sum M_{c,i}\right). \tag{3}$$

Here, $m_i$denotes the mass of the particle, $F_{c,\,i}$ stands for the contact force v_i specifies the translational velocities, g is the acceleration of gravity, I_i is the moment of inertia, ω_i is the angular velocity vector, R_i is the torque acting on the body, and $M_{c,i}$ is the contact torque associated with rolling friction. The Hertz-Mindlin contact model, along with the elastic-plastic spring dashpot (EPSD2) rolling friction model, was employed to simulate particle-particle and particle-wall contacts. The elastic-plastic spring-dashpot (EPSD) rolling friction model has been formulated to consider additional torque contribution to the motion of particles. In this study, we used the EPSD2 model [13], which excludes the viscous damping torque component and considers only the mechanical spring torque, in contrast to the original EPSD model [14].

Particle model

A number of methods have been described in the literature for generating non-spherical particles for DEM simulation. Among these, the multi-sphere method [15, 16], which involves creating non-spherical particles by using clamps made of overlapping spheres with fixed local positions, and the superquadrics method [17-19], which generates particles of varying shapes by adjusting the parameters of superquadrics, are the most frequently employed. In the current study, the multi-sphere approach was utilized to generate particles of complex shapes. To enhance the accuracy of the obtained results, particle shapes for numerical simulation were generated based on SEM images and size distribution analysis of aluminum alloy and alumina particles.The aim was to simulate the shapes and sizes of particles as closely as possible to the actual particles. Two types of particle shapes were used for the aluminum alloy (Fig. 2a): spherical particles with a radius of 0.5 mm and elongated particles represented by five overlapping spheres, each with a constant radius of 0.4 mm (Fig. 3). Furthermore, to account for the bulky shapes and sharp edges of alumina particles, three types of complex-shaped particles were selected from the SEM image, as depicted in Figure 2b. Then, multi-sphere particles with shapes resembling the selected actual particles were generated using six, eight, and fifteen overlapping spheres, as illustrated in Figure 4.

(a) (b)

Figure 3. 3D model of generated aluminum alloy particles: a) sphere, b) elongated particle made of five overlapping spheres.

a) b) c)

Figure 4. 3D model of generated alumina particles consisiting: a) six overalapping spheres, b) eight overalapping spheres, c) fifteen overalapping spheres.

Particle insertion

The Aspherix software (DCS-Computing, Austria) was used to simulate the five cases. The first case involved aluminum alloy particles, the second case included alumina particles, and the other three cases represented mixtures of alumina and aluminum alloy particles, with 2 %, 6 %, and 10 % weight percentages of alumina powder.

The SEM images show that the aluminum alloy powder is composed mostly of spherical and elongated particles. For the DEM simulation runs 200,000 AlSi10Mg particles were randomly inserted into the simulation domain under normal gravity. Of all the particles, 60 % were spherical, while the remaining 40 % were elongated. In the case of pure alumina, 10,000 particles were inserted, with 50 % of them being multi-spherical particles consisting of eight overlapping spheres. The remaining two types of particles, with six and fifteen spheres, were evenly divided by 25 %.

To estimate the filling level of the drum, the volume of each particle in Table 2 was initially simulated by an analytical method using the Avro code developed by Busa et al. [20]. The results of these simulations are summarized in Table 2. Subsequently, the filling level of the drum was computed for each simulation case by utilizing the particle volume, the known number of particles of each type, and the volume of the drum used in the DEM simulations, as presented in Table 3. The filling level affects the flow behavior of particles in the drum and particle bed surface [8].

Table 2

Parameters of multi-sphere model for particle generation

Particle type	Number of overlapping spheres	Volume (mm^3)	Mass (g)
AlSi10M particles			
1	1	0.523	0.00116
2	5	0.66	0.00147
Alumina particles			
3	6	7.49	0.0280
4	8	13.12	0.0498
5	15	32.94	0.125

Table 3

Drum filling level of five simulation cases

Composite	Filling level (%)
Al_2O_3	38.8
AlSi10Mg	29.5
2 % Al_2O_3	28.3
6 % Al_2O_3	27.9
10 % Al_2O_3	27.4

Table 4 lists the material properties of the aluminum alloy and alumina particles, as well as the rotary drum. Stainless steel was chosen as the wall material for the drum to prevent electrostatic effects on the particles. The properties used in DEM simulations were selected to closely reflect real material properties, with one exception. Young's modulus (G) for the aluminum alloy was decreased from 7×10^7Pa to 7×10^6 Pa to reduce computational time. This adjustment does not affect the results obtained, as noted by Chen [9].

Table 4

Material properties for particles and wall

Material property	$AlSi_{10}Mg$	Alumina	Rotary drum
Density, ρ (kg/m^3)	2230	3800	7500
Young's modulus, G (Pa)	7×10^6	3.2×10^7	1.8×10^7
Poisson's ration, v	0.3	0.23	0.3
Coefficient of restitution, e	0.75	0.4	0.7
Coefficient of friction, μ	0.3	0.6	0.3
Coefficient of rolling friction, μ_r	0.001	0.005	0.005

The rotary drum has a diameter of 200 mm and a thickness of 25 mm. To conduct the DEM simulations, particles were initially randomly distributed inside the drum and allowed to settle for 1 second to attain a stable position. Subsequently, the drum was rotated about *y*-axis at a constant speed of 20 rpm for 3 seconds. Finally, the dynamic angle of repose, which is the angle formed between the surface of a particle bed and the horizontal plane, was measured using the open-source software ImageJ.

To measure the upper and lower angles of repose in this study, the method proposed by Marigo and Stitt [21] and previously used by Jadidi et al. [22] was employed. The upper angle (α) was determined by drawing a line from the leftmost side to the center of the powder bed in the rotary drum, while the lower angle (β) was measured from the drum's center to the rightmost side. Figure 5 (a) shows a schematic representation of the drum in a stable position, while Figure 5 (b) depicts the drum during rotation about *y*-axis.

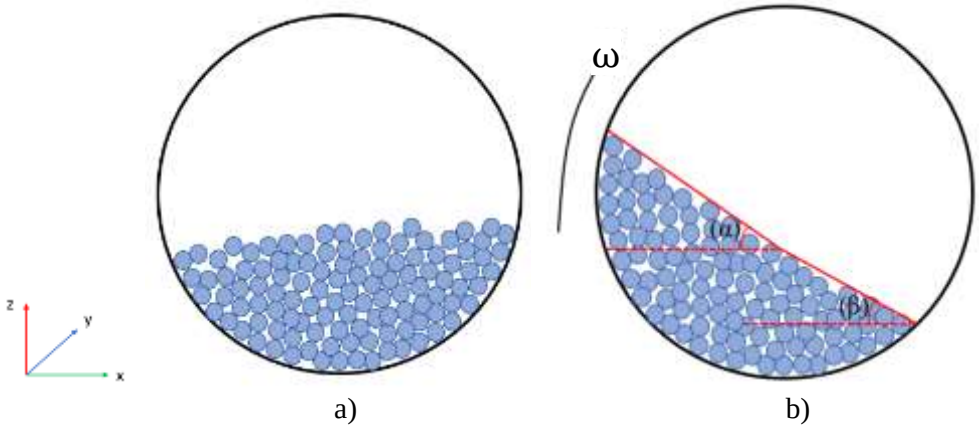

Figure 5. Schematic representation of a) drum in stable position b) drum during rotation about y-axis

Results and Discussion

Although the concept of a rotary drum is simple, the particle flow inside the drum is highly complex. Several studies [23, 24] have identified four distinct particle flow regimes: slipping, rolling, cascading, and cataracting. These regimes depend on various factors such as drum size, rotational speed, filling level, particle size distribution, and particle shape. To differentiate between these flow regimes in the rotary drum, the Froude number (*Fr*) is often used. The Froude number, given by $Fr = \omega^2 \cdot R/g$, characterizes the balance between gravitational and centrifugal forces. Here, ω represents the angular velocity in radians per second, and R denotes the radius of the rotating drum in meters. In our case, the *Fr* value is equal to 1.1×10^{-3}. The Froude number, along with the high filling level exceeding 10 % (as indicated in Table 3), suggests that the particle flow in the drumis in the cascading regime. This type of motion generates an S-curve particle bed surface, which is further supported by the DEM simulation results illustrated in Figure 6.

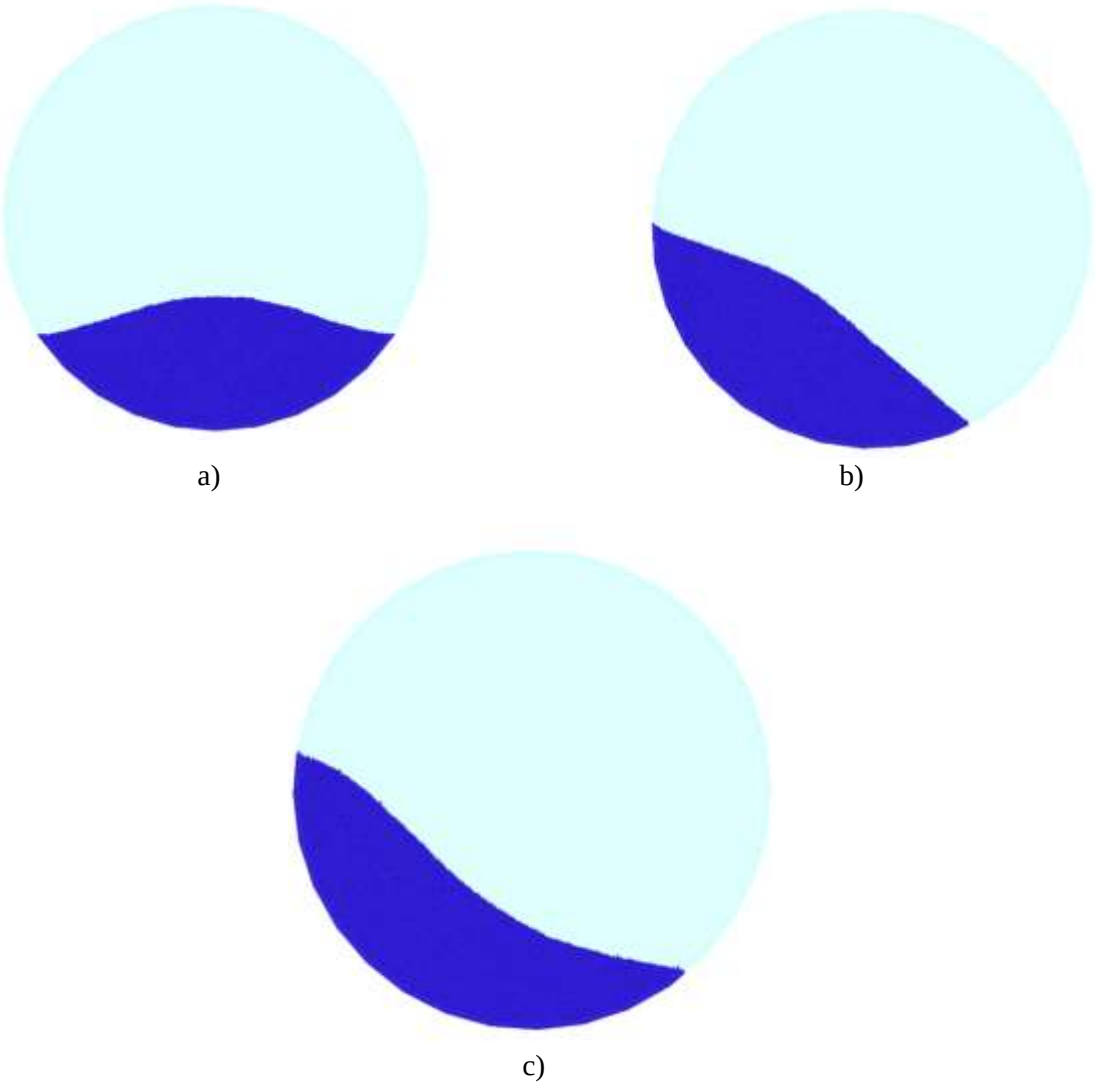

a) b)

c)

Figure 6. Progressive visualization of cascading particle motion dynamics in rotating drum: a) particle insertion b) intermediate phase c) established cascading regime

Figure 7 illustrates the outlines of the particle bed surfaces formed in the rotating drum at various times. The bed surface outline was reconstructed from the DEM output files by detecting the maximum height of the particle bed in each bin along the *x*-axis direction. The higher and steeper surface outlines are detected for powder beds containing alumina particles (case 1). This can be attributed to the hardness and abrasiveness of alumina particles, which can increase inter-particle friction [25] and affect the behavior of the particle bed surface in the rotary drum. Moreover, the irregular shapes of alumina particles increase their

tendency to form clusters and aggregates within the powder bed, resulting in an uneven surface with steeper upper and lower angles of repose. This can be observed in the S-curve profile of the bed surface. On the other hand, aluminum alloy particles (case 2) have smoother surfaces, which can reduce the tendency for clustering and aggregation, resulting in a more uniform bed surface with less steep angles. This smoother bed surface may be observed as a more gradual change in slope and a more linear profile in comparison to the S-curve profile observed for alumina particles. The outlines of the bed surface for the mixtures of aluminum alloy and alumina particles (cases 3, 4, and 5) follow the trend of the aluminum alloy, displaying smooth bed surfaces. This can be attributed to the small amount of alumina added to the alloy, which is less than 10 %, as well as to the different filling levels of the drum.

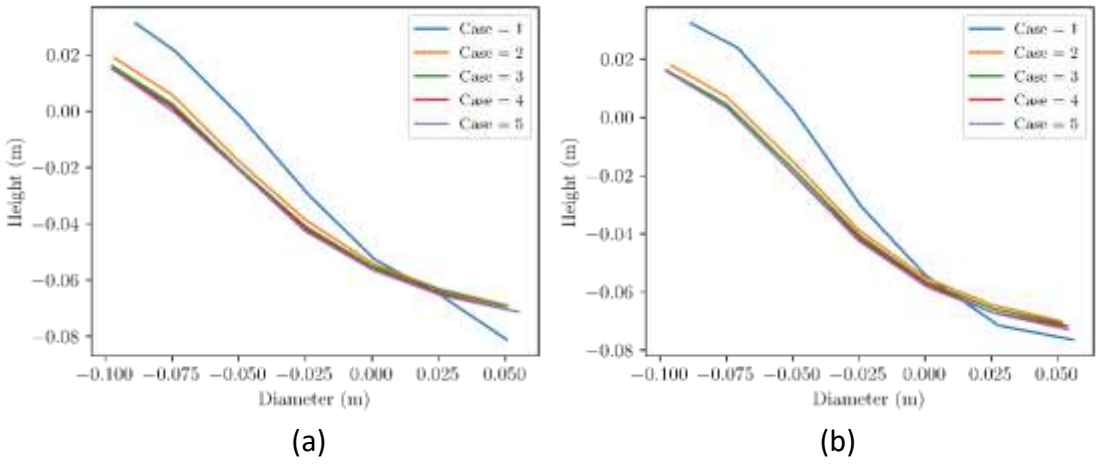

Figure 7. Particle bed surface profiles of AlSi10Mg, alumina, and their mixtures in drums after rotation for a) 1s and b) 3s

Table 5 summarizes the upper and lower dynamic angles of repose for aluminum alloy, alumina, and their mixtures, which were measured using ImageJ image analysis software on snapshots of DEM simulation results. The upper angles of repose exhibited a tendency to increase with simulation time in all cases. However, the lower angles of alumina particles decreased over time. The rotation of the drum's wall lifts the particles upward, but due to the high flow resistance, the particles encounter difficulties in freely flowing down. Consequently, the particles tend to accumulate and form a steeper pile in the upper region of the drum, while the lower region displays a flatter distribution of particles. Regarding the mixture of 10 % alumina particles in AlSi10Mg (case 5), we observed an initial increase in the lower angle of repose, which can be attributed to the addition of alumina particles. However, as time progressed, the lower angle of repose decreased, reaching a value lower than it was at 1 second. On the other hand, the upper and lower angles of repose for the other two powder mixtures (cases 3 and 4) increased with time, following the trend observed for the aluminum alloy particles. However, it should be noted that the angles of repose of the powder mixtures in both the upper and lower regions were smaller than those of the aluminum alloy particles. Despite the presence of alumina particles in the mixtures, the particle bed surfaces appeared flatter. This phenomenon can be attributed to the filling level of particles in the drum. A slight decrease in the filling level (refer to Table 3) could impact the flow of mixtures, resulting in increased angles of repose in the upper regions.

Table 5

Upper (α) and lower (β) dynamic angles of repose of aluminum alloy, alumina and their mixtures

Time, s	AlSi10Mg		Alumina		2 %		6 %		10 %	
	Dynamic angle of repose:									
	α	β	α	β	α	β	α	β	α	β
1	40.07	13.53	45.34	33.3	37.11	14.49	37.8	15.35	33.59	17.61
2	41.53	14.4	47.04	30.18	39.2	17.07	38.9	16.25	35.5	17.96
3	41.73	14.46	48.68	29.37	40.08	17.79	39.85	16.92	35.65	16.83

Additionally, the movement of particles during drum rotation was analyzed for each case. The maps of particle displacement magnitudes are shown in Figure 8 for cases 1 and 2. The magnitude of particle displacement is calculated using the Euclidian formula as follows:

$$d = \sqrt{(x_2 - x_1)^2 + (y_2 - y_1)^2 + (z_2 - z_1)^2}, \qquad (5)$$

where (x_1, y_1, z_1) and (x_2, y_2, z_2) denotes the particle positions at time t and $t + \Delta t$, respectively. The analysis of the displacement of alumina and aluminum alloy particles in the rotary drum suggests that there is a variation in mobility among particles located in different regions. Specifically, the results indicate that alumina particles in the drum's upper side exhibit greater mobility than those in the lower side. Moreover, the displacement of aluminum alloy particles is greater for particles positioned on the lower side of the drum compared to the alumina particles located in the same positions.

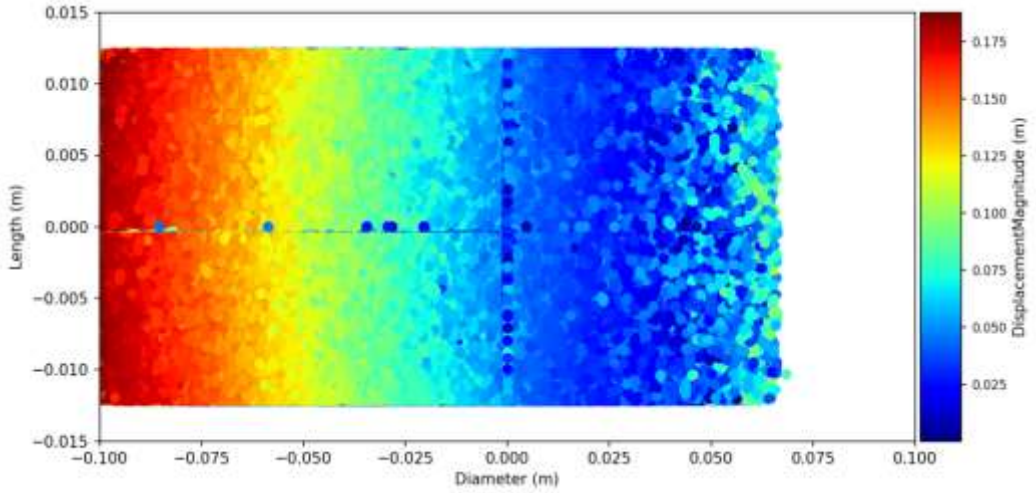

a)

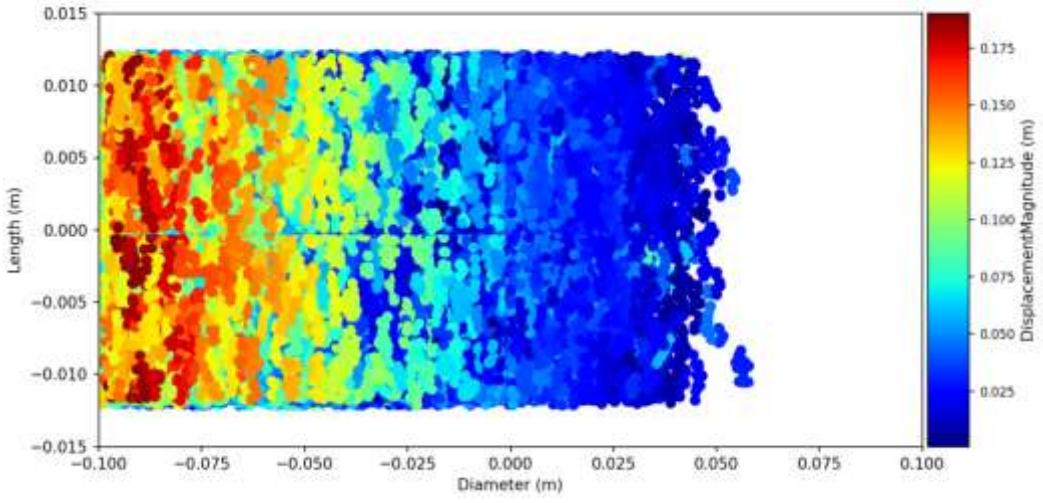

b)

Figure 8. Maps of particle displacement magnitudes along the diameter and length of rotary drum for a) aluminum alloy and b) alumina particles

The particle velocity is an important parameter for predicting the flow behavior of particles. Figure 9 shows the maps of particle velocity magnitudes for aluminum alloy and alumina powders. Based on these magnitudes, the particle bed in the rotary drum can be divided into two layers: active and passive. The boundary between these layers is indicated by dark blue color, representing particles with velocities close to zero. Particles within the active layer flow downward due to gravitational force, while particles in the passive layer possess a tangent velocity equal to the velocity of the drum wall. This is a result of the no-slip condition at the drum wall. As particles move from the drum wall towards the center of the drum, their

velocities gradually increase and then subsequently decrease until they eventually match the velocity of the drum wall in the lower region. The velocity maps of mixtures containing alumina and aluminum alloy particles emphasize the dominant influence of the aluminum alloy particles. The mixtures tend to display velocity patterns that closely resemble those observed for pure aluminum alloy particles.

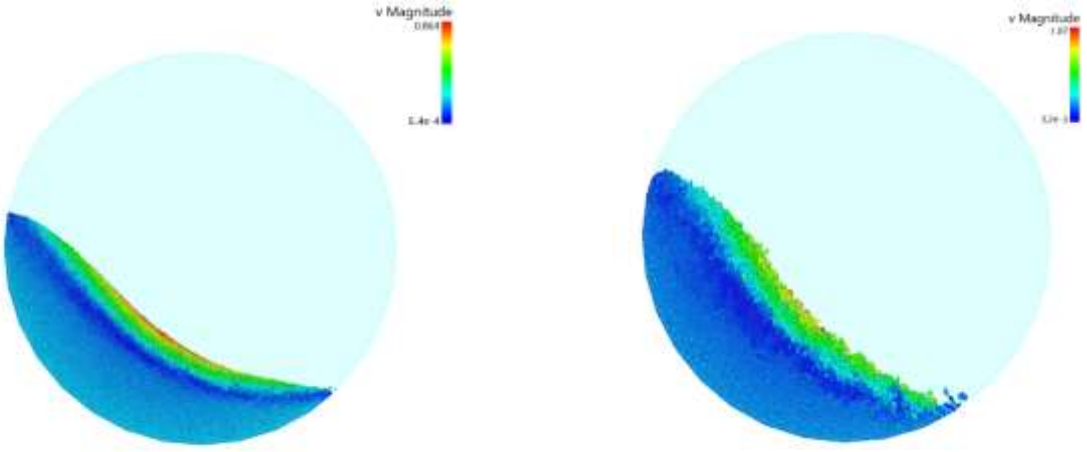

a) b)

Figure 9. Maps of velocity magnitudes of a) aluminum alloyand b) alumina particles in rotary drum

Conclusion

In this study, the flow behavior of mixtures of particles with different shapes in a rotating drum was analyzed employing DEM. The simulations were conducted for mixtures containing 2 %, 6 %, and 10 % alumina particles in aluminum alloy particles, as well as for pure alumina and pure aluminum alloy particles. To accurately represent the particle shapes, they were digitally replicated based on SEM images of actual particles, utilizing the multi-sphere method. Using the DEM simulation results, the upper and lower dynamic angles of repose of the particles were measured using ImageJ software. Additionally, the outlines of the particle bed surface, particle displacement, and particle velocity were examined to gain insights into the particle flow phenomena.

The study's findings indicated that as the simulation time increased, the upper angles of repose consistently showed a tendency to increase for all cases. However, the lower angles of repose behaved differently for the alumina particles and the mixture containing 10 % alumina in aluminum alloy particles, exhibiting an opposite trend compared to the lower angles of repose observed in the other three cases.

The s-shaped outline of the powder bed was observed for alumina particles. In the case of mixtures containing aluminum alloy and alumina particles, the bed surfaces closely resembled the pattern of the aluminum alloy, appearing smooth. This similarity can possibly be explained by variations in the particle distribution within the drum due to the different filling levels. The displacement analysis of alumina and aluminum alloy particles in a rotary drum shows that particles in different regions have varying mobility. Alumina particles on the upper side of the drum are more mobile than those on the lower side. Additionally, aluminum alloy particles on the lower side of the drum experience greater displacement compared to alumina particles in the same positions. Particle velocity maps revealed the presence of two distinct layers. In the active layer, particles were observed flowing downward under the influence of gravitational force. Conversely, in the passive layer, particles displayed a tangent velocity that matched the velocity of the drum wall, owing to the no-slip condition at the drum wall.

Acknowledgments

This research was funded by the Science Committee of the Ministry of Education and Science of the Republic of Kazakhstan, grant number AP09260422.

References

1 Sadhu, K.K., Mandal, N. & Sahoo, R.R. (2023). SiC/graphene reinforced aluminum metal matrix composites prepared by powder metallurgy: A review. *Journal of Manufacturing Processes, 91*, 10-43. doi:10.1016/j.jmapro.2023.02.026.

2 Malaki, M., Tehrani A.F. & Niroumand, B. (2020). Fatgiue behavior of metal matrix nanocomposites. *Ceramics International, 46*(15), 2020, 23326-23336. doi:10.1016/j.ceramint.2020.06.246.

3 Aramideh, S., Xiong, Q., Kong, S.-C. & Brown, R.C. (2015). Numerical simulation of biomass fast pyrolysis in an auger reactor. *Fuel,156*, 234-242. doi:10.1016/j.fuel.2015.04.038.

4 Sinnott, M.D. & Cleary, P.W. (2016). The effect of particle shape on mixing in a high shear mixer. *Computational Particle Mechanics, 3*, 477–504. doi:10.1007/s40571-015-0065-4.

5 Höhner, D., Wirtz, S. & Scherer, V. (2015). A study on the influence of particle shape on the mechanical interactions of granular media in a hopper using the Discrete Element Method. *Powder Technology, 278*, 286-305. doi:10.1016/j.powtec.2015.02.046.

6 Hua, X., Curtis, J., Hancock, B., Ketterhagen, W. & Wassgren, C. (2013). The kinematics of non-cohesive, sphero-cylindrical particles in a low-speed, vertical axis mixer. *Chemical Engineering Science, 101*, 144-164.doi:10.1016/j.ces.2013.05.063.

7 Chung, Y., Yeh, C. & Liao, C. (2022). Experimental investigation into the wet non-spherical granular segregation and mixing in rotating drums. *Powder Technology, 409*, 117844. doi:10.1016/j.powtec.2022.117844.

8 He, S.Y., Gan, J.Q., Pinson, D., Yu, A.B. & Zhou, Z.Y. (2019). Radial segregation of binary-sized ellipsoids in a rotating drum.*Powder Technology, 357*, 322-330. DOI: 10.1016/j.powtec.2019.08.075.

9 Chen, H., Xiao, Y.G., Liu, Y.L. & Shi, Y.S. (2017). Effect of Young's modulus on DEM results regarding transverse mixing of particles within a rotating drum. *Powder Technology, 318*, 507-517.doi: 10.1016/j.powtec.2017.05.047.

10 Norouzi, H.R., Zarghami, R. & Mostoufi, N. (2015). Insights into the granular flow in rotating drums. *Chemical Engineering Research and Design, 102*, 12-25.doi: 10.1016/j.cherd.2015.06.010.

11 He, S.Y., Gan, J.Q., Pinson, D., Yu, A.B. & Zhou, Z.Y. (2021). Particle shape-induced axial segregation of binary mixtures of spheres and ellipsoids in a rotating drum. *Chemical Engineering Science, 235*, 116491. DOI: 10.1016/j.ces.2021.116491.

12 Cundall, P.A. & Strack, O.D.L. (1979). A discrete numerical model for granular assemblies. *Géotechnique, 29*(1), 1751-7656. DOI: 10.1680/geot.1979.29.1.47

13 Iwashita, K. & Oda, M. (2000). Micro-deformation mechanism of shear banding process based on modified distinct element method. *Powder Technology, 109*(1–3), 192-205. doi:10.1016/S0032-5910(99)00236-3

14 Ai, J., Chen, J.-F., Rotter, J.M. & Ooi, J.Y. (2011). Assessment of rolling resistance models in discrete element simulations. *Powder Technology, 206*(3), 269-282. doi:10.1016/j.powtec.2010.09.030.

15 Han, Y., Zhao, D., Jia, F., Qui, H., Li, A. & Bai, S. (2020). Experimental and numerical investigation on the shape approximation of rice particle by multi-sphere particle models. *Advanced Powder Technology, 31*(4), 1574-1586. doi:10.1016/j.apt.2020.01.025.

16 Berkinova, Z., Yermukhambetova, A. & Golman, B. (2021). Simulation of flow properties of differently shaped particles using the discrete element method.*Computer Applications in Engineering Education, 29*(5), 1061-1070. doi:10.1002/cae.22359.

17 Wang, S., Zhou, Z. & Ji, S. (2021). Radial segregation of a gaussian-dispersed mixture of superquadric particles in a horizontal rotating drum. *Powder Technology, 394*, 813-824. doi:10.1016/j.powtec.2021.09.012.

18 Boribayeva, A., Iniyatova, G., Uringaliyeva, A. & Golman, B. (2021). Porous Structure of Cylindrical Particle Compacts. *Micromachines, 12*(12), 1498. doi:10.3390/mi12121498.

19 Iniyatova, G., Yermukhambetova, A., Boribayeva, A. & Golman, B. (2023). Approximate Packing of Binary Mixtures of Cylindrical Particles. *Micromachines, 14*(1), 36. DOI: 10.3390/mi14010036.

20 Buša, J., Džurina, J., Hayryan, E., Hayryan, S., Hu, C.-K., Plavka, J., Pokorný, I., Skřivánek, J. & Wu, M.-C. (2005). ARVO: A Fortran package for computing the solvent accessible surface area and the excluded volume of overlapping spheres via analytic equations. C*omputer Physics Communications, 165*(1), 59-96. doi:10.1016/j.cpc.2004.08.002.

21 Marigo, M. & Stitt, E.H. (2015). Discrete element method (DEM) for industrial applications: comments on calibration and validation for the modelling of cylindrical pellets. *KONA Powder and Particle Journal, 32*, 236–252.doi:10.14356/kona.2015016.

22 Jadidi, B., Ebrahimi, M., Ein-Mozaffari, F. & Lohi, A. (2022). Mixing performance analysis of non-cohesive particles in a double paddle blender using DEM and experiments. *Powder Technology, 397*, 117122. doi:10.1016/j.powtec.2022.117122.

23 Mellmann, J. (2001).The transverse motion of solids in rotating cylinders—forms of motion and transition behavior. *Powder Technology. 118*(3), 251-270. doi:10.1016/S0032-5910(00)00402-2.

24 Henein, H., Brimacombe, J.P. & Watkinson, A.P. (1983). Modelling Transverse Motion of Solids in Rotary Kilns. *Metallurgical TransactionB, 14B*(2), 207-220.

25 Zhu, L., Lu, H., Guo, X. & Liu, H. (2022). Structural relaxation and avalanche dynamics of particle piles under vertical vibration. *Particuology, 68*, 65-74. doi:10.1016/j.partic.2021.11.002.https://doi.org/10.1016/j.partic.2021.11.002

Ж. Беркинова, Б. Гольман

Айналмалы барабандардағы күрделі пішінді бөлшектер қоспаларының ағыс сипаттамасы Дискреттік элементтер әдісі бойынша зерттеу

Металл матрицалық композиттер энергияны үнемдеу саласында қолдануға арналған функционалды материалдар ретінде үлкен әлеуетке ие. Бұл композиттер ұнтақты металлургия әдістерімен, яғни әртүрлі формалары бар ұсақ бөлшектерді қолдана отырып жасалады. Әртүрлі пішіндегі бөлшектер қоспаларының ағындылығын түсіну өнеркәсіптік процестерді оңтайландыру үшін өте маңызды. Мақалада дискретті элементтер әдісін қолдана отырып, алюминий оксиді мен алюминий қорытпасының бөлшектерінен тұратын қоспалар ағысының өтімділігі мен сипаттамалары қарастырылған. Бөлшектердің пішіндері барынша шынайы бөлшек пішіндеріне ұқсастырып алынады және олардың айналмалы барабандағы ағысының әрекеті симуляцияланады. Күрделі пішінді бөлшектердің ағысын сипаттау үшін бөлшек қабатының жоғарғы және төменгі көлбеу динамикалық бұрыштары, бөлшектер қабат бетінің контурлары, бөлшектердің орын ауыстыруы және жылдамдықтарының таралымы талданған. Бөлшектердің пішіндері ұнтақ қоспаларының ағысының әрекетіне әсер ететінін растайтын талдау нәтижелері процестерді оңтайландыру және жобалау үшін пайдалы ақпарат береді.

Кілт сөздер: күрделі пішінді бөлшектер, ұнтақ қоспалары, металл матрицалық композиттер, айналмалы барабан, дискретті элементтер әдісі, аққыштық, динамикалық көлбеу бұрышы, ағыс сипаттамасы.

Ж. Беркинова, Б. Гольман

Характеристики течения смесей частиц сложной формы во вращающихся барабанах Исследование методом дискретных элементов

Металлические матричные композиты обладают большим потенциалом в качестве функциональных материалов для применения в области энергосбережения. Эти композиты производятся методами порошковой металлургии, с использованием мелких частиц с различными формами. Понимание текучести смесей частиц с различными формами является важным для оптимизации промышленных процессов. В статье изучены текучесть и характеристики течения потока смесей, состоящих из частиц оксида алюминия и алюминиевого сплава, с применением метода дискретных элементов. Формы частиц моделируются таким образом, чтобы максимально приблизить их к реальным частицам, и их поведение при движении потока частиц во вращающемся барабане симулируется. Верхний и нижний углы откоса, контуры поверхности слоя частиц, перемещения частиц и распределения скорости частиц проанализированы для понимания характеристик потока частиц сложной формы. Результаты анализа, подтверждающие, что формы частиц влияют на поведение потока смесей порошков, дают полезную информацию для оптимизации и проектирования процессов.

Ключевые слова: частицы сложной формы, смеси порошков, металлические матричные композиты, вращающийся барабан, метод дискретных элементов, текучесть, динамический угол откоса, характеристика течения.

DOI 10.31489/2023PH3/86-90

UDC 535.215; 535.3

C. Bozada

Department of Engineering Physics, Gaziantep University, Turkey
(E-mail: b.ankara@yandex.com)

Effects of Sm doping on EuB_6

A solid-state reaction was used to investigate the nanocrystalline particles of Sm-doped EuB_6 and their optical, thermionic emission and mechanical properties were investigated. The tapered nanoawls had a length of 3–12 μm and a diameter ranging from 40 to 200 nm at the roots and 20–100 nm at the tip as shown by in scanning electron microscopy (SEM). As the temperature of the material increases, the thermionic emission current density also increases. J_o as the zero-field current densities for $Eu_{0.6}Sm_{0.4}B_6$ at 1500 K, 1673 K, 1773 K, 1873 K were 0.72 A cm^{-2}, 4.25 A cm^{-2}, 10.06 A cm^{-2} and 20.05 A cm^{-2}. By increasing the Sm doping content, electrical density of $Eu_{1-x}Sm_xB_6$ decreases. In all materials, the electrical resistivities increased linearly with temperature from 200 to 1200 °C, indicating metallic conductivity. $Eu_{0.6}Sm_{0.4}B_6$ has a lower Vickers hardness and higher flexural strength than EuB_6.

Keywords: nanocrystalline, mechanical properties, dielectric function, thermionic emission, electrical resistivity.

Introduction

Europium hexaboride (EuB_6) is the rare-earth metal hexaboride (REB_6). Among ferromagnetic semiconductors, EuB_6 shows extraordinary magnetoresistance and is commonly believed to include magnetic polarons [1]. The characteristics of EuB_6 include chemical stability, excellent thermal conductivity, high hardness, high melting point, high wear resistance and a low thermal expansion coefficient. Both boron (B) and europium (Eu) atoms exhibit high neutron absorption cross sections, EuB_6 acts as an excellent neutron absorber and is used as a control rod in fast breeder reactor [2].

Samarium hexaboride (SmB_6) is both Kondo insulator(KIs) and heavy fermion semiconductor as well as an exotic material by means of powerful electronic relationships where occupied 4f electrons lead to novel ground states [3]. It is an intermediate-valence compound, that which is a narrow-gap semiconductor [4]. SmB_6 is a very hard and stable rare-earth hexaboride(REB_6). When the temperature is low, SmB_6 becomes ferromagnetic [5]. SmB_6 applications include field emitters, photodetectors, cathodes and energy storage [6].

Bao et al. [7] studied the structure and optical adsorption of the powder of Eu-doped SmB_6 via a solid-state reaction. They reported that the reaction temperature improved the grain size and powder distribution of the synthesized samples. By increasing Eu doping, the transmissivity as a function of the wavelength of SmB_6 increases rectilinear from visible light to near-infrared (NIR). Menth et al. [8] reported that Eu does not significantly change the electrical properties of SmB_6 at low temperatures. SmB_6 exhibits a non-magnetic semiconductor behavior at low temperatures. Yeo et al. [9] investigated the magnetic susceptibilities, resistivities, and Hall effects of Eu-doped SmB_6 ($Sm_{1-x}Eu_xB_6$). EuB_6 is a polaronic ferromagnet and SmB_6 is a Kondo insulator. A narrow f band and broad conduction band hybridize less strongly with Eu doping, and magnetically active ions participate in the AF superexchange interaction as well. Yamaguchi et al. [10] suggested that Eu doping increases the Sm valence and reduces the hybridization of the valence band with Sm 4f. The According to a study Yeo et al. [11], the substitution of Sm for EuB_6 significantly changes its magnetic and transport properties, leading to a transition from ferromagnet to EuB_6 to produce antiferromagnetic and metal-insulator transitions (MITs). The doping of magnetic carriers alters both the itinerant carrier density and magnetic interactions simultaneously.

In this study, nanocrystalline Sm-doped EuB_6 were fabricated via by a solid-state reaction and its optical properties of Sm-doped EuB_6 were investigated. We also investigated their optical properties using first-principle calculations.

Experimental and computational methods

The synthesized nanocrystalline powders were prepared from Eu_2O_3(99.97 %), $SmCl_3 \cdot 6H_2O$ (99.96 %), and $NaBH_4$ (99.98 %). Initially, 600 °C, 800 °C, 1000 °C, and 1200 °C were chosen as the reaction

temperatures for SmB_6 to produce a uniformly distributed nanocrystalline powder. In order to synthesize nanocrystalline Eu-doped SmB_6, the reaction temperature was optimized at 1200 °C. $Sm_{1-x}Eu_xB_6$ powder was examined for phase identification, grain morphology, and microstructure employing field emission scanning electron microscopy(HITACHI SU-8010, FESEM), transmission electron microscopy(TEM, FEI-Tecnai F20 200 kV) and X-ray diffraction (PW1830 with Cu-Kα1 radiation, Philips, XRD).

Sm-doped EuB_6 was analyzed using first-principles calculations based on density-functional theory (DFT) implemented in the VASP computational code [12]. In our calculation, projector augmented wave pseudopotentials with generalized gradient approximation (GGA) and 500 eV kinetic cutoff energy were employed. The surface calculation was sampled using 16×16×1 k-point grids of the Brillouin zone (BZ).

Results and discussion

A graph of the XRD models of $Eu_{1-x}Sm_xB_6$ nanocrystalline powders employed at 1200 °C with x=0, 0.2, 0.4, 0.6, and 0.8 is shown in Figure 1. It appears that the Sm atoms randomly substitute for the Eu atoms in (100), (110), (111), (210), (211), (220), (221), (310), and (222), as indicated by the well-indexed and assigned diffraction peaks. Neither Sm nor Eu peaks were observed in the patterns, indicating that no impurity phase was present in the samples. As can be seen from the patterns, these samples exhibit well-defined peaks, indicating that they were highly crystallized. As shown in Figure 1, all samples consisted of a single phase with a space group of Pm-3m.

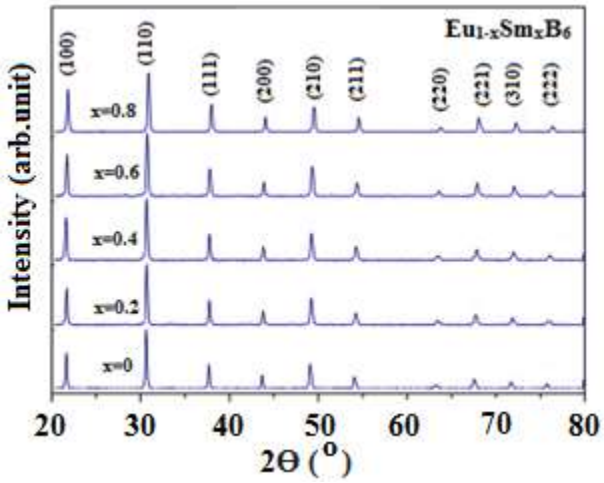

Figure 1. XRD pattern of $Eu_{1-x}Sm_xB_6$ nanopowder prepeared at 1200 °C.

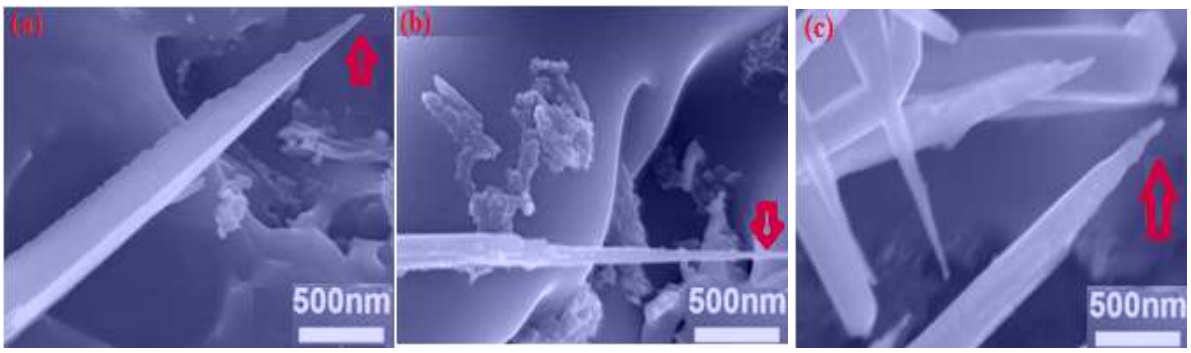

Figure 2. SEM images of the $Eu_{1-x}Sm_xB_6$ nanopowder aquired at 1200 °C

The SEM images of the $Eu_{1-x}Sm_xB_6$ nanopowder were taken at 1200 °C and is depicted in Figure 2. The enlarged images of the $Eu_{1-x}Sm_xB_6$ (x=0.2, 0.4, and 0.6) nanopowders which marked by red arrows with diameters range from approximately 20–100 nm at tip and 40–200 nm at root are presented in Figure 2a-c. In field-induced electron emission, $Eu_{1-x}Sm_xB_6$ are very important and beneficial.

The Vickers hardness, flexural strength, and relative density of $Eu_{0.6}Sm_{0.4}B_6$ were examined at different sintering temperatures. Figure 3 depicts a similar trend, where Vickers hardness, flexural strength, and

relative density gradually increase with temperature until they reach a maximum at 1300 °C. It is considered overfiring when the temperature reaches 1350 C, as evidenced by decrease in the density. Vickers hardness and flexural strength increased with increasing bulk density. The Vickers hardness and flexural strength values have been measured at 1300 °C to be 22.4 GPa, 241 MPa and respectively. EuB_6 has a Vickers hardness and flexural strength of 26.1GPa and 183MPa, respectively [2]. Hence the Vickers hardness of $Eu_{0.6}Sm_{0.4}B_6$ is smaller than EuB_6 and flexural strength of $Eu_{0.6}Sm_{0.4}B_6$ are higher than EuB_6.

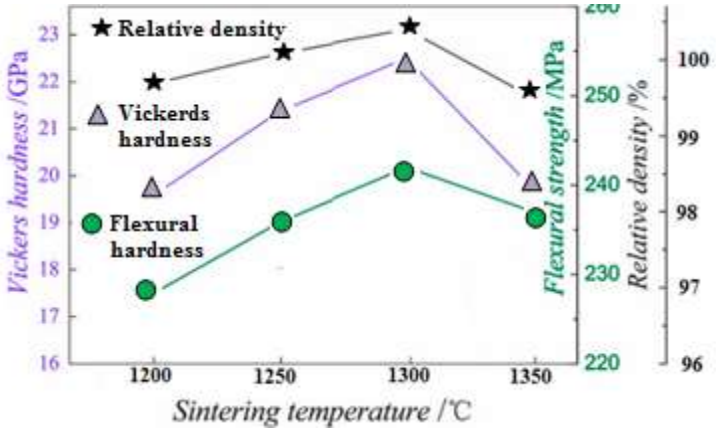

Figure 3. Flexural strength, Vickers hardness, and relative density of $Eu_{0.6}Sm_{0.4}B_6$ at different sintering temperatures.

Figure 4 shows typical Schottky plots (logJ–$U^{1/2}$ curves) for $Eu_{0.6}Sm_{0.4}B_6$. Temperature-limited values are extrapolated back to zero-field theory in the evaluation of the work function. The Richardson–Dushman formula can be written as follows: $Lg(J/T^2) = LgA - 5040\ \phi/T$. A(120 A cm^{-2} K^{-2}) is Richardson's constant, ϕ (eV) is the emitter work function, T (K) is the temperature and J(A cm^{-2}) is the emission current density. The zero field current densities(J_o) of $Eu_{0.6}Sm_{0.4}B_6$ are obtained at 1500K, 1673 K, 1773 K, 1873 K were 0.72 A cm^{-2}, 4.25 A cm^{-2}, 10.06 A cm^{-2} and 20.05 A cm^{-2}, respectively. Thermal emission current density increases as material temperature increases.

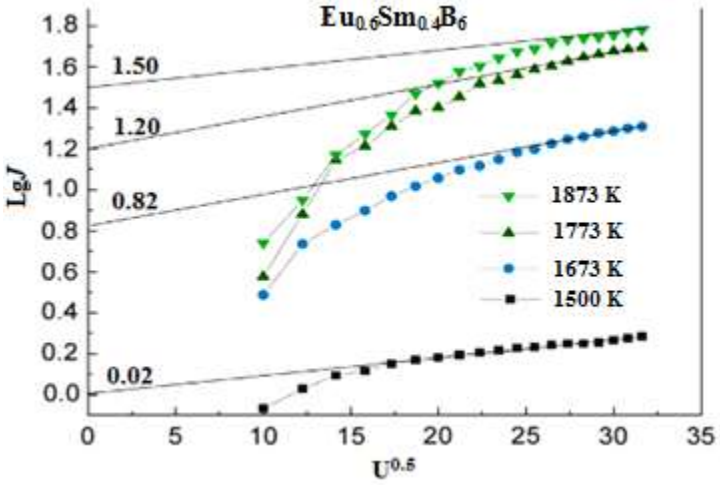

Figure 4. Typical Schottky plots for $Eu_{0.6}Sm_{0.4}B_6$

The UV-VIS absorption spectra of EuB_6 and $Eu_{0.4}Sm_{0.6}B_6$ are shown in Figure 5. The pure EuB_6 and $Eu_{0.4}Sm_{0.6}B_6$ peaks have an absorption shoulder centered at 220 nm. When the absorption peak positions were compared, they were considerably shifted towards the red region. Pure EuB_6 exhibited stronger light absorption at 150 nm than Sm doped with EuB_6.

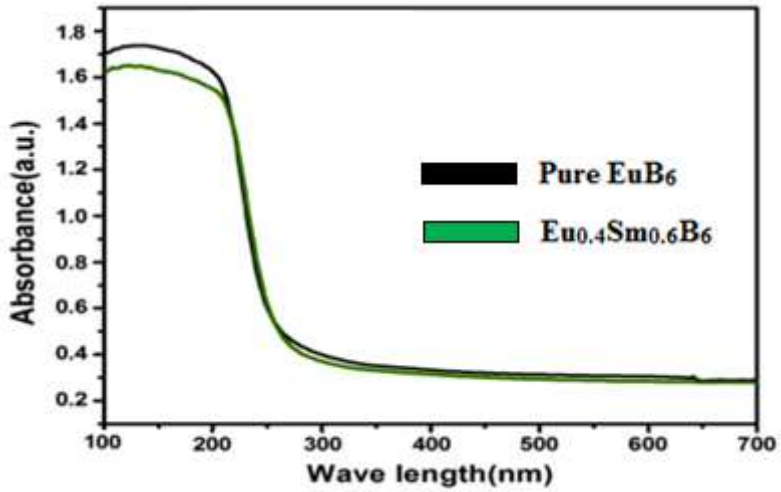

Figure 5. Absorption spectra of pure EuB_6 and $Eu_{0.4}Sm_{0.6}B_6$

The electrical resistivity is shown in Figure 6 as a function of the temperature for different doping contents. Metallic conducting behavior is observed in all samples, as their electrical resistivities increased linearly with temperature from 200 to 1200 °C. Using a 60 % Sm doping content, the electrical resistivity became 4350 Ω cm at 200 °C and 9000 Ω cm at 1200 °C. Additionally, a decrease in the electrical resistivity is also observed when the Sm doping content increases to 80 and 100 at.%, indicating that electrical resistivity is decreased by Sm doping.

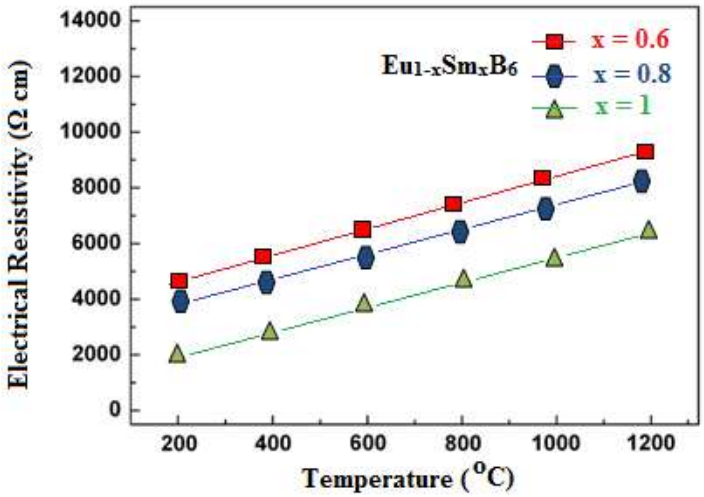

Figure 6. Electric resistivity for $Eu_{1-x}Sm_xB_6$ as a function of temperature.

Conclusions

The Optical, thermoelectric and mechanical properties of Sm-doped EuB_6 nanocrystalline particles were investigated using solid-state reactions. Tapered nanoawls shown by scanning electron microscopy (SEM) have a length of 3–12 μm and a diameter ranging from 40 to 200 nm at the roots and 20–100 nm at the tip. The thermionic emission current density increases with increasing material temperature. Eu0.6Sm0.4B6 had zero field current densities(J_o) of 0.72 A cm^{-2}, 4.25 A cm^{-2}, 10.06 A cm^{-2} and 20.05 A cm^{-2} at 1500 K, 1673 K, 1773 K, and 1873 K, respectively. The electrical density of $Eu_{1-x}Sm_xB_6$ decreases with increasing Sm doping content. In the temperature range of 200 — 1200 °C, the electrical resistivity of all materials increased linearly, indicating that they were metallically conductive. In contrast to EuB_6, $Eu_{0.6}Sm_{0.4}B_6$ has a smaller Vickers hardness and higher flexural strength.

Data Availability

The raw/processed data required to reproduce these findings cannot be shared at this time due to technical or time limitations.

References

1 Sivananda, D. J. & et al. (2018). Stepwise disintegration of magnetic domains in a EuB 6 single crystal observed by magneto-optical imaging.

2 Sonber, J. K., Murthy, T. S. R. C., Subramanian C., Hubli R. C. & Suri A. K.(2013). Synthesis, densification and characterization of EuB6. *Int. J. Refract. Met. Hard Mater., 38*, 67–72.

3 Jiang, J. et al. (2013). Observation of possible topological in-gap surface states in the Kondo insulator SmB6 by photoemission. *Nat. Commun., 4*(1), 1–8.

4 Sluchanko, N. E. et al. (2000). Intragap states in SmB 6. *Phys. Rev. B., 61*(15), 9906.

5 Xiao, L., Su, Y., Peng, P. & Tang, D. (2017). First-principles study of electronic, mechanical and optical properties of mixed valence SmB 6. *IOP Conf. Ser. Mater. Sci. Eng., 207*(1). doi: 10.1088/1757-899X/207/1/012084.

6 Wang, Z. & Han, W. (2021). Recent Developments on Rare-Earth Hexaboride Nanowires, Sustainability, *13*(24), 13970.

7 Bao, L., Ning, J. & Liu, Z. (2021). Mechanism for transmittance light tunable property of nanocrystalline Eu-doped SmB6: Experimental and first-principles study. *J. Rare Earths, 39*(9), 1100–1107.

8 Geballe, T. H., Menth, A., Buehler, E. & Hull, G. W. (1970). Properties of SmB6 doped with Eu and Gd. J. *Appl. Phys., 41*(3), 904–905.

9 Yeo, S., Song, K., Hur, N., Fisk, Z. & Schlottmann, P. (2012). Effects of Eu doping on SmB 6 single crystals. *Phys. Rev. B., 85*(11), 115125.

10 Yamaguchi, J. et al. (2010). Strongly correlated electronic states of Yb1− xLuxB12 and Smi1− yEuyB6 studied by highly bulk-sensitive photoelectron spectroscopy. *Journal of Physics: Conference Series, 200*(1), 12230.

11 Yeo, S.J. Bunder, E., Lin, H.-H., Jung, M.-H. & Lee, S.-I. Concurrent magnetic and metal-insulator transitions in Eu 1− x Sm x B 6 single crystals. *Appl. Phys. Lett., 94*(4), 42509.

12 Hobbs, D., Kresse, G. & Hafner, J. Fully unconstrained noncollinear magnetism within the projector augmented-wave method. *Phys. Rev., B. 62*(17), 11556.

Ч. Бозада

Легирленген Sm-нің EuB_6-ға әсері

Қатты фазалық реакция көмегімен легирленген Sm-нің EuB_6 нанокристалды бөлшектері зерттеліп, олардың оптикалық, термиялық және механикалық қасиеттері зерттелді. Сканерлеуші электронды микроскопияның көмегімен көрсетілгендей, конустық наноқабықшаларының ұзындығы 3-12 мкм және диаметрі тамырларда 40-тан 200 нм-ге дейін және ұшында 20-100 нм-ге дейін болды. Материалдың температурасы көтерілген сайын термоэлектрлі эмиссиялық токтың тығыздығы да артады. 1500 К, 1673 К, 1773 К, 1873 К кезінде $Eu_{0.6}Sm_{0.4}B_6$ үшін Jo нөлдік өріс ток тығыздығы 0,72 А см-2, 4,25 А см-2, 10,06 А см-2 және 20,05 А см-2 құрады. Sm легирленуінің мөлшері артқан сайын Eu1-xSmxB6 электр тығыздығы төмендейді. Барлық материалдарда меншікті электр кедергісі 200-ден 1200 °C-қа дейінгі температурада сызықтық түрде өсті, бұл металл өткізгіштігін көрсетеді. $Eu_{0.6}Sm_{0.4}B_6$ EuB_6. қарағанда Виккерс бойынша қаттылығы төмен және иілу беріктігі жоғары.

Кілт сөздері: нанокристалдар, механикалық қасиеттер, диэлектрлік функция, термоэлектрондық эмиссия, меншікті электр кедергісі.

Ч. Бозада

Влияние легирования Sm на EuB_6

С помощью твердофазной реакции исследованы нанокристаллические частицы EuB_6, легированные Sm, и исследованы их оптические, термоэмиссионные и механические свойства. Как показано, с помощью сканирующей электронной микроскопии конические наностержни имели длину 3–12 мкм и диаметр в диапазоне от 40 до 200 нм у корней и 20–100 нм на кончике. С повышением температуры материала плотность тока термоэлектронной эмиссии также увеличивается. Jo, поскольку плотности тока в нулевом поле для $Eu_{0.6}Sm_{0.4}B_6$ при 1500 К, 1673 К, 1773 К, 1873 К, составляли 0,72 А см-2, 4,25 А см-2, 10,06 А см-2 и 20,05 А см-2. При увеличении содержания легирования Sm электрическая плотность $Eu_{1-x}Sm_xB_6$ снижается. Во всех материалах удельное электрическое сопротивление линейно возрастало с температурой от 200 до 1200°C, что указывает на металлическую проводимость. $Eu_{0.6}Sm_{0.4}B_6$ имеет более низкую твердость по Виккерсу и более высокую прочность на изгиб, чем EuB_6.

Ключевые слова: нанокристаллы, механические свойства, диэлектрическая функция, термоэлектронная эмиссия, удельное электрическое сопротивление.

DOI 10.31489/2023PH3/91-97

UDC 535.34, 535.372, 54.05

G. Amanzholova[1*], E. Seliverstova[1], N. Ibrayev[1], E.I. Terukov[2]

[1]*Institute of Molecular Nanophotonics, Karaganda University of the name of academician E.A. Buketov, Kazakhstan;*
[2]*Ioffe Institute, R&D Center of Thin Film Technologies in Energetics, St. Petersburg, Russian Federation*
([*]E-mail: gulnur_as@inbox.ru)

Structural and optical properties of carbon nanodots based on citric acid doped with nitrogen atoms

A study of the luminescent properties of carbon nanodots obtained by microwave and hydrothermal methods of synthesis from citric acid and urea was performed. The resulting nanoparticles were characterized using transmission electron microscopy, dynamic light scattering, and Fourier transform infrared spectroscopy. The sizes of the obtained carbon nanodots after dialysis was varied from 2 to 8 nm. FTIR spectra confirm the presence of oxygen-containing –OH, –CN and –NH groups in the resulting solutions. For all studied carbon nanodots, the maximum fluorescence intensity is observed upon excitation at a wavelength of 350 nm. The fluorescence spectrum does not change its position on the wavelength scale for the samples under study due to changes in the molar ratio of precursors and the method of synthesis. The highest fluorescence quantum yield was obtained for carbon nanodots with a ratio of citric acid and urea 1:4 obtained by the microwave synthesis method. The fluorescence lifetime of carbon nanodots doped with nitrogen atoms is ~7.4 ns. It is shown that a change in the ratio of precursors does not significantly affect the size and morphology of carbon nanodots.

Keywords: carbon nanodots; microwave synthesis; hydrothermal synthesis; optical properties; citric acid; urea.

Introduction

Carbon nanodots appeared not so long ago and they are showing great interest as a new class of carbon nanomaterials. Carbon nanodots (CNDs) can become as promising alternative to semiconductor quantum dots and dyes due to their good biocompatibility, low cytoxicity, high photostability, variety of surface functional groups, ease of preparation and unique photophysical properties [1-3].

The most interesting from the point of view of fluorescent properties are carbon nanodots obtained by pyrolysis of citric acid [4-6]. These materials have a number of advantages, such as biocompatibility, simple synthesis, and excitation-dependent luminescence spectra, but they have a relatively low quantum yield of <10 % [4, 5]. For the solution of this problem, many researchers used various amine-based agents for surface passivation and doping of CNDs with various functional groups [7-10]. Doping of citric acid-based organic dots with nitrogen greatly improves their luminescent properties. A large number of studies were devoted to the synthesis of carbon nanodots based on citric acid using urea as a nitrogen source [7, 8, 11-13].

In the present work, the effect of the precursor composition and synthesis conditions on the structural and optical properties of carbon nanodots was studied. Microwave and hydrothermal synthesis methods were used to obtain CNDs. These methods of CNDs obtaining are simple, safe and cheap. In addition, when synthesizing CNDs by the microwave method, it is possible to control the main parameters of the reaction (pressure, temperature, time, power).

Experimental

CNDs were obtained using hydrothermal and microwave synthesis. Citric acid was used as a carbon source, and urea was used for doping with nitrogen atoms. The starting materials were taken in molar ratios of 1:1, 1:4, 1:5, and 1:6. Figure 1 shows the structural formulas of the starting materials.

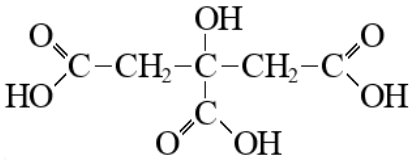

Citric acid

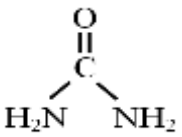

Urea

Figure 1. Structural formulas of starting substances

Microwave synthesis. The necessary amount of citric acid and urea was dissolved during ultrasound treatment in 5 mL of deionized water in a borosilicate glass tube. The synthesis was carried out in a Monowave 200 microwave reactor (Anton Paar) at a temperature of 160 °C for 1 hour with continuous mixing. Then the solution was cooled to 70 °C in a microwave reactor and further, to room temperature in natural conditions. The resulting product was centrifuged at a speed of 10000 rpm for 30 minutes, and then dialyzed. The carbon dots obtained by the microwave method at different ratios of citric acid and urea are further designated as CNDs(m) 1:1 and CNDs (m) 1:4.

Hydrothermal synthesis. The necessary amount of citric acid and urea was dissolved in 5 mL of deionized water during ultrasound treatment. The resulting transparent colorless solution was placed in an autoclave with a teflon vessel and heated in an oven at 160 °C for 6 hours. After this time, the autoclave was cooled in an open oven. As a result of the synthesis, a greenish-brown solution was obtained. To separate large particles, the solution was centrifuged at 10000 rpm for 30 minutes, and then purified by dialysis. The carbon points obtained by the microwave method at different ratios of citric acid and urea are further designated as CNDs(g) 1:1 and CNDs(g) 1:4.

Results and Discussion

The structure and dimensions of the obtained CNDs were studied using a transmission electron microscope (Jeol JEM-1400plus) and the method of dynamic light scattering on a ZetasiserNano ZS (Malvern) submicron particle size analyzer.

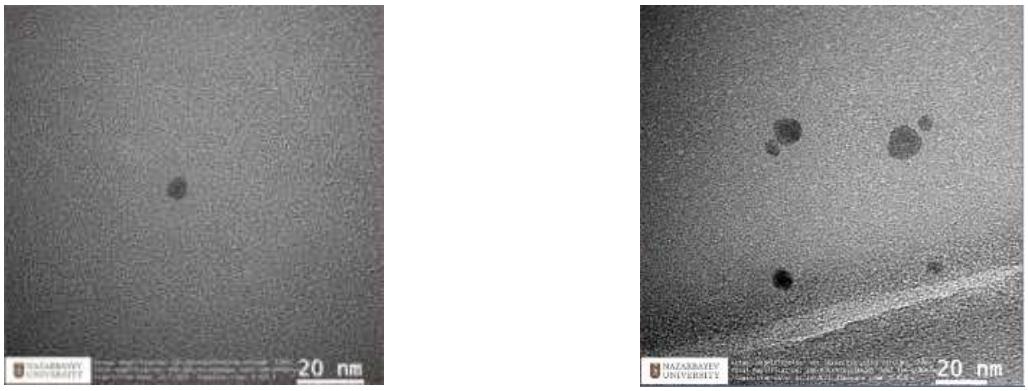

a) CNDs 1:1 b) CNDs 1:4

Figure 2. TEM images of CNDs synthesized by the microwave method

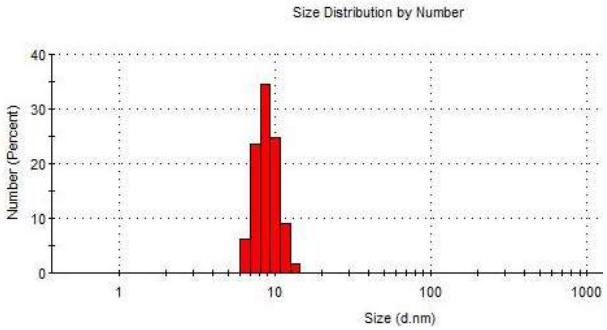

Figure 3. CNDs(m) (1:4) size distribution obtained by dynamic light scattering

As can be seen from the obtained TEM images (Fig. 2), the prepared CNDs are of spherical shape, their sizes vary from 5 to 16 nm. Similar data were obtained by the method of dynamic light scattering (Fig. 3). The different ratio of precursors did not affect the size of the CNDs. The average size was 9 nm.

The structure of the synthesized CNDs was studied on the basis of FTIR spectra, which were registered on an FSM 1201 IR Fourier spectrometer (Infraspec) in the transmission mode. The obtained FTIR spectrum exhibits maxima at 3417 and 3216 cm^{-1}, which belong to the stretching vibrations of –OH and –NH bonds (Fig. 4). Peaks at 1717, 1409 and 1452 cm^{-1} are caused by stretching vibrations of –C=O, –CN bonds

and vibrations of the benzene core, respectively. Thus, the recorded FTIR spectra confirm the doping of the synthesized CNDs with groups containing oxygen and nitrogen. The FTIR spectra of CNDs synthesized at different molar ratios of precursors are practically the same.

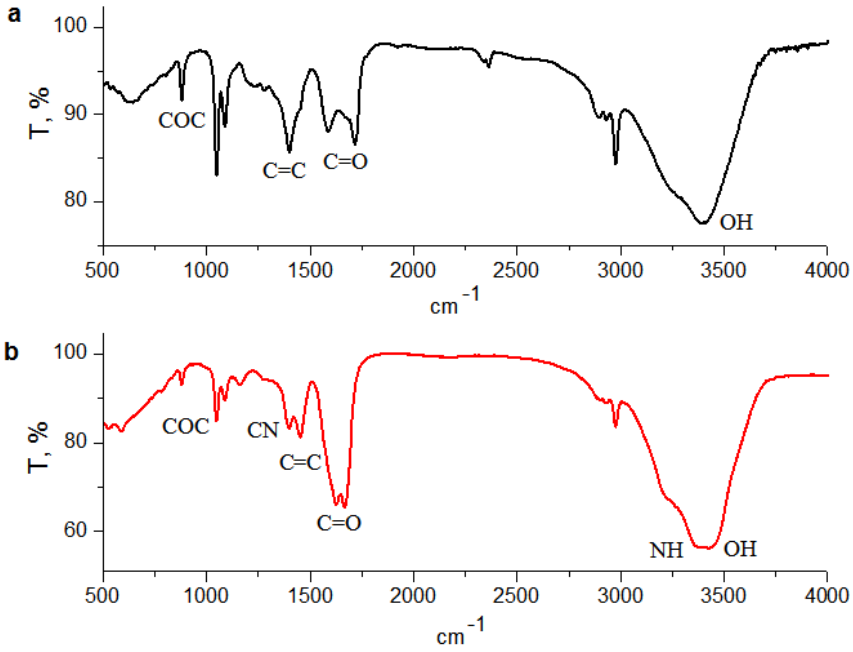

Figure 4. FTIR spectrum a) CNDs (m) 1:1; b) CNDs (m) 1:4.

The absorption and fluorescence spectrum of the obtained CNDs were measured on Carry 300 and Eclipse (Agilent) spectrometers, respectively. The studied solutions were prepared so that their optical densities were almost the same.

The absorption spectra of CNDs (Fig. 5) have a maxima in the region of 234 nm and 330–340 nm. The absorption band at 200–250 nm is caused by π–π* transition in conjugated carbon bonds of carbon dots, the long-wavelength absorption band is the result of n–π* transitions in C=O bonds of CNDs. Absorption on the long-wavelength wing (λ>400 nm) is the result of the presence of surface groups, which include –CN, –NH bonds.

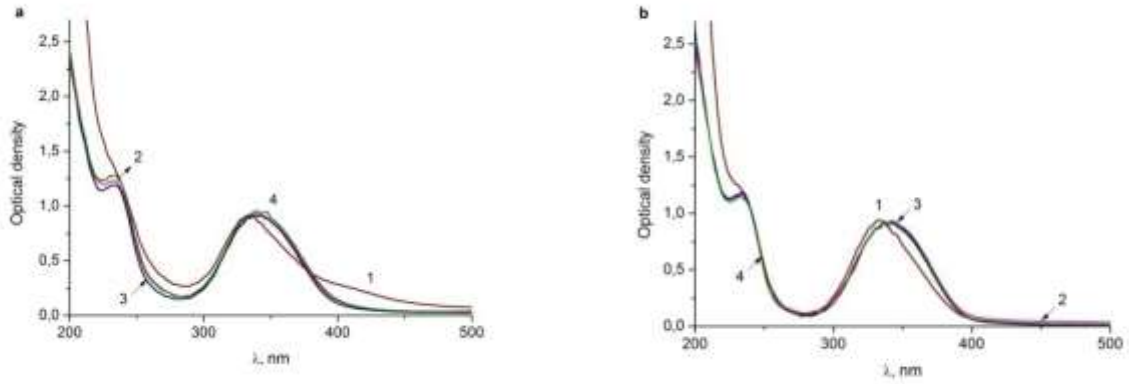

Figure 5. Absorption spectra of CNDs obtained by hydrothermal (a) and microwave (b) methods of synthesis with different molar ratios of precursors: 1 — CNDs 1:1, 2 — CNDs 1:4, 3 — CNDs 1:5, 4 — CNDs 1:6

It can be noted that the short-wavelength absorption band, regardless of the method of synthesis and the ratio of precursors, practically coincides for all samples, and the long-wavelength band of carbon dots obtained by the microwave method is slightly redshifted. At the same time, in both series, the long-

wavelength absorption maxima of CNDs with a ratio of 1:1 exhibits in the shorter-wavelength region, compared with the spectra of other CNDs (Table 1).

Table 1

Absorption maxima and full width at half maximum of absorption spectra of the studied CNDs

Solution	λ_{max1}, nm	λ_{max2}, nm	$FWHM_2$, nm
CNDs (h) 1:1	234	334	66
CNDs (h) 1:4	234	340	64
CNDs (h) 1:5	233	340	64
CNDs (h) 1:6	233	340	64
CNDs (m) 1:1	234	332	54
CNDs (m) 1:4	234	342	60
CNDs (m) 1:5	234	342	60
CNDs (m) 1:6	234	340	60

Since CNDs often exhibit excitation wavelength dependent luminescence [14-16], the fluorescence spectra of the obtained carbon dots were measured over a wide excitation range from 230 to 450 nm (Fig. 6). With an increase in the excitation wavelength from 230 to 350 nm, an increase in the emission intensity is observed; above 350 nm, a decrease in the fluorescence intensity is observed. At the same time, in the excitation range of 230–370 nm, the position of the emission maximum remains practically unchanged. Upon excitation at a wavelength of 390 nm and above, a shift of the emission band to the long wavelength region of the spectrum was observed.

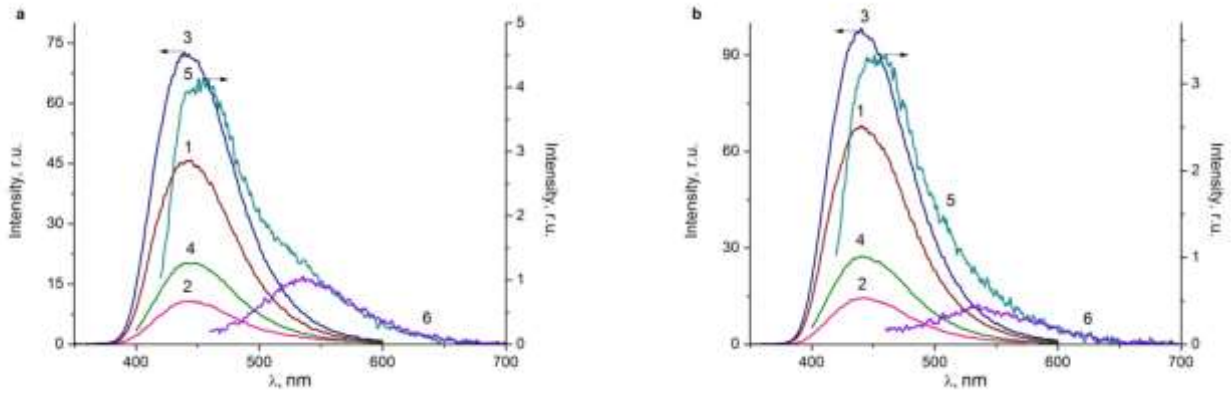

Figure 6. Fluorescence spectra of CNDs (1:4) obtained by hydrothermal (a) and microwave (b) methods upon excitation at different wavelengths, nm: 1 — 230; 2 — 330; 3 — 350; 4 — 390; 5 — 410; 6 — 450.

As the obtained emission spectra show, the maximum fluorescence intensity is observed upon excitation at 350 nm and does not depend on the method of synthesis of UT and the ratio of precursors. For both series of CNDs, the emission maximum falls at 443 nm.

Figure 7 shows the fluorescence spectra of the obtained CNDs depending on the composition of the precursors. The highest radiation intensity is observed for CND(g) 1:5 and CND (m) 1:4. Fluorescence quantum yields were measured for CND by the relative method [17]. As a standard, a 0.5 M solution of quinine sulfate in sulfuric acid was used, the quantum yield (QY) of which is 0.54 at an excitation wavelength of 345 nm. Table 2 shows the calculated fluorescence quantum yields. The data obtained show that the highest values of fluorescence quantum yield was demonstrated by carbon dots obtained by microwave synthesis at a ratio of citric acid and urea equal to 1:4.

Table 2

Fluorescence quantum yields of synthesized CNDs.

Sample	Quantum yield	Sample	Quantum yield
CNDs (h)1:1	0.1	CNDs (m)1:1	0.22
CNDs (h)1:4	0.4	CNDs (m)1:4	0.55
CNDs (h)1:5	0.43	CNDs (m) 1:5	0.49
CNDs (h)1:6	0.34	CNDs (m) 1:6	0.47

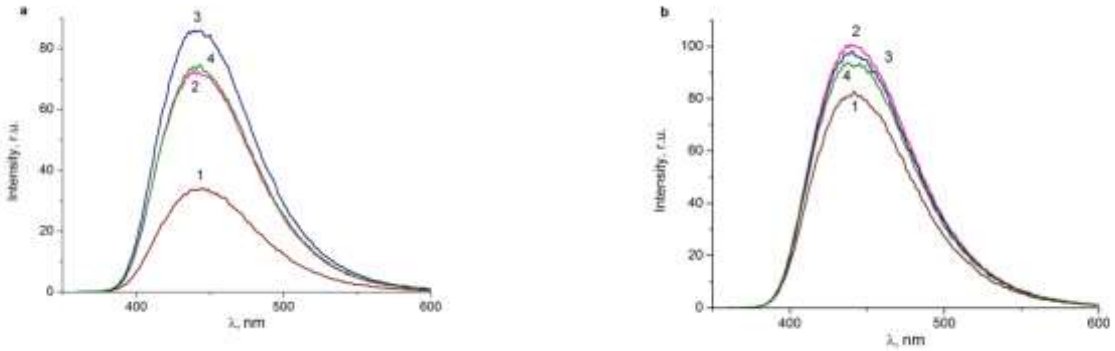

1 — CNDs 1:1; 2 — CNDs 1:4; 3 — CNDs 1:5; 4 — CNDs 1:6.

Figure 7. Fluorescence spectra of CNDs obtained by hydrothermal (a) and microwave (b) methods, with different ratios of citric acid and urea under photoexcitation at 350 nm.

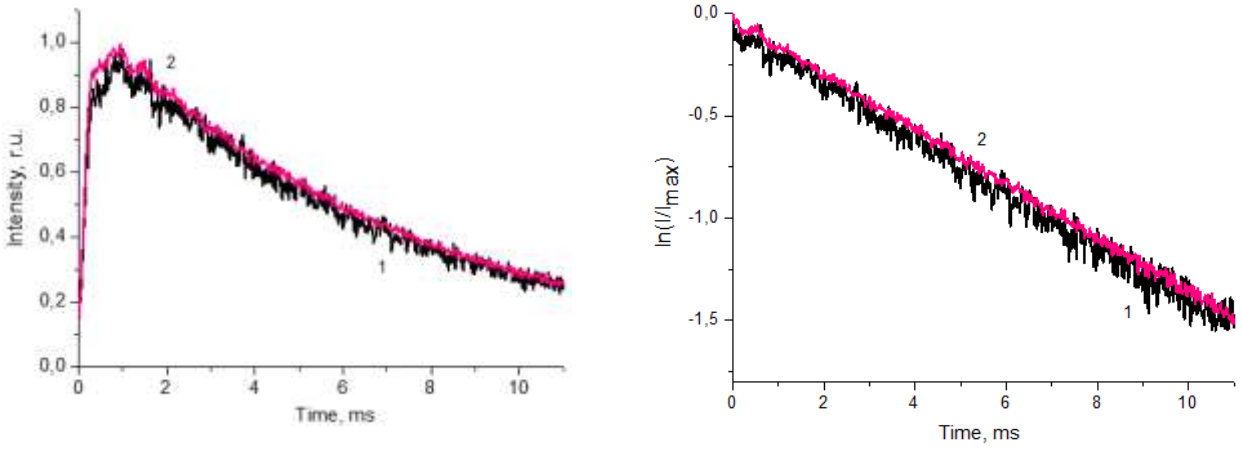

Figure 8. Normalized fluorescence decay kinetics of CND(m) 1:1 and CND(m) 1:4 under the registration at 440 nm,.

The fluorescence lifetime of the studied carbon nanodots was estimated from the decay kinetics, approximated with monoexponential law. The measurements showed (Fig. 8, Table 3) that the average fluorescence lifetime in CNDs is 7.4 ns.

Table 3

Fluorescence lifetime of CNDs(m) of various composition quantum yields of synthesized CNDs

Solution	τ, ns
CNDs 1:1	7.3
CNDs 1:4	7.4
CNDs 1:5	7.4
CNDs 1:6	7.4

Conclusions

The influence of the composition of precursors and synthesis conditions on the structural and optical properties of carbon dots, prepared by microwave and hydrothermal synthesis, was studied. Their structural properties showed that a change in the ratio of precursors does not significantly affect the size and morphology of carbon dots. The sizes of synthesized CNDs after dialysis were varied from 2 to 8 nm. The maximum fluorescence intensity of both types of CNDs was observed upon excitation at 350 nm. The highest fluorescence quantum yield (55 %) is exhibited by CNDs synthesized by the microwave method. The fluorescence lifetime averages ≈7.4 ns for all studied solutions.

Acknowledgments

This research is funded by the Science Committee of the Ministry of Education and Science of the Republic of Kazakhstan (Grant No. AP09259913).

References

1 Molaei, M. J. (2020). The optical properties and solar energy conversion applications of carbon quantum dots: A review. *Solar Energy, 196*, 549–566. doi: 10.1016/j.solener.2019.12.036

2 Jhonsi, M. A. (2018). Carbon Quantum Dots for Bioimaging. *State of the Art in Nano-Bioimaging*. doi:10.5772/intechopen.72723

3 Wang, Y. & Hu, A. (2014). Carbon quantum dots: synthesis, properties and applications. *J. Mater. Chem. C., 2*(34), 6921-6939. doi: 10.1039/C4TC00988F

4 Dong, Y., Shao, J., Chen, C., Li, H., Wang, R., Chi, Y., Lin, X. & Chen, G. (2012). Blue luminescent graphene quantum dots and graphene oxide prepared by tuning the carbonization degree of citric acid. *Carbon., 50*(12), 4738–4743. doi:10.1016/j.carbon.2012.06.002

5 Zhu, A., Ding, C. & Tian, Y. (2013). A two-photon ratiometric fluorescence probe for Cupric Ions in Live Cells and Tissues. *Sci. Rep., 3*(1), 2933. doi:10.1038/srep02933

6 Kasprzyk, W., Świergosz, T., Bednarz, S., Walas, K., Bashmakova, N.V. & Bogdał, D. (2018). Luminescence phenomena of carbon dots derived from citric acid and urea–a molecular insight. *Nanoscale, 10*(29), 13889–13894. doi: 10.1039/c8nr03602k

7 Dong, Y.Q., Pang, H.C., Yang, H.B., Guo, C.X., Shao, J.W., Chi, Y.W., Li, C.M. & Yu, T. (2013). Carbon-based dots co-doped with nitrogen and sulfur for high quantum yield and excitation-independent emission. *Angew. Chem. Int. Ed., 125*(30), 7954–7958. doi:10.1002/ange.201301114

8 Qu, D., Zheng, M., Zhang, L., Zhao, H., Xie, Zh., Jing, X., Haddad, R.E., Fan, X. & Sun, Z. (2014). Formation mechanism and optimization of highly luminescent N-doped graphene quantum dots. *Sci. Rep., 4*(1), 5294. doi:10.1038/srep05294

9 Guo, X., Xu, L., Zhang, L., Wang, H., Wang, X., Liu, X., Yao, J. & Hao, A. (2018). One-pot solid phase pyrolysis synthesis of highly fluorescent nitrogen-doped carbon dots and the interaction with human serum albumin. *J. Lumin., 196*, 100–110. doi:10.1016/j.jlumin.2017.12.029

10 Chahal, Sh., Yousefi, N. & Tufenkji, N. (2020). Green Synthesis of High Quantum Yield Carbon Dots from Phenylalanine and Citric Acid: Role of Stoichiometry and Nitrogen Doping. *ACS Sustainable Chem. Eng., 8*, 5566-5575. doi:10.1021/acssuschemeng.9b07463

11 Zholobak, N.M., Popov, A.L., Shcherbakov, A.B. et al. (2016) Facile fabrication of luminescent organic dots by thermolysis of citric acid in urea melt, and their use for cell staining and polyelectrolyte microcapsule labeling. *Beilstein J. Nanotechnol.,* 7, 1905–1917. doi:10.3762/bjnano.7.182

12 Qu, S., Liu, X, Guo, X., Chu, M., Zhang, L. & Shen, D. (2014). Amplified Spontaneous Green Emission and Lasing Emission From Carbon Nanoparticles. *Adv. Funct. Mater., 24*(18), 2689–2695. doi:10.1002/adfm.201303352

13 Lai, X., Liu, Ch., He, H., Li, J., Wang, L., Long, Q., Zhang, P. & Huang, Y. (2020). Hydrothermal synthesis and characterization of nitrogen-doped fluorescent carbon quantum dots from citric acid and urea. *Ferroelectrics, 566*(1), 116–123. doi:10.1080/00150193.2020.1762435

14 Lin, H., Huang, J. & Ding, L. (2019). Preparation of carbon dots with high-fluorescence quantum yield and their application in dopamine fluorescence probe and cellular imaging. *J. Nanomater., 2019*, 1-9. doi:10.1155/2019/5037243

15 Xia, C., Hai, X., Chen, X.W. & Wang, J.H. (2017). Simultaneously fabrication of free and solidified N, S-doped graphene quantum dots via a facile solvent-free synthesis route for fluorescent detection. *Talanta., 168*, 269–278. doi:10.1016/j.talanta.2017.03.040

16 Ibrayev, N.Kh., Dzhanabekova, R.Kh. & Amanzholova, G.S. (2021). Spectral and luminescent properties of carbon quantum dots functionalized with N- and S-contaning groups. *Eurasian Phys. Tech. J., 18*(36), 12-17. doi:10.31489/2021No2/12-17

17 Sahiner, N., Suner, S.S., Sahiner, M. & Silan, C. (2019). Nitrogen and sulfur doped carbon dots from amino acids for potential biomedical applications. *J. Fluoresc., 29*(5), 191–1200. doi:10.1007/s10895-019-02431-y

Г. Аманжолова, Е. Селиверстова, Н. Ибраев, Е.И. Теруков

Азот атомдары енгізілген лимон қышқылына негізделген көміртекті нанонүктелердің құрылымдық және оптикалық қасиеттері

Лимон қышқылы мен мочевинадан микротолқынды және гидротермиялық синтездеу әдістері арқылы алынған көміртекті нанонүктелердің люминесценттік қасиеттерін зерттеу жұмыстары жүргізілді. Алынған нанобөлшектер трансмиссиялық электронды микроскопия, жарықтың динамикалық шашырауы және Фурье түрлендіруі бар инфрақызыл спектроскопия арқылы сипатталды. Диализден кейін алынған көміртекті нанонүктелердің өлшемдері 2 нм-ден 8 нм-ге дейін өзгереді. Алынған ерітінділер құрамында оттегі атомы бар OH, CN және -NH топтарының болуын Фурье түрлендіруі бар инфрақызыл спектрлері растайды. Барлық зерттелген көміртекті нанонүктелер үшін флуоресценцияның максималды интенсивтілігі 350 нм толқын ұзындығында қоздыру кезінде байқалады. Сонымен қатар, прекурсорлардың молярлық қатынасы мен синтездеу әдісінің өзгеруіне байланысты зерттелген үлгілер үшін флуоресценция спектрі толқын ұзындығы шкаласы бойынша өз орнын өзгертпейді. Флуоресценцияның ең үлкен кванттық шығымы микротолқынды синтездеу әдісімен алынған лимон қышқылы мен мочевина қатынасы 1:4 болатын көміртекті нанонүктелер үшін алынды. Азот атомдары енгізілген көміртекті нанонүктелердің флуоресценциясының өмір сүру уақыты орта есеппен 7,4 нс тең. Прекурсорлардың молярлық қатынасының өзгеруі көміртекті нанонүктелердің мөлшері мен морфологиясына айтарлықтай әсер етпейтіні көрсетілді.

Кілт сөздер: көміртекті нанонүктелер, микротолқынды синтез, гидротермиялық синтез, оптикалық қасиеттері, лимон қышқылы, мочевина.

Г. Аманжолова, Е. Селиверстова, Н. Ибраев, Е.И. Теруков

Структурные и оптические свойства углеродных наноточек на основе лимонной кислоты, допированных атомами азота

Проведено исследование люминесцентных свойств углеродных наноточек, полученных микроволновым и гидротермальным методами синтезирования из лимонной кислоты и мочевины. Наночастицы были охарактеризованы с помощью просвечивающей электронной микроскопии, динамического рассеяния света и инфракрасной спектроскопии с преобразованием Фурье. Размеры полученных углеродных наноточек после диализа варьируются от 2 до 8 нм. ИК спектры с Фурье преобразованием подтверждают наличие кислородсодержащих OH и CN, -NH групп в полученных растворах. Для всех исследованных углеродных наноточек максимальная интенсивность флуоресценции наблюдается при возбуждении на длине волны 350 нм. Спектр флуоресценции не изменяет своего положения по шкале длин волн для исследуемых образцов от изменения молярного соотношения прекурсоров и метода синтезирования. Наибольший квантовый выход флуоресценции наблюдается у углеродных наноточек с соотношением лимонной кислоты и мочевины 1:4, полученных микроволновым методом синтезирования. Время жизни флуоресценции допированных атомами азота углеродных наноточек в среднем составляет 7,4 нс. Показано, что изменение соотношения прекурсоров не оказывает заметного влияния на размеры и морфологию углеродных наноточек.

Ключевые слова: углеродные наноточки, микроволновый синтез, гидротермальный синтез, оптические свойства, лимонная кислота, мочевина.

DOI 10.31489/2023PH3/98-106

UDC 538.971, 620.97

M.M. Kubenova[1], K.A. Kuterbekov[1], M.Kh. Balapanov[2], R.Kh. Ishembetov[2], K.Zh. Bekmyrza[1], A.M. Kabyshev[1], Sh. Afroze[1], R.Sh. Palymbetov[1], Zh.A. Mukhanova[1], E. Shukalov[1]

[1]L.N. Gumilyov Eurasian National University, 2 Satpayev str., 010008 Astana, Kazakhstan;
[2]Ufa University of Science and Technology, 32 Zaki Validi str., 450076 Ufa, Bashkortostan, Russia
(E-mail: kubenova.m@yandex.kz)

Analysis of the problems of synthesis of new nanocrystalline chalcogenide materials for thermoelectric generators and sodium-ion batteries

The paper analyzes the problems of the synthesis of new nanocrystalline chalcogenide materials for thermoelectric generators and sodium-ion batteries. The objectives of the synthesis will determine the best method to use to create chalcogenide materials for electrodes in real-world applications. The method of direct solid-phase reaction in a vacuum or in an environment of pure inert gas is the most effective way to generate novel chalcogenide materials in tiny amounts for the investigation of physicochemical and other features.With this approach, which is more dependable, it is feasible to produce a pure result free of contaminants that are inescapable when working with other solvents and precursors. Additionally, in a consistent synthesis regime, it is differentiated by the stability of the acquired attributes of the compounds. Synthesis modes, reagents, and post-processing depend on the specific material. The method of synthesizing alloys in a melt media made up of a combination of potassium and sodium hydroxides is one of the key techniques employed in the present research. The melting point drops to 165 °C at a certain ratio of the concentrations of these hydroxides, allowing for the execution of salt exchange processes in the melt. The size of the resultant chalcogenide particles can be reduced to a few nanometers by lowering the synthesis temperature, adding water, and shortening the annealing period.

Keywords: thermoelectric materials, copper sulfide, crystal structure, conductivity, diffusion, thermal conductivity, Seebeck coefficient, superionic conductors.

Introduction

The main reason hindering the creation of competitive sodium-ion batteries (SIB) is the low efficiency of the available electrode materials. The aim of this research is to generate a very energy-intensive nanostructured electrode material for sodium-ion batteries that operate at ambient temperature and can be recharged several times.

SIB cannot currently work at large current densities due to a significant disadvantage of the sodium-ion electrochemical system, which is a relatively long charge/discharge time. For this reason, one of the goals of the work is also to increase the rate of charge and discharge processes in SIB electrode materials by increasing the chemical diffusion coefficient.

As candidates for cathode materials in the framework of this study, highly non-stoichiometric phases of copper sulfide (digenite and anilite) in the nanoscale state are considered, which can exhibit superionic properties at room temperature and, in addition, have a high electronic conductivity of the order of 10^2 — $10^3 Om^{-1}cm^{-1}$. The structure of digenite and anilite contains many copper vacancies, which can reduce lattice mechanical stresses and extend the cycle life of the cathode to 100 or furthermore.

Transition metal chalcogenides (TMCh), such as cobalt sulfides, molybdenum sulfides, and tin sulfides, have been extensively investigated as potential anode materials with high sodium content, easy availability, and improved safety [1]. However, transition metal chalcogenides have certain defects and disadvantages, such as low conductivity and large volume changes, which can prevent the diffusion of Na + ions and reduce the operating current of the cells, and large volume changes can accelerate particle reunification and grinding (crushing) of active materials. These two unfavorable factors significantly limit the widespread use of transition metal chalcogenides, which are used exclusively in NIB. Therefore, to minimize volume expansion and enhance Na^+ diffusivity, transition metal chalcogenides are typically coupled with conductive carbon materials [1].

CPM electrodes for NIB based on carbon have been stated fairly often nowadays. The Mai group, for instance, developed a unique method for synthesizing a mesoporous “yolk” consisting of cobalt sulfide and an alveolar carbon shell (M-CoS@C) [2]. A mesoporous cobalt sulfide “yolk” and an alveoloid-like carbon

shell (M-CoS@C) emerged after annealing, etching in HF, coating with silica and resorcinol formaldehyde, and annealing.

After 100 cycles at 0.2 A g^{-1}, the M-CoS@C electrode still has a high reversible capacity of 532 mAh g^{-1}, corresponding to a retention of 87.2 % capacity. On the contrary, the capacity of M-CoS rapidly decreased to 55 mAh g^{-1} within five cycles, indicating deterioration of the structure due to a shortage of the spatially constrained structure provided by the carbon shell.

In addition, the structure of the "yolk" shell also endowed the M-Co@C electrode with impressive speed characteristics with capacities of 635, 570, 530, 490, 440, 360, 295, and 190 mAh g^{-1} at 0.1, 0.2, 0.5, 1, 2, 5, 10 and 20 A g^{-1} respectively.

A study by Zhang et. al. [3] obtained self-organizing polygonal CoS_2 nanoparticles doped with nitrogen and coated with a carbon layer (N-CoS_2@C composites) as an anode electrode for NIB. Figures A and B depict the configuration and microstructure of N-CoS2@C, where high magnification TEM images show that the ordered CoS_2 is tightly encapsulated in a carbon layer with an average thickness of 0.5 nm, which should provide a strong barrier to protect intermediate reactants from being dissolved in electrolyte and create a better conductive path for active materials [1].

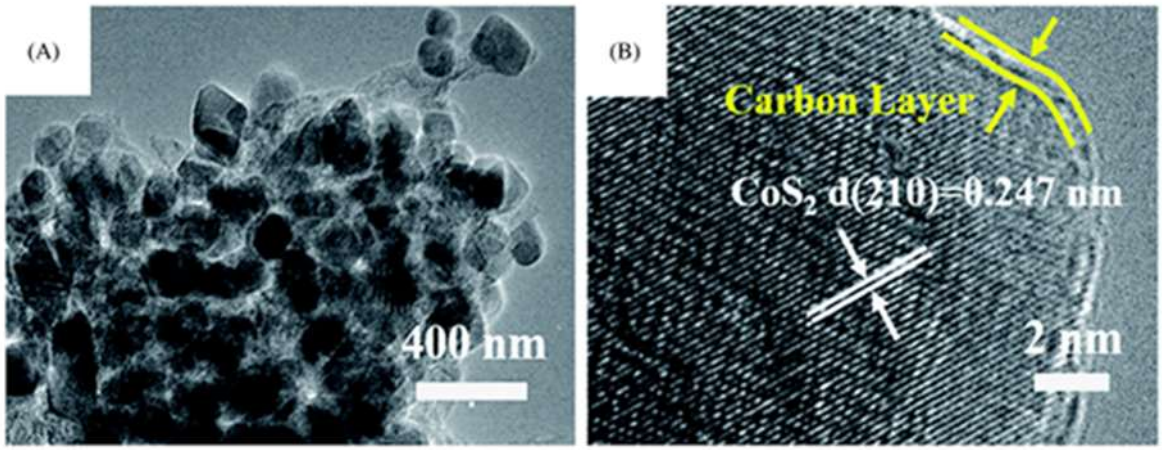

Figure 1 — (A) TEM and (B) HREM images of N-CoS2@C composites by [1]

N-CoS_2@C provides sodium incorporation reversibility, demonstrating a high incorporation rate. At a current density of 0.1 A g-1, the N-CoS_2@C electrode exhibits an initial high discharge capacity of 814 mA h g -1. The material showed an impressive reversible capacity of 559 mAh g^{-1} after 1000 cycles at 1 A g^{-1}. This is indicative of the excellent stability and reliability of the carbon-coated structure. The data obtained show that CoS_2 nanostructures with high sodium storage capacity, easy accessibility, low losses, and excellent safety can serve as promising anode materials for NIB [1].

Copper chalcogenides.

J. -S. Kim et al. were the first to investigate rechargeable batteries based on sodium/copper sulfide (Na/Cu_2S) [4] using the liquid electrolyte 1M $NaCF_3SO_3$-TEGDME at room temperature. The initial discharge curve of Na/Cu_2S cells had a slanting form and no apparent plateau area. After 20 cycles, the capacity dropped to 220 mAh g^{-1} from 294 mAh g^{-1} at the initial discharge. The integration of sodium into the Cu_2S chalcocite lattice without disentanglement in the second phase explains how the discharge mechanism occurs.

In the work of J. -L. Yue et. al. [5] Cu_2Se electrodes on a copper grid substrate were directly fabricated by a simple post-selenization method and tested as a positive electrode for sodium-ion batteries. Cu_2Se showed a large reversible capacity (about 250 mAh g^{-1}), good cyclic stability, and low polarization. These findings demonstrate that Cu_2Se is a promising candidate as a NIB cathode material.

J.Y. Park et. al. [6] obtained and studied electrodes from covellin CuS nanoplates in a sodium-ion cell. CuS undergoes a series of crystallographic rearrangements throughout the intercalation procedure, and many of the intermediate phases share crystal structures with one another. A novel capacity recovery behavior is also demonstrated by the material, which is in stark contrast to the normal conversion reaction systems, which suffer from substantial capacity loss upon cycling.

After the initial 13 cycles, the capacity of CuS nanoplatelets with a current density of 0.2 C rapidly declines to 80 mAh/g. The capacity progressively upsurges to ≈570 mAh/g, which is near the theoretical capacity, during the course of the following 90 cycles. The capacity recovers after the initial decline to ≈ 246 mAh g^{-1} in under 20 cycles at a greater current density (i.e., 3 C), which is an intriguing finding.

When exposed to different current densities between 1 and 5 C, bulk CuS with particle sizes in the hundreds of micrometers demonstrates outstanding stability. Bulk CuS also offers long-term cyclic stability; after 1000 cycles at 1C and 5C currents, respectively, the specific capacities were 415 and 406 mAh/g, correspondingly. With ≈ 93 % capacity retention after the second cycle, cyclic stability is preserved even after 2100 cycles. Akin to CuS nanoplates, bulk CuS also exhibited capacitance recovery, electrical property changes, and a plateau in the discharge. The capacity of CuS initially decreases significantly to 392 mAh/g over the initial 8 cycles at 1C current. The capacity does, nevertheless, return to 429 mAh/g during the next 500 cycles. After a more significant capacity lessening to 276 mAh g^{-1}, the capacity recovers more hastily after 100 cycles at a greater current density of 5 C [6].

According to the conclusions of the authors of [6], the ability of Na_xCuS nanoplates to regain their electrode capacity and resistance to grinding is facilitated by the development of stable grain boundaries and interphase boundaries. Astoundingly, the aforementioned process is applicable to all materials, as bulk coarse-grained CuS also shows electrochemical characteristics resembling those of nanowafers.

CuS can be beheld as a potential anode contender for sodium-ion batteries based on contrasts with its equivalents in lithium-ion batteries. As an outcome, it can be hypothesized that the crystallographic bonds between the sodium intercalation phases are a crucial part of materials that can be cycled mechanically with high levels of reliability for sodium-ion battery high-performance conversion processes.

Evaluation of existing methods for the synthesis of chalcogenides.

The intentions of the synthesis will determine the best technique for producing chalcogenide materials for oxygen reduction catalysts. It is quickly accomplished using the direct solid-phase reaction approach in a vacuum or in an environment of pure inert gas to synthesize novel chalcogenide materials in tiny quantities for the investigation of their physicochemical and other features. With this approach, which is more dependable, it is feasible to produce a pure result free of contaminants that are inescapable when working with other solvents and precursors. Furthermore, in a consistent synthesis regime, it is differentiated by the stability of the acquired attributes of the compounds. Synthesis regimes, reagents, and subsequent processing depend on the specific material and are developed in this work for binary and complex sulfides, selenides, tellurides of monovalent and transition metals, substituted or doped with other metals, and having different nonstoichiometry.

The key objective of synthesizing a catalytic material features of which are recognized for profit-making applications is to provide low-cost goods while preserving valuable qualities discovered via laboratory research. Since this is thought to lower manufacturing expenditures, nearly all topmost laboratories now working on functional materials use “soft” chemistry techniques that allow for synthesis at low temperatures, ideally close to room temperature.

A process for synthesizing alloys in a melt media made of an amalgamation of potassium and sodium hydroxides was devised. It is feasible to conduct exchange reactions between salts in the melt when the melting point drips to 165 °C at a certain ratio of the concentrations of these hydroxides. The size of the resultant chalcogenide particles can be abridged to a few nanometers by lowering the synthesis temperature and cutting the annealing period.

Synthesis of nanocrystals of metal sulfides.

Metal sulfide nanoparticles were manufactured using a number of techniques, such as solvothermal synthesis [7], microwave radiation [8], ultrasonication [9], and surface-passivating high-boiling solvents used in the thermolysis of precursors from a single source [10-13]. In order to synthesize CuS nanocrystals, various methods [14–17] for obtaining nanoparticles were also used with different morphologies, such as nanotubes [18, 9], nanowires [19], and nanoplates [20, 11, etc. [21, 22]. Among the methods for synthesizing nanocrystals, the method of a single precursor source allows for the acquisition of nanocrystals with good monodispersity [23], and studies showed that the size and shape of the obtained nanocrystals depended on the precursor concentration [24], reaction time [25], and temperature [26]. Due to the distinctiveness of the size-dependent physical and chemical features of nanocrystals [27, 28], researchers continue to pay close attention to the synthesis of monodisperse nanocrystals [29, 30].

Synthesis of nanocrystals of copper sulfides.

Longer alkyl chain precursors result in the development of nanosheets, whereas shorter alkyl chain precursors yield two-dimensional nanosheets. It has also been investigated how one specific precursor mechanism works. Cu-dithiocarbamate, for instance, is used to create nanowires, quantum dots, and nanobarrels.

In recent years, most research has focused on the colloidal solution-based synthesis method. Typically, two separate copper and sulfur precursors are dissolved in an organic solvent such as oleylamine (OLA). CuCl and copper acetylacetonate are the two utmost prominent copper precursors. The most common form of sulfur is elemental sulfur. A 7:3 amalgamation of oleylamine (OLA) and octadecene (ODE) was employed to dissolve the precursors CuCl and element S for the $Cu_{2-x}S$ synthesis, for instance.

The heating technique and the hot injection method are two categories for solution-based synthesis. In the heating method, the reaction temperature is reached after heating two precursors that have been combined at a low temperature. Using CuCl and S powder as precursors and a solution of oleylamine and octadecene as solvents, it was possible to grow monodisperse CuS nanoplatelets. In addition, it was found that changing the ratio of Cu to S can preciously modify the plasma characteristics of CuS particles without altering their shape and size.

To make assured $Cu_{2-x}S$ nanoparticles are used industrially, it is necessary to develop a scalable and reliable synthesis. In order to accomplish this goal, Robinson's team of researchers [31] developed an ultra-high concentration heating method and synthesized more than 200 g (80 % yield) of nanoparticles as a result of a single synthesis. In addition, even the large-scale synthesis of 8 — nm roxbyite ($Cu_{1,81}S$) had a size dispersion of fewer than 10 %. CuCl and S were employed as precursors in this synthesis, while an oleylamine (OLA)/octadecene (ODE) (7:3) combination was used as the solvent. Distinctively, dissolving CuCl and S, they are then combined at 50 °C and heated for two hours at 185 °C. The items are then centrifuged three times while being cleaned with acetone-hexane. The high concentration of the precursor is indispensable for this process (1000 mMCuCl and 5000 mM S).

Apart from the heating technique, the hot injection technique is yet another sort of colloidal synthesis. In this case, the sulfur forerunner is usually introduced into the copper forerunner solution at the reaction temperature. Due to the high stirring temperature, the hot injection reaction is completed much faster compared to the heating method. For example, $Cu_{2-x}S$ monodisperse particles ranging in size from 2.8 nm to 13.5 nm can be synthesized by hot injection within 1.5-3 minutes. Size change can be achieved with variations in injection temperatures (115 °C — 140 °C). Moreover, the choice of solvent strongly affects the phase of the synthesized $Cu_{2-x}S$ particle. While OLA is used as a solvent, jarleite ($Cu_{1.94}S$) and oleic acid (OA) are produced, and these substances then cause the covellin (CuS) phase to develop in the form of particles [32].

Electrochemical deposition, or anodizing, is another simple, inexpensive, and high-throughput method for directly fabricating a copper sulfide nanostructure on a substrate. Like many other metal oxides, copper sulfide nanostructures are also grown on Cu substrates or Cu foil as the anode and Ti metal as the cathode in a voltage range of 1.5 — 8 V in an aqueous solution of Na_2S. Accordingly, Cu_2S and CuS nanorod and nanowall arrays were obtained by controlling the voltage and reaction temperature [32].

Hydrothermal method. It is currently one of the methods for synthesis that are employed most frequently for nanomaterials. The technique makes it possible to increase the solubility of the reagents in the solvent and accelerate the chemical reaction, achieving rapid supersaturation at elevated temperatures and pressure. The application of stabilizing/coating agents is also widely used to stabilize narrow size distributions in 0D and specific high-energy surfaces in 1D and 2D copper sulfide nanostructures. Although the hydrothermal method is commonly used for slow-growing large single-crystal particles, it demonstrated that it could create $Cu_{2-x}S$ nanocrystals with different morphologies. $Cu_{2-x}S$ nanowires, nanotubes, and nanovesicular structures synthesized employing the hydrothermal synthesis technique effectively. 1-D structures consist of self-assemblies of $Cu_{2-x}S$ nanoplates and nanoparticles. In addition, it demonstrated that the methods of hydrothermal and solvothermal synthesis were efficient in the synthesis of $Cu_{2-x}S$ 3-D superstructures. A three-dimensional structure made of four hexagonal CuS plates, for instance, was generated by heating copper nitrate and sulfur powder to 140 °C for 24 hours. It measured 200 nm in thickness and 1 to 1.5 microns in diameter. The 14 chambers in this material, which may be used for applications like photocatalysts, are intriguing. Other layered structures of CuS, such as color-like structures and nanospheres, are also synthesized [32, 33].

Experimental part

Synthesis of nanodispersed phases with sodium-ion conductivity $Na_xCu_{2-y}S$ ($0<x<0.25$, $0<y<0.25$).

As a priority synthesis method, low-temperature chemical synthesis in a liquid medium was considered, which requires a minimum of time and ensures the yield of a sufficiently pure product in a nanoscale form.

Nanomaterials based on superionic copper sulfide, $Cu_{2-x}S$ were chosen as electrode materials.

To select the optimal synthesis technique, an analysis was made of the available literature on the synthesis of copper chalcogenides over the past decade.

Due to its promising qualities, copper sulfide is the copper chalcogenide that was examined the most. The direct band gap of $Cu_{2-x}S$, a p-type semiconductor, ranges from 1.2 eV (Cu_2S) to 2.0 eV (CuS). Since it consists of non-toxic and common elements in the earth's crust, it is environmentally friendly. In addition, numerous non-stoichiometric defects contribute to the ability to control the density of current carriers, and thus the electrical conductivity of the material, by changing the ratio of Cu to S during synthesis. Compared to most noble metal nanocrystals, the tunability of the carrier concentration is unique. Controlling the phase composition, size, and shape of $Cu_{2-x}S$ nanoparticles advanced significantly over the past ten years as a result of the benefits highlighted above. Numerous synthesis techniques are taken into account, such as solvent-free synthesis, hydrothermal synthesis, solvothermal synthesis, and colloidal hot injection techniques.

Shorter alkyl chains of the precursor cause the emergence of two-dimensional nanosheets, nonetheless, a longer chain results in the fabrication of nanosheets. In another work, for the synthesis of nanobarrels, quantum dots, and $Cu_{2-x}S$ nanowires, Cu-dithiocarbamate is employed.

In a melt of NaOH and KOH hydroxides, a method established for the manufacture of nanocrystalline copper sulfides, $Cu_{2-x}S$.

The research is carried out in a fume hood with a coating resistant to heated alkalis and equipped with a forced ventilation system. The Teflon vessel, in which the reaction is carried out in an alkaline melt, is reinforced on the outside with a strong metal edging to prevent rupture due to increased pressure inside during the reaction.

In a Teflon jar, the produced combination of sodium and potassium hydroxides is put in the proper ratio and heated to melt (about 165 °C). Heat is supplied to the vessel both from below and along the side walls, for uniform heating throughout the volume. The lid of the vessel should not be tight so that excess vapors can freely escape from the vessel. The power of the heater after boiling is reduced to a minimum in order to avoid violent boiling. The operator must wear a respirator and protective gloves.

All reagents (CuCl, Na_2S*9H_2O) are pre-weighed in the calculated proportion and simultaneously heating put into a Teflon container.

The vessel is then firmly sealed with an argon fill once the charge has been full, and a steam release hole is drilled in the screw cap. During the reaction, a small flow of argon continues to flow into the top section of the vessel, which creates some excess pressure above the melt surface.

$Cu_{2-x}S$ nanoparticles are formed after several hours, usually 15 hours are maintained. The formed crystals are in the melt in the form of a gel. By incorporating a little amount of water into the melt, nanocrystal sizes can be lessened. The final result, which takes the shape of a gel clot, is cleaned three times with warm distilled water before being cleaned again with pure ethanol and allowed to air dry. Particle sizes ranging from 15 to 90 nm make up the majority of the resultant powder. The process of sedimentation in an alcohol-filled column is used to separate distinct particle fractions according to size.

Low-temperature liquid-phase chemical synthesis requires less time and cost to obtain a synthesis product, but has a number of features. Residues of organic components used in the synthesis are difficult to completely remove, which does not always allow for the acquisition of a chemically pure product, and the presence of several percent of foreign components in the synthesized phase is almost inevitable. In this case, X-ray phase analysis does not fix the presence of foreign phases, but the presence of impurities is manifested in studies on a scanning electron microscope and in spectral chemical analysis. Homogenization at a temperature not lower than 400 °C allows for minimizing the content of volatile components and increasing the repeatability of the outcomes of investigations of electronic kinetic coefficients (conductivity, thermal conductivity, etc.).

In the chemical synthesis of copper chalcogenide nanopowder, the result strongly depends on the reaction time. The size of the resultant nanocrystals may be dwindled to 8–12 nm by cutting the annealing period to 5-8 hours. The use of a dispersing medium (for example, diethylene glycol) changes the shape of

the nanocrystals and reduces their size. In the synthesis of $Na_xCu_{2-x}S$ superionic materials, the incorporation of a trace quantity of water also makes it possible to vary the size of the obtained nanocrystals.

Electron microscopy.

An examination of the periphery of the samples using a MIRA3 TESCAN scanning electron microscope confirmed the estimate of the crystallite sizes from the X-ray line half-width. In figures 2-5 below, the materials have a loose structure of blocks of crystallites separated by large pores.

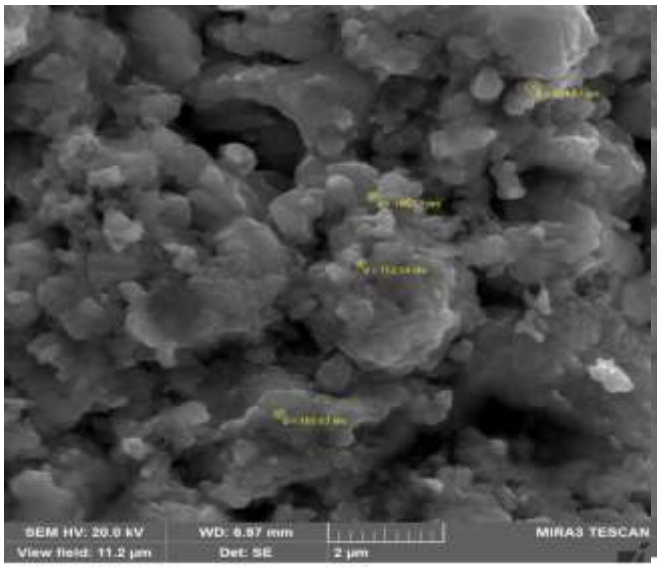

Figure 2 — Photograph of the etched $Na_{0.15}Cu_{1.85}S$ surface on a MIRA3 TESCAN scanning electron microscope. Visible loose nanocrystalline structure

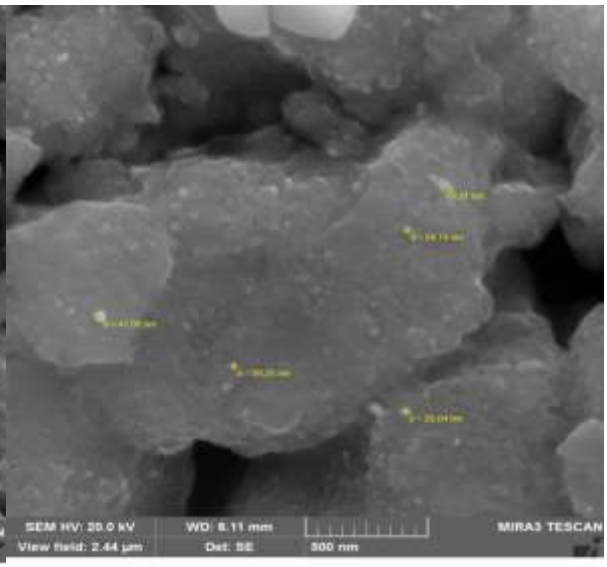

Figure 3 — Photograph of another area of the etched $Na_{0.15}Cu_{1.85}S$ surface on a MIRA3 TESCAN scanning electron microscope. Visible nanocrystalline grain structure and large pores

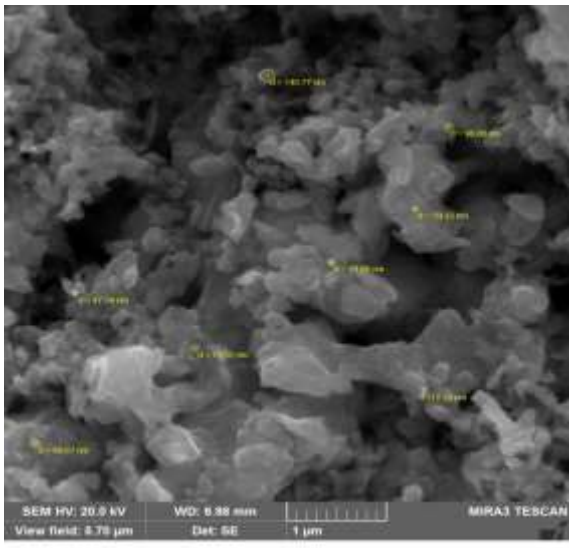

Figure 4 — Photograph of the etched $Na_{0.125}Cu_{1.75}S$ surface on a MIRA3 TESCAN scanning electron microscope. Loose nanocrystalline structure and pores are visible

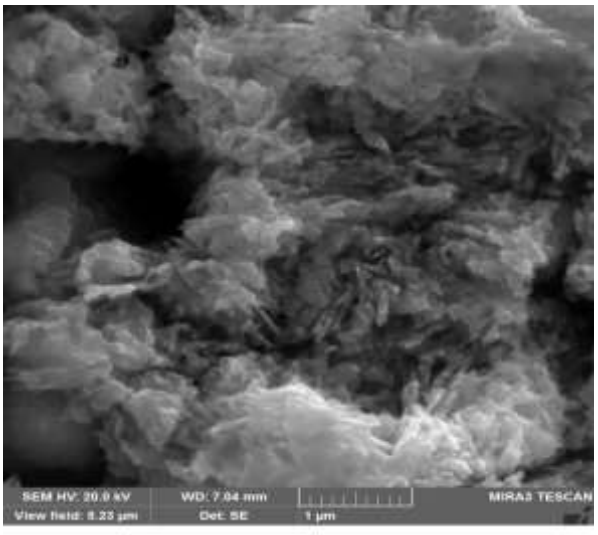

Figure 5 — Photograph of another area of the etched $Na_{0.125}Cu_{1.75}S$ surface on a MIRA3 TESCAN scanning electron microscope. Loose nanocrystalline structure and pores are visible

Conclusion

Depending on the purposes of the synthesis, the best technique for producing chalcogenide materials for sodium-ion battery electrodes will be chosen. It is ideal to use the direct solid-phase reaction approach in a vacuum or in an environment of pure inert gas when synthesizing a novel chalcogenide material in tiny

quantities for the investigation of its physicochemical and other features. With this approach, which is more dependable, it is feasible to produce a pure result free of contaminants that are inescapable when working with other solvents and precursors. Additionally, in a consistent synthesis regime, it is differentiated by the stability of the acquired attributes of the compounds. Synthesis modes, reagents, and post-processing depend on the specific material.

The main challenge in the synthesis of an electrode material features of which are known for commercial applications is to produce low-cost goods while keeping relevant qualities discovered in laboratory investigations. Due to the lower manufacturing costs, nearly all top laboratories now working on functional materials use "soft" chemistry techniques that enable synthesis at low enough temperatures.

In this work, as one of the main ones, it is used to generate alloys using a procedure that involves melting a combination of potassium and sodium hydroxides. The melting point drips to 165 °C at a certain ratio of the concentrations of these hydroxides, letting for the conduct of exchange processes between salts in the melt. The resultant chalcogenide particles can be shrunk to a few nanometers in size by lowering the temperature during synthesis, adding water, and shortening the annealing period.

As studies of recent years show, one of the promising materials for electrodes in sodium-ion batteries is currently considered covelline CuS. Hundreds of micrometer-sized particles in bulk CuS reveal outstanding stability and high capacity for a range of current densities from 1 to 5 C. Bulk CuS also offers long-term cyclic stability, with a specific capacity retention of 406 mAh/g at high current densities (5C) after 1000 cycles. In Na_xCuS nanoplates, the development of stable grain boundaries and interfacial boundaries also helps to restore the electrode capacity and resistance to grinding, prolonging the service life of the cathode.

In light of the results of recent research, the greatest success in the development of electrodes for sodium-ion batteries can be achieved for composites that combine the active material with nanosized carbon materials, including those that create a protective shell for particles of the electrode material, which increases the resistance of the electrode to repeated overcharging.

In consequence, in line with the current trend of looking for novel electrode materials for sodium-ion batteries, work on the synthesis of copper sulfides of varied compositions and morphologies offers optimism that the acquired materials may soon be used in practical applications.

Acknowledgments

The Science Committee of the Republic of Kazakhstan, which is part of the Ministry of Science and Higher Education, provided funding for this research (No. AP14871197).

References

1 Tang, Zh. & Yang, H. (2020). Advanced Nanomaterials for Electrochemical Energy Conversion and Storage. CHAPTER 11: Transition metal chalcogenides for energy storage and conversion. *ELSEVIER,* P. 355-391.

2 Li, Q., Li, L., Owusu, K.A., Luo, W., An, Q. & Wei, Q. (2017). Self-adaptive mesoporous CoS@alveolus-like carbon yolk-shell microsphere for alkali cations storage. *Nano Energy, Vol. 41,* P. 109-116.

3 Pan, Y., Cheng, X., Gong, L., Shi, L., Deng, Y. & Zhang, H. (2018). Highly reversible Na ion storage in N-doped polyhedral carbon-coated transition-metal chalcogenides by optimizing the nanostructure and surface engineering. *J. Mater. Chem. A., Vol. 6,* P. 18967-18978.

4 Kim, J.-S., Kim, D.-Y., Cho, G.-B., Nam, T.-H., Kim, K.-W., Ryu, H.-S., Ahn, J.-H. & Ahn, H.-J. (2009). The electrochemical properties of copper sulfide as cathode material for rechargeable sodium cell at room temperature. *J. Power Sources, Vol. 189,* P. 864-868.

5 Yue, J.-L., Sun, Q. & Fu, Z.-W. (2013). Cu_2Se with facile synthesis as a cathode material for rechargeable sodium batteries. *Chem. Commun, Vol. 49,* P. 5868-5870.

6 Park, J.Y., Kim, S.J., Yim, K., Dae, K.S., Lee, Y., Dao, K.P., Park, J.S., Jeong, H.B., Chang, J.H. & Seo, H. (2019). Pulverization-Tolerance and Capacity Recovery of Copper Sulfide for High-Performance Sodium Storage. *Adv. Sci,* P. 1900264.

7 Park, J., Joo, J., Kwon, S.G., Jang, Y. & Hyeon, T. (2007). Synthesis of monodisperse spherical nanocrystals. *Angew. Chem. Int. Ed., Vol. 46,* P. 4630-4660.

8 Wada, Y., Kuramoto, H., Anand, J., Kitamura, T., Sakata, T., Mori, H. & Yanagida S. (2001). Microwave-assisted size control of CdSnanocrystallites. *J. Mater. Chem, Vol. 11,* P. 1936-1940.

9 Ghows, N. & Entezari, M.H. (2011). A novel method for the synthesis of CdS nanoparticles without surfactant. *Ultrason. Sonochem, Vol. 18,* P. 269-275.

10 Sohrabnezhad, S.H. & Pourahmad. (2010). A. CdS semiconductor nanoparticles embedded in AlMCM-41 by solid-state reaction. *J. Alloys Compd., Vol. 505,* P. 324-327.

11 Nirmal, R.M., Pandian, K. & Sivakumur, K. (2011). Cadmium (II) pyrrolidinedithiocarbamate complex as single source precursor for the preparation of CdS nanocrystals by microwave irradiation and conventional heating process. *Appl. Surf. Sci., Vol. 257,* P. 2745-2751.

12 Trindade, T. & O'Brien, P. (1997). Synthesis of CdS and CdSeNanocrystallites Using a Novel Single-Molecule Precursors Approach. *Chem. Mater., Vol. 9*, P. 523-530.

13 Zhang, Y.C., Wang, G.Y. & Hu, X.Y. (2007). Solvothermal synthesis of hexagonal CdS nanostructures from a single-source molecular precursor. *J. Alloys Compd., Vol. 437,* P. 47-52.

14 Huang, Y., Xiao, H., Chen, S. & Wang, C. (2009). Preparation and characterization of CuS hollow spheres. *Cer Inter., Vol. 35,* P. 905-907.

15 Dhassade, S.S., Patil, J.S., Han, S.H., Rath, M.C. & Fulari, V.J. (2013). Copper sulfide nanorods grown at room temperature for photovoltaic application. *Mater. Lett, Vol. 90,* P. 138-141.

16 Maji, S.K., Mukherjee, N., Dutta, A.K., Srivastaca, D.N., Paul, P., Karmakar, B., Mondal, A. & Adhikary, B. (2011). Deposition of nanocrystallineCuS thin film from a single precursor: Structural, optical and electrical properties. *Mater. Chem. Phys., Vol. 130,* P. 392-397.

17 Ma, G., Zhou, Y., Li, X., Sun, K., Liu, S., Hu, J. & Kotov, N.A. (2013). Self-assembly of copper sulfide nanoparticles into nanoribbons with continuous crystallinity. *ACS Nano, Vol. 7,* P. 9010-9018.

18 Zhang, H.T., Wu, G. & Chen, X.H. (2006). Controlled synthesis and characterization of covellite (CuS) nanoflakes. *Mater. Chem. Phys., Vol. 98*, P. 293-303.

19 Wu, C., Shi, J.B., Chen, C.J., Chen, Y.C., Lin, Y.T., Wu, P.F. & Wei, S.Y. (2008). Synthesis and optical properties of CuS nanowires fabricated by electrodeposition with anodic alumina membrane. *Mater. Lett, Vol. 62,* P. 1074-1077.

20 Liu, J. & Xue, D.F. (2009). Solvothermal synthesis of CuS semiconductor hollow spheres based on a bubble template route. *J. Cryst. Growth, Vol. 311,* P. 500-503.

21 Thongtem, T., Phuruangrat, A. & Thongstem, S. (2009). Formation of CuS with flower-like, hollow spherical, and tubular structures using the solvothermal-microwave process. *Curr. Appl. Phys., Vol. 9,* P. 195-200.

22 Tan, C.H., Lu, R., Xue, P.C., Bao, C.Y. & Zhao, Y.Y. (2008). Synthesis of CuS nanoribbons templated by hydrogel. *Mater. Chem. Phys., Vol. 112,* P. 500-503.

23 Pradhan, N., Katz, B. & Efrima, S. (2003). Synthesis of High-Quality Metal Sulfide Nanoparticles from Alkyl Xanthate. Single Precursors in Alkylamine Solvents. *J. Phys. Chem. B., Vol. 107,* P. 13843-13854.

24 Mondal, G., Acharjya, M., Santra, A., Bera, P., Jana, S., Pramanik, N.C., Mondal, A. & Bera P. (2015). A new pyrazolyldithioate function in the precursor for the shape controlled growth of CdS nanocrystals: Optical and photocatalytic activities. *New J. Chem., Vol. 39,* P. 9487-9497.

25 Flor, J., Marques de Lima, S.A. & Davalos, M.R. (2004). Effect of reaction time on the particle size of ZnO and ZnO: Ce obtained by a sol-gel method. *Prog. Colloid Polym. Sci., Vol. 128,* P. 239-243.

26 Sharma, K.N., Joshi, H., Prakash, O., Sharma, A.K., Bhaskar, R. & Singh, A.K. (2015). Pyrazole-Stabilized Dinuclear Palladium (II) Chalcogenolates Formed by Oxidative Addition of Bis [2-(4-bromopyrazol-1-yl) ethyl] Dichalcogenides to Palladium (II)–Tailoring of Pd–S/Se Nanoparticles. *Eur. J. Inorg. Chem., Vol. 29,* P. 4829-4838.

27 Deori, K., Ujjain, S.K., Sharma, R.K. & Deka, S. (2013). Morphology controlled synthesis of nanoporous Co3O4 nanostructures and their charge storage characteristics in supercapacitors. ACS Appl. *Mater. Interfaces, Vol. 5,* P. 10665-10672.

28 Coe, S., Woo, W.K., Bawendi, M. & Bulovic, Y. (2002). Electroluminescence from single monolayers of nanocrystals in molecular organic devices. *Nature, Vol. 420,* P. 800-803.

29 Ajibade, P.A. & Botha, N.L. (2017). Synthesis, Optical and Structural Properties of Copper Sulfide Nanocrystals from Single Molecule Precursors. *Nanomaterials, Vol. 7,* P. 32.

30 Lot, M., Machani, T., Rossi, D.P. & Plass, K.E. (2011). Alpha-Chalcocite Nanoparticle Synthesis and Stability. *Chem. Mater., Vol. 23,* P. 3032-3038.

31 Williamson, C.B., Nevers, D.R., Hanrath, T. & Robinson, R.D. (2015). Prodigious Effects of Concentration Intensification on Nanoparticle Synthesis: A High-Quality, Scalable Approach. *J. Am. Chem. Soc., Vol. 137,* P. 15843-51.

32 Yao, Y. (2018). Reaction Mechanism and Size dependent Electrochemical Properties Study of $Cu_{2-x}S$ Versus Li. *A Thesis of Master of Science of Cornell University*, 85 p.

33 Lu, Q., Gao, F. & Zhao, D. (2002). One-Step Synthesis and Assembly of Copper Sulfide Nanoparticles to Nanowires, Nanotubes, and Nanovesicles by a Simple Organic Amine-Assisted Hydrothermal Process. *Nano Lett., Vol. 2*, P. 725-728.

М.М. Кубенова, К.А. Кутербеков, М.Х. Балапанов, Р.Х. Ишембетов, К.Ж. Бекмырза, А.М. Кабышев, Ш. Афрозе, Р.Ш. Палымбетов, Ж.А. Мұханова, Е. Шукалов

Термоэлектрлік генераторлар мен натрий-ионды аккумуляторларға арналған жаңа нанокристалды халькогенидті материалдарды синтездеу мәселелерін талдау

Мақалада термоэлектрлік генераторлар мен натрий-ионды аккумуляторларға арналған жаңа нанокристалды халькогенидті материалдарды синтездеу мәселелері талданған. Практикалық электродтар үшін халькогенидті материалдарды синтездеудің оңтайлы технологиясы синтез мақсаттарына байланысты. Физика-химиялық және басқа да қасиеттерді зерттеу үшін аз мөлшерде жаңа халькогенидті материалды синтездеу вакуумда немесе тазартылған инертті газ атмосферасында тікелей қатты фазалы реакция әдісімен оңтайлы жүргізіледі. Бұл әдіс сенімдірек және әртүрлі еріткіштер мен прекурсорларды пайдалану кезінде сөзсіз қоспасыз таза өнімді алуға мүмкіндік береді. Сонымен қатар, ол тұрақты синтез режиміне сәйкес алынған қосылыстардың қасиеттерінің тұрақтылығымен ерекшеленеді. Синтез режимдері, реагенттер, кейінгі өңдеу нақты материалға байланысты. Бұл жұмыста калий және натрий гидроксидтері қоспасының балқыма ортасындағы қорытпаларды синтездеу негізгі қолданылатын әдістердің бірі. Осы гидроксидтердің концентрациясының белгілі бір қатынасында балқу температурасы 165 °C дейін төмендейді, бұл қорытпадағы тұздар арасында алмасу реакцияларын жүргізуге мүмкіндік береді. Синтез температурасының төмендеуі, судың қосылуы және күйдіру уақытының қысқаруы нәтижесінде пайда болған халькогенид бөлшектерінің мөлшерін бірнеше нанометрге дейін азайтуға мүмкіндік береді.

Кілт сөздер: термоэлектрлік материалдар, мыс сульфиді, кристалдық құрылым, өткізгіштік, диффузия, жылу өткізгіштік, Зебек коэффициенті, суперионды өткізгіштер.

М.М. Кубенова, К.А. Кутербеков, М.Х. Балапанов, Р.Х. Ишембетов, К.Ж. Бекмырза, А.М. Кабышев, Ш. Афрозе, Р.Ш. Палымбетов, Ж.А. Мұханова, Е. Шукалов

Анализ проблем синтеза новых нанокристаллических халькогенидных материалов для термоэлектрических генераторов и натрий-ионных аккумуляторов

В статье проанализированы проблемы синтеза новых нанокристаллических халькогенидных материалов для термоэлектрических генераторов и натрий-ионных аккумуляторов. Оптимальная технология синтеза халькогенидных материалов для электродов практического применения зависит от целей синтеза. Синтез нового халькогенидного материала в малых количествах для изучения физико-химических и других свойств оптимально проводить методом прямой твердофазной реакции в вакууме или в атмосфере очищенного инертного газа. Этот метод более надежен и позволяет получить чистый продукт, не содержащий примесей, неизбежных при использовании различных растворителей и прекурсоров. Кроме того, его отличает стабильность свойств получаемых соединений при соблюдении постоянного режима синтеза. Режимы синтеза, реагенты, постобработка зависят от конкретного материала. В настоящей работе в качестве одного из основных используется метод синтеза сплавов в среде расплава смеси гидроксидов калия и натрия. При определенном соотношении концентраций этих гидроксидов температура плавления снижается до 165°C, что позволяет проводить обменные реакции между солями в расплаве. Снижение температуры синтеза, добавление воды и сокращение времени отжига позволяют уменьшить размер образующихся частиц халькогенидов до нескольких нанометров.

Ключевые слова: термоэлектрические материалы, сульфид меди, кристаллическая структура, проводимость, диффузия, теплопроводность, коэффициент Зеебека, суперионные проводники.

DOI 10.31489/2023PH3/107-118

UDC 538.9;621.383

T.M. Mukametkali[1], X.S. Rozhkova[1], A.K. Aimukhanov[1], B.R. Ilyassov[2], K. Apshe[1], A.K. Zeinidenov[1*]

[1] Karaganda University of the name of academician E.A. Buketov, Scientific Center of nanotechnology and functional nanomaterials, Karaganda, Kazakhstan;
[2] Astana IT University, Expo C1, Astana, Kazakhstan
([*]E-mail address: a.k.zeinidenov@gmail.com)

The effect of the $CH_3NH_3PbCl_xI_{3-x}$ perovskite layer thickness and grain size on its electrophysical and optical properties

Lead halide perovskite $CH_3NH_3PbCl_xI_{3-x}$ thin films are widely used as photoactive layers in perovskite solar cells. $CH_3NH_3PbCl_xI_{3-x}$ is a low band gap semiconductor with a broad absorption spectrum and a high conductivity showing excellent compatibility with exciting hole and electron selective layers in terms of electronic energy alignment, which provide efficient charge generation, separation and transport in perovskite solar cells. In this paper, $CH_3NH_3PbCl_xI_{3-x}$ layers were deposited on the TiO_2 surface by one step spin-coating technique from a methylammonium iodide (MAI) and lead chloride ($PbCl_2$) solution. To prepare the perovskite solution, $PbCl_2$ (Sigma-Aldrich)230 mg of $PbCl_2$ and 394 mg of MAI were dissolved in 1 ml of N, N-Dimethylformamide (Sigma-Aldrich) solvent. As expected, the elevation of the spin-coating rate resulted in $CH_3NH_3PbCl_xI_{3-x}$ thickness reduction, which should lead to a decrease in the R_3 resistance in $CH_3NH_3PbCl_xI_{3-x}$. However, the impedance spectroscopy revealed that with thickness reduction from 955 nm to 753 nm, the R_3 resistance of $CH_3NH_3PbCl_xI_{3-x}$ declines from about 2590 Ω to 2258 Ω reaching the minimum value at 505 nm. The further decrease in $CH_3NH_3PbCl_xI_{3-x}$ thickness increased $CH_3NH_3PbCl_xI_{3-x}$ film resistance. The study of $CH_3NH_3PbCl_xI_{3-x}$ absorbance and luminescence spectra showed that the change in $CH_3NH_3PbCl_xI_{3-x}$ defect density occurred, which explains the decrease in $CH_3NH_3PbCl_xI_{3-x}$ resistance. According to the absorbance and luminescence spectroscopy study, the $CH_3NH_3PbCl_xI_{3-x}$ thickness reduction led to a decrease in the density of interstitial $CH_3NH_3PbCl_xI_{3-x}^+$ defects. $CH_3NH_3PbCl_xI_{3-x}^+$ species form deep levels trapping free electrons and as a result, increasing $CH_3NH_3PbCl_xI_{3-x}$ resistance. The PSCs based on a 505 nm thick $CH_3NH_3PbCl_xI_{3-x}$ layer showed the highest performance with the improved short current density and fill factor. The champion device had a power conversion efficiency of 9.92 %.

Keywords: Perovskite solar cells, photoactive layer, $CH_3NH_3PbCl_xI_{3-x}$, copper phthalocyanine, iodine ions, impedance meter, electron transport layer, hole transport layer.

Introduction

Organic-inorganic metal halide materials with a perovskite structure are at the stage of intensive studies. Hybrid perovskites are direct-gap semiconductors with a unique set of optical and electronic properties, which makes them practically ideal materials for photovoltaics and optoelectronics. The power conversion efficiency (PCE) of perovskite solar cells (PSCs) has reached 25.7 % [1]. The high PCE in combination with inexpensive fabrication methods makes PSCs the most promising devices for modern photovoltaics. They have become the main competitor to traditional inorganic solar cells [2].

Organic-inorganic metal halide perovskites have bipolar conductivity, which allows effective transport and separation of electrons and holes at perovskite/electron transport layer (ETL) and perovskite/hole transport layer (HTL) interfaces. The electronic energy level consistency at the interface perovskite/charge selective layer (ETL and HTL) plays crucial role for the efficient extraction of charge carriers from the perovskite.

For effective hole extraction, VBM (valence band maximum) level in HTL should be slightly higher than VBM level in the perovskite. In addition, a higher position of CBM (conduction band minimum) level in HTL relative to CBM level in the perovskite blocks electrons and prevents electron transport to the anode [3, 4]. Recent studies have shown that the charge transfer properties at the perovskite/HTL interface are a major factor limiting the efficiency and stability of PSCs [3].

In recent years, improvements in the crystallinity and morphology of the perovskite layers have led to further boost in PCE of PSCs. However, more deep and advanced studies are still needed to optimize charge transfer processes in PSCs in order to minimize charge recombination, eliminate hysteresis and to increase device stability. The perovskite layer's crystallinity, uniformity, roughness and thickness are critical

parameters to control during the film deposition. Obtaining uniform, smooth and pin-holes and crack free perovskite layer are necessary to fabricate high efficient devices. Currently there are two solution processable deposition techniques of perovskite thein films: one step and two-step sequential deposition techniques. Perovskite thin films deposited by the one-step method have large grains, however the film surface is rough and they have relatively high defect density [4]. Kim et al. demonstrated a two-step sequential deposition method, which can alleviate challenges inherent the one-step methods. PSCs fabricated by Kim et al. showed PCE of around 15 % [5]. Except, the solution processable methods, there are other deposition methods, which also demonstrates high efficient PCSs. The Liu et al. reported planar PCSs with PCE of 15.4 % where refers to uniform perovskite layers were deposited by a sputtering technique [6]. It is very easy to study the morphology of the thin film.

The morphology and structure of the perovskite thin films are very sensitive to the synthesis conditions, such as nature of precursors and solvents, deposition and annealing temperature and environment, and a deposition rate [4-7]. Recently, highly smooth perovskite thin films with high crystallinity were obtained by annealing in mixed solvent vapor at room temperature, and PCSs showed PCE of 16.4 % [8]. In 2015, Ko et al. reported PCSs with PCE up to 15.76 % by keeping the substrate temperature at the range of 40 °C-60 °C to control the perovskite layer crystallization [9]. All of these studies imply that the crystallinity and morphology of the perovskite layers are very important to fabricate high-performance solar cells.

In the last few years, record PCE of PSCs has increased from 3.8 % to more than 20 % [7-11]. Compared to other types of solar cells, PCSs have many promising advantages. Compared to silicon-based solar cells, the mass production cost of PSCs will be lower. At the same level of energy conversion efficiency, HPSCs cost only 1/20th the cost of silicon-based solar cells. Currently, record efficiency of PSCs is 25.2 %, which is close to the efficiency of silicon-based solar cells (~27.1 %), and PCE as high as 30 % are predicted for them [10].

With the great efforts of researchers and engineers around the world, PCSs efficiency has now set a record for thin-film solar cells. Structure engineering, morphology optimization and interface modification have been the main research focus to ensure the high efficiency of PSC [8-10]. The morphology and degree of crystallinity of the perovskite films were found to be crucial factors for the development of highly efficient and stable solar cells [11]. The main goal of optimization studies is to deposit highly crystalline perovskite films with large grains and pin-holes free. This is accomplished by optimizing deposition conditions: solution concentration and temperature, drying and annealing conditions [12-14]. In this paper, we also demonstrate the importance of obtaining high-quality perovskite thin films by optimizing crystallization process. Because the morphology of the perovskite absorber thin film is one of the most important factors affecting the overall power, and conversion efficiency of perovskite solar cells [15-16]. To improve the homogeneity of the film, efforts are made to improve the crystallization of the perovskite shell, and these processes should be well understood and studied [17-20].

Methods of making perovskite thin films with low cost, easy energy conversion, quick preparation, and easy application have been studied [21-22]. Therefore, the preparation methods are optimized for growing larger perovskite crystals, improving a homogeneous and pore-free thin film and a closer arrangement of crystal grain boundaries for better interfacial bonding. In this research paper, we investigated the optimization of perovskite morphology to achieve highly efficient and stable perovskite solar cells.

In this work, we optimize the deposition conditions of $CH_3NH_3PbCl_xI_{3-x}$layers, and in addition, study the effect of double hole transport layers based on CuPc and MoO_3 on PSCs performance. The use of CuPc and MoO_3 as HTLs in PSCs will significantly reduce the cost of perovskite solar panels. The optimization and using double HTL led to enhanced absorption and significantly the growth of the current density. The champion device revealed PCE as high as 9.92 %.

Materials and Methods

Sample preparation and deposition process

Solar Cell Fabrication. Perovskite solar cells were fabricated on glass substrates coated with an FTO layer (15 Ohm/cm^2). FTO serves as an external electrode (cathode). First, substrates were thoroughly cleaned in acetone, hot deionized water, and 2-proponal followed by UV-ozone treatment. For the electron transport layer, a TiO_2 sol-gel solution prepared, at first, 15 mL of the aqueous solutions of titanium VI isopropoxide(TTIP)(Ti[$OCH(CH_3)_2$]$_4$ 99.999 % purity, Sigma-Aldrich, USA) was slowly added to 30 mL of acetic acid (HCOOH 99.9 % purity, Sigma-Aldrich, USA) in a three-neck flask, and the mixture was stirred for 5 minutes to avoid agglomeration. The mixture of deionized water (4 mL) and isopropanol

($CH_3CH(OH)CH_3$ 99.9 %, Sigma-Aldrich, USA) (15 mL) was added dropwise to the solution and then stirred vigorously for another 10 minutes. After mixing the solution, 4 mL of nitric acid (HNO_3) was added to the solution as a stabilizer, and the mixture was further subjected to vigorous stirring for 20 minutes. TiO_2 Nano solution formed from the hydrolysis and condensation reactions of titanium Alco oxide precursors. In the presence of water, titanium Alco oxide hydrolyzed and subsequently polymerized to form 3-dimensional TiO_2 nanoparticles, which dispersed on the FTO glass substrates and spun at 5000 rpm. Further, the spin-coated pre-TiO_2 film was annealed at a temperature of 500℃ for 60 minutes to obtain crystalline a TiO_2 layer.

Perovskite Materials. In the next step, a photoactive perovskite layer was deposited on the TiO_2 surface by one step spin-coating technique from a methylammonium iodide (MAI) and lead chloride ($PbCl_2$) solution. To prepare the perovskite solution, $PbCl_2$ (Sigma-Aldrich)230 mg of $PbCl_2$ and 394 mg of MAI were dissolved in 1 ml of N, N-Dimethylformamide (Sigma-Aldrich) solvent. The resulting solution was stirred on a magnetic stirrer at 70 °C for 2 hours to get a uniform solution. The perovskite solution was spin-coated at 2000, 3000, 4000, 5000, and 6000 rpm. The perovskite layer was annealed for 2 hours at a temperature of 90 °C to form a crystalline perovskite layer. The crystallization process was accompanied by a change in the color of the film from yellow to dark brown. All steps including perovskite formation carried out in a glove box filled with nitrogen.

Composition of HTM. After the perovskite layer formation step was done, copper phthalocyanine (CuPc) serving as a hole transport layer (HTL) was deposited on the perovskite surface. HTL with a thickness of 80 nm was deposited by thermal evaporation of CuPc powder (Sigma-Aldrich) at a vacuum level of 10^{-3} Pa. Further, a 30 nm MoO_x layer was thermally evaporated from MoO_3 (Borun New Material Technology Co., Ltd.) on the CuPc surface at the vacuum level of 10^{-2} Pa. Finally, an Ag electrode (anode) with a thickness of 100 nm thermally evaporated at a vacuum of 10^{-3} Pa.

Structural formulas of CuPc, MAI, and $PbCl_2$, a diagram of perovskite solar cell fabrication steps (b), and PSCs structure with functional layers' energy diagrams are shown in Figure 1.

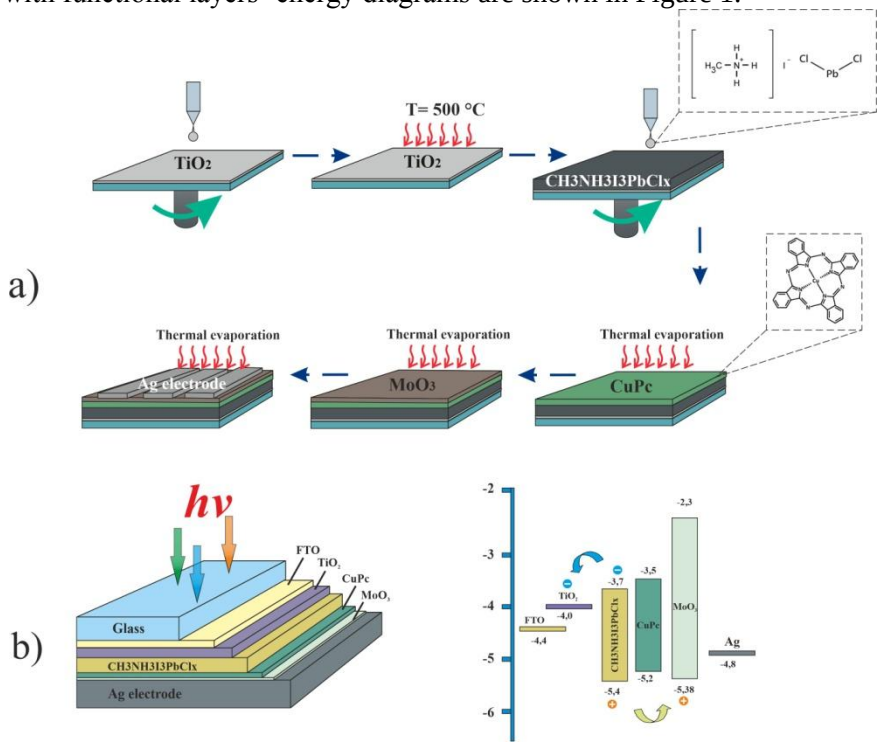

Figure 1. Structural formulas (a), a scheme of perovskite solar cell fabrication steps (b) and PSCs structure with functional layers' energy diagrams

Analysis methods

The surface topography and thickness of the samples were probed by a JEOL JSPM-5400 atomic force microscope (AFM). The AFM data were processed by Gwyddion Data-Processing Software, a modular program for SPM (scanning probe microscopy) data visualization and analysis. To measure the local current

distribution, an AFM SolverP47 (NT-MDT) was used. When measuring the current, a voltage was applied to the sample, while the conductive probe covered with a gold film was grounded. The surface topography and surface standard deviation (rms) were measured in the semi-contact mode (NSC14 probe, Micromash), and the current was measured in the contact mode (CSC37/Au probe, Micromash).

The thickness of the deposited PSCs layers was measured using a scanning electron microscope (SEM, MIRA 3 LMU, Tescan).

The absorption spectra of the samples were measured by an AvaSpec-ULS2048CL-EVO spectrometer (Avantes). A combined deuterium-halogen light source AvaLight-DHc (Avantes) with an optical range of 200–2500 nm was used as a light source.

For thermal deposition, the CY-1700x-spc-2 vacuum sputtering unit (Zhengzhou CY Scientific Instruments Co., Ltd) was used.

The photoluminescence decay kinetics was measured on a pulsed spectrofluorometric with picosecond resolution and registration in the photon-counting mode.

The impedance spectra were measured by a P45X potentiostat-galvanostat with an FRA module. Current-voltage (I-V) characteristics of solar devices were measured with PVIV-1A I-V Test Station under the light illumination from Sol3A Class AAA Solar Simulator (Newport).

Results and Discussion

Structural analysis of the prepared films

Figure 2 shows the top and cross sectional SEM images of perovskite thin films deposited at different spin-coating speeds. As can be seen from SEM images, the surface morphology of the perovskite filmsvaries with increasing the rotation speed (Figures 2a-2c). At lower speeds (2000-4000 rpm), films have irregular grain sizes and have high roughness. At higher speeds, the distribution of grain sizes becomes significantly narrower and it is noticeable that films become smoother (more flat) (Figure 2d-e). Figure 2f shows the dependence of the thickness of the perovskite films on the rotation speed. As it was expected the film thickness decreases with increasing in the rotation speed.

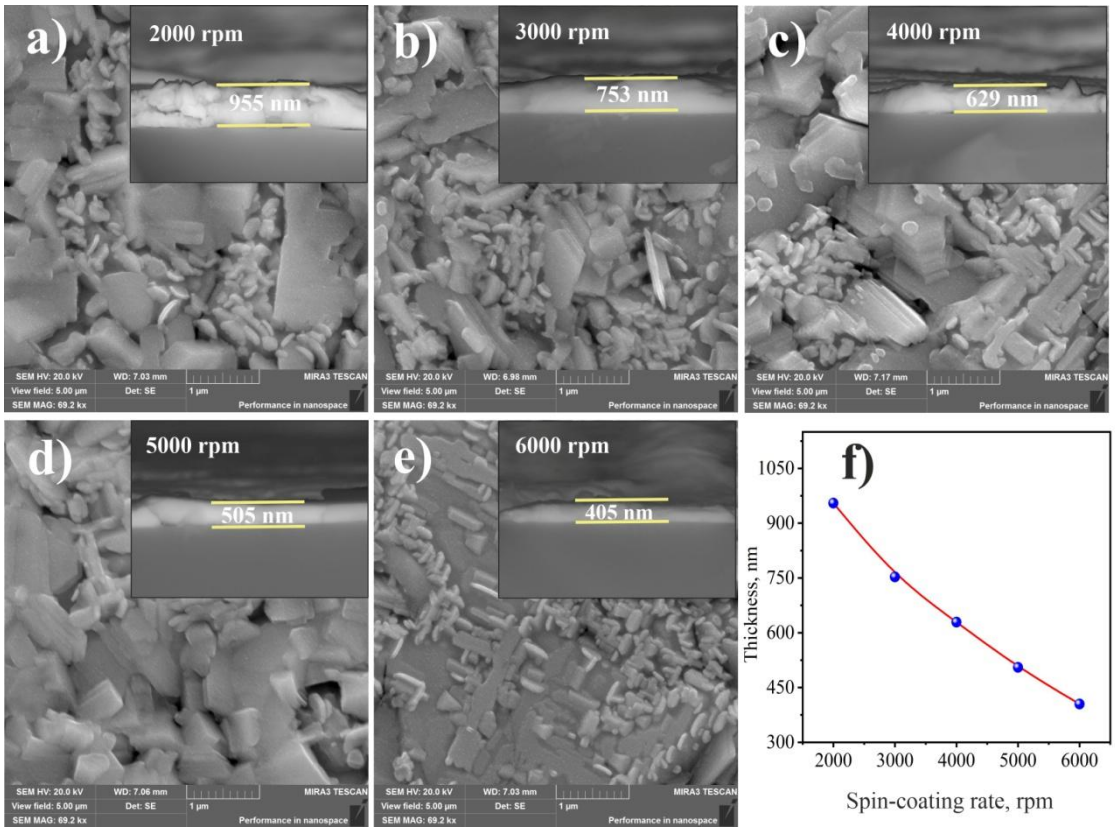

Figure2. SEM images of perovskite films deposited at different spin speeds (a-e) and their thicknesses (f).

Figure 3 shows the AFM images of perovskite films deposited at different rotation speeds. The AFM images are consistent with SEM data. In general, the film roughness decreases as spin-coating rotation speed increases. The observed pores in the films are associated with the evaporation of the solvent during the drying of the films. With an increase in the rotation speed, a structure appears on the surface of the film with characteristic sizes of regions of several hundred nanometers (Figures 3a-3e). The appearance of such a structure can be explained by the FTO substrate surface influence.

Figure 3f shows the dependence of the film surface roughness (RMS) on the rotation speed. As it was expected the surface roughness falls as the rotation speed increases. However, it should be noted that we observe a slight growth in thoroughness at 6000 rpm (Table 1).

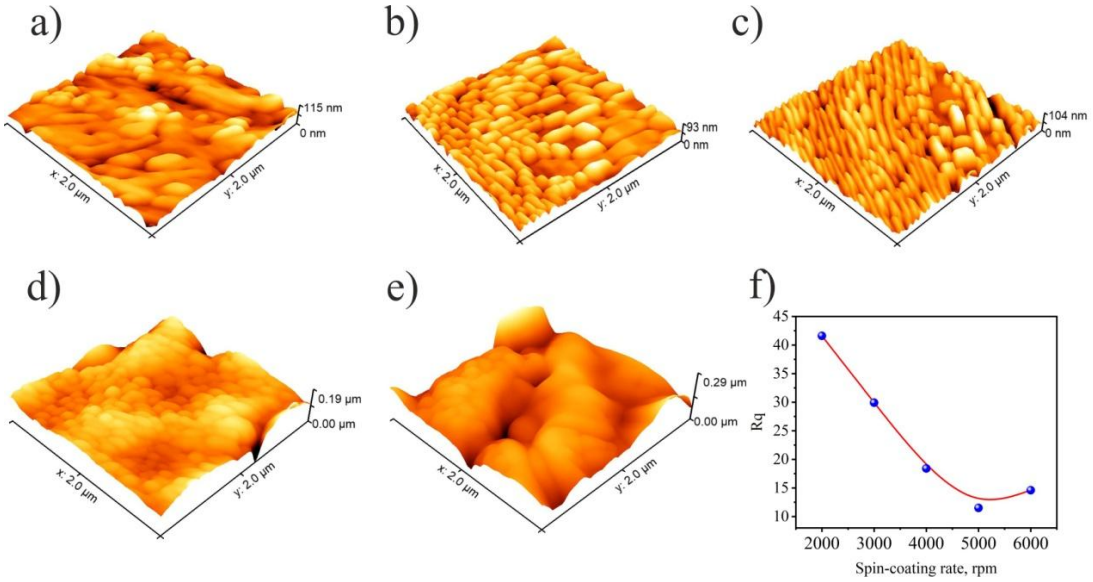

a) 2000 rpm.; b) 3000 rpm.; c) 4000 rpm.; d) 5000 rpm.; e) 6000 rpm.

Figure 3. AFM images of perovskite thin films deposited at different rotation speeds

Table 1

Perovskite film roughness and components surface size

Spin-coating rate, rpm	Layer thickness (t), nm	R_q, nm	$D_{ave.}$, nm
2000	955	41.6	200
3000	753	29.9	220
4000	629	18.4	250
5000	505	11.5	162
6000	405	14.6	120

Optical properties

Figure 4a shows the absorption spectra of the $CH_3NH_3PbCl_xI_{3-x}$ photoactive layer. That's seen from the obtained spectra, absorptions are located at 300 — 700 nm. As known, $CH_3NH_3PbCl_xI_{3-x}$ is a well-absorbing photocell, which has strong absorption in the visible ranges [23, 24]. When measuring the absorption spectra of $CH_3NH_3PbCl_xI_{3-x}$. it was found that with increasing thickness, the maximum of the absorption spectrum shifts from the short-wavelength to the long-wavelength region λ_{max}= 478 nm at a thickness of 400 nm, λ_{max}= 519 nm at a thickness of 505 nm, λ_{max} = 524 nm at a thickness of 640 nm, λ_{max}= 540 nm at a thickness of 753 nm, λ_{max}= 630 nm at a thickness of 955 nm. This shift to the short wavelength region is associated with a change in the surface structure of the $CH_3NH_3PbCl_xI_{3-x}$ films. Figure 4c shows the luminescence spectra of $CH_3NH_3PbCl_xI_{3-x}$ films with different thicknesses. As can be seen from the figure, when $CH_3NH_3PbCl_xI_{3-x}$ films are photoexcited at a wavelength of 650 nm, changes in the luminescence intensity are observed. The maximum luminescence intensity of $CH_3NH_3PbCl_xI_{3-x}$ films with a thickness of 955 nm was observed at 773 nm (1.6 eV).

For $CH_3NH_3PbCl_xI_{3-x}$ films with a thickness of 955 nm, a luminescence peak is observed at a wavelength of λ_{max}= 773 nm and a spectral half-width of FWHM λ=53 nm; 773 nm and spectral half-width FWHM λ=50 nm, films with a thickness of 505 nm are observed λ_{max}= 773 nm and spectral half-width FWHM λ=51 nm, films with a thickness of 405 nm are seen λ_{max}= 774 nm and spectral half-width FWHM λ=51 nm. The band gap was calculated from the intrinsic absorption edge of the UV and visible spectra. The band gap of the $CH_3NH_3PbCl_xI_{3-x}$ films was estimated using the Tauc Plot method. As can be seen from the figure, the $CH_3NH_3PbCl_xI_{3-x}$ film with a thickness of 405 nm has a band gap of about E_g=1.57 eV. With an increase in film thickness from 505 and 629 nm, an increase in the band gap of $CH_3NH_3PbCl_xI_{3-x}$ films is observed, respectively, E_g=1.58 eV and E_g=1.59 eV. A further increase in the thickness of the films 753 and 955 nm does not change the band gap E_g=1.57 eV (Figure 4b). Optical characteristics of $CH_3NH_3PbCl_xI_{3-x}$ films are presented in Table 2.

For hybrid (X = I, Cl) perovskite (Fig. 4a), the optical absorption band between 2.5 and 2.7 eV is due to the Pb-Pb intracomponent transition. When these transitions are further separated into the most important contributions of angular particles, the results show that these transitions mainly came from s (Pb)-p (Pb) and with a smaller proportion of s (I) -p(I) and p(Pb)- p(I). Following our results, this band was attributed [25] to the transition from Pb2+(6s) to Pb2+(6p). Our results also agree with the results of [26], in which three peaks appear in the absorption spectra at approximately 1.65, 2.20, and 3.10 eV. The first peak at about 1.65 eV is mainly associated with the excitation of s(Pb)-p(Pb). The second, with a maximum of about 2.20 eV, is also mainly due to the s(Pb)-p(Pb) transitions with a smaller contribution from the s(I)-p(I) excitation. The last peak at about 3.10 eV is due to similar contributions from s (Pb)-p (Pb), s (I)-p (I), and p (Pb)-p (I).

Further, we studied the dynamics of the perovskite quality and crystallization process depending on photoactive layer thickness by observing the photoluminescence spectra of the perovskite. In Figure 4c photoluminescence spectra of perovskite layers deposited on glass substrates with various photoactive layer thicknesses are illustrated. The photoluminescence band of the perovskite has a maximum at λ_{max} = 785 nm. As seen in PL spectra, the luminescence intensity of the perovskite layer deposited on the spin rate at 5000 rpm had the highest PL intensity. It has indicated that the photoactive layers' best quality and crystallization rate reached a thickness of 505 nm.

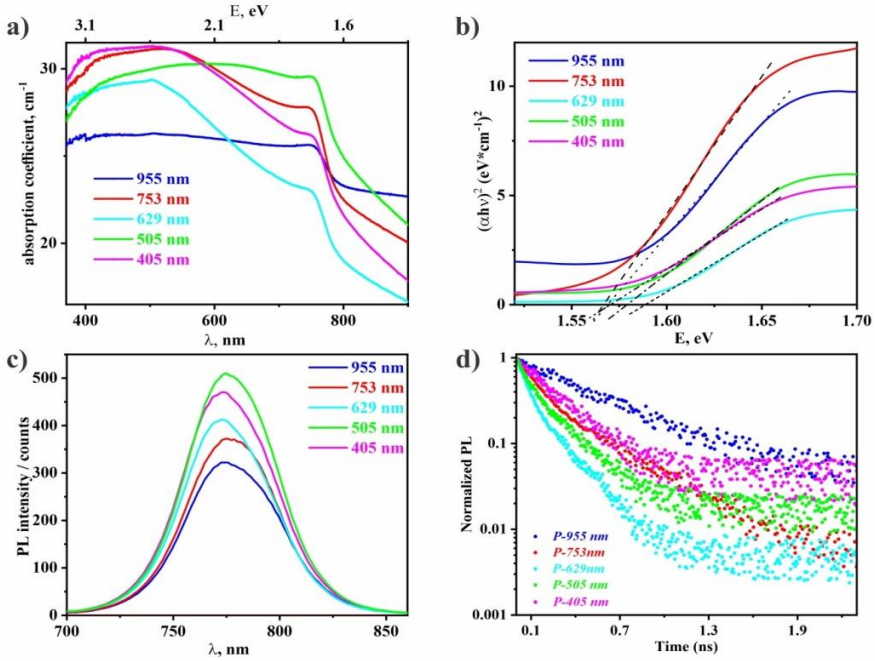

Figure 4. Perovskite films absorbance coefficient (a), optical bandgap (b), PL spectra (c), and TRPL decay plot (d)

We studied the dynamics of charge transfer from a perovskite layer to ETL and how the charge transfer depends on photoactive layer thickness by the time-resolved photoluminescence (TRPL) technique was used to compare PL intensity decays and evaluate PL lifetimes (τ_{PL}) in the perovskite layers with different thicknesses deposited on TiO_2 layer. As seen from TRPL (Figure 4d) and Table 2, the PL intensity decay occurs faster in the perovskite layer with a thickness of 505 nm. Similarly with the PL intensity quenching, at

first, PL lifetime decreases with reducing perovskite layer thickness reaching a minimum value of ~0.8 ns at a perovskite layer thickness of 505 nm, which confirms that effective charge transfer occurs from the perovskite into ETL at the perovskite layer thickness of ~ 500 nm. However, at the lower thickness, the thickness decay time increases indicating the worsened charge transfer.

Table 2

PL, optical bandgap, and TRPL characteristics

t, nm	Maximum PL λ, nm	FWHM λ, nm	Bandgap, eV	τ_{PL}, ns
955	772.66	52.93	1.57	2.3
753	775.49	50.42	1.57	1.9
629	772.66	50.01	1.58	1.1
505	773.23	51.31	1.59	0.8
405	774.36	50.05	1.57	1.0

Photoelectrical characterizations

The current-voltage characteristics and the energy diagram of the components of perovskite solar cells are shown in Figure 5. Figure 5a shows that PSCs with $CH_3NH_3PbCl_xI_{3-x}$ films at a deposition rate of 2000 rpm have the worst photovoltaic parameters, which are due to a low fill factor (FF) of 47.27 %. Cells with $CH_3NH_3PbCl_xI_{3-x}$ films obtained at rotation speeds of 3000 rpm, 4000 rpm, and 6000 rpm show the best solar-to-electrical energy conversion efficiency, which are η=7.93 %, η=8.83 %, and η=8.67 %, respectively, compared to the efficiency of PSCs at 2000 rpm (η=7.13 %). The maximum value of the increase in the CVC parameters is observed for the composite cell obtained at rotation speeds of 5000 rpm, the short circuit current density (J_{sc}) increased by 30 %, and the efficiency value was 9.92 %.

The energy diagram was constructed according to the data from [25, 26]. According to these works, the position of the valence band maximum (VBM) of TiO_2 is 4.0 eV, $CH_3NH_3PbCl_xI_{3-x}$ is 5.4 eV, the VBM for MoO_3 films is 5.38 eV, and for CuPc films the VBM is 5.2 eV. As can be seen from the diagram, the energy levels of the $CH_3NH_3PbCl_xI_{3-x}$ and CuPc MIGs are in good agreement, which should ensure efficient injection of holes from the photoactive layer (PS) into CuPc. The CVC parameters of solar cells are given in Table 3.

However, it is not limited and further optimization is needed to boost photovoltaic performance and eliminate hysteresis (Fig. 5b). We also studied the reproducibility of the PCE of our devices. It fabricated 10 devices for each type of PSC under the same conditions. Figure 5c shows the statistical deviation of PCE from the average value.

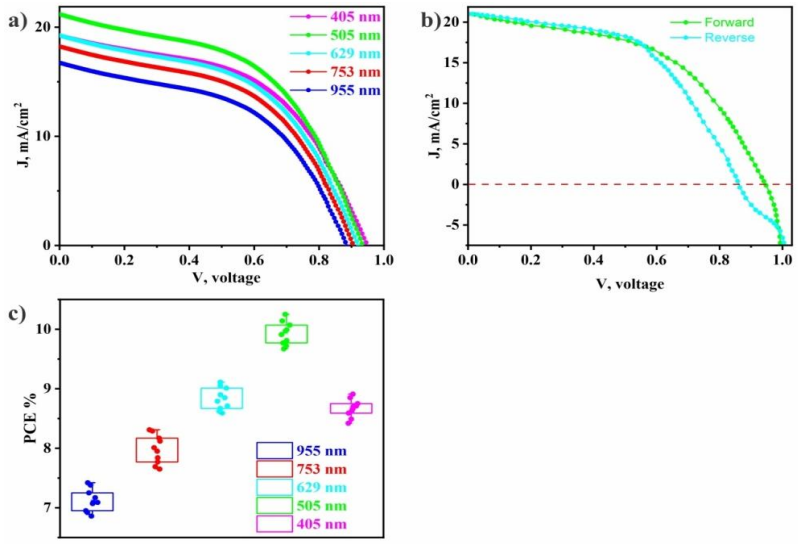

Figure 5. Current-voltage characteristics of perovskite solar cells a), current-voltage characteristics of the champion device for forward and reverse scans b), and PCE statistics c)

Table 3

Parameters of current-voltage characteristics of perovskite solar cells

t, nm	J_{sc} mA/см^2	U_{oc} V	J_{max} mA/см^2	U_{max} V	*FF* %	η %
955	16.96	0.89	11.69	0.61	47.27	7.13
753	18.14	0.90	12.67	0.63	48.87	7.98
629	19.33	0.92	13.58	0.65	48.05	8.83
505	20.76	0.94	15.04	0.66	50.82	9.92
405	19.14	0.95	13.55	0.64	47.68	8.67

To understand the effects of perovskite thickness and defects on charge transfer processes, we used the impedance spectroscopy (IS) technique. IS responses of PSCs were measured in the dark at 0.8 V. In Figure 6 (a) IS spectra in Nyquist coordinates are presented. Dotted and solid lines represent the measured and fitted data, respectively. Overall, in IS spectra we observe two semicircles, one in a high-frequency (HF) region and another in a low-frequency (LF) region. Nowadays, the interpretation of IS spectra of PSCs is controversial [25–27], however, it is accepted that HF is attributed to charge transfer processes in PCSs, whereas R_3C_3 is related to electrochemical processes inside the perovskite layer.

The equivalent circuit shown in Figure 6 (a (insert)) was used to fit IS spectra. According to the works [28], R_1 is a series resistance of charge collectors ETL and hole collectors HTL. R_2C_2 characterizes perovskite/selective contact interfaces, and R_3C_3 is attributed to the slow electrochemical processes inside the perovskite absorber. We are interested in R_1 and R_2 due to these two resistances reflect the effect of perovskite thickness and R_3 reflects the electrochemical processes defects on charge transfer processes. In our work, all functional layers of PSCs, except the perovskite layer, were deposited under the same conditions and for this reason, the changes of R_1, R_2, and R_3 values are related significantly with changes of perovskite properties and HTL/perovskite/ETL interface quality.

Parameters affecting charge transfer processes in PSCs estimated from IS spectra are presented in Table 4. As seen from Table 4, with the reduction of perovskite thickness R_1 becomes lower by reaching a minimum value of 24.3 Ohms at the thickness of 505 nm, and with further thickness decrease it starts to grow. This trend in R_1 is consistent with trends in J_{SC} and FF confirming that by decreasing perovskite layer thickness, HTL/perovskite/ETL interface resistance should decrease, however, the increase of the intrinsic ionic defects density, observed from the absorbance and luminescence study, oppositely influences series R_1 resistance. The two competitive charge transport processes take place in perovskite: electron transport through the $CH_3NH_3PbCl_xI_{3-x}$ conduction band and electron trapping by deep trap levels formed by $CH_3NH_3PbCl_xI_{3-x}^+$ species. Therefore according to the IV and IS studies, the ideal $CH_3NH_3PbCl_xI_{3-x}$ layer thickness at which there is a balance between that competitive photo conversation and charge transport processes is about 505 nm for our deposition condition.

R_2 determines the charge transfer rate at the HLT/perovskite/ETL interface. We observe the increase of R_2, which imply on the electron–hole separation increases with the $CH_3NH_3I_3PbCl_x$ thickness reduction. The charge transfer rate at perovskite/ETL interface depends on the energy level alignment. As seen from Table 2, the decrease of $CH_3NH_3PbClxI_{3-x}$ layer thickness results to widening of $CH_3NH_3PbClxI_{3-x}$ bandgap, which may be due to the rise of the electron quasi-Fermi level. When $CH_3NH_3PbClxI_{3-x}$ electron quasi-Fermi level approaches the perovskite conduction band level the drive force becomes stronger and this will increase the electron transport rate. Additionally, R_2 increase can be associated with the decrease of the recombination rate in perovskite layer. R_3 decrease is associated with the decreased density of $CH_3NH_3PbCl_xI_{3-x}^+$ — related defects, which can form electron trap levels for the electron–hole separation.

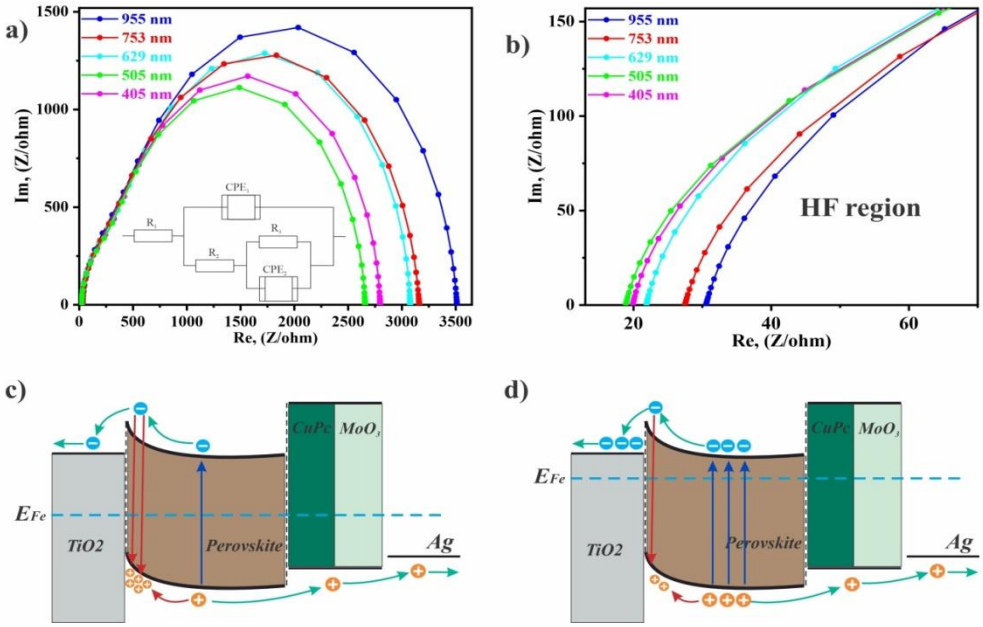

Figure 6. Nyquist impedance curves and equivalent circuit diagrams (insert) (a), increased high-frequency region curves (b), and photocurrent transformation and recombination mechanisms for perovskite solar cells(c), (d)

Figure 6c, d shows the PSCs' photocurrent transformation and recombination mechanisms. As seen in the figure, the sample illuminated electron-hole pairs that were photo-generated inside $CH_3NH_3PbCl_xI_{3-x}$(blue arrow). The holes are transferred to CuPc with MoO_3 (HTL), then transported to the metal contact. While the electrons are moving towards the TiO_2 (ETL), a consequence of the tunnel injection, the electrons will be transferred to the FTO, thus generating a current. However, perovskites have intrinsic ionic defects as iodine ions immigrate rapidly under operating conditions and accumulate at the TiO_2/perovskite interface because of the self-doping effect. These ions explain the trap levels near the valence band, where photo-generated holes accumulations to attract recombination (green arrows).

Decreasing the photoactive layer thickness to 505 nm leads to increases in the graduate of $CH_3NH_3PbCl_xI_{3-x}$ crystals. The increase in crystal size and graduates was the reduction of grain boundaries, which act as the source of mobile defects. Therefore, the light absorption cross-section increases, increasing photo generation and directly improving J_{sc}. Then, recombination decreases at the outer boundaries, resulting in a higher ability to accumulate electrons in the conduction band, which leads to an upward shift in the electron quasi-Fermi level and an increase in V_{oc} (see Figure 6 d). As a result, improving the quality of the TiO_2/perovskite film interface and perovskite/CuPc-MoO_3 films interface leads to a reduction in leak sources, which leads to an increase in FF. Thus, the quality of the photoactive layer simultaneously improves three photovoltaic parameters, which leads to a significant increase in photo conversion efficiency. The exponent n defines the deviation from the capacity ideal behavior and is related to the angle θ, p-capacity. Moreover, for n = 1, p has Farad units indicating that CPE behaves as an ideal capacitor.

Table 4

The value of charge transport parameters of perovskite solar cells

Thickness photoactive layer, nm	**R_s, Ω**	**R_2, Ω**	**R_3, Ω**	p_1	n_1	p_2	n_2
955	30.5	880	2590	$3\cdot10^{-9}$	0.95	$2.4\cdot10^{-8}$	0.93
753	27.5	915	2258	$6.2\cdot10^{-9}$	0.96	$5.7\cdot10^{-8}$	0.88
629	25.9	1003	1779	$2.6\cdot10^{-8}$	0.98	$4.5\cdot10^{-8}$	0.91
505	24.3	1069	1547	$2.5\cdot10^{-7}$	0.98	$1.6\cdot10^{-7}$	0.95
405	29.9	1051	1969	$1.3\cdot10^{-7}$	0.93	$9.1\cdot10^{-7}$	0.96

Conclusions

$CH_3NH_3PbCl_xI_{3-x}$ perovskite films were deposited by spin-coating technique from a methylammonium iodide (MAI) and lead chloride ($PbCl_2$) solution. The effect of the spin-coating rate on $CH_3NH_3PbCl_xI_{3-x}$ thickness and surface roughness was investigated. The $CH_3NH_3PbCl_xI_{3-x}$ films were used as photoactive layers for perovskite solar cells (FTO/TiO_2/$CH_3NH_3PbCl_xI_{3-x}$/CuPc/MoO_x/Ag). The deposition conditions of $CH_3NH_3PbCl_xI_{3-x}$ layer affect recombination resistance in PSCs. We observed two competitive effects on the $CH_3NH_3PbCl_xI_{3-x}$ resistance. As expected, the elevation of the spin-coating rate resulted in $CH_3NH_3PbCl_xI_{3-x}$ thickness reduction, which should lead to a decrease in $CH_3NH_3PbCl_xI_{3-x}R_3$ resistance. However, the impedance spectroscopy revealed that with thickness reduction from 955 nm to 753 nm, the R_3resistance of $CH_3NH_3PbCl_xI_{3-x}$ declines from about 2590Ω to 2258Ω reaching the minimum value at 505 nm. The further decrease in $CH_3NH_3PbCl_xI_{3-x}$ thickness increased $CH_3NH_3PbCl_xI_{3-x}$ film resistance. The study of $CH_3NH_3PbCl_xI_{3-x}$ absorbance and luminescence spectra showed that the change in $CH_3NH_3PbCl_xI_{3-x}$ defect density occurred, which explains the decrease in $CH_3NH_3PbCl_xI_{3-x}$ resistance. According to the absorbance and luminescence spectroscopy study, the $CH_3NH_3PbCl_xI_{3-x}$ thickness reduction led to a decrease in the density of interstitial $CH_3NH_3PbCl_xI_{3-x}^+$ defects. $CH_3NH_3PbCl_xI_{3-x}^+$ species form deep levels trapping free electrons and as a result, increasing $CH_3NH_3I_3PbCl_x$ resistance. The PSCs based on a 505 nm thick $CH_3NH_3PbCl_xI_{3-x}$ layer showed the highest performance with the improved short current density and fill factor. The champion device had a power conversion efficiency of 9.92 %. This work revealed that two competitive charge transport processes occur in $CH_3NH_3PbCl_xI_{3-x}$photoactive layer: electron transport through the $CH_3NH_3PbCl_xI_{3-x}$ conduction band and electron trapping by deep trap levels formed by $CH_3NH_3PbCl_xI_{3-x}^+$ species. The balance between these charge transport processes is about 505 nm for our deposition condition.

Acknowledgments

This research is funded by the Science Committee of the Ministry of Science and Higher Education of the Republic of Kazakhstan (Grant No. AP13067629).

References

1 Kojima, A., Teshima, K., Shirai, Y. & Miyasaka, T. (2009). Organometal Halide Perovskites as Visible-Light Sensitizers for Photovoltaic Cells, *J. Am. Chem. Soc.*, *131*, 6050-6051. https://doi.org/10.1021/ja809598r.

2 Bi, D., El-Zohry, A. M., Hagfeldt, A. & Boschloo, G. (2014). Improved Morphology Control Using a Modified Two-Step Method for Efficient Perovskite Solar Cells, *ACS Appl. Mater. Interfaces*, *6*, 18751-18757. https://doi.org/10.1021/am504320h.

3 Bi, D., Moon, S.-J., Häggman, L., Boschloo, G., Yang, L., Johansson, E.M.J., Nazeeruddin, M.K., Grätzel, M. & Hagfeldt, A. (2013). Using a two-step deposition technique to prepare perovskite ($CH_3NH_3PbI_3$) for thin film solar cells based on ZrO_2 and TiO_2mesostructures, *RSC Adv.*, *3*, 18762-18766. https://doi.org/10.1039/C3RA43228A

4 Jeon, N.J., Noh, J.H., Yang, W.S., Kim, Y.C., Ryu, S., Seo J. & Seok, S.I. (2015). Compositional engineering of perovskite materials for high-performance solar cells, *Nature*, *517*, 476-480. https://doi.org/10.1038/nature14133.

5 Yang, W. S., Park, B.-W., Jung, E. H., Jeon, N.J., Kim, Y.C., Lee, D.U., Shin, S.S., Seo, J., Kim, E.K., Noh, J.H. & Seok, S.I. (2017). Iodide management in formamidinium-lead-halide–based perovskite layers for efficient solar cells, *Science*, *356*, 1376-1379. https://doi.org/10.1126/science.aan2301.

6 Burschka, J., Pellet, N., Moon, S. J., Humphry-Baker, R., Gao, P., Nazeeruddin M.K. & Gratzel, M. (2013). Sequential deposition as a route to high-performance perovskite-sensitized solar cells, *Nature*, *499*, 316-319. https://doi.org/10.1038/nature12340

7 Chen, Q., Zhou, H., Hong, Z., Luo, S., Duan, H.S., Wang, H.H., Liu, Y., Li, G. & Yang, Y. (2014). Interface engineering of highly efficient perovskite solar cells, *J. Am. Chem. Soc.*, *136*, 622-625. https://doi.org/10.1021/ja411509g

8 Snaith, H.J. (2013). Perovskites: The Emergence of a New Era for Low-Cost, High-Efficiency Solar Cells. *J. Phys. Chem. Lett.*, *4*, 3623-3630. https://doi.org/10.1021/jz4020162

9 Choi, K., Lee, J., Kim, H.I., Park, C.W., Kim, G., Choi, H., Park, S., Park, S.A. & Park, T. (2018). Thermally stable, planar hybrid perovskite solar cells with high efficiency, *Energy Environ. Sci.*, *11*, 3238-3247.https://doi.org/10.1039/C8EE02242A

10 Correa-Baena, J.P., Abate, A., Saliba, M., Tress, W., Jacobsson, T.J., Gratzel, M. & Hagfeldt, A. (2017). The rapid evolution of highly efficient perovskite solar cells, *Energy Environ. Sci.*, *10*, 710-727. https://doi.org/10.1039/C6EE03397K

11 Dubey, A., Adhikari, N., Mabrouk, S., Wu, F., Chen, K., Yang, S. & Qiao, Q. (2018). A strategic review on processing routes towards highly efficient perovskite solar cells, *J. Mater. Chem. A*, *6*, 2406-2431. https://doi.org/10.1039/C7TA08277K

12 Stolterfoht, M., Grischek, M., Caprioglio, P., Wolff, C. M., Gutierrez-Partida, E., Pena-Camargo, F., Rothhardt, D., Zhang, S., Raoufi, M., Wolansky, J., Abdi-Jalebi, M., Stranks, S. D., Albrecht, S., Kirchartz, T. & Neher, D. (2020). How To Quantify the

Efficiency Potential of Neat Perovskite Films: Perovskite Semiconductors with an Implied Efficiency Exceeding 28, *Adv Mater.*, *32*(17), 2000080. https://doi.org/10.1002/adma.202000080

13 Lu, J., Lin, X., Jiao, X., Gengenbach, T., Scully, A.D., Jiang, L., Tan, B., Sun, J., Li, B., Pai, N., Bach, U., Simonov, A.N. & Cheng, Y.-B. (2018). Interfacial benzenethiol modification facilitates charge transfer and improves stability of cm-sized metal halide perovskite solar cells with up to 20 % efficiency, *Energy Environ. Sci.*, *11*, 1880-1889. https://doi.org/10.1039/C8EE00754C

14 Wu, Z., Liu, Z., Hu, Z., Hawash, Z., Qiu, L., Jiang, Y., Ono, L.K. & Qi, Y. (2019). Highly Efficient and Stable Perovskite Solar Cells via Modification of Energy Levels at the Perovskite/Carbon Electrode Interface, *Adv. Mater.*, *31*, e1804284. https://doi.org/10.1002/adma.201804284

15 Christians, J.A., Schulz, P., Tinkham, J.S., Schloemer, T.H., Harvey, S.P., de Villers, B. J.T., Sellinger, A., Berry, J.J. & Luther, J.M. (2018). Tailored interfaces of unencapsulated perovskite solar cells for >1,000 hour operational stability, *Nat. Energy*, *3*, 68-74. https://doi.org/10.1038/s41560-017-0067-y

16 Feng, M., You, S., Cheng, N. & Du, J. (2019). High quality perovskite film solar cell using methanol as additive with 19.5 % power conversion efficiency, *Electrochim. Acta*, *293*, 356-363. https://doi.org/10.1016/j.electacta.2018.09.195

17 Jamal, M.S., Bashar, M.S., Hasan, A.K.M., Almutairi, Z.A., Alharbi, H.F., Alharthi, N.H., Karim, M.R., Misran, H., Amin, N., Sopian, K.B. & Akhtaruzzaman, M. (2018). Fabrication techniques and morphological analysis of perovskite absorber layer for high-efficiency perovskite solar cell: A review, *Renew. Sust.Energ. Rev.*, *98*, 469-488. https://doi.org/10.1016/j.rser.2018.09.016

18 Li, Y., Ji, L., Liu, R., Zhang, C., Mak, C.H., Zou, X., Shen, H.-H., Leu, S.-Y. & Hsu, H.-Y. (2018). A review on morphology engineering for highly efficient and stable hybrid perovskite solar cells, *J. Mater. Chem. A*, *6*, 12842-12875. https://doi.org/10.1039/C8TA04120B

19 AbdMutalib, M., Aziz, F., Ismail, A.F., Wan Salleh, W.N., Yusof, N., Jaafar, J., Soga, T., Sahdan, M.Z. & Ludin, N.A. (2018). Towards high performance perovskite solar cells: A review of morphological control and HTM development, *Appl. Mater. Today*, *13*, 69-82. https://doi.org/10.1016/j.apmt.2018.08.006

20 Kim, H.S., Hagfeldt, A. & Park, N.G. (2019). Morphological and compositional progress in halide perovskite solar cells, *Chem. Commun.*, *55*, 1192-1200. https://doi.org/10.1039/C8CC08653B

21 Guo, Q., Yuan, F., Zhang, B., Zhou, S., Zhang, J., Bai, Y., Fan, L., Hayat, T., Alsaedi A. & Tan, Z. (2018). Passivation of the grain boundaries of $CH_3NH_3PbI_3$ using carbon quantum dots for highly efficient perovskite solar cells with excellent environmental stability, *Nanoscale*, *11*, 115-124. https://doi.org/10.1039/C8NR08295B

22 van Franeker, J.J., Hendriks, K.H., Bruijnaers, B.J., Verhoeven, M.W.G.M., Wienk, M.M. & Janssen, R.A.J. (2017). Monitoring Thermal Annealing of Perovskite Solar Cells with In Situ Photoluminescence, *Adv. Energy Mater.*, *7*, 1601822. https://doi.org/10.1002/aenm.201601822

23 Agiorgousis, M.L., Sun, Y.Y., Zeng, H. & Zhang, S. (2014). Strong covalency-inducedrecombination centers in perovskite solar cell material $CH_3NH_3PbI_3$, *J. Am. Chem. Soc. 136*(41), 14570-14575. https://doi.org/10.1021/ja5079305

24 Fu, Y., Song, Q., Lin, T., Wang, Y., Sun, X., Su, Z., Chu, B., Jin, F., Zhao, H., Li, W. & Lee, C.S. (2017). High performance photomultiplication perovskite photodetectors with PC60BM and NPB as the interlayers, *Organic Electronics*, *51*, 200-206. https://doi.org/10.1016/j.orgel.2017.09.028

25 Hirasawa, M., Ishihara, T. & Goto, T. (1994). Exciton features in 0-, 2-, and 3-dimensional networks of [PbI6]4- octahedra, *J. Phys. Soc. Jpn.*, *63*, 3870-3879. https://doi.org/10.1143/JPSJ.63.3870

26 Im, J.-H., Lee, C.-R., Lee, J.-W., Park, S.-W. & Park, N.-G. (2011). 6.5 % efficient perovskite quantum-dot-sensitized solar cell, *Nanoscale*, *3*, 4088-4093, https://doi.org/10.1039/C1NR10867K

27 Yang, T., Wang, M., Cao, Y., Huang, F., Huang, L., Peng, J., Gong, X., Cheng, S.Z.D. & Cao, Y. (2012). Polymer Solar Cells with a Low-Temperature-Annealed Sol–Gel-Derived MoOx Film as a Hole Extraction Layer, *Adv. Energy Mater.*, *2*, 523-527. https://doi.org/10.1002/aenm.201100598

28 Wang, S., Sakurai, T., Wen, W. & Qi, Y. (2018). Energy Level Alignment at Interfaces in Metal Halide Perovskite Solar Cells, *Adv. Mater. Interfaces*, *5*(22), 1800260.https://doi.org/10.1002/admi.201800260

Т.М. Мұқаметқали, К.С. Рожкова, А.К. Аймуханов, Б.Р. Ильясов,
К. Апше, А.К. Зейниденов

$CH_3NH_3PbCl_xI_{3-x}$ перовскит қабатының қалыңдығы және түйіршіктер мөлшерінің электрофизикалық және оптикалық қасиеттеріне әсері

Қорғасын галогенді перовскит $CH_3NH_3PbCl_xI_{3-x}$ пленкалары перовскит күн батареяларында фотоактивті қабаттар ретінде кеңінен қолданылады. $CH_3NH_3PbCl_xI_{3-x}$ -жұтылу спектрі, энергияны түрлендіру тиімділігі және тыйым салынған аймақта өткізгіштігі кең жолақты жартылай өткізгіш, энергияны теңестіру тұрғысынан металлогалидті перовскиттерде жоғары фотоактивті қабатты көрсетеді, бұл электрондарды тасымалдау кезінде зарядтардың тиімді бөлінуін және электрондардың энергияның аз жоғалуын қамтамасыз етеді. Бұл жұмыста $CH_3NH_3PbCl_xI_{3-x}$ қабаттары метиламмоний йодидінен (MAI) және қорғасын хлориді (PbCl2) ерітіндісінен бір сатылы айналдыру әдісімен TiO2 бетіне жағылады. Перовскит ерітіндісін дайындау үшін PbCl2 (Sigma-Oldrich) 230 мг PbCl2 және 394 мг MAI 1 мл N, N-Диметилформамид (Сигма-Олдрих) еріткішінде ерітілді. Күтілгендей, айналдыру

жабыны жылдамдығының жоғарылауы $CH_3NH_3PbCl_xI_{3-x}$ қалыңдығының төмендеуіне әкелді, бұл $CH_3NH_3PbCl_xI_{3-x}$ R3 кедергісінің төмендеуіне әкелуі керек. Дегенмен, кедергі спектроскопиясы қалыңдығы 955 нм-ден 753 нм-ге дейін қысқарған кезде $CH_3NH_3PbCl_xI_{3-x}$ R3 кедергісі шамамен 2590 Ω-дан 2258 Ω-ге дейін төмендеп, 505 нм-де минималды мәнге жететіні анықталды. $CH_3NH_3PbCl_xI_{3-x}$ қалыңдығының одан әрі төмендеуі $CH_3NH_3PbCl_xI_{3-x}$ пленка кедергісін арттырды. $CH_3NH_3PbCl_xI_{3-x}$ жұтылу және люминесценция спектрлерін зерттеу $CH_3NH_3PbCl_xI_{3-x}$ ақаулық тығыздығының өзгеруі орын алғанын көрсетті, бұл $CH_3NH_3PbCl_xI_{3-x}$ кедергісінің төмендеуін түсіндіреді. Абсорбция және люминесценция спектроскопиясының зерттеуіне сәйкес, $CH_3NH_3PbCl_xI_{3-x}$қалыңдығының азаюы интерстициалды $CH_3NH_3PbCl_xI_{3-x}$ + ақауларының тығыздығының төмендеуіне әкелді. $CH_3NH_3PbCl_xI_{3-x}$ + түрлері бос электрондарды ұстайтын терең деңгейлерді құрайды және нәтижесінде $CH_3NH_3PbCl_xI_{3-x}$ кедергісін арттырады. Қалыңдығы 505 нм CH3NH3PbClxI3-x қабатына негізделген PSCs қысқа ток тығыздығы және толтыру коэффициенті жақсартылған ең жоғары өнімділікті көрсетті. Ең жақсы құрылғының қуатты түрлендіру тиімділігі 9,92 % болды.

Кілт сөздер: перовскит күн батареялары, фотоактивті қабат, $CH_3NH_3PbCl_xI_{3-x}$, мыс фталоцианин, йод иондары, импедансометр, электронды тасымалдау қабаты, кемтіктерді тасымалдау қабаты.

Т.М. Мукаметкали, К.С. Рожкова, А.К. Аймуханов, Б.Р. Ильясов,
К. Апше, А.К. Зейниденов

Влияние толщины и размера зерен на электрофизические и оптические свойства перовскитного слоя $CH_3NH_3PbCl_xI_{3-x}$

Пленки перовскита из галогенида свинца $CH_3NH_3PbCl_xI_{3-x}$ широко используются в качестве фотоактивных слоев в перовскитных солнечных элементах. $CH_3NH_3PbCl_xI_{3-x}$ представляет собой полупроводник с более узкой запрещенной зоной с широким спектром поглощения, эффективностью преобразования энергии и проводимостью, демонстрирующий превосходный фотоактивный слой в металлогалогенидных перовскитах с точки зрения выравнивания энергии, обеспечивающего эффективное разделение зарядов и меньшую потерю энергии электронами во время переноса электронов. В настоящей работе слои $CH_3NH_3PbCl_xI_{3-x}$ были нанесены на поверхность TiO_2 методом одноэтапного центрифугирования из раствора иодида метиламмония (MAI) и хлорида свинца ($PbCl_2$). Для приготовления раствора перовскита $PbCl_2$ (Sigma–Aldrich), 230 мг $PbCl_2$ и 394 мг MAI растворяли в 1 мл растворителя N, N-диметилформамида (Sigma–Aldrich). Как и ожидалось, увеличение скорости центрифугирования привело к уменьшению толщины $CH_3NH_3PbCl_xI_{3-x}$, что должно было привести к снижению сопротивления $R_3CH_3NH_3PbCl_xI_{3-x}$. Однако импедансная спектроскопия показала, что при уменьшении толщины с 955 нм до 753 нм сопротивление $R_3CH_3NH_3PbCl_xI_{3-x}$ снижается примерно с 2590 Ом до 2258 Ом, достигая минимального значения при 505 нм. Дальнейшее уменьшение толщины $CH_3NH_3PbCl_xI_{3-x}$ увеличивало сопротивление пленки $CH_3NH_3PbCl_xI_{3-x}$. Изучение спектров поглощения и люминесценции $CH_3NH_3PbCl_xI_{3-x}$ показало, что произошло изменение плотности дефектов $CH_3NH_3PbCl_xI_{3-x}$, что объясняет снижение устойчивости $CH_3NH_3PbCl_xI_{3-x}$. По данным спектров поглощения и люминесценции, уменьшение толщины $CH_3NH_3PbCl_xI_{3-x}$ привело к снижению плотности межузловых дефектов $CH_3NH_3PbCl_xI_{3-x}$+. Частицы $CH_3NH_3PbCl_xI_{3-x}$+ образуют глубокие уровни, захватывающие свободные электроны и, как следствие, увеличивающие сопротивление $CH_3NH_3PbCl_xI_{3-x}$. PSC на основе слоя $CH_3NH_3PbCl_xI_{3-x}$ толщиной 505 нм показали наилучшие характеристики с улучшенными плотностью короткого тока и коэффициентом заполнения: КПД преобразования энергии устройства достигли 9,92 %.

Ключевые слова: перовскитные солнечные элементы, фотоактивный слой, $CH_3NH_3PbCl_xI_{3-x}$, фталоцианин меди, ионы йода, импедансометр, транспортный слой электронов, транспортный слой дырок.

DOI 10.31489/2023PH3/119-127

UDC 621.077

B.K. Rakhadilov[1], L.B. Bayatanova[1,2], Z.A. Satbayeva[1,3], R.S. Kozhanova[1,3], G.U. Yerbolatova[2], R.Ye. Sakenova[1]

[1]PlasmaScience LLP, Ust-Kamenogorsk, Kazakhstan;
[2]D. Serikbayev East Kazakhstan Technical University, Ust-Kamenogorsk, Kazakhstan;
[3]Shakarim University, Semey, Kazakhstan
*(*E-mail:* satbaeva.z@mail.ru*)*

Investigation of changes in phase composition and tribological properties of 65G steel during electrolyte-plasma hardening

This paper presents the results of studies of phase composition and tribological properties of 65G steel, before and after electrolytic-plasma hardening at different regimes. The technology of electrolyte-plasma hardening and laboratory installation for implementation of electrolyte-plasma hardening are described. It was found that after electroplasma hardening a modified layer consisting of α'-phase (martensite) and cementite M_3C is formed. The developed technological process of hardening of a part made of 65G steel makes it possible to obtain layers on the surface of the part that provide an increase in wear resistance by 2 times and in resistance to abrasive wear by 1.7 times. The carried out investigations have shown perspective and expediency of application of the developed method to increase operational properties of parts working in conditions of friction and wear. This technology can be used to increase the service life of working elements of agricultural machinery.

Keywords: hardening; phase composition; plasma-electrolyte hardening; wear resistance.

Introduction

The durability of parts depends not only on the material properties determined by the manufacturing technology and volume hardening, but also to a large extent on the surface properties. Its role in ensuring the operational properties of products is constantly increasing, which has contributed, along with extensive use of traditional methods of chemical-thermal treatment, to the emergence and development of a new direction — surface engineering by methods of energy and physical-chemical effects. The implementation of this concept in the choice of material will improve the performance properties of parts, and in some cases reduce the consumption of expensive materials. Thus, recently, due to the use of protective coatings and surface hardening, more and more low-alloy structural and tool steels are used and produced, which allowed reducing the cost of expensive high-alloy steels and alloys. At the same time, an important role in the application of protective coatings and surface hardening is the use of resource-saving technologies that help to reduce resource and energy costs and increase labor productivity [1, 2].

Recently, the research on electrolyte-plasma hardening of materials has been conducted quite intensively. As a result, various technologies for surface modification of metals and alloys based on the electrolyte-plasma method have been developed: oxidation [3], polishing [4], diffusion saturation with nitrogen [5], carbon [6, 7], boron [8], multicomponent saturation [9, 10] and surface hardening [11]. Among them, electrolyte-plasma hardening (surface hardening) is of specific interest [11, 12].

The surface hardening process by surface hardening was usually performed by laser beam, electron beam and plasma beam [13, 14]. Compared to these hardening processes, electrolyte-plasma hardening is a simple and inexpensive method. All methods of surface hardening are usually used to increase the surface hardness of steels. However, experience shows that surface hardening under certain conditions forms a fine-dispersed structure that increases the wear resistance of steel depending on its alloying. In addition, electrolyte-plasma hardening (surface hardening) differs favorably from plasma hardening processes (surface hardening) due to the high cooling rate and a smaller degree of oxide layer formation. Since, plasma discharges are formed between the surface of the metal and the electrolyte, and the cooling process takes place in the flowing electrolyte. Electric circuit closes between the electrodes through the electrolyte (aqueous salt solution). The transformation of electrical energy into heat energy occurs mainly in the layer adjacent to the product. As a result of heating, this layer transitions to a vapor-gas state, and micro-arcs are excited in it under the influence of the applied voltage. The power density reaches up to 3×10^3 W/cm^2 [15].

The technology makes it possible to change the heating and cooling rate and the thickness of the hardened layer within a wide range. By adjusting the temperature-rate regimes of plasma surface heating and cooling, as well as the use of various electrolytes, high values of mechanical and tribological characteristics of the surface layer of steels can be obtained.

In connection with the above, the purpose of this work is to study the effect of electrolyte-plasma hardening on the phase composition and tribological properties of 65G steel.

Materials, equipment and methods of experiments.

The object of the study was selected constructional 65G steel, which is used for the manufacture of working elements of tillage machines.

The chemical composition of 65G steel is presented in Table 1.

Table 1

Chemical composition in % of steel 65G (GOST 14959 — 79)

Steel grade	C	Si	Mn	Ni	S	P	Cr	Cu
65G	0.62 — 0.7	0.17 — 0.37	0.9 — 1.2	up to 0.25	up to 0.035	up to 0.035	up to 0.25	up to 0.2

Electrolytic-plasma hardening (EPH) of 65G steel samples was carried out on the laboratory unit in the Research Center “Surface Engineering and Tribology” of S. Amanzholov EKU. The general view and the scheme of installation of electrolyte-plasma processing are shown in Figure 1. The installation structurally consists of a power supply and a chamber for electrolyte-plasma treatment of materials.

EPH of steel samples is carried out as follows. Before starting work, the working bath is filled with electrolyte. Then the electrolyte is pumped into the electrolytic cell by means of a pump installed at the bottom of the working bath. The electrolyte flows out through the opening of the cone-shaped baffle in the form of a jet and fills the electrolytic cell. The electrolyte is then discharged through the edge of the electrolytic cell into the tray and then back into the working bath. Thus, the electrolyte is in circulating regimes. The feed rate of the electrolyte (flow rate) is 4-7 l/min. Feeding rate of cooling flow water into the heat exchanger is 3-6 l/min. The accepted parameters of cooling electrolyte allow maintaining the temperature within 40-70°C when heating the samples to the temperature of 800-900°C. Using the device for fixing the processed product, the processed product is dipped into the electrolyte so that the treated zone of the product was at a distance of 2-3 mm from the hole of the cone-shaped partition. The electrolyte jet is directed through the opening of the cone-shaped partition which is 10-15 mm lower than the height of the electrolytic cell. Then the anode is connected to the positive pole of the power supply, and the processed product — cathode to its negative pole. For heating to the hardening temperature 320 V voltage is applied between the electrodes and the current density is 25-30 A/cm^2. At these voltages an intensively glowing plasma layer is formed in the pre-cathode area and the product is heated at a rate of 450-500 °C/s. In this case an anomalous arc discharge is formed between the electrodes, due to which the workpiece is quickly heated [1, 8].

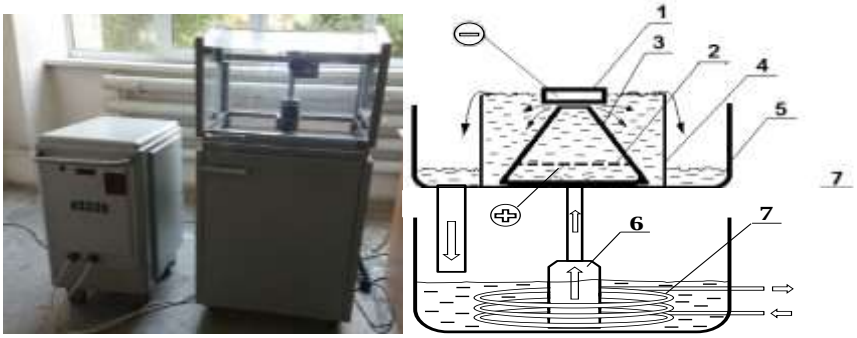

1 — sample to be treated (cathode), 2 — stainless steel anode with holes, 3 — cone-shaped partition, 4 — working chamber — bath with electrolyte, 5 — pan, 6 — pump, 7 — heat exchanger

Figure 1. General view and diagram of the electrolytic plasma treatment installation

Samples of 65G steel were treated at different regimes of EPH. The EPH regimes are shown in Table 2. The EPH was carried out by alternating high (320 V), medium (200 V) and low (50 V) voltages, as well as by cyclic exposure. An aqueous solution containing 15 percent sodium carbonate was used as the electrolyte. Distilled water was used to prepare the electrolyte.

Table 2

Regimes of thermocyclic electrolyte-plasma treatment of 65G steel sample

No.	Sample	Cycle 1			Cycle 2			Cycle 3			Cycle 4		
		320 V	200 V	50 V	320 V	200 V	50 V	320 V	200 V	50 V	320 V	200 V	50 V
	10-65G	1 s	-	1 s	1 s	-	-	-	-	-	-	-	-
	11-65G	2s	-	-	-	-	-	-	-	-	-	-	-
	17-65G	1s	3s	7s	1s	1s	7s	1s	-	-	-	-	-
	18-65G	1s	-	1s	1s	-	7s	1s	-	12s	1s	-	-

X-ray studies of steel samples were carried out using the well-known methods of X-ray structural analysis on X'PertPRO diffractometers. Diffractograms were taken using CuKα-radiation (λ=2.2897 A^0) at 40 kV. The diffractograms were manually transcribed using standard techniques and the PDF-4 database, and quantitative analysis was performed using Powder Cell software.

Tribological sliding friction tests were performed on a TRB^3 tribometer using the standard ball on disk technique (Figure 2a) (ASTM G 133-95 and ASTM G 99 international standards). A 6.0 mm diameter ball of certified Al_2O_3 material was used as a counterbody. Tests were conducted at a load of 1 N and a linear velocity of 2 cm/s, a wear radius of curvature of 5 mm, and a friction path of 40.1 m. Tribological characteristics of the modified layer were characterized by wear intensity and friction coefficient [12].

The samples were tested for abrasion on an experimental installation for abrasion testing in friction against non-rigidly fixed abrasive particles according to the scheme "rotating roller — flat surface" in accordance with GOST 23.208-79, which coincides with the American standard ASTM C 6568 (Fig. 2 b). To test the abrasion on the rubber wheel, the surfaces of the samples were ground and polished, as well as they were cleaned with acetone and dried. A cylindrical rubber roller pressed by the radial surface to the flat surface of the test sample with a force of 22 N was rotated at a frequency of 1 s^{-1}. The scheme of the device is shown in Figure 2b. The rate of arrival of abrasive particles between the rubber wheel and the sample, i.e. in the test zone was 41-42 g/min. As abrasive particles, electrical corundum with granularity of 200-250 μm was used.

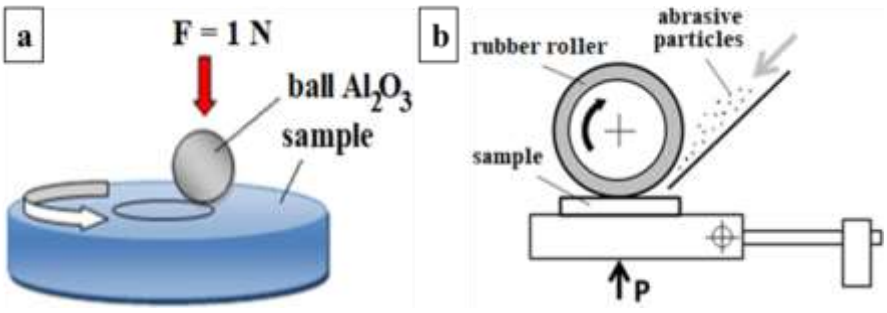

a — according to the scheme "ball on disk", b — according to the scheme "rotating roller — plane surface"

Figure 2. Tribological tests of samples

The wear resistance of the tested treated sample was evaluated by comparing its wear with the wear of the reference sample (untreated sample). Wear was measured by weight method on analytical scales ADV-200 with accuracy to 0.0001 g. Samples were weighed every minute and tested for three minutes, the length of the whole wear was 28.8 m. Before weighing, the samples were blown with compressed air to remove any remaining sand particles on the samples. Wear resistance of the tested material was evaluated by weight loss of the samples during the test according to GOST-23.208-79.

Tests of samples on shock-abrasive wear were carried out on the experimental bench according to GOST 23.207-79. For comparative evaluation of wear resistance of 65G steel samples before and after electrolyte-plasma treatment at different regimes. Tests were carried out in the following regimes: impact energy E = 3.3 J, impact velocity υ = 1 m/s and impact frequency n = 200 min^{-1}. The scheme of the device is presented in Figure 3. The rate of abrasive particles entering the test zone was 75-80 g/min. Electro-corundum with granularity 200-250 μm was used as abrasive particles. The wear resistance of the tested samples was evaluated by comparing the wear of the hardened sample with the wear of the unhardened sample. Wear was measured by weight method on analytical scales ADV-200 with accuracy 0.0001 g. Samples were tested for five minutes. Before weighing, the samples were blown with compressed air to remove the remaining sand particles on the samples.

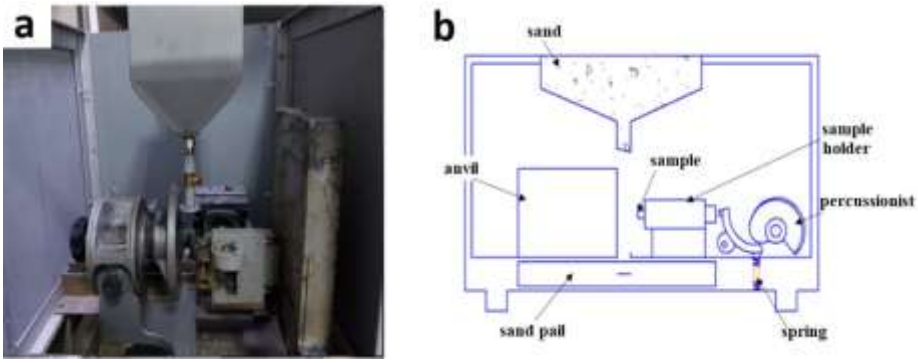

Figure 3. Experimental bench for shock-abrasive wear according to GOST 23.207-79

Bench tests of 65G steel samples on air-erosion resistance of coatings were carried out on a special bench designed and manufactured in the Research Center “Surface Engineering and Tribology” in accordance with ASTM G76 standard. The general view of the bench and the test chamber is shown in Figure 4.

Figure 4. Bench for erosion testing

Tests on air-erosion resistance of samples were carried out as follows: air-abrasive jet is supplied to the sample from the nozzle with diameter of 5 mm. Air pressure at nozzle inlet is 0.4 MPa, distance from nozzle to sample surface is 11 mm. The duration of exposure to air-abrasive jet was 60 seconds.

Results and discussion.

Figure 5 shows the results of the tribological tests. Tribological tests were performed using Si_3N_4 counterbodies (ball diameter of 6 mm) and 100Cr6 (ball diameter of 3 mm). The amount of wear was

determined by examining the profilogram of the wear tracks. The results showed that the wear volume decreased after the EPH, sample 11-65G showed a higher wear volume when the Si_3N_4 counterbody was used, while the 100Cr6 counterbody had a low wear volume compared to the initial sample. And sample 10-65G showed the lowest wear volume values compared to the other samples with both the Si_3N_4 and 100Cr6 counterbodies.

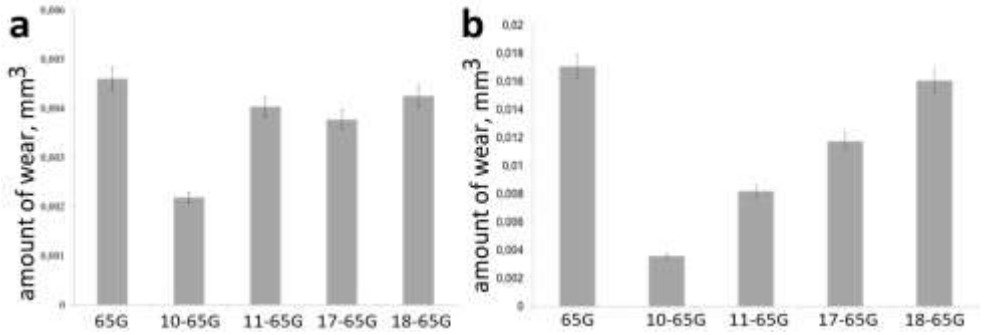

Figure 5. Data on the wear volume of samples after test with counterbodies of Si_3N_4 (a) and 100Cr6 (b)

Figure 6 shows the friction coefficient curves of 65G steel samples after wearing with counterbodies made of Si_3N_4 (ball with diameter of 6 mm) and 100Cr6 (ball with diameter of 3 mm). The test results when using Si_3N_4 counterbodies showed that the friction coefficient varies greatly depending on the EPH regime. An increase in the friction coefficient was observed in all samples except 18-65G. And when the 100Cr6 counterbody was used, an increase in the friction coefficient was observed in all samples. This may be due to the fact that the treated samples had a high roughness compared to the initial sample.

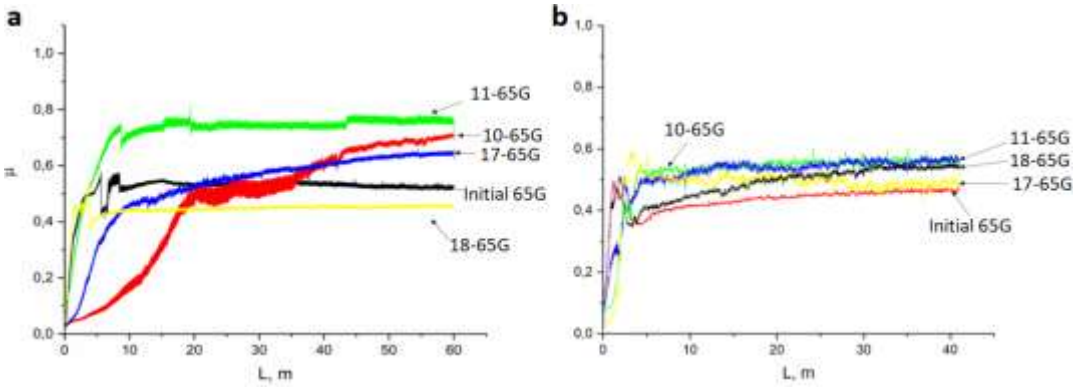

Figure 6. Friction coefficient curves of 65G steel samples at wear with counterbodies of Si_3N_4 (a) and 100Cr6 (b)

Wear tests of samples on abrasion on the special bench according to GOST 23.208-79 were carried out. Wear resistance was estimated by weight method. Weight of samples was measured by means of analytical scales Gibertini CRYSTAL 100 CE with magnetic compensation. Table 3 shows the masses of the samples before and after the tests. From the table it is seen that the weight loss of all treated samples is low compared to the initial sample. At the same time, samples 10-65G and 18-65G showed higher resistance to abrasive wear. Thus, it is possible to assert that EPH allows to increase resistance of steel 65G to abrasive wear by 1.7 times.

Table 3

Results of measuring the weight of samples before and after testing

No.	Samples	Weight before, g	Weight after, g	Weight loss, g
1	Initial sample-65G	60.084	60.0746	0.0094
2	10-65G	57.159	57.1509	0.0081
3	11-65G	58.148	58.1425	0.0055
4	17-65G	62.130	62.1223	0.0077
5	18-65G	54.7845	54.7789	0.0056

Figure 7 shows X-ray diffractograms of 65G steel samples before and after EPH. X-ray diffraction analysis showed that in the initial state in the structure of 65G steel only α-phase is present. After the EPH in samples 10-65G, 11-65G and 18-65G a reflex (121) of cementite is observed. Also after the EPH, broadening of the -phase interference lines is observed on the diffractograms. The broadening of the -phase interference lines is associated with the growth of dislocation density, martensite formation and is determined mainly by the martensite tetragonality [16-18]. In sample 17-65G, a slight broadening of interference line 110 is observed, and no cementite formation is detected in this sample. Apparently, this is due to the fact that this sample is characterized by a fine-grained ferrite-bainite structure formed during partial melting of the surface.

Thus, the main advantage of EPH is the possibility of obtaining a modified martensite layer on the steel surface. In this case, the base of the material does not change, i.e. the part retains its ductile core. The formation of a modified layer of fine-grained martensite with a small amount of cementite in the surface layers will have a positive effect on the performance properties of parts.

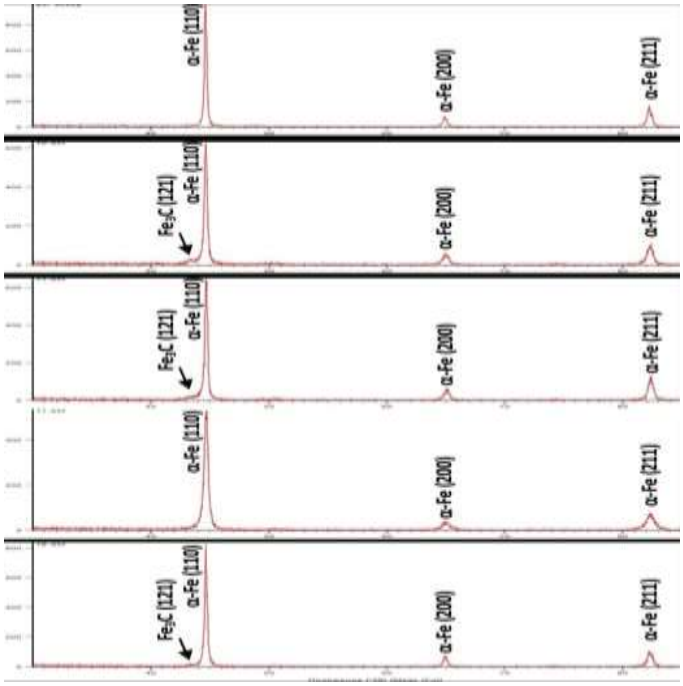

Figure 7. Diffractograms of 65G steel samples

As the results of the study after electrolyte-plasma surface hardening the steel has high wear resistance and strength characteristics.

On the basis of phase composition study it was found that after EPH a modified layer consisting of α'-phase (martensite) and cementite M_3C is formed. The increase in wear resistance of 65G steel after EPH is associated with the formation of martensite as well as the formation of defective substructure.

The bench tests of 65G steel samples on the test bench for air-erosion resistance and on the test bench for shock-abrasion wear were carried out.

The test results are shown in Table 4. It can be seen from the table that the weight loss of the treated samples is almost 2 times less than that of the initial samples. Thus, test results show that all samples that underwent electrolyte-plasma hardening are characterized by sufficiently lower erosion wear than the initial samples.

Table 4

Results of air-erosion resistance tests

Sample No.	Material	Erosion wear, g/min
10-65G initial	fragment of lancet paws made of 65G steel	0.045
10-65G		0.027

Table 5 shows the results of the shock-abrasion test. It can be seen that the weight loss of the hardened sample is less than that of the initial sample, which indicates an increased resistance to impact-abrasive wear. The high resistance of the hardened samples to shock-abrasive wear is caused by the formation of martensitic structure.

Table 5

Results of the shock-abrasion test

No.	Samples name	Material	Mass loss, mg (shock abrasion)
2	10-65G initial	fragment of lancet paws made of 65G steel	0.0475
3	10-65G		0.0426

Conclusion

Analyzing the experimental results obtained, the following conclusions can be made:

1. As shown by the results of the study the considered steel after electrolyte-plasma surface hardening have high wear resistance and strength characteristics. Based on the study of the phase composition it was found that after EPH a modified layer consisting of α'-phase (martensite) and cementite M_3C is formed. The increase in wear resistance of 65G steel after EPH is connected with formation of martensite as well as formation of defective substructure.

2. The developed technological process of hardening of a part made of 65G steel makes it possible to obtain layers on the surface of the part ensuring a twofold increase in wear resistance, a 1.7-fold increase in resistance to abrasive wear, as well as to ensure uniform distribution of all phase formations in a thin surface layer, which, in general, will result in improvement of operating characteristics of the 65G steel part. In addition, local hardening ensures the achievement of technical and economic effect due to the absence of the need to isolate undesirable areas of the part, treating only the areas requiring hardening.

Thus, the conducted studies have shown the prospects and feasibility of using the developed method to improve the operating properties of parts working in conditions of friction and wear. The conducted studies have shown that EPH technology, which allows increasing hardness and wear resistance of 65G steel can be used to increase the service life of working elements of agricultural machinery. It is recommended to apply this method of EPH for hardening of working elements of agricultural machinery made of 65G steel without additional heat treatment. The EPH provides achievement of technical and economic effect due to the use of simple equipment, not expensive aqueous solutions, reduction of processing time, as well as due to increase of wear resistance, microhardness of steels.

Acknowledgment

This research has been funded by the Science Committee of the Ministry of Science and Higher Education of the Republic of Kazakhstan (Grant No. AP09058547).

Reference

1 Рахадилов Б.К. Плазменно-лучевые технологии модификации поверхности материалов и нанесения покрытий: моногр. / Б.К. Рахадилов, М.К. Кылышканов, З.Б. Сагдолдина. — Усть-Каменогорск: Изд-во «Берел», 2018. — 202 с.

2 Перевертов В.П. Технологии обработки материалов концентриррованным потоком энергии / В.П. Перевертов, И.К. Андрончев, М.М. Абулкасимов // Надежность и качество сложных систем. — 2015. — № 3(11). — С. 69–79.

3 Исмаил М.И.С. Экспериментальное проектирование и анализ производительности при плазменно-дуговом упрочнении поверхности / М.И.С. Исмаил, З. Таха // Всемирная академия наук, техники и технологий. — 2011. — Т. 56. — С. 1052–1058.

4 Леонхардт Д. Основы и приложения системы плазменной обработки, основанной на ионизации электронным пучком / Д. Леонхардт, С.Г. Уолтон, Р.Ф. Фернслер // Физика плазмы. — 2007. — Т. 14(5). — С. 057103.

5 Не Х. Характеристики износа при скольжении чугуна и стали, азотированных электролитической плазмой / Х. Не, Л. Ван, З.С. Яо, Л. Чжан, Ф. Чен // Surf.Coat. Технология. — 2005. — Т. 200 (5–6). — С. 1745–1750.

6 Балановский А.Е. Плазменное поверхностное упрочнение металлов / А.Е. Балановский. — Иркутск: Изд-во ИГТУ, 2006. — 180 с.

7 Скаков М.К. Микроструктура и трибологические свойства быстрорежущей стали, азотированной электролитной плазмой / М.К. Скаков, Б.К. Рахадилов, М. Шеффлер // Испытания материалов. — 2015. — Т. 4 (57). — С. 360–365.

8 Белкин П.Н. Плазменно-электролитическое упрочнение сталей: обзор / П.Н. Белкин, С.А. Кусманов // Технология обработки поверхности и прикладная электрохимия. — 2016. — Т. 52. № 6. — С. 531–546.

9 Баринова Л.В. Металлографическое травление металлов и сплавов: руководство / Л.В. Баринова, Э.Л. Демина. — М.: Металлургия, 1986. — 256 с.

10 Приборы и методы физической металлургии / под ред. Ф. Вайнберга; пер. с англ. — М.: Мир, 1973. — Т. 1. — 427 с.

11 Оливер У.С. Усовершенствованный метод определения твердости и модуля упругости с использованием экспериментов по вдавливанию с измерением нагрузки и смещения / У.С. Оливер, Г.М. Фарр // Журн. исслед. материалов. — 1992. — 7 (6). — С. 1564–1583.

12 Григорьевич В.К. Твердость и микротвердость металлов / В.К. Григорьевич. — М.: Наука, 1976. — 230 с.

13 Полетика И.М. Электронно-лучевое упрочнение поверхностного слоя стали вне вакуума / И.М. Полетика, М.Г. Голковский, М.В. Перовская // Физическая мезомеханика. — 2006. — С. 181–184.

14 Смирнова Н.А. Особенности структурообразования при лазерной обработке / Н.А. Смирнова, А.И. Мисюров // Инженер. журн. «Наука и инновации». — 2012. — № 6 (6). — С. 11.

15 Ерохин А.Л. Плазменный электролиз для обработки поверхностей / А.Л. Ерохин, Х. Ни, А. Лейланд, А. Мэтьюз, С. Дж. Доуи / Технология поверхностей и покрытий. — 1999. — Т. 122 (2–3). — С. 73–93.

16 Хомутов О.И. Исследование электролитно-плазменного процесса / О.И. Хомутов, Г.В. Плеханов, С.Д. Терентьев, С.О. Хомутов // Альманах Ползунова. — 2001. — С. 10–19.

17 Терентьев С.Д. Исследование вольт-амперной характеристики электролитно-плазменного разряда / С.Д. Терентьев, Г.В. Плеханов // Высшее образование в современном мире: тез. докл. Междунар. науч. -техн. конф. — Рубцовск, 1999. — С. 118, 119.

18 Райзер Ю.П. Распространение разряда и поддержание плотной плазмы электромагнитными полями / Ю.П. Райзер // Успехи физических наук. — 1972. — Т. 108. — С. 429–461.

Б.К. Рахадилов, Л.Б. Баятанова, З.А. Сатбаева, Р.С. Кожанова, Г.У. Ерболатова, Р.Е. Сакенова

Электролитті-плазмалық өңдеу кезінде 65Г болатының фазалық құрамы мен трибологиялық қасиеттерінің өзгеруін зерттеу

Жұмыста әртүрлі режимдерде электролиттік-плазмалық шынықтыруға дейінгі және одан кейінгі 65Г маркалы болаттың фазалық құрамы мен трибологиялық қасиеттерін зерттеу нәтижелері келтірілген. Электролиттік-плазмалық қатайту технологиясы және электролиттік-плазмалық қатайтуды жүзеге асыруға арналған зертханалық қондырғы сипатталған. Электроплазмалық қатайтудан кейін α'фазасынан (мартенсит) және М3С цементиттен тұратын модификацияланған қабат пайда болатыны анықталды. 65Г болаттан жасалған бөлшекті қатайтудың дамыған технологиялық процесі бөлшектің бетінде тозуға төзімділікті 2 есе және абразивті тозуға төзімділікті 1,7 есе арттыруды қамтамасыз ететін қабаттарды алуға мүмкіндік береді. Жүргізілген зерттеулер үйкеліс пен тозу жағдайында жұмыс істейтін бөлшектердің пайдалану қасиеттерін арттыру үшін әзірленген әдісті қолданудың келешегі мен мақсаттылығын көрсетті. Бұл технологияны ауылшаруашылық техникасының жұмыс органдарының қызмет ету мерзімін ұзарту үшін пайдалануға болады.

Кілт сөздер: қатайту, фазалық құрам, плазмалық-электролиттік қатайту, тозуға төзімділік.

Б.К. Рахадилов, Л.Б. Баятанова, З.А. Сатбаева, Р.С. Кожанова, Г.У. Ерболатова, Р.Е. Сакенова

Исследование изменений фазового состава и трибологических свойств стали 65Г при электролитно-плазменном упрочнении

В работе представлены результаты исследований фазового состава и трибологических свойств стали марки 65Г до и после электролитно-плазменной закалки при различных режимах. Описаны технология электролитно-плазменного упрочнения и лабораторная установка для осуществления электролитно-плазменного упрочнения. Было обнаружено, что после электролитно-плазменного упрочнения образуется модифицированный слой, состоящий из α'-фазы (мартенсита) и цементита М3С. Разработанный технологический процесс упрочнения детали из стали 65Г позволяет получить на поверхности детали слои, обеспечивающие повышение износостойкости в 2 раза и стойкости к абразивному износу в 1,7 раза. Проведенные исследования показали перспективность и целесообразность применения разработанного метода для повышения эксплуатационных свойств

деталей, работающих в условиях трения и износа. Эта технология может быть использована для увеличения срока службы рабочих органов сельскохозяйственной техники.

Ключевые слова: трение, износ, фазовый состав, плазменно-электролитическое упрочнение, износостойкость.

Reference

1 Rakhadilov, B.K., Kylyshkanov, M.K. & Sagdoldina, Z.B. (2018). Plazmenno-luchevye tekhnologii modifikatsii poverkhnosnti materialov i naneseniia pokrytii [Plasma and beam technologies of modifying materials surface and coating application]. Ust-Kamenogorsk: Izdatelstvo «Berel» [in Russian].

2 Perevertov, V.P., Andronchev, I.K. & Abulkasimov, M.M. (2015). Tekhnologii obrabotki materialov kontsentrirovannym potokom energii [Technologies of materials processing by concentrated energy flow]. *Nadezhnost i kachestvo slozhnykh sistem — Reliability and quality of complex systems, 3*(11), 69–79 [in Russian].

3 Ismail, M.I.S. & Taha, Z. (2011). Eksperimentalnoe proektirovanie i analiz proizvoditelnosti pri plazmenno-dugovom uprochnenii poverkhnosnti [Experimental design and performance analysis in plasma arc surface hardening]. *Vsemirnaia akademiia nauk, tekhniki i tekhnologii — World Academy of Science, Engineering and Technology, 56,* 1052–1058 [in Russian].

4 Leonhardt, D., Walton, S.G. & Fernsler, R.F. (2007). Osnovy i prilozheniia sistemy plazmennoi obrabotki, osnovannoi na ionizatsii elektronnym puchkom [Fundamentals and applications of a plasma-processing system based on electron-beam ionization]. *Fizika plazmy — Physics of Plasma, 14*(5), 057103 [in Russian].

5 Nie, X., Wang, L., Yao, Z.C., Zhang, L. & Cheng, F. (2005). Kharakteristiki iznosa priskolzhenii chuguna i stali, azotirovannykh eletroliticheskoi plazmoi [Sliding wear behaviour of electrolytic plasma nitrided cast iron and steel]. *Surf. Coat. Tekhnologiia — Surf. Coat. Technol., 200*(5–6), 1745–1750 [in Russian].

6 Balanovsky, A.E. (2006). Plazmennoe poverkhnostnoe uprochnenie metallov [Plasma surface hardening of metals]. Irkutsk: Izdatelstvo Irkutskogo gosudarstvennogo tekhnicheskogo universiteta [in Russian].

7 Skakov M.K., Rakhadilov, B.K. & Scheffler, M. (2015). Mikrostruktura i tribologicheskie svoistva bystrorezhushchei stali, azotirovannoi elektrolitnoi plazmoi [Microstructure and Tribological Properties of Electrolyte Plasma Nitrided High Speed Steel]. *Ispytaniia materialov — Materials testing, 4*(57), 360–365 [in Russian].

8 Belkin, P.N. & Kusmanov, S.A. (2016). Plazmenno-elektroliticheskoe uprochnenie stalei: obzor [Plasma Electrolytic Hardening of Steels: Review]. *Tekhnologiia obrabotki poverkhnosti i prikladnaia elektrokhimiia — Surface Engineering and Applied Electrochemistry, 52*(6), 531–546 [in Russian].

9 Baranova, L.V. & Demina, E.L. (1986). Metallograficheskoe travlenie metallov i splavov: rukovodstvo [Metallographic etching of metals and alloys. Handbook]. Moscow: Metallurgy [in Russian].

10 Weinberg, F. (Ed.). (1973). Pribory i metody fizicheskoi metallurgii [Instruments and methods of physical metallurgy]. Transl. from English. Moscow: Mir, Vol. 1, 427 [in Russian].

11 Oliver, W.C. & Pharr, G.M. (1992). Usovershenstvovannyi metod opredeleniia tverdosti i moduliia uprugosti s ispolzovaniem eksperimentov po vdavlivaniiu s izmereniem nagruzki i smeshcheniia [An improved technique for determining hardness and elastic modulus using load and displacement sensing indentation experiments]. *Journal of Materials Research, 7*(6), 1564–1583 [in Russian].

12 Grigorevich, V.K. (1976). Tverdost i mikrotverdost metallov [Hardness and microhardness of metals]. Moscow: Nauka [in Russian].

13 Poletika, I.M., Golkovsky, M.G. & Perovskaya, M.V. (2006). Elektronno-luchevoe uprochnenie poverkhnostnogo sloia stali vne vakuuma [Electron-beam hardening of steel surface layer outside vacuum]. *Fizicheskaia mezomekhanika — Physical Mesomechanics* [in Russian].

14 Smirnova, N.A. & Misyurov, A.I. (2012). Osobennosti strukturoobrazovaniia pri lazernoi obrabotke [Features of structure formation during laser processing]. *Inzhenernyi zhurnal «Nauka i innovatsii» — Engineering Journal: Science and Innovations, 6*(6), 11 [in Russian].

15 Yerokhin, A.L., Nie, X., Leyland, A., Matthews, A. & Dowey, S.J. (1999). Plazmennyi elektroliz dlia obrabotki poverkhnostei [Plasma electrolysis for surface engineering]. *Tekhnologiia poverkhnostei i pokrytii — Surface and Coatings Technology, 122*(2–3), 73–93 [in Russian].

16 Khomutov, O.I., Plekhanov, G.V., Terentyev, S.D. & Khomutov, S.O. (2001). Issledovanie elektrolitno-plazmennogo protsessa [Investigation of the electrolyte-plasma process]. *Almanakh Polzunova — Polzunov Almanac,* 10–19 [in Russian].

17 Terentiev, S.D. & Plekhanov, G.V. (1999). Issledovanie volt-ampernoi kharakteristiki elektrolitno-plazmennogo razriada [Study of volt-ampere characteristic of electrolyte-plasma discharge]. *Vysshee obrazovanie v sovremennom mire: tezisy dokladov Mezhdunarodnoi nauchno-tekhnicheskoi konferentsii — Higher Education in the Modern World: Abstracts of International Scientific and Technical Conference. Rubtsovsk*, P. 118, 119 [in Russian].

18 Raiser, Y.P. (1972). Rasprostranenie razriada i podderzhanie plotnoi plazmy elektromagnitnymi poliami [Discharge propagation and maintenance of dense plasma by electromagnetic fields]. *Uspekhi fizicheskikh nauk — Advances in Physical Sciences, Vol. 108,* 429–461 [in Russian].

DOI 10.31489/2023PH3/128-135

UDC 621.548.2

N.K. Tanasheva, M.A. Burkov, A.N. Dyusembayeva, S. Suleimenova, A.S. Tussupbaeva, Sh.S. Kyzdarbekova

Karaganda University of the name of academician E.A. Buketov, Kazakhstan
*(*E-mail: maxim19990202@gmail.com)*

Determination of the optimal deflection angle of the sail blade of a wind power plant

This article presents the results of studies of a sailing wind power plant at various parameters. For this purpose, a model of a wind power plant controlled by a system of sail blades was developed. Studies of aerodynamic forces at different angles of deflection of the sail blade system were carried out: 0°; 30°; 60°; 90°. The air flow velocity varied in the range from 3 to 14 m/s. The experiments were carried out in a T-1-M wind tunnel designed to measure forces and moments acting on a sailing wind turbine. As a result of experiments, it was found that with an increase in the air flow velocity, the frequency of rotation of the shaft of the wind power plant increased. The maximum rotational speed of the shaft was reached at $\alpha = 0°$ deflection of the sail blade system of the wind power plant. A number of experiments were carried out and aerodynamic characteristics were obtained depending on the deflection angle (α) of the sail blade system of the wind power plant and the air flow velocity. As the deflection angle of the blade system increases, the drag force decreases depending on the air flow velocity. It was experimentally established that at $\alpha = 30°$ deflection of the blade system created the maximum lift force. Based on the data obtained, it was found that with an increase in the speed of the incoming air flow, the aerodynamic forces acting on the sailing wind power plant increased.

Keywords: Sail blade, wind power plant, shaft rotation speed, wind turbine, deflection angle, frontal resistance, thrust force, T-1-M wind tunnel.

Introduction

Due to its geographical features, Kazakhstan has high potential for wind energy, which can be harnessed to generate electricity and reduce dependence on oil and gas resources. In recent years, Kazakhstan has been actively developing wind energy, attracting foreign investment and building new wind farms, to achieve energy independence and reduce greenhouse gas emissions. The average wind speed reaches 3-4 m/s in most of the territory, while in open areas, the air flow velocity is 6 m/s or higher [1].

When analyzing wind energy technologies, it is evident that the most common type is wind generators with blade rotors used in turbine wind power plants. However, these installations face challenges related to the unpredictability of wind speed and direction, as well as limited operating speed range, making them less effective in Kazakhstan [2]. Traditional bladed wind power plants also have low efficiency at low wind speeds, particularly in the repetitive wind range of 6-7 meters per second [3, 4]. To address this issue, a sailing wind power plant is being used.

One advantage of a sailing wind power plant is its ability to generate electrical energy from low wind speeds, as low as 3 m/s [5]. The wind turbine operates by utilizing the kinetic energy of the wind, converting it into mechanical energy through the rotation of the shaft with the help of torque resulting from the aerodynamic lift force on the sails. However, existing sailing wind power plants lack a mechanism to regulate the deflection angle of the blades.

The novelty of this installation lies in the use of a controlled system of blades, which provides optimal conditions for operation [6]. By adjusting the deflection angle of the sail blades, the load on the wind power plant can be reduced during high wind speeds. The objective of this study is to investigate the aerodynamic characteristics of a sailing wind power plant using a controlled system of blades in the form of a triangular sail, calculate the drag and thrust coefficients, determine the optimal deflection angle of the blades, and demonstrate the effectiveness of this wind power plant.

Experimental

In this study, experiments were conducted using a mock-up of an eight-bladed sailing wind power plant to investigate the effect of flow direction on its aerodynamic characteristics.

An experimental model of an eight-bladed sailing wind power plant was created for the purpose of research. Aerodynamic characteristics were measured at least five times. The wind power wheel had a diameter of d = 0.43 [m], the cross-sectional diameter of the model was S = 0.145 [m], the area covered by the rotor was R = 0.215 [m], the air density was p = 1.21, and the kinematic viscosity of the air was v = $14.9 \cdot 10^{-5}$ [Pa·s]. The measurement error was within 4 %.

The experiments were conducted in the working section of the T-1-M wind tunnel, which had a diameter of the working part D = 0.5 m and a length L = 0.8 m. Drag force measurements were carried out using three-component aerodynamic scales with high measurement accuracy. Figure 1 shows a diagram of the experimental eight-blade sailing wind power plant.

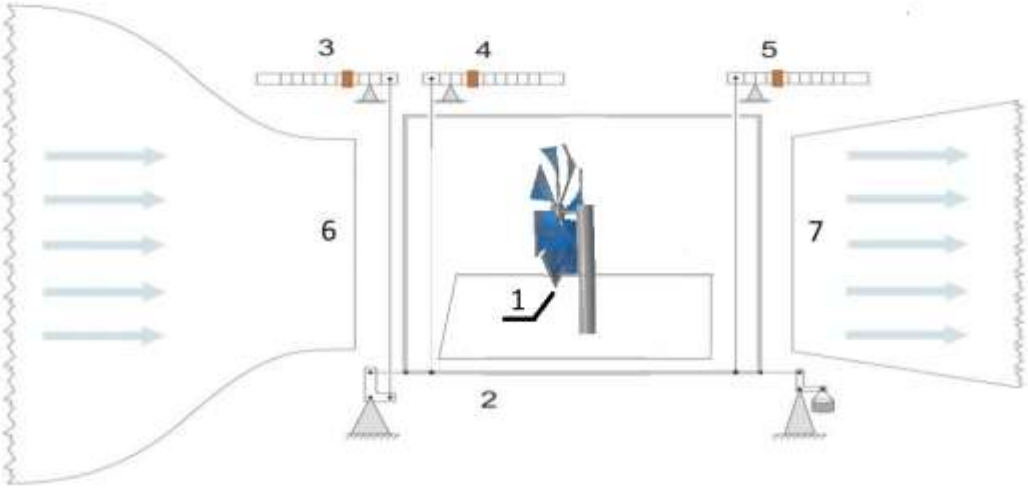

Figure 1. Diagram of an experimental sailing wind turbine
1 — Sailing blades of a wind power plant; 2 — a frame for mounting a mock-up with aerodynamic scales; 3 — scales measuring drag force; 4 — scales measuring lift; 5 — confuser; 6 — wind tunnel diffuser [7].

The angle of deflection of the blades is an important parameter for the energy efficiency of the wind turbine, as it affects the direction and speed of the air flow passing through the turbine. In Figure 2, the angle of deflection of the sail was varied to the following values: 0°, 15°, 30°, 45°, and 60°.

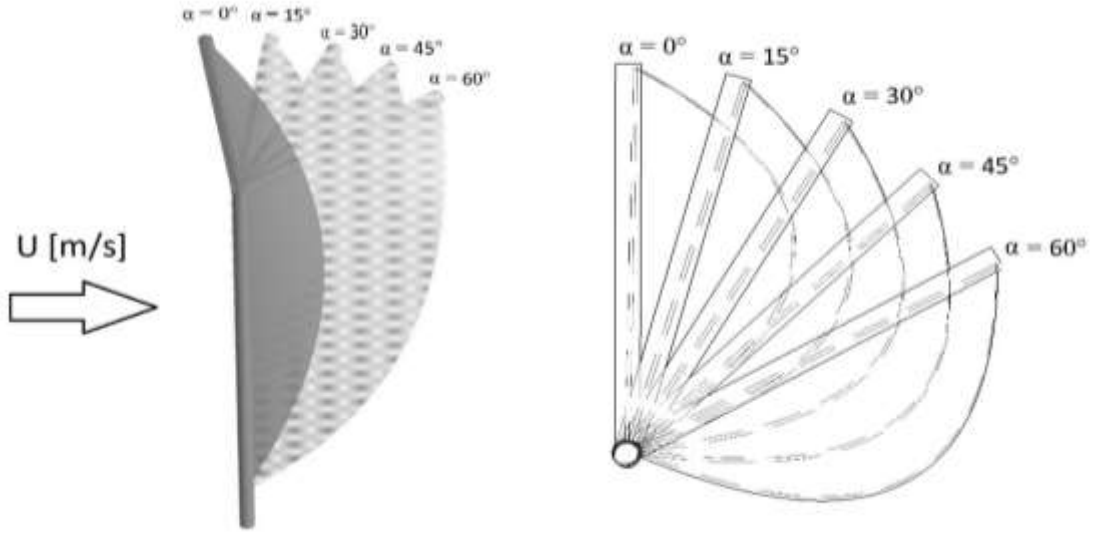

Figure 2. Changes in the deflection angle (α) of the blades of a sailing wind power plant.

During the experiments, a decrease in efficiency was observed at flow installation angles exceeding α = 60°. Experiments were not conducted at angles α greater than 60°.

The following formula (1) was used to determine the drag coefficient (C_x), thrust coefficient, and Reynolds number (Re):

$$C_x = \frac{F_x}{\rho \cdot \frac{u^2}{2} \cdot S}, C_m = \frac{F_m}{\rho \cdot \frac{u^2}{2} \cdot S}, \mathrm{Re} = \frac{u \cdot d}{\nu} \quad (1)$$

,

where F_t is the drag force [N], F_t is the thrust force [N], p is the air density [kg/m^3], u is the air flow velocity [m/s], S is the midsection area of the rotor [m^2], d is the diameter [m], and v is the kinematic viscosity of the air [m^2/s] [8].

During the experiments, the air flow velocity varied from 3 m/s to 14 m/s. The number of revolutions was measured using a digital laser photo tachometer AT-8, and the velocity of the incoming air flow was measured using a Skywatch Atmos cup anemometer [9-10].

Results and Discussion

Based on experimental data (Fig. 3), the dependence of the number of rotations of the shaft of a sailing wind turbine (N) on the wind speed (U) and the angle of deflection of the sailing blades (α) is obtained.

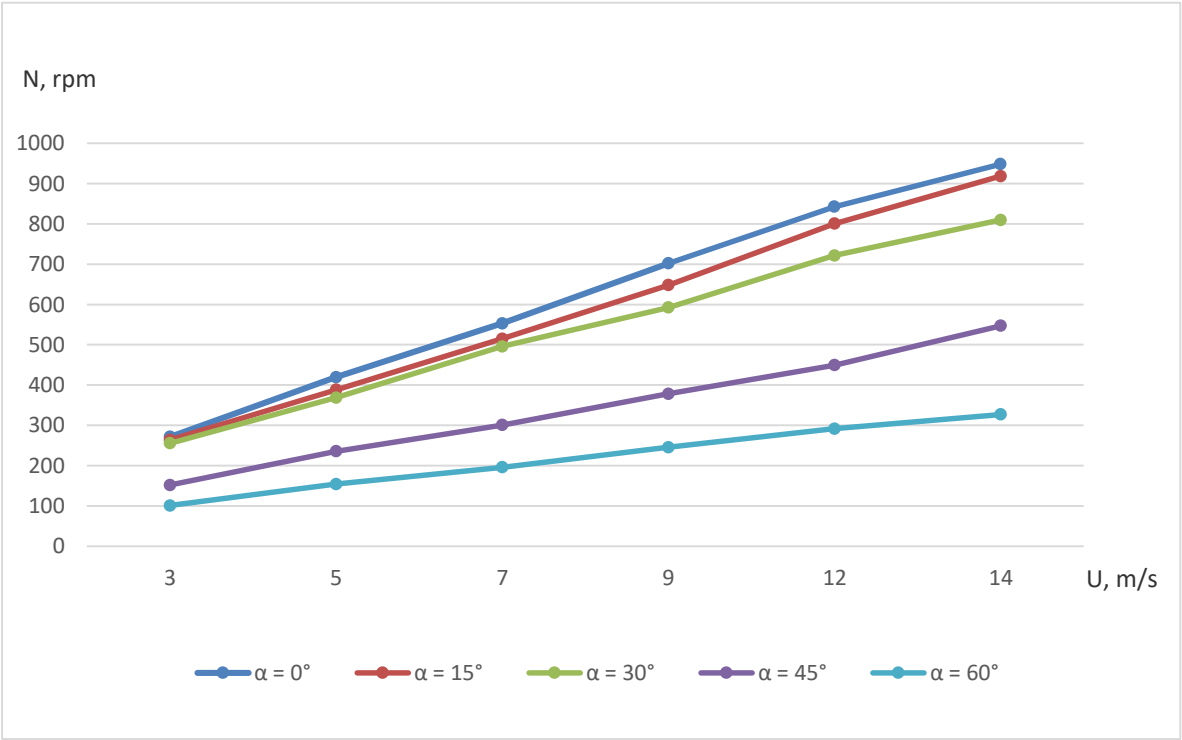

Figure 3. The dependence of the number of revolutions (N) of a sailing wind power plant on the wind speed (U) and the angle of deflection of the sailing blades (α).

From the data obtained, the maximum value of the drag force of a sailing wind power plant is reached at α=0°, with a rotational speed of n=271 [rpm] at U=3 m/s, and gradually increases (from 4 m/s to 14 m/s) depending on the air flow velocity (n=948 [rpm], U=14 m/s).With a change in the angle of deflection of the sailing blades, the number of revolutions rapidly decreases. The minimum rotation speed of the wind turbine shaft is n=195 [rpm] at α=60° and U=3 m/s, and n=326 [rpm] at U=14 m/s.

The rise in wind speed leads to a smooth increase in the dynamic air pressure on the soul blade of the wind power plant, which contributes to its acceleration. Further experiments were carried out to measure the drag force (F_d). Figure 4 describes the dependence of the drag force (F_d) of a sailing wind power plant on the wind speed (U) at different angles of deflection of the sailing blades (α).

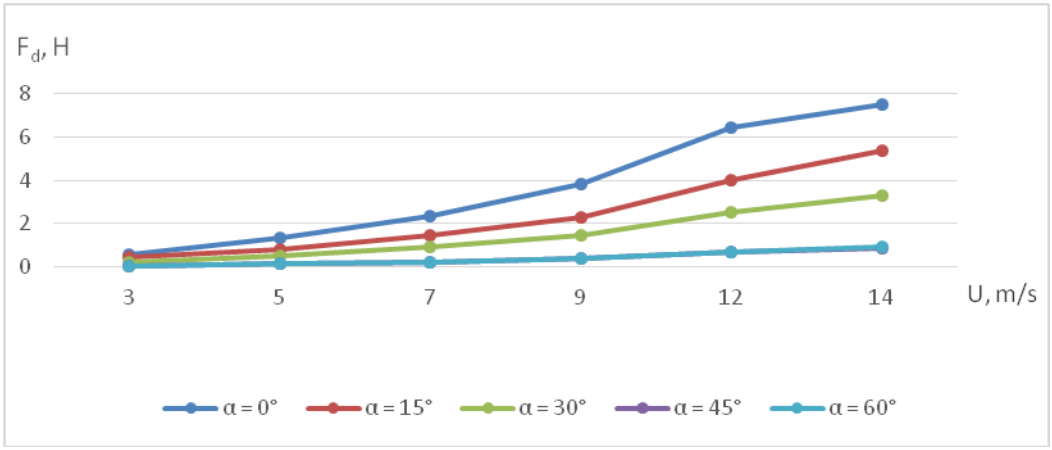

Figure 4. Dependence of the drag force (F_d) of a sailing wind power plant on wind speed at different angles of deflection of the sailing blades (α).

With a minimum deflection angle α = 0° (Fig. 4), the maximum drag force F_d = 0.575N (for U = 3 m/s) is observed, and it gradually rises with higher wind speeds, reaching F_t = 7.506 N at U = 14 m/s. When the deflection angle of the blades changes, the drag force (α = 15 — 60°) decreases rapidly, reaching F_t = 26 N at α = 15° and U = 3 m/s, and gradually climbs with higher air flow velocities, reaching F_t = 0.911 N at α = 60° and U = 14 m/s. As the air flow velocity increases, the dynamic pressure effect leads to an augmentation in the drag force on the surface of the blades. Consequently, with a minimum angle of deflection of the blade (α = 0°), the flow passes more smoothly and with minimal energy losses, allowing for maximum frontal pressure on the surface of the blade. Further studies were carried out to measure the thrust force of a sailing wind power plant as a function of the air flow velocity (Fig. 5).

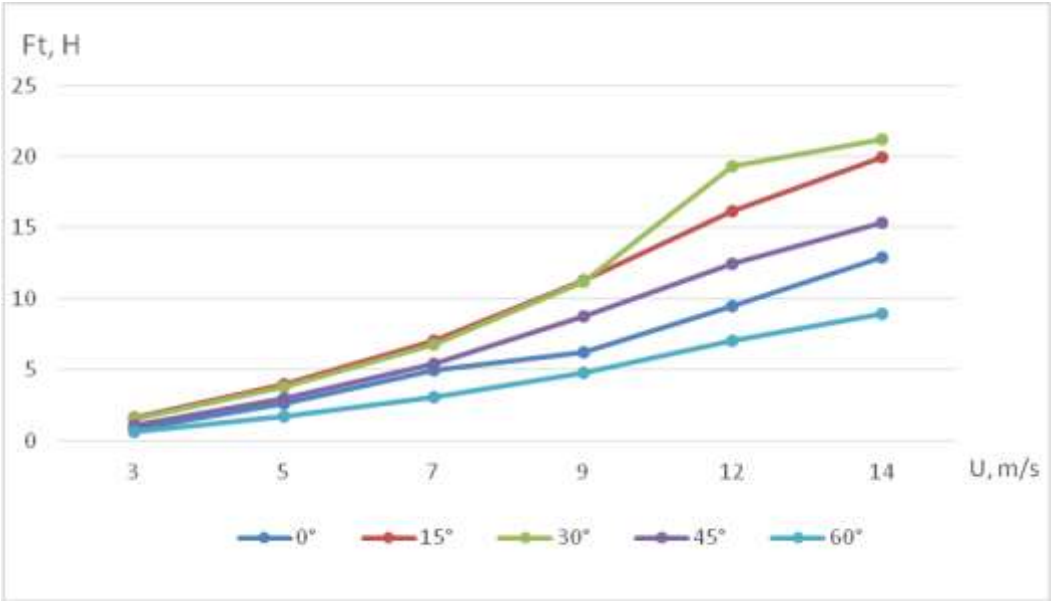

Figure 5 The thrust force (F_t) of a sailing wind power plant as a function of the air flow velocity (U)

As can be seen from Figure 5, the thrust force (F_t) on the sail blades depends on the deflection angle (α) of the air flow. At small deflection angles (α = 0 — 30 °), the air flow is almost parallel to the surface of the blades, which creates a large thrust force. Consequently, at α = 0°, the thrust force is F_t =0.81 N (at U=3m/s) and F_t=12.9 N (at U=14 m/s). When the angle of the sail blades changes, the part of the kinetic energy of the wind is converted into the potential energy of the sail. The sail begins to work like a wing, creating not only horizontal thrust, but also vertical lift. Consequently, at α = 30° deflection of the blades, the thrust force has a maximum value of F_t = 1.6 N (at U = 3 m/s) and reaches (F_t=19.99 N at U= 14 m/s.)

Thus, at large deflection angles (more than α = 30 °), the air flow begins to break and form vortices behind the blades (α = 45° F_t=1.56 at U=3 m/s) and (F_t= 21.25 N at U=14 m/s), which leads to a smooth decrease in the thrust force (α = 60° F_t=0.7 N at U=3 m/s and (F_t= 8.96 at U=14 m/s).

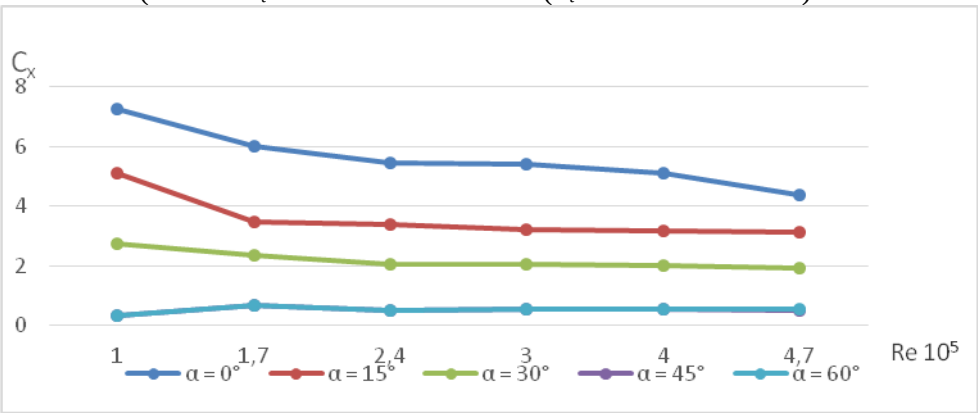

Figure 6. Dependence of the drag coefficient on the Reynolds number for a sailing wind power plant at different angles of deflection of the sailing blades

As the Reynolds number increases (Fig. 6), the pressure on the surface of the sail blades gradually rises. This phenomenon leads to a decrease in the frontal coefficient at α = 0° C_x = 0.73 (at Re = 10^5) and C_x = 0.44 (at Re= 4.7*10^5).

When the deflection angle changes, the vector of the force acting on the sail blades changes. As a result, the resistance force also changes, which is displayed on the charts depending on the angle of deviation in the range: α = from 0 to 60 °. At a deflection angle α = 60° (C_x = 0.0329 at Re = 10^5) and (C_x = 0.077 at 4.7 * 10^5).

Thus, the changes in the drag coefficients on the graph are due to changes in the Reynolds number and the deflection angle of the sail blades.

Figure 7 shows the dependence of the thrust coefficient (C_x) on the Reynolds number (Re) for a sailing wind power plant.

The studies were carried out at different angles of deflection of the blades (from α = 0° to 60 °) for this wind power plant.

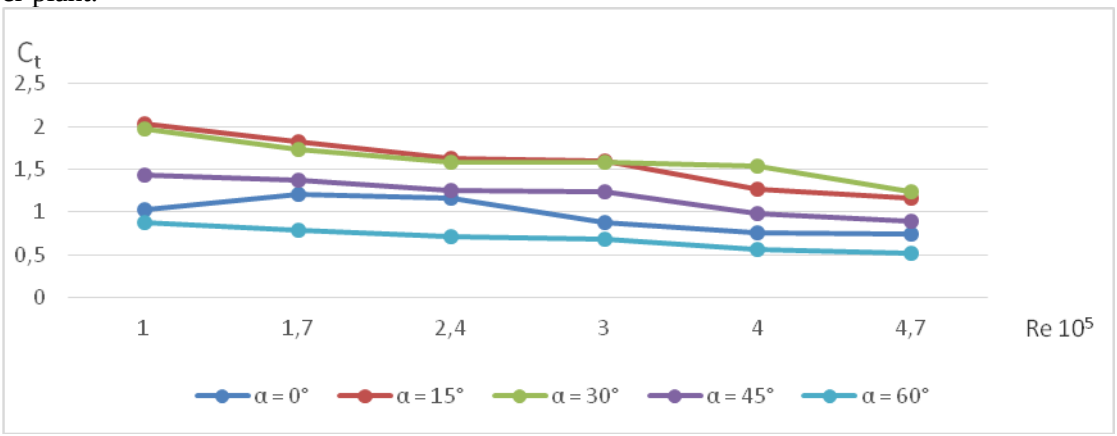

Figure 7. Dependence of the thrust coefficient on the Reynolds number for a sailing wind power plant

With an increase in the Reynolds number (Fig. 7), the thrust coefficient growths and reaches a maximum at the angle of deflection of the blades α = 30 ° C_t = 2 (at Re = 10^5) and C_t = 1.16 (at Re = 4.7·10^5), then decrease with a further increase in the angle of attack. This is due to changes in the flow conditions of the installation surface at different wind speeds and deflection angles of the blades.

Conclusions

Based on the results obtained, the following conclusions can be drawn:

- an experimental model with the specified parameters was developed, which was subsequently carried out experimental studies in the T-1-M wind tunnel in order to obtain data on aerodynamic characteristics.

- the number of rotations of the shaft of the wind power plant from the air flow velocity is set. The maximum rotation speed of the wind turbine shaft is fixed at N= 948 [rpm] at U=14 m/s. A high number of revolutions leads to excessive wear and damage to the equipment, as well as to an excess of noise and vibrations. The data obtained will help to choose the angle of deflection of the sail blades for optimal operation of the wind power plant.

- the dependence of the drag force on the air flow velocity is obtained. It is established that with an increase in the air flow velocity, the drag force rises smoothly. The maximum drag force was reached at U=14 m/s (F_d = 0.911 N).

Experimental data showed that in order to obtain the maximum thrust force, it is necessary to select the optimal angle of deflection of the blades, in our case, with a deflection angle $\alpha = 30°$ of peak values, the thrust force reached F_t = 1.607 N (U = 14 m/s).

- the optimal deflection angle $\alpha = 30$ ° is determined, where the maximum coefficient of thrust of the sail blades ($C_t = 2$) is fixed (Reynolds number $1{,}7 \cdot 10^5$). With a slight deflection of the blades, the wind acts on the blades at a certain angle, creating a lifting force that leads to the rotation of the rotor of the wind turbine and an increase in the thrust force. However, as the deflection angle of the sail blades increases, the lifting force reaches its maximum and begins to decrease, as the wind ceases to affect the blades at the same angle. This leads to a decrease in the thrust force on the blades, which in turn leads to a slowdown in the rotation of the wind turbine rotor.

Thus, the data obtained will make it possible to create and develop a wind energy system. An installation that will allow rational and efficient use of wind energy resources. Also, with the help of a controlled system of blades, you can choose the optimal angle of deviation for more productive use of the wind power plant.

Acknowledgment

The work was carried out with the financial support of the Science Committee of the Ministry of Science and Higher Education of the Republic of Kazakhstan (IRN AP14870066 “Development and creation of an energy-efficient combined vertical-axial wind power plant using a gearless low-speed electric generator”).

References

1 Тлеубергенова А.Ж. Исследование аэродинамических сил треугольной лопасти ветротурбины при низких скоростях ветра / А.Ж. Тлеубергенова, Н.К. Танашева, К.М. Шаймерденова, Л.Л. Миньков, С.Ж. Узбергенова // Eurasian Physical Technical Journal. — 2021. — Т. 18, № 4 (38). — С. 59–64.

2 Алибекова А.Р. Экспериментальные испытания опытной ветроэнергетической установки в условиях естественного ветра при различных климатических условиях // А.Р Алибекова, К.К. Кусаиынов, Ж.Т. Камбарова, Н.К. Танашева, М.Б. Карагаева // Вестн. Караганд. ун-та.Сер. Физика. — 2015. — № 2 (78). — С. 44–49.

3 Танашева Н.К. Исследование зависимости аэродинамических характеристик вращающихся цилиндров от угла скоса воздушного потока / Н.К. Танашева, Н.Н. Шуюшбаева, Н.К. Мусенова // Письма в ЖТФ. — 2018. — Т. 44, № 17. — С. 63–65.

4 Han J-B. An aerodynamic model for insect flapping wings in forward flight / J-B. Han, JW. Chang, J-H. Han // Journal of Bioinspiration and Biomimetics. — 2017. — Vol. 12. — P. 3600 –36014

5 Noest R.M. Optimal wing hinge position for fast ascent in a model fly / R.M. Noest, Z.J. Wang // Journal of Fluid Mechanics — 2018. — Vol. 849. — P. 498-509.

6 Hosseinie R. Parametric study of a novel oscillatory wind turbine / R. Hosseinie, R. Roohi, G Ahmadi // Journal of Energy Equipment and Systems — 2018. — Vol. 7, No. 4 — P. 377 — 387

7 Hosseinie R. Parametric study and performance analysis of a swinging sail wind machine / R. Hosseinie, R. Roohi, G. Ahmadi // Journal of Energy Conversion and Management. — 2020. — Vol. 205 — P. 112452—112465

8 Wang Z.J. Insect flight: from Newton's law to neurons / Z.J. Wang // Annual Review of Condensed Matter Physics. — 2016. — Vol. 7. — P. 281—300.

9 Kumar A. Performance analysis of a Savonius hydrokinetic turbine having twisted blades. / A. Kumar, R.P. Saini // Journal of Renewable Energy. — 2017. — Vol. 108. — P. 502—522.

10 Kumar A. Performance analysis of a single stage modified Savonius hydrokinetic turbine having twisted blades / A. Kumar, R.P. Saini // Journal of Renewable Energy. — 2017. — Vol. 113. — P. 461—478.

Н.К. Танашева, М.А. Бурков, А.Н. Дюсембаева, С. Сулейменова, А.С. Тусупбаева, С.С. Кыздарбекова

Жел энергетикалық қондырғының желкенді қалақшасының оңтайлы ауытқу бұрышын анықтау

Мақалада желкенді жел қондырғысын әртүрлі параметрлерде зерттеу нәтижелері келтірілген. Осы мақсатта басқарылатын қалақ жүйесі бар жел қондырғысының макеті жасалды. Желкенді қалақшаның ауытқуының әртүрлі бұрыштарындағы аэродинамикалық күштерге зерттеулер жүргізілді: 0°; 30°; 60°; 90°. Тәжірибелер желкенді жел турбинасына әсер ететін күштер мен моменттерді өлшеуге арналған Т-1-М жел туннелінде жүргізілді. Жүргізілген тәжірибелер нәтижесінде ауа ағынының жылдамдығы артқан сайын жел электр станциясының білігінің айналу жиілігі артатыны анықталды. Біліктің максималды айналу жиілігіне жел қондырғысының желкенді қалақтары α = 0°ауытқыған кезде қол жеткізіледі. Жел электр станциясының желкенді қалақтарының ауытқу бұрышына (α) және ауа ағынының айналу жылдамдығына байланысты бірқатар эксперименттер жүргізіліп, аэродинамикалық сипаттамалар алынды. Тәжірибе барысында қалақшаның ауытқу бұрышы артқан кезде ауа ағынының жылдамдығына байланысты кедергі күші азаятыны анықталды. α = 30° кезінде желкенді қалақшалардың ауытқуы максималды тарту күшін тудыратыны тәжірибе негізінде дәлелденді. Алынған мәліметтер негізінде аэродинамикалық коэффициенттердің өзгеру графиктері (фронтальды кедергі, жел электр станциясының тартылуы) ұсынылған. Қарсы ауа ағынының жылдамдығының жоғарылауымен желкенді жел қондырғысына әсер ететін аэродинамикалық күштер көбейетіні анықталды. Бұл зерттеудің нәтижелері басқарылатын қалақша жүйесі бар желкенді жел қондырғыларын одан әрі дамыту үшін пайдалы болуы және жел энергиясын өндіруде осындай жүйелердің тиімділігін арттыруға ықпал етуі мүмкін.

Кілт сөздер: желкенді қалақша, жел энергетикалық қондырғы, біліктің айналу жиілігі, жел турбинасы, ауытқу бұрышы, маңдай кедергі, тарту күші, Т-1-маэродинамикалық құбыр.

Н.К. Танашева, М.А. Бурков, А.Н. Дюсембаева, С. Сулейменова, А.С. Тусупбаева, Ш.С. Кыздарбекова

Определение оптимального угла отклонения парусной лопасти ветроэнергетической установки

В статье приведены результаты исследований парусной ветроэнергетической установки при различных параметрах. Для данной цели разработан макет ветроэнергетической установки, управляемой системой лопастей. Проведены исследования аэродинамических сил при различных углах отклонения парусных лопастей: 0°; 30°; 60°; 90°. Скорость воздушного потока варьировалась в диапазоне от 3 до 14 м/с. Эксперименты проводились в аэродинамической трубе Т–1–М, предназначенной для измерений сил и моментов, действующих на парусную ветротурбину. В результате проведенных экспериментов установлено, что с увеличением скорости воздушного потока возрастает частота вращения вала ветроэнергетической установки. Максимальная частота вращения вала достигнута при α=0° отклонения парусных лопастей ветроэнергетической установки. Проведен ряд экспериментов и получены аэродинамические характеристики в зависимости от угла отклонения (α) парусных лопастей ветроэнергетической установки и скорости обтекания воздушным потоком. В ходе проведения экспериментов установлено, что при увеличении угла отклонения лопасти сила лобового сопротивления уменьшается в зависимости от скорости воздушного потока. Экспериментально доказано, что при α=30° отклонения парусных лопастей создается максимальная сила тяги. На основе полученных данных представлены графики изменения аэродинамических коэффициентов (лобового сопротивления, тяги ветроэнергетической установки). Определено, что с увеличением скорости набегающего потока воздуха аэродинамические силы, действующие на парусную ветроэнергетическую установку, возрастают.

Ключевые слова: парусная лопасть, ветроэнергетическая установка, частота вращения вала, ветротурбина, угол отклонения, лобовое сопротивление, сила тяги, аэродинамическая труба Т–1–М.

References

1 Tleubergenova, A.Zh., Tanasheva, N.K., Shaimerdenova, K.M., Minkov, L.L. & Uzbergenova, S.Zh. (2021). Issledovanie aerodinamicheskikh sil treugolnoi lopasti vetroturbiny pri nizkikh skorostiakh vetra [Investigation of the aerodynamic forces of a triangular wind turbine blafe for the low wind]. *Eurasian Physical Technical Journal, 18, 4*(38), 59–64 [in Russian].

2 Alibekova, A.R., Kusaiynov, K.K., Kambarova, Z.T., Tanasheva, N.K. & Karagaeva, M.B. (2015). Eksperimentalnye ispytaniia opytnoi vetroenergeticheskoi ustanovki pri razlichnykh klimaticheskikh usloviiakh [Experimental tests of an experimental wind power plant in natural wind under different climatic conditions]. *Vestnik Karagandinskogo universiteta. Seriia Fizika — Bulletin of the Karaganda University. Physics series, 2*(78), 44–49 [in Russian].

3 Tanasheva, N.K., Shuyushbaeva, N.N. & Musenova, N.K. (2018). Issledovanie zavisimosti aerodinamicheskikh kharakteristik vrashchaiushchikhsia tsilindrov ot ugla skosa vozdushnogo potoka [Investigation of the dependence of the aerodynamic characteristics of rotating cylinders on the angle of the bevel of the air flow]. *Pisma v ZhTF — Letters to the Journal of Technical Physics*, *44*, 17, 63–65 [in Russian].

4 Han, J-B., Chang, J.W. & Han, J-H. (2017). An aerodynamic model for insect flapping wings in forward flight. *Journal of Bioinspiration and Biomimetics, 12*, 3600–36014.

5 Noest, R.M. & Wang, Z.J. (2018). Optimal wing hinge position for fast ascent in a model fly. *Journal of Fluid Mechanics. 849*, 498–509.

6 Hosseinie R., Roohi R. & Ahmadi, G. (2018). Parametric study of a novel oscillatory wind turbine. *Journal of Energy Equipment and Systems, 7*(4), 377—387

7 Hosseinie, R., Roohi, R. & Ahmadi, G. (2020). Parametric study and performance analysis of a swinging sail wind machine. *Journal of Energy Conversion and Management, 205*, 112452—112465

8 Wang, Z.J. (2016). Insect flight: from Newton's law to neurons. *Annual Review of Condensed Matter Physics, 7*, 281—300.

9 Kumar, A. & Saini, R.P. (2017). Performance analysis of a Savonius hydrokinetic turbine having twisted blades. *Journal of Renewable Energy, 108*, 502—522.

Kumar, A. & Saini, R.P. (2017). Performance analysis of a single stage modified Savonius hydrokinetic turbine having twisted blades. *Journal of Renewable Energy, 113*, 461—478.

DOI 10.31489/2023PH3/136-142

UDC 621.7.02

B.K. Rakhadilov[1,2], N.E. Berdimuratov[1,2], L.G. Zhurerova[1,2], L.B. Bayatanova[2], Sh.R. Kurbanbekov[3], Z.A. Satbayeva [2]

[1]Research Center "Surface Engineering and Tribology", Sarsen Amanzholov East Kazakhstan University, Ust-Kamenogorsk, 070000, Kazakhstan;
[2]PlasmaScience LLP, Ust-Kamenogorsk, 070010, Kazakhstan;
[3]Khoja Ahmed Yasawi International Kazakh-Turkish University, Turkestan, 161200, Kazakhstan
(E-mail: nurbol.ber@gmail.com)

Study of the VAC of the EPCTT process with varying electrode parameters

Nowadays the treatment of machine parts, instruments is one of the actual topics in the modern world. One of the modern processing method is chemical-thermal treatment of parts, in which there is an increase of hardness in the surface part to increase wear resistance, while the core of the part remains in a ductile state for resistance to shock loading. The solution to this problem could be the electrolytic plasma chemical-thermal treatment of the parts. This method has a number of advantages over traditional methods, such as cost-effectiveness and speed of processing. In the present work the influence of changes in technological parameters on the volt-ampere characteristics of electrolyte-plasma chemical-thermal treatment unit is presented. A solution of soda ash (Na_2CO_3), urea (CH_4N_2O) in distilled water was used as an electrolyte. According to the results of the study current-voltage diagrams were plotted by varying the diameter of the anode (D=90; 110;130 mm) and the distance between the electrodes (L=50;70; 90 mm). According to the analysis, in the voltage range of 180-220 V, with anode diameter D=110 mm and electrode spacing D=70 mm, a more stable vapor-gas envelope is formed. It was found that by changing the anode diameter, respectively the ratio of active and passive electrodes we can significantly influence the formation of stable vapor gas shell and establishment of the optimum mode of treatment of parts.

Keywords: electrolytic-plasma chemical-thermal treatment, volt-ampere characteristic, electrodes, vapor-gas shell, anode.

Introduction

The problem of increasing the hardness and wear resistance of machine parts, tools and equipment is a very urgent task in modern industry and mechanical engineering. The modern manufacturing industry has many solutions to this issue. The physical and chemical state of the parts surface has a significant impact on the equipment operability. The chemical-thermal treatment (CTT) is one of the actual solutions of this issue. This process can produce a hardened layer on the surface of steel by diffusing the atoms of various chemical elements into the atomic-crystalline lattice of iron by heating the steel parts in an environment enriched with these elements. Surface hardness increases in the surficial part, while the core of the part remains in a ductile state. The surface hardness provides increased wear resistance, while the ductile core provides resistance to impact loading of the parts [1].

There are traditional methods of chemical-thermal treatment of steels such as detail treatment in a gas environment, in a solid environment, etc. All of these methods are complicated by the fact that such treatment takes a lot of time, energy resources and is difficult to perform.

Currently, another method of chemical heat treatment is electrolyte-plasma chemical heat treatment of steels used in mechanical engineering. This method of part treatment is one of the effective methods that allow improving the required physical and mechanical properties of parts in much less time, compared to traditional chemical heat treatment processes, which require somewhat more time for processing [2].

During EPCTT, the area around the active electrode is heated by a current flowing through the electrolyte, leading the electrolyte to a "boiling-evaporating" state, which contributes to the "gaseous formation" process. Further heating of the gaseous state leads to the separation of free electrons from the particles followed by the formation of positive ions with free electrons. The free electrons are current conductors, and form a plasma layer on the surface of the cathode (detail) in the area of the "vapor-gas shell" (VGS), where the conversion of electrical energy into heat occurs. The plasma layer appears as a glow discharge, and can heat the steel to a temperature of up to 2000℃. [3, 4].

As a result of the high temperature, the surface of the detail is saturated with evaporation elements from the electrolyte in the VGS, due to thermal decomposition of components and electrochemical reactions on the surface of the detail, through diffusion [5].

During EPCTT, the establishment of stable VGS depends on such parameters as the ratio of the areas of the active and passive electrodes, shape, electrolyte parameters (composition, concentration, volume, flow rate), and the distance between the electrodes [6].

The stability of VGS in the treatment process provides the system with a stable temperature and a steady flow of the treatment process. The author's work [7] previously studied the behavior of the system VAC during EPCTT of details. And there were distinguished zones of electrolyte boiling, VGS formation zone, VGS steady state zone, etc. During the study of these works we concluded that the VAC has a direct influence on the selection of the parts treatment mode. However, to date, in spite of the vast knowledge base, this issue has not yet been fully explored.

In accordance with the above facts, the purpose of this research work is to study the change of VAC in the EPCTT process with varying the technological parameters (anode size and distance between the anode and cathode) of EPCTT.

Materials and methods

As samples for the test we chose steel 20X which is widely used in industry for the manufacture of parts such as: bushings, gears, clutches, etc. which require high surface hardness and low core strength, parts operating in conditions of frictional wear [8]. The chemical composition of steel 20X (according to GOST 4543 — 71 following: C (0.17 — 0.24 %), Si (0.17 — 0.37), Mn (0.35 — 0.65), S to 0.04, P to 0.04, Ni to 0.25, Cr to 0.25, Cu to 0.25, As to 0.08, Fe ~98.

Before the experiment, the surface of the samples cut from bars of steel 20X (size 2 × 2 × 1 cm3) were polished on sandpaper with a grain size of P100 to P2000, followed by polishing with diamond paste size 0.25-0.5 microns and cleaned with ethanol.

Experimental works were carried out at the EPCTT unit assembled at Plasmascience LLP. Schematic diagram of the EPCTT unit is shown in Figure 1, which consists of a direct current source (1), electrodes (cathode (3) and anode (2)), an electrolyte bath (4), a valve (5) to control the electrolyte flow and a pump (6) to circulate the electrolyte.

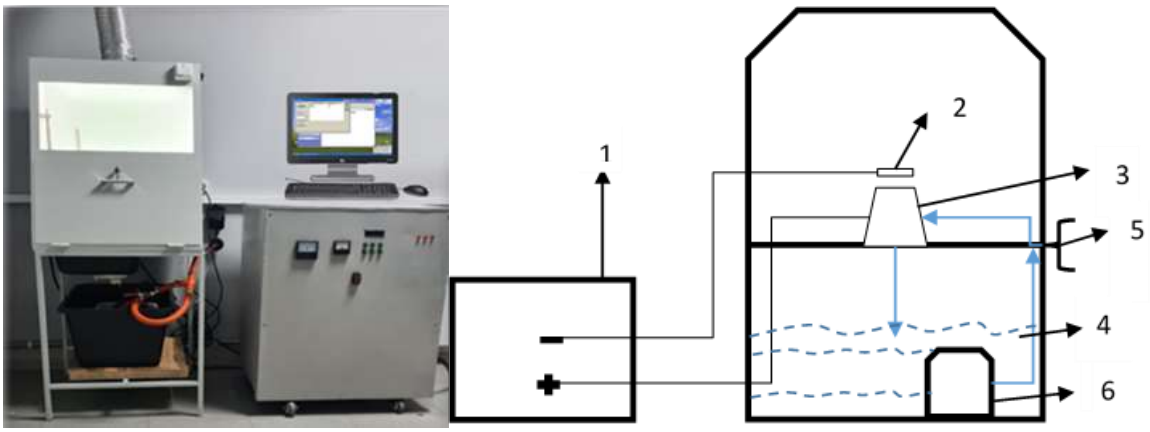

Figure 1. Schematic diagram of the electrolyte-plasma chemical and thermal treatment unit.

The EPCTT unit consists of a power source in the form of a powerful rectifier, which gives a maximum output value of 360V/100A in the form of direct current and electrodes (anode and active cathode). The cathode is a detail, the anode is presented in the form of a round plate having a group of holes for uniform distribution and passage of electrolyte (Fig. 2). The anode is located inside the electrolytic cell with a cover in the form of a truncated cone (Fig. 2). The cone has an upper hole with diameter D=25 mm for uniform feeding of electrolyte. Based on our previous studies [9], an aqueous solution (distilled water) of 10 % soda ash (Na_2CO_3) and 20 % carbamide (CH_4N_2O) (mass %) was used as an electrolyte, which is considered to be more efficient and optimal for the formation of stable plasma.

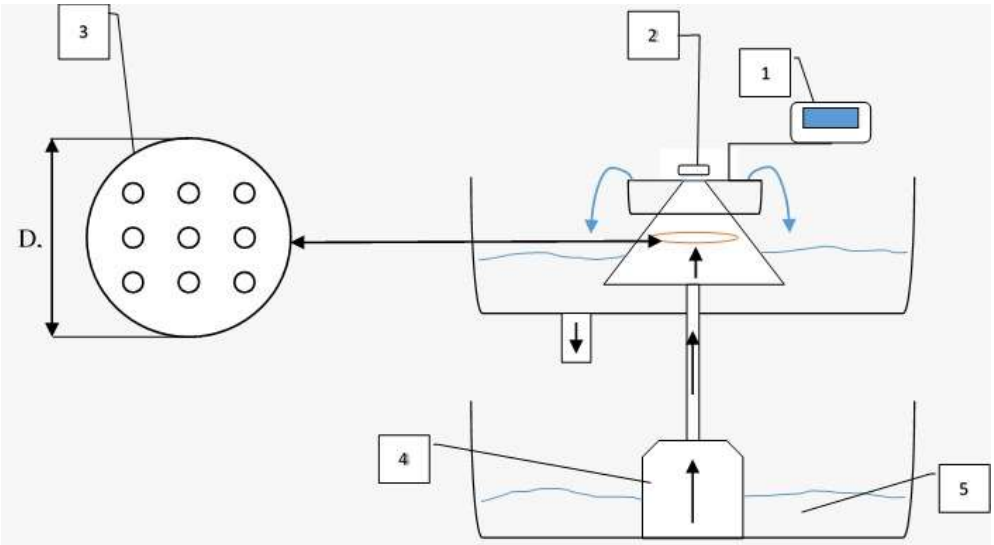

Figure 2. Schematic diagram of an electrolytic cell:
1 — thermocouple to measure the electrolyte temperature; 2 — cathode; 3 — anode; 4 — pump; 5 — bath with electrolyte

At the beginning of the experiment, the active electrode (cathode) was partially immersed in the electrolyte by 1-2 mm and a thermocouple was placed nearby to measure the electrolyte temperature near the active electrode. Then, voltages were applied to the electrodes from the constant power supply starting from 20 V up to 340 V, and the readings of amperemeter and voltmeter placed on the power supply were recorded. Based on the results of the data obtained during the experiment, a graph of the VAC was plotted.

Results and Discussion

1. Research of the VAC at different values of the anode diameter.

For heating the active electrode (cathode) to the temperature of stable EPCTT process flow, we need to choose the optimal size of the anode, contributing to the formation of stable VGS [10]. Table shows the values of varying parameters in the estimation of the VAC of the EPCTT process.

T a b l e

Values of the varying parameters in the estimation of the EPCTT process's VAC

№	1	2	3
DiameterD, mm	86	110	130
DistanceL, mm	50	70	90

Based on the results of the experiment, we plotted the volt-ampere characteristics of the electrolyte, where we can observe the areas of voltage and current changes (Fig. 3).

The first region, the value of current changes proportional to the applied voltage (U=0-140V in Fig. 3) In this region, we can observe that the electrode and electrolyte temperatures in this region are less than the boiling point. As the voltage increases from 140 to 160V in the second region, we can observe an increase in the current up to the maximum value. In this area the electrolyte temperature increases near the cathode with the generation of vapor and the formation of a bubble layer. At the end of this region there is a sharp decrease and oscillation of the current. This is possible due to the instability of the system and rapid boiling of the electrolyte with the occurrence of separate current discharges. Rapid decrease of current value in this area is explained by formation of VGS, and steep jump of resistance in the system cathode-VGS-electrolyte. The third area at voltage values of 180-220V the current becomes constant, which forms a stable VGS around the cathode. As the voltage increases further, an abnormal discharge is observed, which leads to a rapid increase of current followed by an increase in temperature until the melting of the electrode [9, 11].

An important factor in EPCTT is the VGS area, we will observe the behavior of VGS by varying parameters such as anode diameter and the distance between the electrodes.

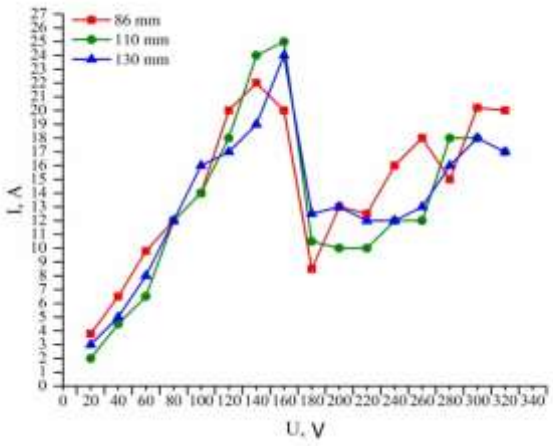

Figure 3: Graphic of volt-ampere characteristics as a function of anode size.

According to the presented Figure 3 at the anode diameter D=86 mm, we can observe on the section 180-200V the instability of VGS. We can assume that due to low value of current VGS is thinned, which is accompanied by decrease of system resistance and electric discharges with splashing of electrolyte, which cools the cathode, occur. Based on our observations, the vapor-gas shell becomes unstable, there appear current surges and electrolyte splashing, which are also described in the works of the authors [10].

In the second case, at anode diameter D=110 mm, we observe in the area of VGS formation at voltages of 180-200 V the stability of the system, which is explained by the steadiness of VGS.

The results of the experiment with the anode D=130 mm at a voltage range of 180-200V showed that the VGS is stable, but the value of the current is high, due to which the sample is heated, causing partial melting the surface of the sample part.

2. Study of the anode's VAC varied with the anode-cathode distance.

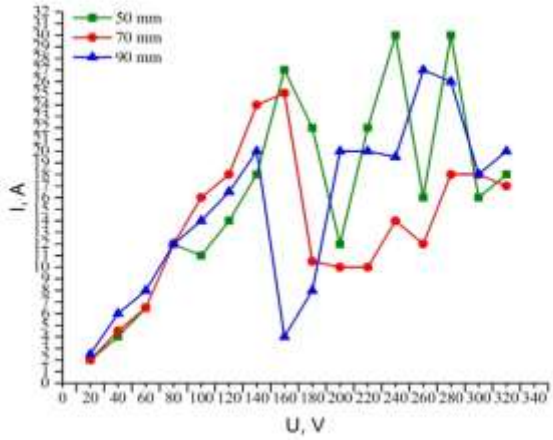

Figure 4: Graph of volt-ampere characteristics as a function of the distance between the anode and cathode.

In Figure 4 we can observe the inversely proportional dependence between parameters of current strength and distance between electrodes: in a zone of 140-160 V voltage at distance L=50 mm we see a steep increase in current, and with increasing distance to L=90 mm we see a steep decrease in current strength. According to the literature analysis we suppose that in the first case during boiling and bubbling of bubble layer the cathode surface is bombarded with arc discharges of high energy due to short distance between the electrodes and small resistance path which makes useful energy of the system very high which

leads to strong discharge of system with the following burst of discharges. Strong discharges, in their turn, constantly destabilize the system by disrupting the VGS.

Thereby, considering the system at values of L=90 mm due to the large distance between the electrodes, the current passes a larger resistance path, and the system does not have enough energy for strong discharges, which leads to a decrease in the current strength. Further we observe that with increasing voltage the energy of the system increases, and at 200 V, there is enough energy to create and maintain VGS.

At the value of distance L=50 mm we observe in the voltage range of 180-200 V a stable area of VGS formation, with the current parameter satisfying the requirements of VGS stability.

Also during the experimental work, when measuring the temperature of the electrolyte with a thermocouple, we observed that the temperature changes linearly up to the value of 160V from room temperature 24℃ to 90℃ boiling point of the electrolyte. According to the analysis of the VAC diagram of the EPCTT process, the resistance value in the electrolyte decreases and the conductivity increases with increasing temperature.

Conclusion

In the present work, we studied and investigated the VAC of the EPCTT process by changing the diameter of the anode and the distance between the electrodes. Based on the analysis of the obtained results we can make the following conclusions:

1. It was found that by changing the anode diameter and the ratio between the active and passive electrodes respectively we can influence essentially to the formation of stable VGS and establishment of the optimal mode of detail treatment.

2. It was revealed that decreasing the distance of active and passive electrodes leads to the growth of useful energy, which contributes to the formation of stable VGS.

Therefore, by changing the above-mentioned parameters of the EPCTT unit we can select the optimal mode for treatment and hardening of parts.

Acknowledgment

This research is funded by the Science Committee of the Ministry of Science and Higher Education of the Republic of Kazakhstan (Grant No. AP09058547).

References

1 Корецкий Я. Цементация стали / Я. Корецкий. — Л.: Гос. союз. изд-во судостроит. пром., 1962. — 9 с.

2 Baizhan D. Investigation of Changes in the Structural-Phase State and the Efficiency of Hardening of 30CrMnSiA Steel by the Method of Electrolytic Plasma Thermocyclic Surface Treatment / D. Baizhan, B. Rakhadilov, L. Zhurerova, Y. Tyurin, Zh. Sagdoldina, M. Adilkanova, R. Kozhanova // Coatings. — 2022. — Vol. 12(11). — P. 1696. DOI: https://doi.org/10.3390/coatings12111696

3 Рахадилов Б.К. Структурное превращение в стали 20 ГЛ после электролитно-плазменной поверхностной закалки / Б.К. Рахадилов, Д.Р. Байжан, Ж.Б. Сагдолдина, А.Б. Кенесбеков // Вестн. НЯЦ РК. — 2018. — № 3. — С. 103–109.

4 Vitthal R. Application of Electrolytic Plasma Process in Surface Improvement of Metals: A Review / R. Vitthal, A.Ch., Jumbad, V. Updesh, K. Geetanjali // Letters in Applied NanoBioScience. — 2020. — Vol. 9(3). — P. 1249-1262. DOI: doi.org/10.33263/LIANBS93.12491262

5 Белкин П.Н. Электролитно-плазменная цементация металлов и сплавов / П.Н. Белкин, С.А. Кусманов // Электронная обработка материалов. — 2020. — № 5. — С. 40–74. DOI: 10.5281/zenodo.4045823

6 Попов А.И. Анализ тепловых явлений при струйной фокусированной электролитно-плазменной обработке / А.И. Попов, М.И. Тюхтяев, М.М. Радкевич, В.И. Новиков // Материаловедение. Энергетика. — 2016. — № 4 (254). — С. 141–150. DOI 10.5862/JEST.254.15

7 Сатбаева З.А. Структурообразование в легированных сталях при электролитно-плазменном поверхностном упрочнении: дис. ... д-ра филос. (PhD) / З.А. Сатбаева. — Усть-Каменогорск, 2022.

8 Воробьева Г.А. Конструкционные стали и сплавы / Г.А. Воробьева, Е.Е. Складнова, В.К. Ерофеев, А.А. Устинова. — СПб.: АО «Издательство ”Политехника”», 2013. — 440 с.

9 Рахадилов Б.К. Электролитно-плазменное азотирование поверхностных слоев быстрорежущих сталей: дис. ... д-ра филос. (PhD) / Б.К. Рахадилов. — Усть-Каменогорск, 2014.

10 Суминов И.В. Плазменно-электролитическое модифицирование поверхности металлов и сплавов / И.В. Суминов, П.Н. Белкин, А.В. Эпельфельд, В.Б. Людин, Б.Л. Крит, А.М. Борисов. — М.: Техносфера, 2011. — Т. I. — 45 с.

11 Словецкий Д.И. Механизм плазменно-электролитного нагрева металлов / Д.И. Словецкий, С.Д. Терентьев, В.Г. Плеханов // ТВТ.— 1986. — Т. 24 (2). — С. 353–363.

Б.К. Рахадилов, Н.Е. Бердімуратов, Л.Г. Журерова, Л.Б. Баятанова,
Ш.Р. Курбанбеков, З.А. Сатбаева

Электродтардың параметрлерін өзгертудің ЭПХТӨ тәсілінің ВАС-қа әсерін зерттеу

Қазіргі әлемде машиналар мен құралдардың бөлшектерін өңдеу өзекті тақырыптардың бірі. Өңдеудің заманауи әдістерінің бірі — бөлшектерді химиялық-термиялық өңдеу, онда тозуға төзімділікті арттыру үшін беткі бөлікте қаттылық жоғарылайды, ал бөліктің өзегі соққы жүктемесінің тұрақтылығы үшін тұтқыр күйде қалады. Бұл мәселенің шешімі ретінде электролиттік-плазмалық химиялық-термиялық өңдеуді қарастыруға болады. Осы әдіс дәстүрлі әдістерге қарағанда бірқатар артықшылықтарға ие, мысалы: үнемділік және өңдеу жылдамдығы бойынша. Жұмыста технологиялық параметрлердің өзгеруінің электролиттік-плазмалық химиялық-термиялық өңдеу қондырғысының вольт-ампер сипаттамаларына әсері қарастырылған. Электролит ретінде тазартылған суда кальцийленген сода (Na_2CO_3), карбамид (CH_4N_2O) ерітіндісі қолданылды. Зерттеу нәтижелері бойынша анодтың диаметрі (D=90;110;130 мм) және электродтар арасындағы қашықтық (l=50;70;90 мм) өзгерген кезде токтың кернеуге тәуелділігі графиктері салынды. Талдауға сәйкес 180-220 В кернеу аралығында d=110 мм в анодының диаметрі және D=70 мм электродтар арасындағы қашықтық кезінде неғұрлым тұрақты бу-газ қабығы пайда болады. Анодтың диаметрін, сәйкесінше белсенді және пассивті электродтардың арақашықтығын өзгерту арқылы біз тұрақты бу-газ қабығының түзілуіне және бөлшектерді өңдеудің оңтайлы режимін орнатуға айтарлықтай әсер ете алатынымыз анықталды.

Кілт сөздер: электролиттік-плазмалық химиялық-термиялық өңдеу, вольт-ампер сипаттамасы, электродтар, бу-газ қабығы, анод.

Б.К. Рахадилов, Н.Е. Бердімуратов, Л.Г. Журерова, Л.Б. Баятанова,
Ш.Р. Курбанбеков, З.А. Сатбаева

Изучение ВАХ процесса ЭПХТО при варьировании параметров электродов

В современном мире обработка деталей машин, инструментов является одной из актуальных тем. Одним из современных методов обработки является химико-термическая обработка деталей, при которой происходит повышение твердости в поверхностной части для повышения износостоикости, а сердцевина детали остается в вязком состоянии для стойкости при ударной нагрузке. Решением данной проблемы может оказаться электролитно-плазменная химико-термическая обработка деталей. Данный способ имеет ряд преимуществ перед традиционными способами, такими как экономичность и скорость обработки. В настоящей работе рассмотрено влияние изменений технологических параметров на вольт-амперные характеристики установки электролитно-плазменной химико-термической обработки. В качестве электролита использовали раствор кальцинированной соды (Na_2CO_3), карбамида (CH_4N_2O) в дистиллированной воде. По результатам исследования были построены графики зависимости тока от напряжения, при варьировании диаметром анода (D=90; 110; 130 мм) и расстоянием между электродами (L=50; 70; 90 мм). Согласно анализу в интервале напряжения 180–220 В, при диаметре анода D=110 мм и расстоянии между электродами D=70 мм формируется более устойчивая парогазовая оболочка. Установлено, что, изменяя диаметр анода, соответственно соотношение активного и пассивного электродов, мы можем существенно повлиять на образование стабильной ПГО и установление оптимального режима обработки деталей.

Ключевые слова: электролитно-плазменная химико-термическая обработка, вольт-амперная характеристика, электроды, парогазовая оболочка, анод.

References

1 Koreckii, Ya. (1962). Tsementatsiia stali [Cementation of steel]. Leningrad: Gosudarstvennoe soiuznoe izdatelstvo sudostroitelnoi promyshlennosti [in Russian].

2 Baizhan, D., Rakhadilov, B., Zhurerova, L., Tyurin, Y., Sagdoldina, Zh., Adilkanova, M., & Kozhanova, R. (2022). Investigation of Changes in the Structural-Phase State and the Efficiency of Hardening of 30CrMnSiA Steel by the Method of Electrolytic Plasma Thermocyclic Surface Treatment. *Coatings, 12*(11), 1696. DOI: https://doi.org/10.3390/coatings12111696

3 Rakhadilov, B.K., Baizhan, D.R., Sagdoldina, Zh.B., & Kenesbekov, A.B. (2018). Strukturnoe prevrashchenie v stali 20 GL posle elektrolitno-plazmennoi poverkhnostnoi zakalki [Structural transformation in steel of 20 HL after electrolytic-plasma surface

quenching]. *Vestnik Natsionalnogo yadernogo tsentra Respubliki Kazakhstan — Bulletin of the National Nuclear Center of the Republic of Kazakhstan, 3,* 103–109 [in Russian].

4 Vitthal, R., Jumbad, A.Ch., Updesh V., & Geetanjali, K. (2020). Application of Electrolytic Plasma Process in Surface Improvement of Metals: A Review. *Letters in Applied NanoBioScience*, *9*(3), 1249-1262. DOI: doi.org/10.33263/LIANBS93.12491262

5 Belkin, P.N., & Kusmanov, S.A. (2020). Elektrolitno-plazmennaia tsementatsiia metallov i splavov [Electrolytic plasma cementation of metals and alloys]. *Elektronnaia obrabotka materialov — Electronic processing of materials, 5,* 40–74. DOI: 10.5281/zenodo.4045823 [in Russian].

6 Popov, A.I., Tyukhtyaev, M.I., Radkevich, M.M., & Novikov, V.I. (2016). Analiz teplovykh yavlenii pri struinoi fokusirovannoi elektrolitno-plazmennoi obrabotke [Analysis of thermal phenomena in jet focused electrolyte-plasma treatment]. *Materialovedenie. Energetika — Materials science. Energy,* (254), 141–150. DOI 10.5862/JEST.254.15 [in Russian].

7 Satbaeva, Z.A. (2022). Strukturoobrazovanie v legirovannykh staliakh pri elektrolitno-plazmennom poverkhnostnom uprochnenii [Structure formation in alloy steels during electrolytic-plasma surface hardening]. *Doctor`s thesis.* Ust-Kamenogorsk [in Russian].

8 Vorobeva, G.A., Skladnova, E.E., Erofeev, V.K., & Ustinova, A.A. (2013). Konstruktsionnye stali i splavy [Structural steels and alloys]. Sankt-Peterburg: AO «Izdatelstvo “Politekhnika”» [in Russian].

9 Rakhadilov, B.K. (2014). Elektrolitno-plazmennoe azotirovanie poverkhnostnykh sloev bystrorezhushchikh stalei [Electrolyte-plasma nitriding of surface layers of high-speed steels]. *Doctor`s thesis*. Ust-Kamenogorsk [in Russian].

10 Suminov, I.V., Belkin, P.N., Epelfeld, A.V., Lyudin, V.B., Krit, B.L., & Borisov, A.M. (2011). Plazmenno-elektroliticheskoe modifitsirovanie poverkhnosti metallov i splavov [Plasma-electrolytic modification of the surface of metals and alloys]. *Tekhnosfera*, *1*, 45 [in Russian].

11 Sloveckii, D.I., Terentev, S.D., & Plekhanov, V.G. (1986). Mekhanizm plazmenno-elektrolitnogo nagreva metallov [Mechanism of plasma-electrolyte heating of metals]. *TVT*, *Vol. 24*(2), 353–363 [in Russian].

DOI 10.31489/2023PH3/143-150

UDC 621.548.9

A.Zh. Tleubergenova[1,2*], A.N. Dyusembayeva[1], N.K. Tanasheva[1,2],
Sh.S. Kyzdarbekova[1], A.R. Mukhamedrakhim[1]

[1]Karaganda University of the name of academician E.A. Buketov, Kazakhstan;
[2]Scientific Center "Alternative Energy", Karaganda, Kazakhstan
*(*e-mail: shymkent.a7@mail.ru)*

Analysis of aerodynamic characteristics of a two-bladed wind power plant containing combined power elements

In this article, the aerodynamic characteristics of a wind turbine of various parameters are studied. For this purpose, an experimental two-cylinder model with fixed blades was made. A schematic diagram of a wind turbine with fixed blades and rotating cylinders is obtained. The airflow velocity varied from 3 to 12 m/s. The dependences of the aerodynamic forces of a wind power plant on the flow velocity were investigated. The analysis of the results of the experiment on changing the angle α of the fixed blade relative to the cylinder from the airflow velocity of the wind turbine is carried out. When the position of the blade changes, the drag changes relative to the airflow. A graph is constructed based on the dependence of drag and lift forces on the flow velocity. It is established that at the maximum angle relative to the cylinder α = 30° that the value of the lifting force and the drag force of the fixed blade is higher. From the dependence of the coefficient of lift and drag force on the Reynolds number, it was found that at an angle of 30° degrees, there is a minimum lifting force of 0.04 and a maximum drag force of 1.479 at $Re=1\cdot10^4$. The results of the experiment show that it is possible to use an additional force driven by the Magnus effect that occurs when rotating cylinders with a horizontal axis. These results are considered useful for us in practice since these results can be used in combined wind engines operating at low wind speeds. This wind power plant can generate electricity starting from a wind speed of 2.8 m/s.

Keywords: Wind power plant, flow velocity, aerodynamic force, wind tunnel T-1-M, drag force, lifting force.

Introduction

Energy is the basis of the climate problem and the key to solving it. A significant part of the greenhouse gases covering the Earth and trapping solar heat is generated during energy production when fossil fuels are burned to generate electricity and heat. Fossil fuels such as coal, oil, and gas are by far the biggest contributors to global climate change: they account for more than 75 percent of global greenhouse gas emissions and almost 90 percent of all carbon dioxide emissions.

Scientific evidence clearly shows that to avoid the worst effects of climate change, it is necessary to reduce emissions by almost half by 2030 and achieve net zero emissions by 2050.

To achieve this goal, we need to end our dependence on fossil fuels and invest in alternative energy sources that are clean, affordable, inexpensive, sustainable, and reliable.

Renewable energy sources, which are abundant around us thanks to the sun, wind, water, waste, and heat of the Earth, are replenished naturally and practically do not emit greenhouse gases or pollutants into the atmosphere.

Fossil fuels still account for more than 80 percent of global energy production, but cleaner energy sources are gradually gaining ground. Currently, about 20 percent of electricity comes from renewable sources [1].

Wind power is the most successful way out of the situation. The fact is that with the help of one or two wind turbines, it is possible to provide energy to the entire estate without creating a large network with a lot of expensive equipment [2]. As a result, there is a high demand for improving the operational reliability, availability, and performance of wind turbine systems [3].

There are many discoveries and works in the field of wind energy that many scientists around the world are doing.

One of them, the invention [4] is aimed at obtaining the maximum possible energy from the wind flow. The trailing edges of all aerodynamic wings move synchronously. Feature A wind turbine mounted on the main horizontal shaft has aerodynamic wings attached to rods and a mechanism for changing the angles of attack of the a-wings.

In [5], a mathematical model of a horizontal-axial wind power plant is considered, in the design of which Savonius rotors are used instead of classical blades. The Magnus force formed during the autorotation of the Savonius rotors creates a moment that supports the rotation of the central shaft of the turbine. The main difference between this work and previous studies in this area is that the change in the width of the blades along the radius is taken into account. At the same time, within the framework of the model, the conical Savonius rotor is replaced by a pair of cylindrical rotors of different diameters, which makes it possible to use experimental force-moment characteristics, taking into account a significant change in the velocity field along the radius of the blade. The model considers the possibility of controlling the value of the external electrical resistance in the local circuit of the generator of the installation.

The wind energy industry has been constantly updated in recent decades to explain the development of recent decades, it relies on an extensive dataset consisting of 35-year-old inventions of several megawatt wind turbines. According to forecasts, the size of onshore and offshore wind turbines will continue to increase, although, according to forecasts, the largest increase will occur with offshore wind turbines [6].

The article [7] also provides an overview of the most important and updated methods of condition monitoring based on non-destructive testing and methods applied to wind turbine blades. In addition, it analyzes future trends and problems related to systems for monitoring the condition of wind turbine blade structures.

In this regard, the experimental model proposed by us is a two-cylinder wind turbine with fixed blades.

At the D.A. Kunaev Institute of Mining, under the leadership of N.S. Buktukov, a promising design of the Buktukov wind farm was developed [8], in which the change in the area of the swept surface occurs not by shifting the half-cylinders, but by turning, which allows significantly increasing the power (many other domestic studies on the development of wind power plants were also studied in detail).

The aerodynamic element described in [9] was adopted as a prototype of the aerodynamic element that creates the Magnus effect on the wind turbine blades. The disadvantage of this wind turbine is the huge consumption of electricity for the operation of the drive.

A distinctive feature in this work from the previous ones is the mutual combination of two different blades (rotating cylinders and fixed blades), which ensures high aerodynamic quality of the wind turbine.

The purpose of the work is to analyze the aerodynamic characteristics of a two-bladed wind power plant containing combined power elements.

Based on the goal, the following tasks are set:

1. Investigation of aerodynamic forces depending on the flow velocity.

2. Analysis of the coefficients of lift and drag force from the Reynolds number for various variants of the location of the fixed blade relative to the cylinder.

Experimental methodology

Experiments were carried out in a wind tunnel, which is a channel in which an artificial airflow is created with the help of a fan.

A wind tunnel is an installation that creates a flow of air or gas for an experiment, studying the phenomena accompanying the flow of bodies. Experiments in a wind tunnel are based on the principle of reversibility of motion, according to which the movement of a body relative to air (or liquid) can be replaced by the movement of air running into a stationary body. To simulate the motion of a body in stationary air, it is necessary to create a uniform flow in a wind tunnel, having equal and parallel velocities at any point (a uniform velocity field), the same density, and temperature. Usually, in a wind tunnel, the flow around the model of the projected object or its parts is investigated and the forces acting on it are determined [10-12].

The T-1-M wind tunnel includes a working part, a diffuser, a fan, a transition channel, rotating blades, leveling grids, a pre-chamber, and a collector (nozzle) [13].

The main part of the T-1-M wind tunnel is its working part. The working part of the pipe is the place where the model of the test body is attached to the aerodynamic scales (Fig. 1). Especially serious requirements are imposed on the flow of the working part. The dimensions of the model should be smaller than the corresponding dimensions of the working part so that the flow boundaries do not affect the flow around the model [14].

The most accurate and reliable is the direct method of measuring forces and moments using aerodynamic scales. To measure the lifting force and drag force at different flow rates, three-component aerodynamic scales were used (Fig. 1). Measurements of air flow velocities were carried out by the Skywatch Atmos anemometer.

Figure 1 shows the appearance of a two-bladed layout with fixed blades and rotating cylinders with a diameter of 0.05 m.

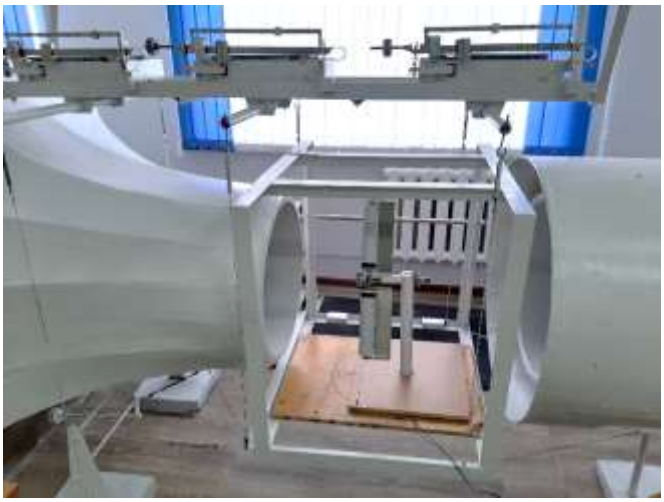

Figure 1. An experimental sample of a two-bladed layout

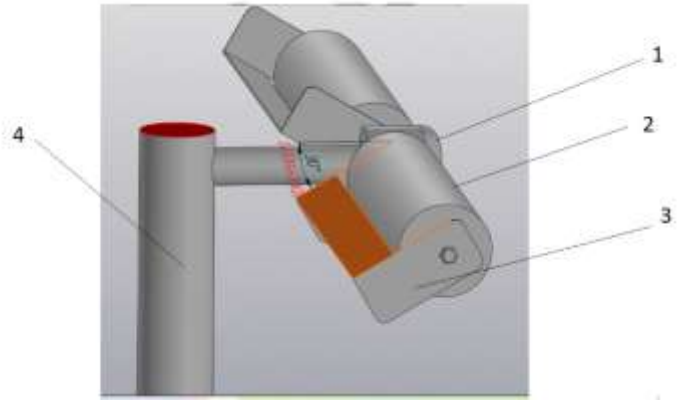

1 — generator, 2 — cylinder, 3 — fixed blade, 4 — mast

Figure 2. Schematic diagram of a wind turbine with fixed blades and rotating cylinders

The addition of rotating cylinders with fixed blades creates additional lifting force, which leads to an increase in the speed of rotation of the wind wheel.

The essence of this process lies in the fact that the fixed blade added to the rotating cylinder enhances the curvature of the profile of the wind-wheel blade. In this case, not only the curvature increases but also the immediate area of the blade. As a result of changes in these indicators, the flow pattern completely changes. These factors are decisive in increasing the lift coefficient.

In the frontal part of the blade to the point of separation of the boundary layer, there is a gradual delamination of experimental data for different elongations. With an increase in the length of the blade, the value of dimensionless pressure at a fixed angle decreases, a gradual transition from the pressure distribution characteristic of spatial motion — the flow around the cylinder and the fixed blade, to the pressure distribution characteristic of flat motion — the flow around an infinitely long cylinder.

A non-contact laser tachometer is used to measure the rotational speed.

In engineering practice, the formula is often used to calculate the lift coefficient:

$$C_y = \frac{\Delta F_y}{\rho \cdot \frac{u^2}{2} \cdot S} \quad \text{or} \quad C_y = \frac{2F_y}{\rho u^2 \cdot S}. \tag{1}$$

To calculate the drag coefficient C_x during the work, the following formula was used:

$$C_x = \frac{\Delta F_x}{\rho \cdot \frac{u^2}{2} \cdot S}, \text{ or } C_x = \frac{2F_x}{\rho u^2 \cdot S}. \quad (2)$$

Here ΔF_x — drag force, [H]; ΔF_y – lifting force, [H];

ρ — air density, [kg/m^3]; u– air flow rate, [m/s]; S — midsection area, [m^2].

To obtain universal dimensionless dependences in experiments, the Reynolds *Re* — the number is used as a dimensionless velocity, which characterizes the ratio of inertia forces to viscosity forces:

$$\mathrm{Re} = \frac{u \cdot d_ц}{\nu}, \quad (3)$$

where $d_ц$ — cylinder diameter, [m]; ν — kinematic viscosity of air, [m^2/s].

Under experimental conditions, the values of air density and viscosity are equal, respectively: $\rho = 1.21$ kg/m^3, $\nu = 1.49 \times 10^{-5}$ and m^2/s.

Research results

Figures 3 and 4 present the results of the experimental calculation of the lifting force and drag force from the flow velocity with different variants of the fixed blade relative to the cylinder.

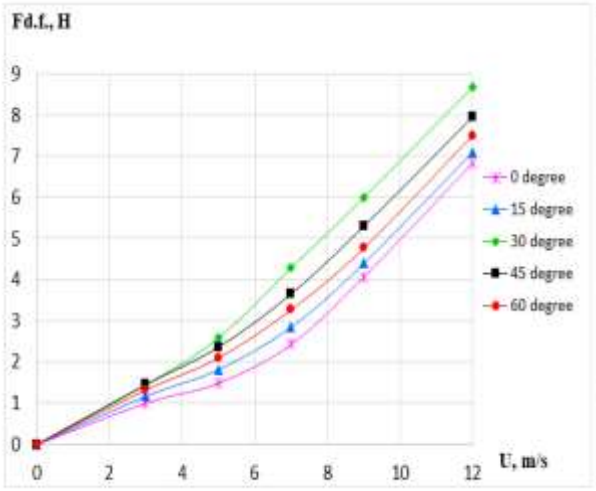

Figure 3. Graph of the dependence of drag forces on the flow velocity

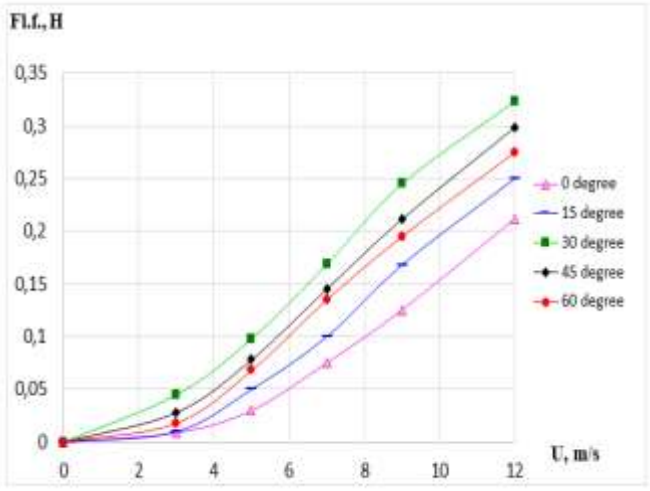

Figure 4. Graph of the dependence of the lifting force on the flow velocity

From the obtained dependences (Fig. 3-4), the proportional dependence of the lifting force and the drag force of the blades on the flow velocity is visible. From comparing the dependencies of a fixed blade relative to a cylinder with different angles α, it is shown that the value of the lifting force of a wind turbine with fixed blades and rotating cylinders with an angle relative to the cylinder α = 30° is higher than that of the others.

This is explained by the fact that when deflecting with an angle α = 30° of the fixed blade, the lifting force increases due to an increase in the curvature of the profile.

Thus, fixed blades with an angle α = 30° relative to the cylinder have optimal aerodynamic characteristics.

Figures 5 and 6 show the dependences of the lift and drag coefficients on the Reynolds number for different variants of the fixed blade relative to the cylinder.

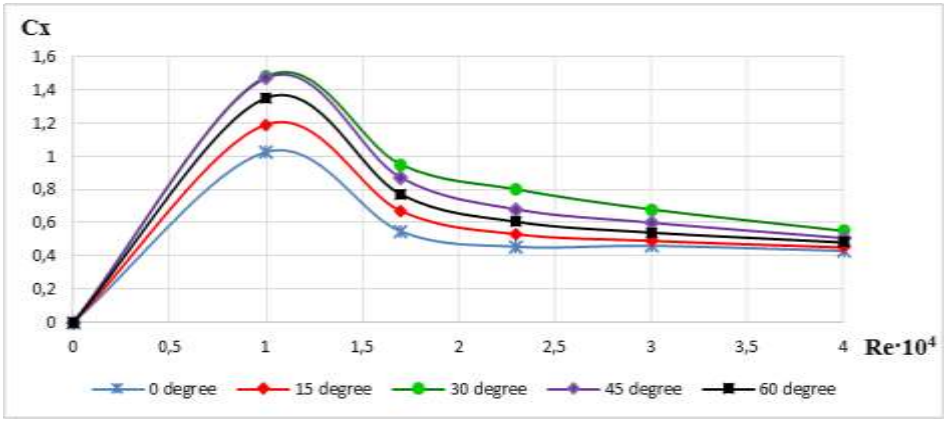

Figure 5. Dependence of the drag coefficient on the number of Re

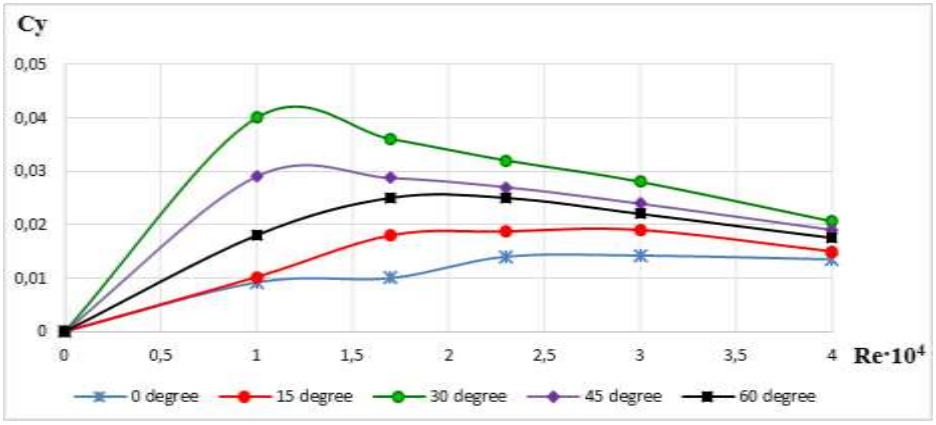

Figure 6. Dependence of the lift coefficient on the number of Re

As can be seen from Figures 5 and 6, when the fixed blade is positioned relative to the cylinder at 30 degrees, the optimal values of the lift and drag coefficients are obtained: 0.04 and 1.479 with a Reynolds number of $1 \cdot 10^4$.Compared with the other three samples at 0°, 15°, and 45°, at 60°, the combined blade produces maximum drag force and minimum lift.

The rotating movements of the cylinders lead to the formation of a sufficiently voluminous vortex zone of reverse currents behind the cylinders, the dimensions of which depend on the speed of the incoming flow.

Conclusion

In the course of the study, the following optimal results were obtained:

- It is established that the dependence of aerodynamic forces on the flow velocity for different variants of the fixed blade relative to the cylinder. It was found that at the maximum angle relative to the cylinder $\alpha = 30°$ that the value of the lifting force and the drag force of the fixed blade is higher than the rest. Based on this, it was found that at an angle $\alpha = 30°$ stationary, the blade has optimal aerodynamic characteristics;

- From the dependence of the coefficient of lift and drag force on the Reynolds number, it was found that at an angle of 30°, there is a minimum lifting force of 0.04 and a maximum drag force of 1.479 at $Re=1 \cdot 10^4$.

- It was found that with the angle of the fixed blade of 30° degrees, the indicators of the entire combined blade are the most effective.

- It is determined that as a result of the interaction between the rotational movement of each cylinder and the stationary blade, a lifting force arises due to the Magnus effect, leading to the rotation of the horizontal shaft, which, in turn, drives the mechanism that generates electrical energy.

The work was carried out with the financial support of the Science Committee of the Ministry of Science and Higher Education of the Republic of Kazakhstan (IRN AP14972704 "Numerical study of a new design of wind turbine blades with a horizontal axis of rotation").

References

1 Возобновляемая энергия — обеспечение более безопасного будущего. ООН. Меры по борьбе с изменением климата. — [Электронный ресурс]. — Режим доступа: https://www.un.org/ru/climatechange/raising-ambition/renewable-energy#

2 Альтернативные источники: энергия ветра, плюсы и минусы. — [Электронный ресурс]. — Режим доступа: https://energo.house/veter/energiya-vetra.html

3 Zhiwei G. An Overview on Fault Diagnosis, Prognosis and Resilient Control for Wind Turbine Systems / G. Zhiwei, L. Xiaoxu // MDPI Processes 2021, Vol. 9(2). — P. 300-319.

4 Патент РФ № RU 2692602 C 2. Экологичная и энергоэффективная ветротурбина на горизонтальном валу. Опубл. 2019. Ю.Б. Соколовский, Д.Ю. Соколовский, А.Ю. Соколовский, О.Ю. Иванова.

5 Ишханян М.В. Ветротурбина класса «Савониус–Магнус» с коническими лопастями: динамика и управление / М.В. Ишханян, Л.А. Климина // Изв. РАН. Теория и системы управления. — 2020. — 4. — С. 160–168.

6 Peter E. Examining the trends of 35 years growth of key wind turbine components / E. Peter, X. George // Energy for Sustainable Development, 2019. ― Vol 50. — P. 18-26.

7 Fausto P.M. A review of non-destructive testing on wind turbines blades / P.M. Fausto, M.C. Ana // Renewable Energy, 2020. Vol 161. P. 998-1010.

8 Буктуков Н.С. Ветроэлектростанция Буктукова 6 (варианты) / Н.С. Буктуков, Б.Ж. Буктуков, Г.Ж. Молдыбаева, А.К. Жакып // Опубл. 18.12.2013 г. — Бюлл. — № 12. — 4 с.

9 Бычков Н.М. Ветродвигатель с эффектом Магнуса: 1 Результаты модельных исследований / Н.М. Бычков // Теплофизика и аэромеханика. — 2004. — Т. 11. — № 4. — С. 583−596.

10 Хозяинов Б.П. Методика проведения испытаний моделей ветроэнергетической установки в аэродинамической трубе 3–АТ–17.5/3 фирмы «УНИКОН» / Б.П. Хозяинов, М.А. Березин // Вестн. КузГТУ. — 2000. — № 4. — С. 38−42.

11 Верховский В.П. Газодинамическое проектирование профилированных сопел аэродинамических труб: дис. ... д-ра техн. наук: 01.02.05 — «Механика жидкости, газа и плазмы. Физико-математические науки» / В.П. Верховский // Центр. аэродинам. ин-т им. Н.Е. Жуковского. — М., 2005. — 250 с. — Инв. № 004410413.

12 Tleubergenova A.Zh. Study of aerodynamic parameters of the sail blade / A.Zh. Tleubergenova, N.K. Tanasheva, K.M. Shaimerdenova, L.L. Minkov, A.N. Dyusembaeva, S.Zh. Uzbergenova // Bulletin of the Karaganda university, Physics series, 2022. ― Vol. 1(105) — P. 58-65.

13 Tanasheva N.K. Investigation of the aerodynamic forces of a triangular wind turbine blade for the low wind speeds / N.K. Tanasheva, A.Zh. Tleubergenova, K.M. Shaimerdenova, L.L. Minkov, S.Zh. Uzbergenova // Eurasian physical technical journal, 2021. ― Vol. 4(38) — P. 59—64.

14 Гарипова Л.И. Определение аэродинамических характеристик модели несущего винта на режиме осевого обтекания / Л.И. Гарипова, А.С. Батраков, А.Н. Кусюмов, А.С. Михайлов, Дж. Баракос // Изв. вузов. Авиационная техника. — 2014. — № 3. — С. 7–13.

А.Ж. Тлеубергенова, А.Н. Дюсембаева, Н.К. Танашева, Ш.С. Кыздарбекова, А.Р. Мұхамедрахим

Біріктірілген күш элементтері бар екіқалақшалы жел энергетикалық қондырғысының аэродинамикалық сипаттамаларын талдау

Мақалада әртүрлі параметрлердегі жел қондырғысының аэродинамикалық сипаттамалары зерттелген. Осы мақсатта қозғалмайтын қалақшаларымен екі цилиндрлі тәжірибелік үлгі жасалды. Қозғалмайтын қалақшаларымен және айналмалы цилиндрлері бар жел қондырғысының принципиальды сүлбесі алынды. Ауа ағынының жылдамдығы 3-тен 12 м/с-қа дейін өзгерді. Жел энергетикалық қондырғының аэродинамикалық күштерінің ағын жылдамдығына тәуелділігі зерттелді. Ауа ағынының жылдамдығынан жел қондырғысының цилиндріне қатысты қозғалмайтын қалақшаның орналасу α бұрышын өзгерту бойынша эксперимент нәтижелеріне талдау жүргізілді. Қалақшаның орналасуы өзгерген кезде ауа ағынына қатысты маңдайлық кедергі өзгереді. Маңдайлық кедергі күші мен көтеру күштерінің ағын жылдамдығына тәуелділігі бойынша график салынды. Қозғалмайтын қалақшаның цилиндрге қатысты максималды α=30º бұрыш кезінде көтеру күші мен маңдайлық кедергі күшінің мәні жоғары екендігі анықталды. Маңдайлық кедергі күші мен көтеру күшінің коэффициентінің Рейнольдс санына тәуелділігінен 30º градус бұрышта минималды көтеру күші 0,04 және максималды маңдайлық кедергі күші 1,479 мәндері $Re=1\cdot10^4$ кезінде болатындығы анықталды. Эксперимент нәтижелері көлденең осьті цилиндрлерді айналдыру кезінде пайда болатын, Магнус эффектісімен қозғалатын қосымша күш қолдануға болатындығын көрсетеді. Бұл нәтижелер іс жүзінде біз үшін пайдалы болып саналады, өйткені бұл нәтижелерді желдің төмен жылдамдығымен жұмыс істейтін біріктірілген жел қозғалтқыштарында қолдануға болады. Осы жел қондырғысы 2,8 м/с жел жылдамдығынан бастап электр қуатын өндіре алады.

Кілт сөздер: жел энергетикалық қондырғы, ағын жылдамдығы, аэродинамикалық күш, Т-1-М аэродинамикалық құбыр, маңдайлық кедергі күші, көтеру күші.

А.Ж. Тлеубергенова, А.Н. Дюсембаева, Н.К. Танашева, Ш.С. Кыздарбекова, А.Р. Мухамедрахим

Анализ аэродинамических характеристик двухлопастной ветроэнергетической установки, содержащей комбинированные силовые элементы

В статье изучены аэродинамические характеристики ветряной установки различных параметров. Для данной цели был изготовлен экспериментальный образец двухцилиндровый с неподвижными лопастями. Получена принципиальная схема ветроустановки с неподвижными лопастями и вращающимися цилиндрами. Скорость воздушного потока варьировалась, начиная от 3 до 12 м/с. Исследовалась зависимость аэродинамических сил ветроэнергетической установки от скорости потока. Проведен анализ результатов эксперимента по изменению угла α расположения неподвижной лопасти относительно цилиндра от скорости воздушного потока ветряной установки. При изменении положения лопасти лобовое сопротивление меняется относительно воздушного потока. Построен график по зависимости сил лобового сопротивления и подъемной силы от скорости потока. Установлено, что при максимальном угле $\alpha=30^0$ относительно цилиндра неподвижной лопасти значение подъемной силы и силы лобового сопротивления выше. Из зависимости коэффициента подъемной силы и силы лобового сопротивления от числа Рейнольдса определено, что при угле 30º градусов наблюдается минимальная подъемная сила 0,04 и максимальная сила лобового сопротивления 1,479 при $Re=1\cdot10^4$. Результаты эксперимента показывают, что можно использовать дополнительную силу, движимую эффектом Магнуса, возникающим при вращении цилиндров с горизонтальной осью. Эти результаты считаются полезными для нас на практике, поскольку они могут быть использованы в комбинированных ветряных двигателях, работающих при малых скоростях ветра. Эта ветроэнергетическая установка может вырабатывать электроэнергию, начиная со скорости ветра 2,8 м/с.

Ключевые слова: ветроэнергетическая установка, скорость потока, аэродинамическая сила, аэродинамическая труба Т–1–М, сила лобового сопротивления, подъемная сила.

References

1 Vozobnovliaemaia energiia — obespechenie bolee bezopasnogo budushchego. OON. Mery po borbe s izmeneniem klimata [Renewable energy — ensuring a safer future. UN. Measures to combat climate change]. (n.d.). *base.garant.ru.* Retrieved from https://www.un.org/ru/climatechange/raising-ambition/renewable-energy# [in Russian].

2 Alternativnye istochniki: energiia vetra, pliusy i minusy [Alternative sources: wind energy, pros and cons]. (n.d.). *base.garant.ru.* Retrieved from https://energo.house/veter/energiya-vetra.html [in Russian].

3 Zhiwei, G., & Xiaoxu, L. (2021). An Overview on Fault Diagnosis, Prognosis and Resilient Control for Wind Turbine Systems. *MDPI Processes*, *9*(2), 300-319.

4 Sokolovskii, Yu.B., Sokolovskii, D.Yu., Sokolovskii, A.Yu., & Ivanova, O.Yu. (2018). Patent Rossiiskoi Federatsii No RU 2692602 C 2. Ekologichnaia i energoeffektivnaia vetroturbina na gorizontalnom valu [Patent of Russian Federation No RU 2692602 C2. Eco-friendly and energy-efficient wind turbine on a horizontal shaft] [in Russian].

5 Iskhanian, M.V., & Klimina, L.A. (2020). Vetroturbina klassa «Savonius–Magnus» s konicheskimi lopastiami: dinamika i upravlenie ["Savonius–Magnus" class wind turbine with conical blades: dynamics and control]. *Izvestiia Rossiiskoi akademii nauk. Teoriia i systemy upravleniia — Proceedings of the Russian Academy of Sciences. Theory and control systems*, *8*, 160–168 [in Russian].

6 Peter, E., & George, X. (2019). Examining the trends of 35 years growth of key wind turbine components. *Energy for Sustainable Development*, *50*, 18-26.

7 Fausto, P.M., & Ana, M.C. (2020). A review of non-destructive testing on wind turbines blades. *Renewable Energy*, *161*, 998-1010.

8 Buktukov, N.S., Buktukov, B.Zh., Moldybaeva, G.Zh., & Zhakyp, A.K. (2013). Vetroelektrostantsiia Buktukova 6 (varianty) [Wind farm of Butukova 6 (options)]. No. 12, 4 p. [in Russian].

9 Bychkov, N.M. (2004). Vetrodvigatel s effektom Magnusa: 1 Rezultaty modelnykh issledovanii [Wind turbine with Magnus effect: 1 Results of model studies]. *Thermophysics and aeromechanics — Thermophysics and Aeromechanics*, *11*(4), 583–596 [in Russian].

10 Hozjainov, B.P., & Berezin, M.A. (2000). Metodika provedeniia ispytanii modelei vetroenergeticheskoi ustanovki v aerodinamicheskoi trube 3–AT–17.5/3 firmy «UNIKON» [The methodology of testing wind power plant models in the wind tunnel

3–AT–17.5/3 of the company UNICON]. *Vestnik Kuzbasskogo gosudarstvennogo tekhnicheskogo universiteta — Bulletin of the Kuzbass State Technical University*, *4*, 38–42 [in Russian].

11 Verhovskii, V.P. (2005). Gazodinamicheskoe proektirovanie profilirovannykh sopel aerodinamicheskikh trub [Gas-dynamic design of profiled wind tunnel nozzles]. *Tsentralnyi aerodinamicheskii institut imeni N.E. Zhukovskogo — Centre Aerodynamic Institute named after N.E. Zhukovsky*. *Doctor`s thesis.* Moscow [in Russian].

12 Tleubergenova, A.Zh., Tanasheva, N.K., Shaimerdenova, K.M., Minkov, L.L., Dyusembaeva, A.N., & Uzbergenova, S.Zh. (2022). Study of aerodynamic parameters of the sail blade. *Bulletin of the Karaganda University, Physics series*, *1*(105), 58-65.

13 Tanasheva, N.K., Tleubergenova, A.Zh., Shaimerdenova, K.M., Minkov, L.L., & Uzbergenova, S.Zh. (2021). Investigation of the aerodynamic forces of a triangular wind turbine blade for the low wind speeds. *Eurasian Physical Technical Journal*, *4*(38), 59-64.

14 Garipova, L.I., Batrakov, A.S., Kusiumov, A.N., Mihailov, A.S., & Barakos, Dzh. (2014). Opredelenie aerodinamicheskikh kharakteristik modeli nesushchego vinta na rezhime osevogo obtekaniia [Determination of aerodynamic characteristics of the main rotor model in axial flow mode]. *Izvestiia vuzov. Aviatsionnaia tekhnika — News of universities. Aviation equipment*, *3*, 7–13 [in Russian].

DOI 10.31489/2023PH3/151-155

UDC 54.057

D. Deulina, V. Paygin, T. Alishin, S. Stepanov, D. Valiev, E. Dvilis, O. Khasanov, A. Ilela

National Research Tomsk Polytechnic University, Russia
(E-mail: rubinfc@tpu.ru)

Characterization of YAG:Ce ceramics with graphene oxide

Yttrium-aluminum garnet ($Y_3Al_5O_{12}$) is an optical material that shows great potential due to its favorable light-emitting and mechanical properties, as well as its chemical stability and thermal resistance. It is commonly utilized in laser technology, optical instruments, and solid-state light sources as a result of its activation by transition metal or rare earth element ions. In this work, experiments were carried out on the procedure for compacting samples of luminescent ceramics $Y_3Al_5O_{12}:Ce^{3+}$, by single-base pressing followed by sintering. Comprehensive studies of the influence of graphene oxide of variable concentration (x=0.1;0.5; 1 wt.%) on the radiative characteristics of ceramic samples. It was found that the addition of graphene oxide in an amount from 0.1 to 1 wt. % affects the density and luminescent properties of YAG:Ce ceramics. There is a decrease in the value of the density parameter at concentrations of graphene oxide 0.1-1 wt. % before annealing, after annealing, the relative density value increases to ~99 %. The luminescence spectrum when excited by a blue LED chip appears as a wide band in the spectral range 460-750, the nature of which is associated with radiative transitions in the cerium ion. It has been established that the light-emitting characteristics have a downward trend when activated by graphene oxide. The integral luminescence intensity decreases from 27.1 % to 19 % with an increase in the concentration of graphene oxide.

Keywords: YAG ceramics, sintering process, graphene oxide, mechanic properties.

Introduction

Graphene is a superconducting, two-dimensional material with unique properties which are promising for various technological applications in many fields of science and technology [1-4]. Due to the unique band structure [5] graphene oxide has excellent electrical and thermal conductivity [6] high surface area [7] and good optical properties [8]. Graphene-based materials have good nonlinear optical properties [9]. The mechanical characteristics of graphene are similar to those of carbon nanotubes [10]. But unlike carbon nanotubes, graphene oxide penetrates better into the structure of the matrix material and provides more effective compaction comparing to nanotubes [11]. These properties make graphene a promising material for applying in microelectronics, photonic and optoelectronic devices, and laser technique [12-15].

Yttrium-aluminum garnet ($Y_3Al_5O_{12}$) is a highly promising optical material that possesses excellent optical and mechanical properties, as well as chemical stability and thermal resistance. It is commonly used in laser technology, optical instrumentation, and solid-state light sources. These materials are typically activated by transition metal or rare earth ions [16, 17].

The use of yttrium-aluminum garnet activated by cerium ions (YAG:Ce) has experienced a notable rise in the production of white light-emitting diodes (WLEDs). These materials serve as optical radiation converters, allowing for the production of high-quality white light. Modern commercial WLEDs consist of a blue glow crystal and a Ce:YAG phosphor dispersed in an optically transparent coating consisting of organosilicon, polymer or epoxy resin. The main problem of such light-emitting diodes is the local overheating of the resin (compound), which leads to degradation of the coating and changing of optical characteristics [18, 19]. That is why it is possible to use luminescent ceramics based on YAG:Ce as an optical radiation converter, which is devoid of the above disadvantages. The addition of graphene oxide (GO) to such ceramics in relatively small concentrations can improve the optical and luminescent properties of ceramics.

In this work, the effect of graphene oxide on the density and luminescent characteristics of ceramics based on yttrium-aluminum garnet activated by cerium is investigated

Expiremental

Micro powder of yttrium-aluminum garnet activated by cerium (NIIPP, Russia) and commercial suspension of graphene oxide (Graphenea, Spain) were used as starting materials.

Mixing of the initial components was carried out by the wet method in isopropyl alcohol using a ball mill. The mixing duration was 48 hours. As a result, powder suspensions of the YAG:Ce-xGO (where x = 0.1; 0.5; 1 wt. %) composition were obtained. The resulting suspensions were dried by exposing them to air at a temperature of 120 °C until all the moisture evaporated completely.

To compact the powder, cold static pressing was performed on a test press IP500 AUTO from Zipo in Russia, applying a pressure of 400 MPa.

The sintering process was conducted using a high-temperature furnace (LHT 02/18, Nabertherm, Germany) in an air atmosphere. The temperature range for sintering was set between 1250 °C and 1650 °C. The samples were exposed to each sintering temperature for duration of 2 hours. The heating and cooling rate during the process was maintained at 200 °C per hour. The resulting samples had a thickness of approximately 2 mm and a diameter ranging from 8.5 to 9 mm. The selection of the sintering parameters was based on previous findings [20].

Following the sintering process, the samples underwent grinding and polishing using a Buehler AutoMet 300 Pro machine (Switzerland). Polycrystalline diamond suspensions from Kemix (Russia) were used for this purpose.

The density of the samples was determined by measuring their mass and linear dimensions, according to the formula:

$$\rho = m/V \quad (1)$$

X-ray phase analysis of the ceramics was performed using an XRD-7000 X-ray diffractometer (Shimadzu, Japan). The resulting diffractograms were analyzed using specialized software and the international crystallographic database “PDF-4”.

To study the optical properties of the ceramics, measurements were conducted in the ultraviolet, visible, and near-infrared spectral regions using a two-beam scanning spectrophotometer SF-256 UVI (200-1100) (Lomo-Photonics, Russia).

The integral spectral efficiency was measured using an integrating sphere and a calibrated AvaSpec-3648 spectrophotometer (200-1100 nm, inverse linear dispersion 1.2 nm/mm). A light-emitting diode with a wavelength of 447 nm was used as the excitation source. The excitation of the sample was carried out using a flow integrated by a sphere. The spectrum and radiation flux of the diode falling on the geometric location where the test sample was positioned were measured. Next, the radiation spectrum was measured with the sample under study. By employing this technique, it became possible to precisely subtract the diode spectrum from the luminescence spectra of the ceramics, while maintaining the original form of the spectral lines. As a result, it became feasible to ascertain the reflected flux, absorbed flux, and radiation flux of the ceramic sample. The overall spectral efficiency was then computed as the ratio of the integral flux emitted by the sample to the integral flux absorbed by the sample.

Results and discussion

Figure 1 shows the dependence of the relative density of powder compacts before and after sintering at a temperature of 1650 °C on the concentration of graphene oxide.

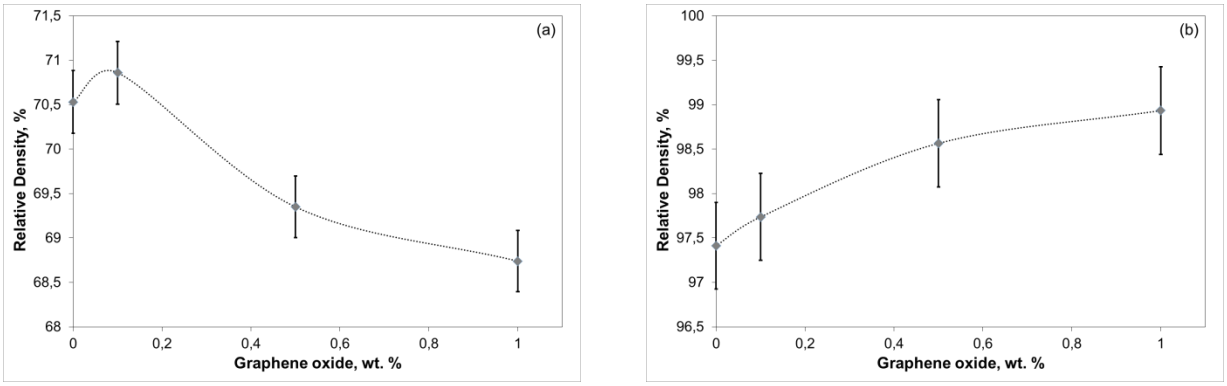

Figure1. Dependence of the relative density of samples on the concentration of graphene oxide (a) before sintering; (b) after sintering at a temperature of 1650 °C.

Relative density of the powder compact from the powder of "pure" yttrium-aluminum garnet activated by cerium is 70.5 ± 0.5 %. The addition of 0.1 wt. % graphene oxide to YAG:Ce leads to a slight increase in the relative density of the compact (up to 70.9 =0.5 %), however, the observed increase in density is within the confidence interval of measuring value. Further increase of graphene oxide concentration from 0.1 wt. % up to 1 wt. % leads to a decrease in the relative density of the compact from 70.9 ± 0.5 % to 68.7 ± 0.5 %.

For samples after sintering, unlike powder compressions, with an increase in graphene oxide concentration from 0 to 1 wt. % there is an increase in the relative density of samples from 97.4 ±0.5 to 98.9±0.5 %. The maximum value of the relative density is observed at a graphene oxide concentration of 1 wt. %.

X-ray phase analysis revealed that the YAG:Ce ceramics samples were composed of cubic YAG in a stoichiometric ratio. All observed peaks corresponded to the YAG phase (PDF-Card#010-83-7850). No additional phases were detected in the samples, and there was no broadening of the peaks or presence of any other peaks on the diffractograms. The absence of peaks characteristic of graphene oxide is due to their relatively low content (less than 5 wt. %), which does not exceed the sensitivity limit of the diffractometer.

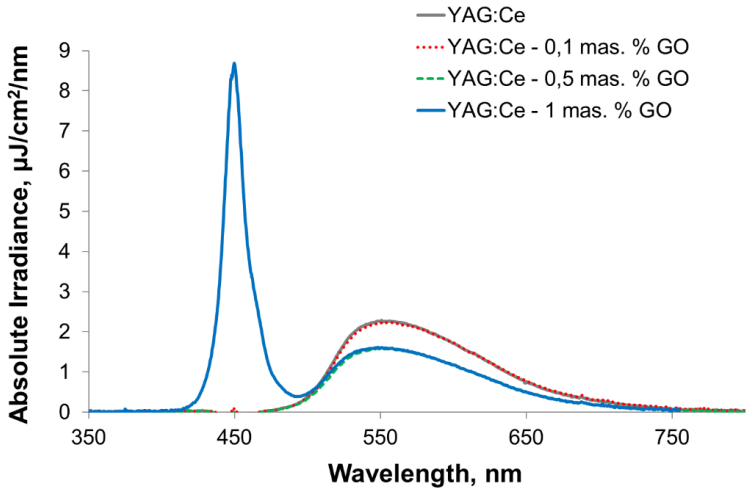

Figure2. Integral photoluminescence spectrum of ceramics based on YAG:Ce

The photoluminescence spectra of the samples excited by an LED with a wavelength of 447 nm are shown in Figure 2. The spectra are typically for the YAG:Ce system [21]. A maximum is observed in the region of 550 nm. Addition of graphene oxide in an amount from 0.5 to 1 wt. % leads to a shift of the maximum position to the region of 545 nm and a decrease in the intensity of radiation.

The results of measuring the efficiency of luminescence and diffuse reflection of the studied samples are shown in Figure 3. It can be seen that the efficiency of luminescence with an increase in graphene oxide concentration from 0 to 1 wt. % varies from 27.1 to 19 %. The lowest luminescence efficiency is observed at a graphene oxide concentration of 0.5 wt. %. Diffuse reflection of samples increases from 13 to 16.8 % with an increase in graphene oxide concentration from 0 to 1 wt. %.

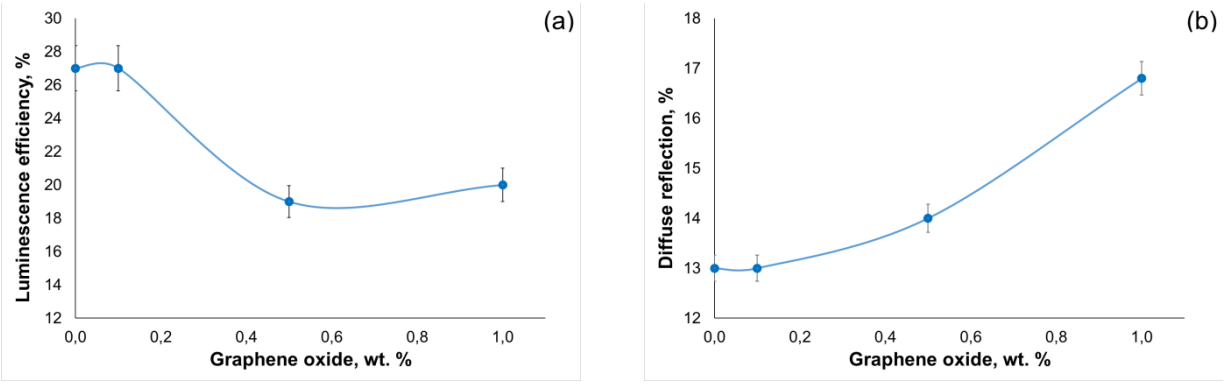

Figure3. Efficiency of luminescence (a) and diffuse reflection (b) of YAG:Ce ceramics with different graphene oxide concentration

Impact of graphene oxide on YAG:Ce ceramics remains ambiguous. Although the inclusion of graphene oxide does result in an increase in ceramic density under identical conditions, it also has a negative effect on the luminescent properties of the ceramics.

Conclusion

As a result of the work samples of luminescent ceramics based on yttrium-aluminum garnet activated with cerium with graphene oxide additives were manufactured. The influence of graphene oxide on the density and luminescent properties of ceramics was investigated.

It was found that the addition of graphene oxide in an amount from 0.1 to 1 wt. % leads to an increase in relative density from 94.7 ± 0.5 to 98.9± 0.5 %, an increase in diffuse reflection from 13 to 16.8 % and a decrease in luminescence efficiency from 27 to 19 %.

It is shown that the addition of up to 1 wt. % graphene oxide to YAG:Ce ceramics provides 1.5 % increase in relative density.

Funding

This work was funded by the Russian Science Foundation (No. 21-73-10100).

The research was carried out using the equipment of the CSU NMNT TPU, supported by the RF MES project #075-15-2021-710.

Acknowledgments

The research was carried out using the equipment of the CSU NMNT TPU supported by the RF MES project #075-15-2021-710. This research was supported by Tomsk Polytechnic University the "Priority 2030" development program. The authors are grateful to Ph.D Evgeniya Sheremet (Tomsk Polytechnic Unversity) for providing a suspension of graphene oxide.

References

1 Geim, A.K., & Novoselov, K.S. (2010). The rise of graphene. *Nanoscience and technology, 1,* 11-19.

2 Geim, A.K., & Macdonald, A. (2010). Graphene: Exploring carbon flatland. *Physics Today, 1,* 35-41.

3 Wang. D., Chen, J-F., & Dai, L. (2015). Recent advances in graphene quantum dots for fluorescence bioimaging from cells through tissues to animals. *Particle and Particle Systems Characterization, 32,* 515–523.

4 Yu, W., Sisi, L., Haiyan, Y., & Jie, L. (2020). Progress in the functional modification of grapheme /graphene oxide. *RSC Advances, 10,* 15328-15345.

5 Sreeja, V.G. (2021). Effects of reduced graphene oxide on nonlinear absorption and optical limiting properties of spin coated aluminium doped zinc oxide thin films. *Thin Solid Films, 722,* 138580.

6 Sang, M. (2019). Electronic and thermal properties of graphene and recent advances in graphene based electronics applications. *Nanomaterials, 9,* 374.

7 Dai, J.F. (2015). Surface properties of graphene: relationship to graphene-polymer composites. *Rev. Adv. Mater. Sci., 40,* 60-71.

8 Ne, L.O. (2017). Electronic optical, properties and widening band gap of graphene with Ge doping. *Optical and Quantum Electronics, 49,* 218.

9 Feng, M., Zhan, H., & Chen, Y. Nonlinear optical and optical limiting properties of graphene families. *Applied Physics Letters, 96,* 033107.

10 Changgu, L., Weijefrey, W., & Kysarand, J.H. (2008). Measurement of the elastic properties and intrinsic strength of monolayer graphene. *Science, 321,* 385-388.

11 Rafiee, M.A., Rafiee, J., Wang, Z., Song, H., Yu, Z., & Koratkar, N. (2009). Enhanced mechanical properties of nanocomposites at low graphene content. *ASC Nano, 3,* 3884–3890.

12 Kim, S.H. (2012). A hybrid reduction procedure for preparing flexible transparent graphene films with improved electrical properties. *Journal of Materials Chemistry, 22,* 18306-18313.

13 Xia, F. (2009). Ultrafast graphene photodetector. *Nature nanotechnology, 4,* 839-843.

14 Liu, M. (2011). A graphene-based broadband optical modulator. *Nature, 474,* 64-67.

15 Bao, Q. (2009). Atomic layer graphene as a saturable absorber for ultrafast pulsed lasers. *Advanced Functional Materials, 19,* 3077-3083.

16 He, X. (2016). Effects of local structure of Ce^{3+} ions on luminescent properties of $Y_3Al_5O_{12}$:Ce nanoparticles. *Scientific reports, 6,* 22238.

17 Xiao, Z. (2020). Materials development and potential applications of transparent ceramics. *Materials Science and Engineering, 139,* 100518.

18 Chen, D. (2015). Advances in transparent glass–ceramic phosphors for white light-emitting diodes. *Journal of the European Ceramic Society, 35,* 859-869.

19 Paygin, V.D. (2021). Spark plasma sintering of transparent YAG:Ce ceramics with LiF flux. *Journal of Physics: Conference Series, 1989,* 012008.

20 Paygin, V.D. (2020). Density and microstructural investigation of Ce: YAG ceramic subjected to powerful ultrasonic treatment during the compaction process. *Materials Science and Engineering: Conference Series, 754,* 012011.

21 Sontakke, A., Ueda, J. & Katayama, Y. (2015). Role of electron transfer in Ce^{3+} sensitized Yb^{3+} luminescence in borate glass. *J. Appl. Phys., 117,* 013105.

Д. Деулина, В. Пайгин, Т. Алишин, С. Степанов, Д. Валиев, Э. Двилис, О. Хасанов, А. Илела

YAG керамикасының сипаттамасы: графен оксиді бар Ce

Итрий алюминий гранатасы ($Y_3Al_5O_{12}$) жақсы жарық шығаратын және механикалық қасиеттері, химиялық тұрақтылығы және термиялық тұрақтылығы бар перспективалы оптикалық материал. Өтпелі металл немесе сирек жер иондары арқылы белсендірілген иттрий-алюминий гранат негізіндегі материалдар лазерлік технологияда, оптикалық аспаптарда және қатты күйдегі жарық көздерінде кеңінен қолданылады. Бұл жұмыста $Y_3Al_5O_{12}:Ce^{3+}$ люминесцентті керамика үлгілерін бір негізді престеу, содан кейін агломерациялау арқылы нығыздау процедурасы бойынша тәжірибелер жасалды. Керамикалық үлгілердің сәуле шығару сипаттамаларына ауыспалы концентрациядағы графен оксидінің (x=0,1; 0,5;1 мас. %) әсеріне кешенді зерттеулер жүргізілді. Графен оксидінің 0,1-ден 1 мас. % дейінгі мөлшердегі қоспасы YAG:Ce керамикасының тығыздық және люминесценция қасиеттеріне әсер ететіні анықталды. Жұмсарғанға дейін графен оксидінің 0,1-1 мас. % концентрация кезінде тығыздық параметрі мәнінің төмендейтіні, ал жұмсарғаннан кейін салыстырмалы тығыздық мәні ~99 % дейін жоғарылайтыны байқалды. Қозу кезіндегі люминесценция спектрі көк болады, ал жарықдиодты чип 460-750 спектрлік диапазонында кең жолақ түрінде көрінеді, оның табиғаты церий ионындағы сәуле шығаратын ауысумен байланысты. Жарық шығаратын сипаттамалардың графен оксидімен белсендірілген кезде төмендеу динамикасы бар екендігі анықталды. Графен оксидінің концентрациясы жоғарылаған кезде жарықтың интегралды қарқындылығы 27,1-ден 19%-ға дейін төмендейді.

Кілт сөздер: YAG-керамика, агломерация процесі, графен оксиді, механикалық қасиеттері.

Д. Деулина, В. Пайгин, Т. Алишин, С. Степанов, Д. Валиев, Э. Двилис, О. Хасанов, А. Илела

Характеристика керамики YAG:Ce с оксидом графена

Иттрий-алюминиевый гранат ($Y_3Al_5O_{12}$) является перспективным оптическим материалом с хорошими светоизлучающими и механическими свойствами, химической стабильностью и термической стойкостью. Материалы на основе иттрий-алюминиевого граната, активированного ионами переходных металлов или редкоземельных элементов, широко используются в лазерной технике, оптическом приборостроении и твердотельных источниках света. В настоящей работе были проведены эксперименты по процедуре компактирования образцов люминесцентной керамики $Y_3Al_5O_{12}:Ce^{3+}$, путем одноосновного прессования с последующим спеканием. Проведены комплексные исследования влияния оскида графена переменной концентрации (x=0,1; 0,5; 1 вес. %) на излучательные характеристики образцов керамики. Было установлено, что добавка оксида графена в количестве от 0,1 до 1 мас. % влияет на плотность и люминесцентные свойства YAG:Ce керамики. Наблюдается снижение значения параметра плотности при концентрациях оксида графена 0,1–1 вес. % до отжига, после отжига значение относительной плотности повышается до ~99 %. Спектр люминесценции при возбуждении синий, чипом светодиода проявляется в виде широкой полосы в спектральном диапазоне 460–750, природа которой связана с излучательными переходами в ионе церия. Установлено, что светоизлучающие характеристики имеют динамику к снижению при активации оксидом графена. Интегральная интенсивность свечения уменьшается с 27,1 до 19 % при повышении концентрации оксида графена.

Ключевые слова: YAG керамика, процесс спекания, оксид графена, механические свойства.

DOI 10.31489/2023PH3/156-162

UDC 628.477

B.R. Nussupbekov[1], M.S. Duisenbayeva[1]

Karaganda University of the name of academician E.A. Buketov, Kazakhstan
(E-mail: m_o_l_d_i_r_89@mail.ru)

Processing of organic waste by electrohydroimpulse method

The article considers the regularities, parameters of technology and installations for electrohydroimpulse extraction of fat from bone mass. To date, the growth of production and increasing its efficiency in industries processing agricultural raw materials largely depends not only on raw materials and their quality, but also on the completeness of extraction of valuable components. Reducing the loss of the extracted product in production, for example, sugar, starch, fat, can significantly increase the yield of finished products when using optimal extraction methods and methods. The result is powerful hydraulic shocks with pressure pulses sufficient to break the bonds, retain fat cells in the tissue and destroy the cells themselves. This article discusses the technology of extracting fat from bones. The priority direction of technical policy in the agro-industrial complex, as well as in the light and food industries, is currently the development of a system of operational and promising measures to provide agricultural producers with high-quality, environmentally friendly, safe and highly reliable equipment. The dominant and extremely unfavorable production conditions force the manufacturer not to process, but to sell raw materials.

Keywords: spark discharge, fat, organic waste, shock wave, crushing, bone mass.

Introduction

The currently existing physical and chemical methods of fat extraction are not effective in terms of economy, labor intensity and ecology. Therefore, the search for new effective solutions for extracting fat from bone mass using alternative methods, including underwater spark discharge, is relevant at the moment.

Our proposed method is based on the use of a pulsed shock wave resulting from a spark discharge in a liquid. This method of extracting fat does not require fine grinding of the bone. The discharge-pulse technology makes it possible to successfully solve and is widely used in the technological processes of cleaning castings, metal stamping, fixing pipes in the pipe boards of heat exchangers, processing industrial waste in order to extract valuable phosphorus components from phosphorus sludge, crushing mineral media and separating impurities from various kinds of crushed materials, etc. [1, 2].

The existing physical and chemical methods of oil extraction are economically inefficient, labor-intensive and environmentally friendly. Therefore, the search for new effective solutions for obtaining fat from bone mass using alternative methods, including underwater spark generators, is currently relevant [3].

Our proposed method is based on the use of a pulsed shock wave generated by spark radiation in a liquid. This method of obtaining fat does not require easy grinding of the bone. The exhaust-pulse technology makes it possible to successfully solve and widely apply it in the technological processes of cleaning fabrics, metal stamping, fixing pipes with tubular plates of heat exchangers, extracting valuable phosphorous components from phosphoric clay, grinding mineral media and processing industrial waste into individual impurities of various types of crushed materials, etc [4, 5].

Experimental

An experimental setup was assembled to grind and extract the fat mass from the bone. The influence of an underwater spark of an electrohydroimpulse installation was studied to determine the optimal parameters. Figure 1 below shows the object of the study [6].

Figure 1. The object of the study

The study of fat extraction from cattle was carried out on an experimental electrohydroimpulse installation. Various cattle bones were taken for testing in the sausage shop of JSC “Tulpar” in Karaganda. According to laboratory tests in the workshop, the bones had a low average fat content.

Before the start of the test, 15 kg of bone raw materials were crushed to size $5-10mm$. Certain fractions were weighed on electronic scales. After that, the bone mass was left for 6 hours in a container with industrial water. To determine the mass, after the expiration of time, the soaked bones were weighed [7].

Figure 2 shows an electrohydroimpulse installation for extracting fat from organic compounds.

Figure 2. Electrohydroimpulse unit for extracting fat from organic compounds

Below is Figure 3, which shows the main part of the experimental setup. We immerse the prepared bone mass into the working cell. At a frequency of 7-15 Hz in an aqueous medium, shock waves arise from the impact of pulses and water enters the bone. When exposed to wave waters, the structure of the bone with a fat content is destroyed and the transition of the fat layer into the solution is observed. The frequency limit was determined by testing.

Figure 3. Working cell for separating fat from organic compounds

The bone mass, which is connected to water and heated to a certain temperature, enters the crushing equipment through the receiver of the guide cone and, after the hatch is tightly closed, acts on the shock wave that occurs when the spark is discharged. The intensity of the degreasing process and the possibility of direct wide regulation during the process are achieved by rotating the DIU housing relative to the central electrode [8].

The temperature set during the tests $32-50^0C$ is sufficient to separate fat from bone mass. At low temperatures, less fat 32^0C is retained by the tissue (skin) and destroyed as a result of adsorption and capillaries, at this time the viscosity and surface tension of the oil increase, and the separation of fat slows down. The study showed that the impulses from electrohydroimpulsive effects are enough to destroy the fat cells holding in the tissue [9].

Results and Discussion

Tests on the electrohydroimpulse installation were carried out in the laboratory of Hydrodynamics and Heat exchange of the Karaganda University of the name of academician E.A. Buketov. The objects of the study are the bones of cattle. As a result of the tests, the optimal exposure power and pulse repetition rate are set for each parameter. The bones were previously crushed to fractions of 10 mm, 5 mm and 2 mm.

Based on the experience developed in the installation shown in Figure 2, the results obtained were analyzed and effective parameters were determined. With the help of the installation, they were able to create electrical discharges in a clean liquid and at a given vapor concentration into the mixture. The fixed volume of bone mass in the fluid was 25 % [10, 11].

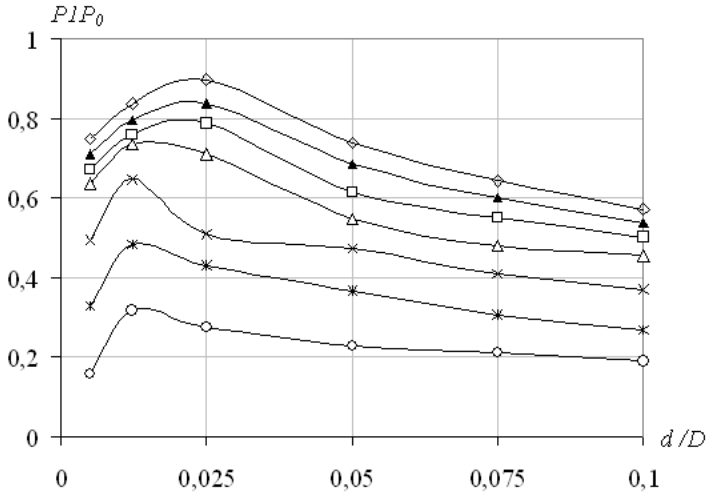

Figure 4. Dependence of the pulse pressure amplitude on the fixed loaded volume of bone mass

As a result of the performed studies, the dependences of pulse pressures for various degrees of vapor content of the working medium are obtained. Experimental work was carried out with fixed electrical and energy parameters of the discharge circuit of the electrohydroimpulse and geometric parameters of the working crushing plant. The variable parameters were the frequency of the supplied pulse and the degree of vapor content.

Figure 5 shows a graph of the effect of the capacitance of the capacitor bank of the electrohydroimpulse device on the fat-free crushed bone at $U = 10kV, \quad l_p = 7mm, \quad t_{\text{mixture}} = 32^0 C$.

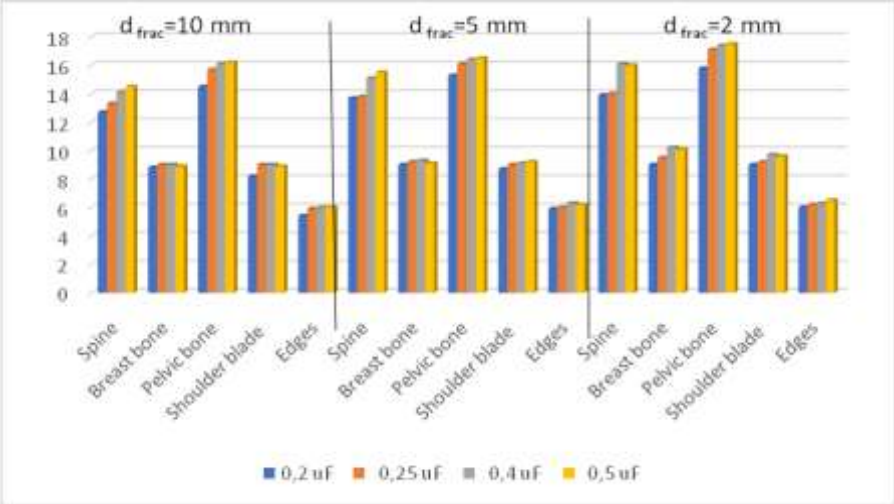

Figure 5. Influence of the capacitance of the capacitor bank of an electrohydroimpulse unit for degreasing crushed bone at $U = 10kV, \quad l_p = 7mm, \quad t_{\text{mixture}} = 32^0 C$

During the study, the voltage was 10 kV, the temperature of the mixture was heated to 32^0C. As you can see on the graph, when grinding the bone to a fraction of 10 mm, the separated fat of the spine was 12.7 %, and during grinding to a fraction of 2 mm was 13.9 %.

The influence of the capacitance of the capacitor bank of the electrohydroimpulse unit for $U = 20kV, \quad l_p = 7mm, \quad t_{\text{mixture}} = 36^0 C$ degreasing crushed bone is shown in Figure 6.

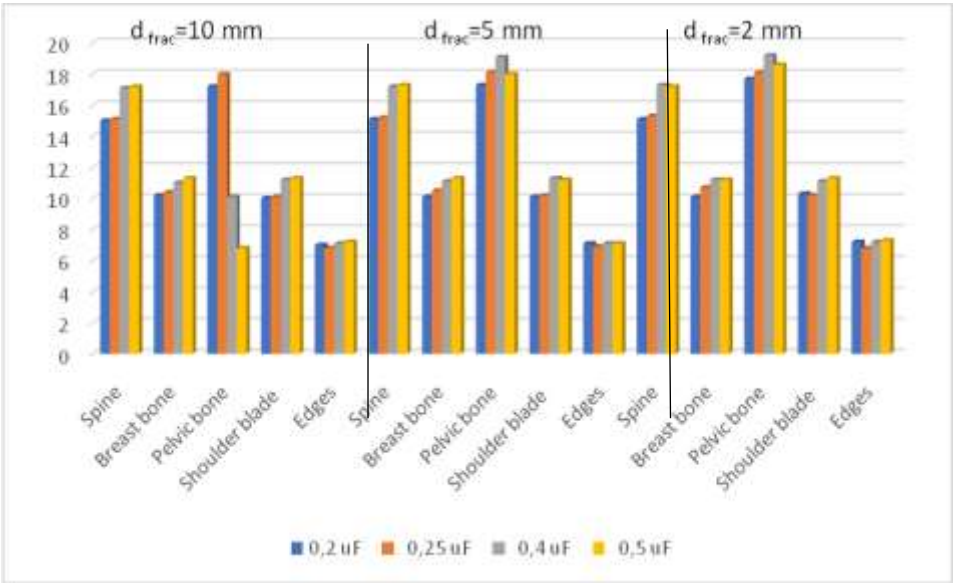

Figure 6. Influence of the capacitance of the capacitor bank of the electrohydroimpulse unit for degreasing crushed bone at $U = 20kV, \quad l_p = 7mm, \quad t_{\text{mixture}} = 36^0 C$

Figure 7 shows the content of the separated fat with an increase in the voltage and temperature of the mixture. According to the schedule, we can say that with an increase in voltage we get good results.

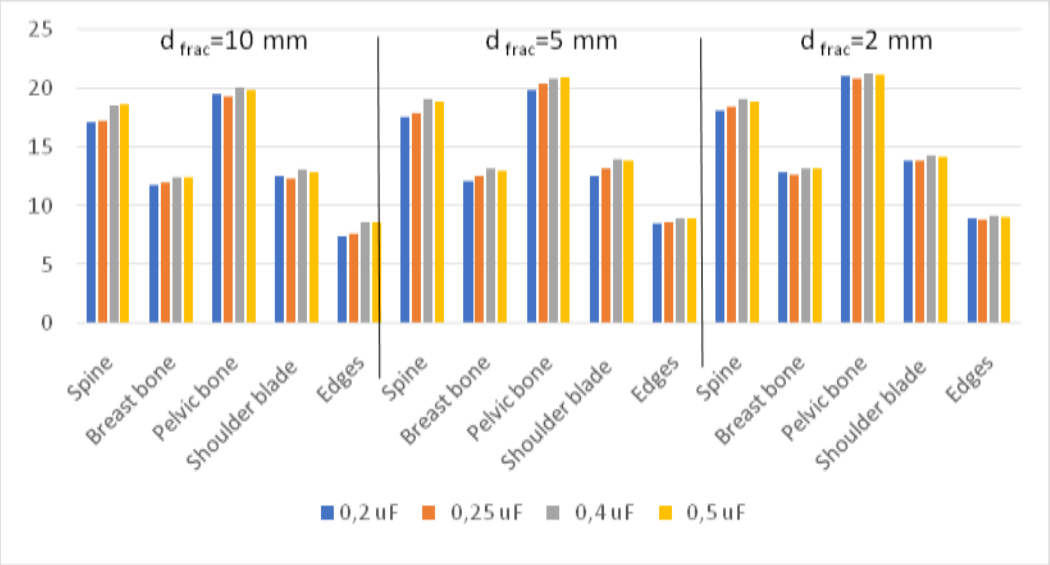

Figure 7. Influence of the capacitance of the capacitor bank of an electrohydroimpulse unit for degreasing crushed bone at $U = 30kV$, $l_p = 12mm$, $t_{\text{mixture}} = 44^0 C$

It can be seen from the figures that with an increase in the capacity of the capacitor bank in energy storage and the length of the discharge gap (l_p), the extraction of fat from bone mass increases, and the intensity of fat removal can stabilize with an increase in capacity. This allows you to select the optimal capacitance values necessary for reproducing experiments.

Based on the research, the optimal parameters of the developed electrohydroimpulse method for extracting fat from bone mass have been determined, where the treatment is carried out in a spark discharge mode with a specific energy of 2,0 104 J / m with a pulse repetition frequency of 10-16 Hz, and the process is carried out at a temperature of $36 - 44^0$ C.

Conclusions

To study the extraction of fat from organic compounds, we developed and assembled an experimental electrohydroimpulse installation, as well as a working cell was assembled. The methodology and conditions for conducting research and the procedure for conducting tests have been developed. The optimal temperature of the mixture was selected in the interval $32 - 50^0 C$ for extracting a valuable component from the bone mass — fat. It was found that at temperatures below $32^0 C$, part of the fat is retained by the skin. As a result of adsorption and capillarity, viscosity and surface fats are reduced, and the extraction process is reduced.

It was found that with an increase in the capacity of the capacitor bank in energy storage and the length of the discharge gap, the extraction of fat from bone mass increases, and the intensity of fat removal stabilizes with an increase in capacity. It was found that with an increase in the capacity of the capacitor bank in energy storage and the length of the discharge gap, the extraction of fat from bone mass increases, and the intensity of fat removal stabilizes with an increase in capacity. Based on the study, the optimal parameters of the developed electrohydroimpulse method for extracting fat from bone mass were determined.

Acknowledgment

This research is funded by the Science Committee of the Ministry of Science and Higher Education of the Republic of Kazakhstan (Grant no. AP19678501).

References

1 Соколов А.А. Технология мяса и мясопродуктов: учеб. / А.А. Соколов. — М.: Пищевая промышленность, 1970. — 740 с.

2 Стабников В.Н. Процессы и аппараты пищевых производств: учеб. / В.Н. Стабников, В.И. Баранцев. — М.: Агропромиздат, 1985. — 509 с.

3 Лысянский В.М. Экстрагирование в пищевой промышленности: учеб. / В.М. Лысянский, С.М. Гребенюк. — М.: Агропромиздат, 1987. — 187 с.

4 Либерман С.Г. Производство пищевых животных жиров на мясокомбинатах: учеб. / С.Г. Либерман. — М.: Пищевая промышленность, 1982. — 256 с.

5 Джафаров А.Ф. Производство желатина: учеб. / А.Ф. Джафаров. — М.: Агропромиздат, 1990. — 287 с.

6 Нусупбеков Б.Р. Влияние температуры на электрогидравлический способ извлечения жира из костной массы / Б.Р. Нусупбеков, А.Ж. Сатыбалдин, Г.Е. Сейсенбек // Вестн. Караганд. ун-та. Сер. Физика. — 2001. — № 1 (21). — С. 103–106.

7 Kusainov K.K. An elektrohydraulic metod of removal of fat from bones / K.K. Kusainov, B.R. Nusupbekov, G.E. Seisenbek // Eurasian Physical Technical Journal. — 2007. — Vol. 4, No. 2(8). — P. 57–61.

8 Сейсенбек Г.Е. Энергетические характеристики электрогидроимпульсного способа извлечения жира и белка из костной массы / Г.Е. Сейсенбек, Б.Р. Нусупбеков, К. Кусаиынов // Вестн. Евраз. нац. ун-та им. Л.Н. Гумилева. Сер. физ. — 2008. — № 2 (62). — С. 165–173.

9 Нусупбеков Б.Р. Способ обезжиривания костного сырья / Б.Р. Нусупбеков, Г.Е. Сейсенбек, Г.М. Шаймерденова, Р.С. Турлыбекова // Научная жизнь. — 2009. — № 2. — С. 30–33.

10 Нусупбеков Б.Р. Способ извлечения жира из костной массы / Б.Р. Нусупбеков, Г.Е. Сейсенбек, Г.И. Мусина, Д.К. Кусаиынова // Валихановские чтения: материалы Междунар. науч.-практ. конф. КГУ им. Ш. Уалиханова. — Кокшетау, 2012. — С. 147–151.

11 Кусаиынов К.Синергетические аспекты процесса извлечения жира из костной массы под воздействием самоорганизующихся подводных импульсов / К. Кусаиынов, Б.Р. Нусупбеков, Г.Е. Сейсенбек // Прикладная синергетика в нанотехнологиях «ФиПС–08»: материалы 5-го Междунар. междисцип. симпоз. — 2008. — С. 268–271.

Б.Р. Нусупбеков, М.С. Дуйсенбаева

Органикалық қалдықтарды электрогидроимпульс әдісімен өңдеу

Мақалада сүйек массасынан майды электрогидроимпульс әдісімен алу заңдылықтары, технология параметрлері және қондырғылар қарастырылған. Бүгінгі таңда ауылшаруашылығы шикізатын өңдейтін өнеркәсіп салаларында өндірістің өсуі және оның тиімділігінің артуы көбінесе шикізат ресурстары мен олардың сапасына ғана емес, сонымен қатар құнды компоненттерді алудың артуына да байланысты. Өндірісте өндірілетін өнімнің жоғалуын азайту, мысалы, қант, крахмал, май, өндірудің оңтайлы жолдары мен әдістерін қолдана отырып, дайын өнімнің шығымдылығын едәуір арттыра алады. Нәтижесінде байланыстарды бұзу, май жасушаларын тіндерде ұстау және жасушалардың өзін бұзу үшін жеткілікті қысым импульстары бар күшті гидравликалық соққылар пайда болады. Сонымен қатар мақалада сүйектен май алу технологиясы қарастырылған. Агроөнеркәсіптік кешеннің негізгі міндеті — ауылшаруашылығы өндірісін орнықты дамыту, Қазақстан Республикасының азық-түлік пен шикізатқа қажеттілігін толық қанағаттандыру. Агроөнеркәсіптік кешендегі, сондай-ақ жеңіл және тамақ өнеркәсібіндегі техникалық саясаттың басым бағыты қазіргі уақытта ауылшаруашылығы өндірушілерін сапалы, экологиялық таза, қауіпсіз және сенімділігі жоғары жабдықтармен қамтамасыз ету жөніндегі жедел-перспективалық шаралар жүйесін әзірлеу. Басым және өте қолайсыз өндірістік жағдайлар өндірушіні қайта өңдеуге емес, шикізатты сатуға мәжбүр етеді.

Кілт сөздер: ұшқын разряды, май, органикалық қалдықтар, соққы толқыны, ұсақтау, сүйек массасы.

Б.Р. Нусупбеков, М.С. Дуйсенбаева

Переработка органических отходов электрогидроимпульсным методом

В статье рассмотрены закономерности, параметры технологии и установки для электрогидроимпульсного извлечения жира из костной массы. На сегодняшний день рост производства и повышение его эффективности в отраслях промышленности, перерабатывающей сельскохозяйственное сырье, в значительной мере зависит не только от сырьевых ресурсов и их качества, но и от полноты извлечения ценных компонентов. Сокращение потерь извлекаемого

продукта в производстве, например, сахара, крахмала, жира, может существенно повысить выход готовой продукции при использовании оптимальных способов и методов извлечения. Результатом являются мощные гидравлические удары с импульсами давления, достаточными для удержания жировых клеток в ткани, разрушения связей и самих клеток. В настоящей статье рассмотрена технология извлечения жира из костей. Основная задача агропромышленного комплекса — устойчивое развитие сельскохозяйственного производства, полное удовлетворение потребностей Республики Казахстан в продовольствии и сырье. Приоритетным направлением технической политики в агропромышленном комплексе, а также в легкой и пищевой промышленности в настоящее время является разработка системы оперативно-перспективных мер по обеспечению сельхозпроизводителей качественным, экологически чистым, безопасным и высоконадежным оборудованием. Доминирующие и крайне неблагоприятные производственные условия вынуждают производителя не на переработку, а на реализацию сырья.

Ключевые слова: искровой разряд, жир, органические отходы, ударная волна, дробление, костная масса.

References

1 Sokolov, A.A. (1970). Tekhnologiia miasa i miasoproduktov [Meat and meat products technology]. Moscow: Pishchevaia promyshlennost [in Russian].

2 Stabnikov, V.N., & Barantsev, V.I. (1985). Protsessy i apparaty pishchevykh proizvodstv [Processes and apparatus of food production]. Moscow: Agropromizdat [in Russian].

3 Lysyanskiy, V.M., & Grebenyuk, S.M. (1987). Ekstragirovanie v pishchevoi promyshlennosti [Extraction in the food industry]. Moscow: Agropromizdat [in Russian].

4 Liberman, S.G. (1982). Proizvodstvo pishchevykh zhivotnykh zhirov na miasokombinatakh [Production of animal fats in meat processing plants]. Moscow: Pishchevaia promyshlennost [in Russian].

5 Dzhafarov, A.F. (1990). Proizvodstvo zhelatina [Gelatin production]. Moscow: Agropromizdat [in Russian].

6 Nussupbekov, B.R., Satybaldin, A.Zh., & Seysenbek, G.E. (2001). Vliianie temperatury na elektrogidravlicheskii sposob izvlecheniia zhira iz kostnoi massy [The effect of temperature on the electrohydraulic method of extracting fat from bone mass]. *Vestnik Karahandinskogo universiteta. Seriia Fizika — Bulletin of the University of Karaganda. Physics series, 1*(21), 103–106 [in Russian].

7 Kusainov, K.K., Nussupbekov, B.R., & Beisenbek, G.E. (2007). An elektrohydraulic metod of removal of fat from bones. *Eurasian Physical Technical Journal, 4, 2*(8), 57–61.

8 Seysenbek, G.E., Nussupbekov, B.R., & Kusaiynov, K. (2008). Energeticheskie kharakteristiki elektrogidroimpulsnogo sposoba izvlecheniia zhira i belka iz kostnoi massy [Energy characteristics of the electrohydroimpulse method for extracting fat and protein from bone mass]. *Vestnik Evraziiskogo natsionalnogo universiteta imeni L.N. Gumilyova. Seriia Fizika — Bulletin of L.N. Gumilyov Eurasian national University, Physics series, 2*(62), 165–173 [in Russian].

9 Nussupbekov, B.R., Seysenbek, G.E., Shaymerdenova, G.M., & Turlybekova, R.S. (2009). Sposob obezzhirivaniia kostnogo syria [Method of degreasing bone raw materials]. *Nauchnaia zhizn — Scientific life, 2*, 30–33 [in Russian].

10 Nussupbekov, B.R., Seisenbek, G.E. Musina, G.I. & Kusaiynova, D.K. (2012). Sposob izvlecheniia zhira iz kostnoi massy [Method of extracting fat from bone mass]. *Vallikhanovskie chteniia: Materialy Mezhdunarodnoi nauchno-prakticheskoi konferentsii Kokshetauskogo gosudarstvennogo universiteta imeni Sh. Ualikhanova — Valikhanov readings: Materials of the International Scientific and Practical Conference of the Kokshetau State University named after Ch. Ualikhanov.* Kokshetau, P. 147-151 [in Russian].

11 Kusaiynov, K., Nussupbekov, B.R., & Seisenbek, G.E. (2008). Synergeticheskie aspekty protsessa izvlecheniia zhira iz kostnoi massy pod vozdeistviem samoorganizuiushichsia podvodnykh impulsov [Synergetic aspects of the process of extracting fat from bone mass under the influence of self-organizing underwater impulses]. *Prikladnaia sinergetika v nanotekhnologiiakh "FiPS-08": materialy piatogo Mezhdunarodnogo mezhdistsiplinarnogo simpoziuma — Applied synergetics in nanotechnology "FiPS-08": 5th Symposium Interdisciplinary International symposium,* 268–271 [in Russian].

DOI 10.31489/2023PH3/163-170

UDC 621.384.327

D.E. Uskenbaev, A.S. Nogai*, A.D. Uskenbaev, E.A. Nogai

S. Seifullin Kazakh Agrotechnical Research University, Astana, Kazakhstan,
*(*E-mail: nogay06@mail.ru)*

Effects of conditions on the synthesis and properties of Bi-2234 HTSC ceramic produced from the melt

The article presents the results of a study aimed at obtaining the formation of superconducting phases and the formation of a high texture of particles that affect the current-carrying characteristics in ceramics of the composition Bi1.6Pb0.4Sr2Ca3Cu4Oy and the study of their properties. For the synthesis of ceramics, precursors from the glass phase were used, which were obtained by melting the starting material under the influence of radiant flux (IR radiation) and quenching the melt in a facility rotating at a speed of 3000 rpm. Platinum wire was used as a substrate. During the heat treatment of samples in the temperature range of 845 — 850 °C and a holding time of 72 hours (with intermediate grinding every 24 hours), the superconducting high-temperature phase Bi-2223 crystallized in the studied samples. Critical temperatures and resistances of superconducting samples were measured by the four-probe method by measuring the dependence of resistance on the temperature in the range from 300 K to 60 K.

Keywords: superconductivity, critical temperature, electrical resistance, diffractogram, glass phase.

Introduction

Superconductors are among the promising materials with special electrical properties for use in various industries. The superconductors developed to date have made it possible to create prototypes of various electronic devices — SQUID magnetometers [1], microwave generators [2], protective devices for sensitive semiconductor elements [3], elements of quantum computers [4, 5], optical sensors [6] and elements of high-speed electronics [7], etc. Due to their high current carrying capacity, they occupy a special place in the power industry for the creation of various high-current elements and devices such as motors and electric generators [8], power cables [9-11], transformers [12, 13], motors [14, 15], current limiters for short circuits [16-18].

With the establishment of superconductivity in the La-Ba-Cu-O oxide system [19], the science of superconductivity moved to a new stage of development, which developed families of a number of superconducting cuprate systems with a critical temperature exceeding the temperatures of cheap liquid nitrogen — yttrium [20], bismuth [21], mercury [22], thallium [23], etc.

Among these superconducting systems, bismuth-containing superconductors can be attributed to one of the most promising.

It is known that in the Bi–Sr–Ca–Cu–O bismuth system, three stable superconducting compounds of the homologous series $Bi_2Sr_2Ca_{n-1}Cu_nO_y$ (n = 1, 2, 3) are established with a transition temperature to the superconducting states of 30-35 K, 80-90 K and 107 — 110 K, respectively. With an increase in the number of Ca and Cu layers, the critical temperature also increases. But on the other hand, with an increase in the critical temperature, the requirements for the condition for obtaining (if phase 2201 crystallizes from the melt, then the temperature interval for the formation of phase 2212 lies in the region of 750-850 C and the synthesis time is 80-1100 hours, and for the phase, the existence interval lies in a narrow temperature region of 848-850 C and long annealing from 150-400 hours). If phase 2201 crystallizes from the melt, then the synthesis of phase 2212 requires several tens of hours of heat treatment at a temperature of 800 — 850 hours. And for the synthesis of phase 2223, more stringent conditions are required — heat treatment in a narrow temperature range with intermediate grinding involving the liquid phase with a time of 100-350 hours of exposure, depending on the approach and method. In [24], when synthesizing HTS of the composition $Bi_{1.65}Pb_{0.35}Sr_2Ca_4Cu_5O_y$by the solid-phase method using the matrix method ($Bi_{1.65}Pb_{0.35}Sr_2Ca_2Cu_3O_y$and Ca_2PbO_4 were used as a matrix), along with phase 2223, a low-temperature superconducting phase 2212 and Ca_2PbO_4 were present. In [25], during the synthesis of HTSP compositions $Bi_{1.7}Pb_{0.3}Sr_{2+x}Ca_{4-x}Cu_5O_y$ (x = 0.2; 0.4; 0.6) with partial substitution of calcium for strontium during heat treatment for 150 h at a temperature of 840-850 °C, a superconducting 2223 phase with Tc =107 K was obtained. In [26], when

synthesizing the composition $Bi_{1.9}Pb_{0.4}Sr_2Ca_{3.1}Cu_{4.2}O_x$ by ceramic technology, the dominant phase was 2223 (about 80 %). Pb(Sr, Ca)$_2O_4$, Ca_2CuO_3, CuO oxides and superconducting phases 2201 and 2212 were also present. In [27], the synthesis of compositions (Bi, Pb)$_4Sr_3Ca_3Cu_{4-m}Fe_mO_x$ (m = 0 — 0.06) was carried out from the glass phase. Melting was carried out in a platinum crucible and tempered by flapping between two massive plates. After annealing at 840 °C for 40 hours, the presence of a low-temperature superconducting phase 2212 (the main phase was 2223) was found in the samples. In [28], superconducting ceramics of the composition $Bi_{1,6}Pb_{0,4}Sr_2Ca_3Cu_4O_y$ were synthesized by casting from a melt. As a result of prolonged annealing (150 hours), the samples consisted of phases 2212 and 2223. In [29-31], the synthesis of HTS was carried out using laser radiation. In [29], new layered bismuth cuprates were obtained by laser ablation in the form of films of the compositions $Bi_2(La, Ca)_2Ca_{n-1}Cu_nO_z$(n = 3, 4, 5, 6, and 7). Measurements of the lattice constant showed that "c" is 3.66 nm; 4.31 nm; 4.94 nm; 5.60 nm and 6.25 nm corresponding to phases 2223, 2234, 2245, 2256 and 2267. But in all samples, the effect of superconductivity was not detected above 4.2 K, which may be related to the defects of crystal structures. In [30, 31], a textured superconductor with a critical current of 5000 A/cm^2 was synthesized by zone melting under the influence of laser radiation.

The analysis of numerous studies shows that in the synthesis of HTS with increased content of calcium and copper by various methods, obtaining a high-temperature monophase sample with 2223 is a difficult task, because low-temperature superconducting phase 2212 is always present in the samples. In many cases, the samples also contain non-superconducting intermediate phases. And in the synthesis of HTS using radiant energy, it can be assumed that the formation of superconducting phases with an increased content of calcium and copper, also obtain superconducting materials with high critical parameters. In this regard, the synthesis of HTS phases in the Bi(Pb)–Sr–Ca–Cu–Os system using IR radiation was of interest.

Materials and methods

The following components were used for the synthesis of HTSP composition $Bi_{1,6}Pb_{0,4}Sr_2Ca_3Cu_4O_y$: Bi_2O_3, $Bi(NO_3)_3 \cdot 5H_2O$, PbO, PbO_2, $SrCO_3$, CaO, CuObrands no worse than "PA". The initial precursors and HSTP samples were annealed in a muffle furnace SNOL –8.2/1100. The phase compositions of amorphous precursors and superconducting samples were controlled by X-ray diffraction using Bruker D8ADVANCEECO and XPertPRO diffractometers (Netherlands). Microstructural and elemental analyses of samples were carried out on scanning electron microscopes JEOL-6490LA (Japan) with an energy dispersive analyzer system "OXFORD Instruments Analytical Limited" (UK) and JSM-6390LV (Japan) with an integrated energy dispersive X-ray analyzer (EDS). The critical temperature was determined by measuring the temperature dependence of the resistance in the temperature range from 300 K to 60 K by a four-probe method using a closed cryo-camera "CryoIndustry REF-1808-ACS", cryo-camera cooled by helium gas, a LakeShoreModel 340 temperature meter and a microvoltmeter. As a contact between the sample and the electrodes, a contractor of the SCP brand based on a silver paste was used.

Results and discussion

This paper presents the results of the synthesis of Bi-HTS composition $Bi_{1,6}Pb_{0,4}Sr_2Ca_3Cu_4O_y$ based on glass phase, which is a kind of melt technique. When obtaining HTSC ceramics from a glass phase, the synthesis of superconducting phases is strongly influenced by the method and conditions for obtaining precursors, since in the bismuth system there are elements of variable valence Cu, Bi, Pb.

Depending on the receiving condition, they may be in different charge states.

And peculiarities of the influence of radiation, such as the electromagnetic field, which can affect the fine structure of the material (defect). Features of the influence of radiation, such as an electromagnetic field, which can affect the fine structure of the material (defect). To obtain precursors, a non-melting method was developed for obtaining a glass phase from a melt under the influence of IR radiation. For comparative analysis, the results obtained using dense optical radiation and glass phase obtained in a muffle furnace by melting in a crucible were also used.

By synthesizing HTSC ceramics with the composition $Bi_2Sr_2Ca_3Cu_4O_y$, it was found that the diffraction patterns of bulk HTSC precursors (glass-crystalline) obtained in a muffle furnace contain low-valence oxide Cu_2O.

On the contrary, Cu_2O oxides are absent in precursors obtained by heating with radiant energy (optical and IR radiation). Studies of the formed superconducting phases have shown that the superconducting phase 2223c T_{sn} = 107-110 K crystallizes in the composition of $Bi_2Sr_2Ca_3Cu_4O_y$ (Fig. 1, 2).

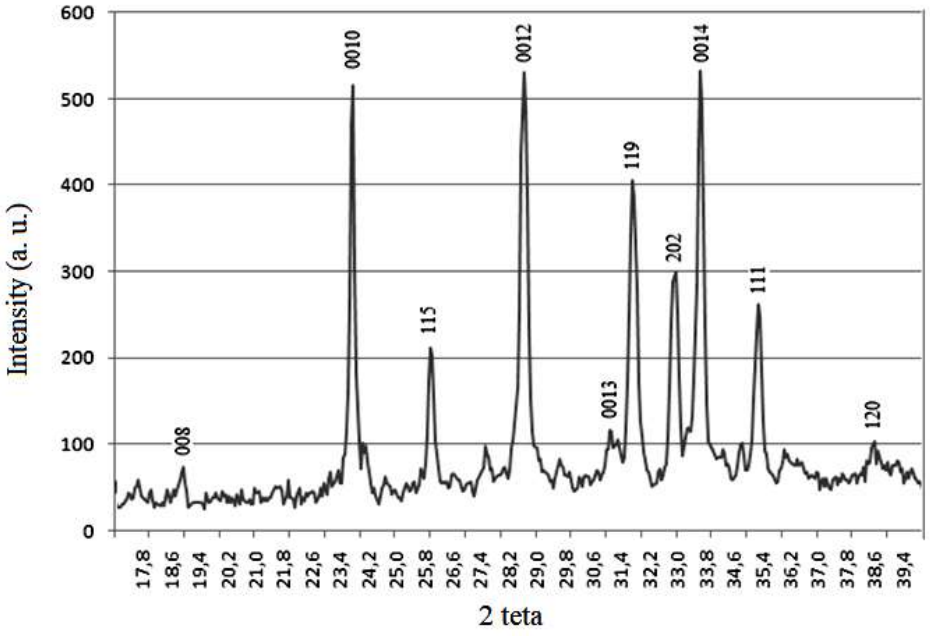

Fig. 1. X-ray diffraction pattern of an HTSC sample of composition Bi1.6Pb0.4Sr2Ca3Cu4Oy synthesized from amorphous precursors obtained by IR heating

The results of the X-ray phase analysis show that all X-ray reflexes are related to the high-temperature superconducting phase Bi-2223.

It follows from the X-ray data (hkl [0010], [0012], and [0014]) that the ceramic sample has a texture along the 00l crystallographic plane.

The results of the study of the electron microscopic analysis of HTSC ceramics show that the crystallites have a lamellar shape (Fig. 2)

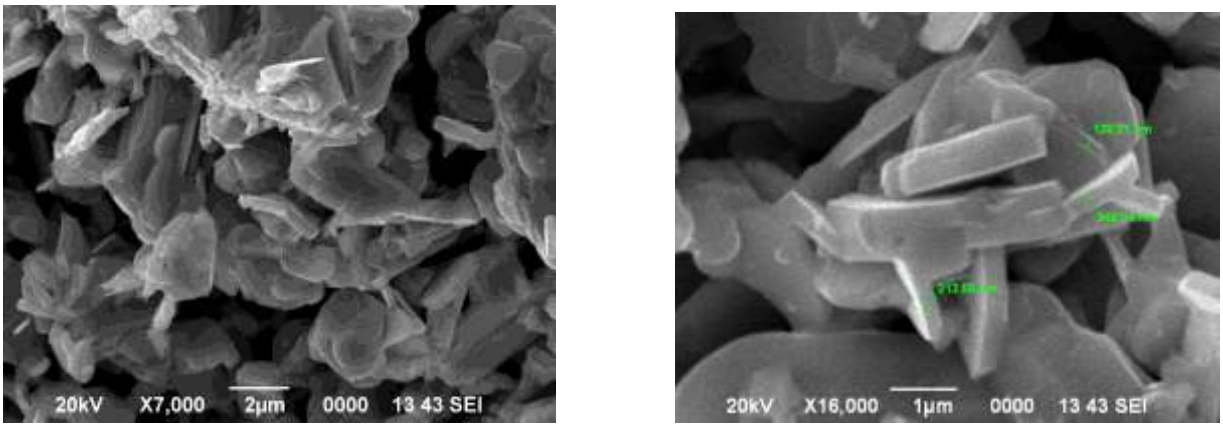

a) b)

Fig. 2. Microstructure of HTSC ceramics of composition $Bi_{1.6}Pb_{0.4}Sr_2Ca_3Cu_4O_y$ synthesized from amorphous precursors obtained by IR heatinga) — x 7000, b) — x16000

The crystallite size is in the range of 2–8 μm (Fig. 2a), and the thickness is in the range of 0.2–0.25 μm. By analyzing the results of studying the content of elements in a sample of superconducting ceramics, it was found that metal cations do not undergo noticeable changes in their content (Fig. 3).

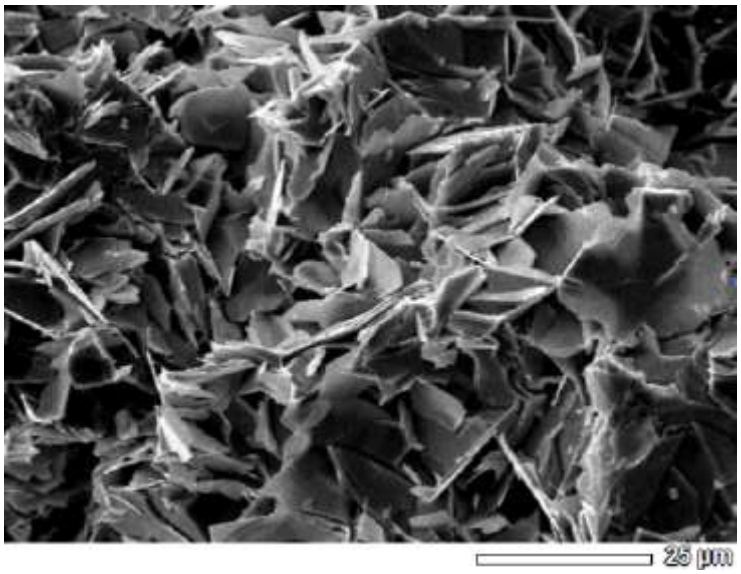

a)

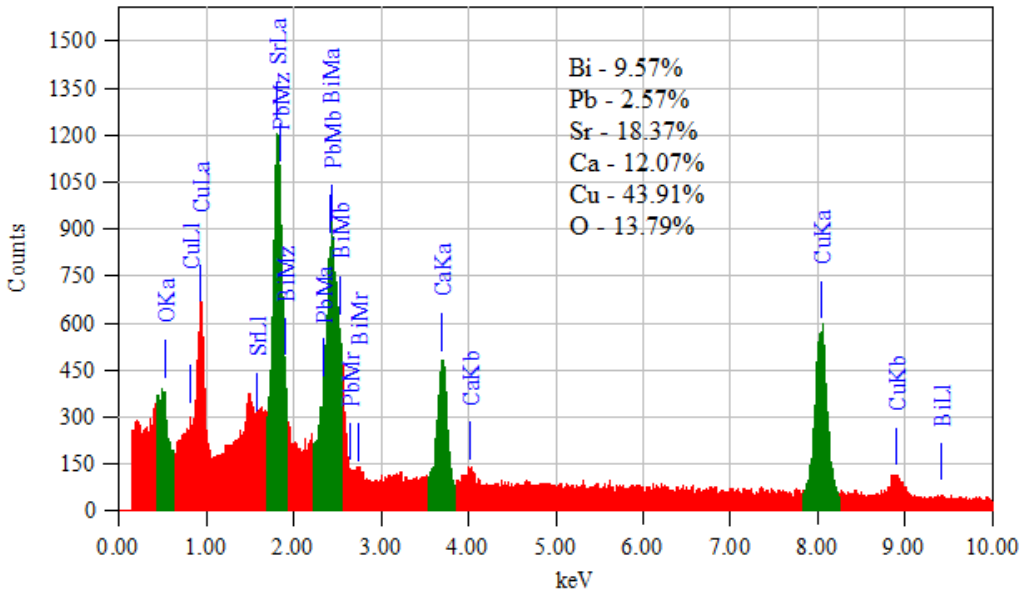

b)

Fig. 3. Elemental analysis of $Bi_{1.6}Pb_{0.4}Sr_2Ca_3Cu_4O_y$ HTS ceramics synthesized from amorphous precursors obtained by IR heating: a) microstructure; b) elemental composition.

The critical temperature was determined in a cryogenic installation by changing the resistance of the sample when the sample temperature was cooled from room temperature (300 K) to 70 K. It was found that the transition to the superconducting state begins at 107 K. Such a transition is typical for the superconducting phase of Bi-2223 (Fig. 4).

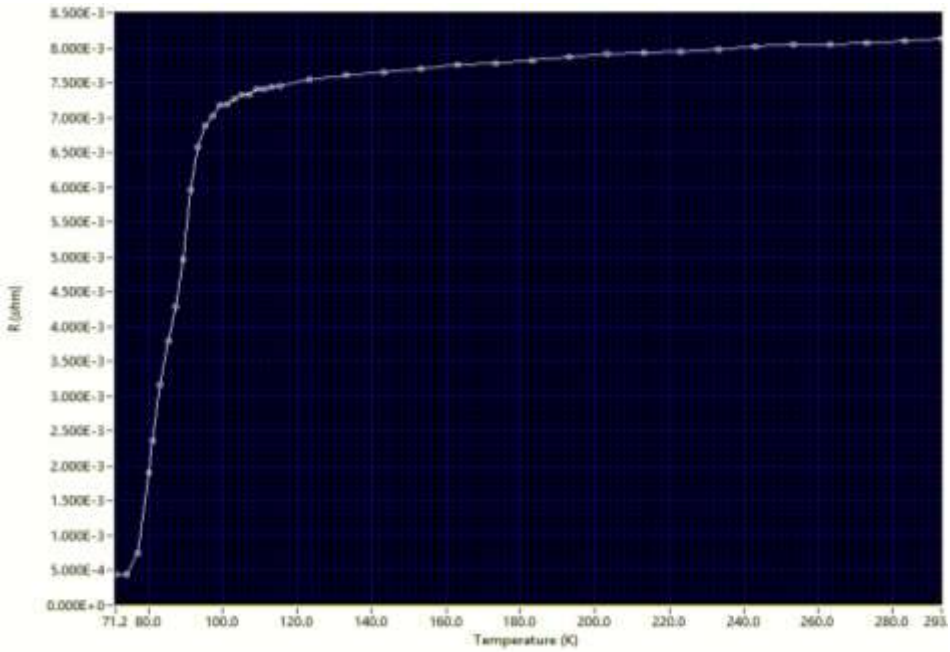

Figure 4. Critical temperature of a $Bi_{1.6}Pb_{0.4}Sr_2Ca_3Cu_4O_y$ sample synthesized from amorphous precursors obtained by IR heating

The complete transition to the superconducting state corresponds to a temperature of 75 K and the resistance of the HTSP sample is $4{,}7 \cdot 10^{-4}$ ohms. It is assumed that such a large transition width is associated with Ca and Cu cations, which can be located on the surface of crystallites and in grain boundaries. It is possible that with the growth of crystallites of the superconducting phase Bi-2223, excess Ca and Cu cations are displaced onto the surface of the crystallites and grain boundaries, forming a non-superconducting layer, which can affect the critical temperature of the superconducting sample, i.e. reduce the T_c.

When synthesizing HTSC samples from amorphous precursors using optical radiation with a high flux density, then single-phase samples 2223 are synthesized at a temperature of 846-848 C with an exposure time of 70-80 hours. In HTSC ceramics synthesized from a melt in a muffle furnace, even with a heat treatment time of more than 150 hours, the 2212 phase is present in the samples, which may be due to the influence of the atmosphere on the valence states of variable valence cations, as well as the peculiarity of the effect of radiation on precursors. When using amorphous precursors obtained under the influence of IR radiation, the synthesis time is reduced to 40-50 hours and the reliability of the formation of single-phase HTS materials increases (Fig. 5).

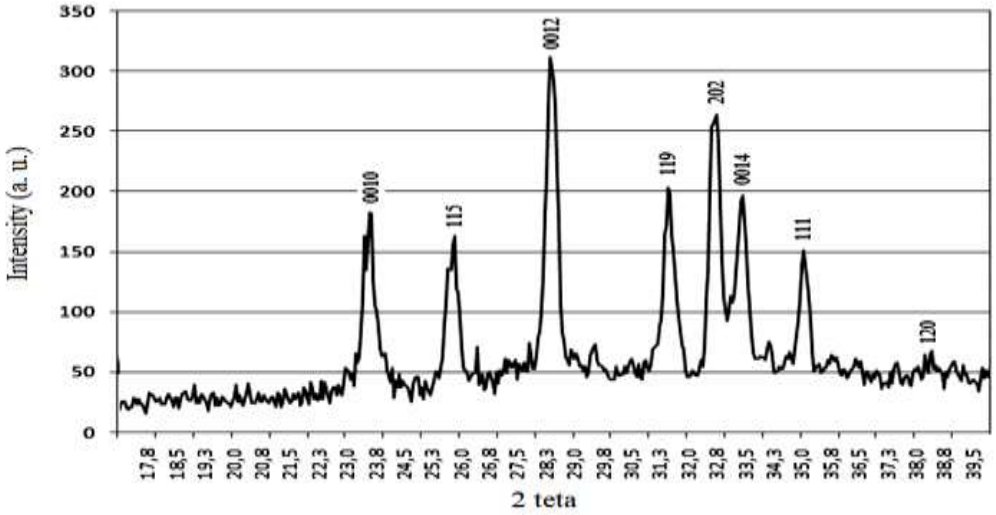

Fig. 5. X-ray diffraction pattern of the HTSC $Bi_{1.6}Pb_{0.4}Sr_2Ca_3Cu_4O_y$ sample synthesized at 850 °C for 48 h from amorphous precursors prepared by IR heating

Analysis of the results of the X-ray diffraction study of the HTS sample composition $Bi_{1.6}Pb_{0.4}Sr_2Ca_3Cu_4O_y$ shows that all X-ray reflection reflexes belong to the high-temperature superconducting phase 2223. A particularly important task of the synthesis process is to achieve a high texture, which can directly affect the current-carrying characteristics of HTS ceramics. To achieve a high texture, it was necessary to increase the duration of the processes of grinding the charge, pressing under high pressure, as well as its heat treatment to improve the perfection of the structure and increase the size of the crystallites. After these successive HTS processes, the ceramics had a high texture with perfect X-ray reflection reflexes (Fig. 6).

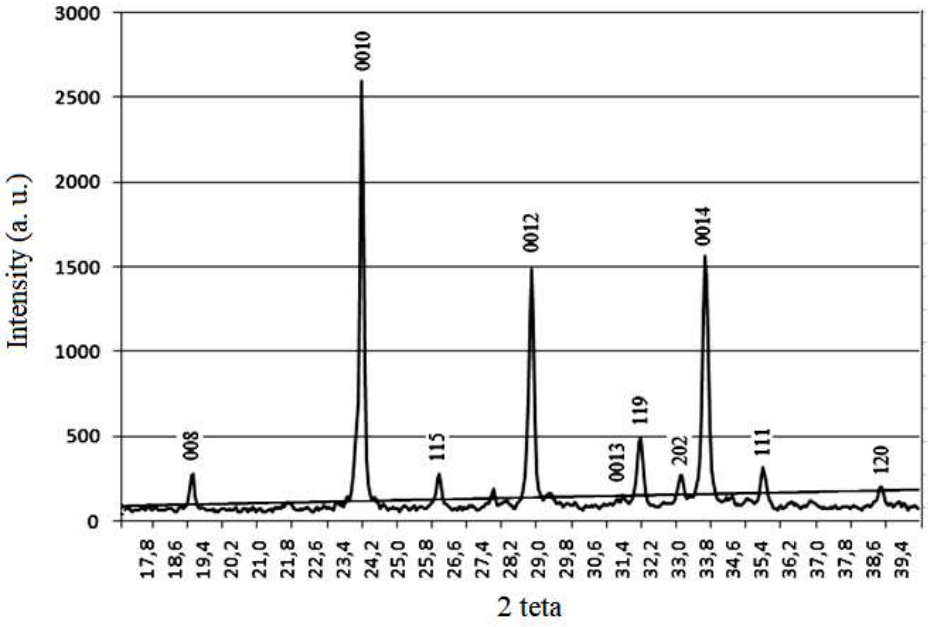

Fig. 6. X-ray diffraction pattern of the HTSC $Bi_{1.6}Pb_{0.4}Sr_2Ca_3Cu_4O_y$ sample synthesized at 850 °C for 120 h from amorphous precursors obtained by IR heating

All X-ray reflection reflexes belong to the superconducting phase 2223. The degree of uniformity of the texture is about 85-90 % and it is directed along the crystallographic plane *00l.*

Conclusions

Thus, based on the above, it can be concluded that in the synthesis of HTS composition $Bi_{1.6}Pb_{0.4}Sr_2Ca_3Cu_4O_y$ based on amorphous precursors, the heating method and conditions for obtaining precursors are important. When precursors are obtained under oxidizing atmospheric conditions and under the influence of IR radiation, the formation time of the high-temperature superconducting phase Bi-2223 is reduced compared to samples obtained by melting (in a crucible) in a muffle furnace. The study of the temperature dependence of the resistance of samples of HTS ceramics found that on samples obtained with the use of IR radiation, the beginning of the transition to a superconducting state corresponds to a temperature of 107 K, and the critical temperature T_c = 75 K. It is assumed that such a wide transition to the superconducting state is associated with the formation of excess cations on the surface and in the grain boundaries, displaced from the volume during the growth of crystallites, having ordinary conductivity (not superconductor).

Acknowledgments

The work was carried of the grant of the Education and Science of the Republic of Kazakhstan AP09260251.

References

1 Keene, M. et al. (1993). Thin film HTS SQUID construction and characterization. *IEEE Transactions on Applied Superconductivity, Vol. 3,* No 1, P. 2430–2433.

2 An, D. et al. (2013).Terahertz emission and detection both based on high-Tc superconductors: Towards an integrated receiver. *Applied Physics Letters, Vol. 102,* No 9, P. 092601.

3 Fyk, O. Kucher, D., Kucher, L., Gonchar, R., Fyk, M., & Besedin, Y. (2018). Analysis of the technology to manufacture a high-temperature microstrip superconductive device for the electromagnetic protection of receivers. *Eastern-European Journal of Enterprise Technologies, Vol. 5,* No 12-95, P. 38—47.

4 Schulz, R.R. et al. (2000). Design and realization of an all d-wave dc π-superconducting quantum interference device. *Applied Physics Letters, Vol. 76,* No 7, P. 912–914.

5 Devoret, M.H., & Martinis, J.M. (2005). Implementing qubits with superconducting integrated circuits. *Experimental Aspects of Quantum Computing. Springer,* P. 163–203.

6 Jurbergs, D.C. et al. (1995). Electrochemical and optical devices based on molecule/high-Tc superconductor structures. *Electrochimica Acta., Vol. 40,* No 10, P. 1319–1329.

7 Xiong, W., Kula, W., & Sobolewski, R. (1994). Fabrication of High-T c Superconducting Electronic Devices Using the Laser-Writing Technique. *Advances in Cryogenic Engineering Materials. Springer,* P. 385–391.

8 Hull, J.R., & Strasik, M. (2010). Concepts for using trapped-flux bulk high-temperature superconductorin motors and generators. *Superconductor Science and Technology, Vol. 23,* No 12, P. 124005.

9 Hajiri, G., Berger, K., Trillaud, F., Lévêque, J., & Caron, H. (2023). Impact of Superconducting Cables on a DC Railway *Network. Energies, No 16*(2), P. 776.

10 Hamabe, M., Sugino, M., Watanabe, H., Kawahara, T., Yamaguchi, S., Ishigur, Y., & Kawamura, K. (2011). Critical current and its magnetic field effect measurement of HTS tapes forming DC superconducting cable. *IEEE Transactions on Applied Superconductivity, No 21,* P. 1038-1041.

11 Bulinski, A., & Densley, J. (1999). High voltage insulation for power cables utilizing high temperature superconductivity. *IEEE Electrical Insulation Magazine, No 15*(2), P. 14-22.

12 Kumar, M., Joshi, P., & Gupta, R.A. (2023). 50 kA Superconducting Transformer for the Upcoming High-Field High-Current Testing Station at the BNL. *IEEE Transactions on Applied Superconductivity, No 33*(5), P.5500305.

13 Orosz, T. (2022). FEM-Based Power Transformer Model for Superconducting and Conventional Power Transformer Optimization. *Energies, No 15*(17), P. 6177.

14 Lu, M., & Cao, R.A. (2021). Novel Double-Sided High Temperature Superconducting Linear Modular Flux-Switching Motor. *IEEE Transactions on Applied Superconductivity, No 31*(5), P. 9357980.

15 Ma, E., Wu, H., & Li, Y. (2021). Development and testing of a cryogenic induction motor with a novel Dewar structure. *Cryogenics, No 116,* P.103283.

16 Kozak, J. (2022). Forces and Stresses in the Windings of a Superconducting Fault Current Limiter. *Energies, No 15*(18), P. 6519.

17 Choi, Y., Song, S., Kim, J., Choi, Y.S., & Ko, T.K. (2022). Thermal and Electrical Characteristics of Hollow Former With Fault Current Limiting Function for Superconducting Power Cable. *IEEE Transactions on Power Delivery, No 37*(2), P. 1100-1108.

18 Lim, S.H. (2010). Study on current limiting characteristics of SFCL with two trigger current levels. *Physica C: Superconductivity and its Applications, No 470*(20), P. 1631-1635.

19 Bednorz, J.G., & Muller, K.A. (1986). Possible high Tc superconductivity in Ba-La-Cu-O system. *Z. Phys., Vol. 64B,* No 1, P.189-193.

20 Wu, M.K., Ashburn, J.R., & Torng, C.J. et. al. (1987). Superconductivity at 93 K in a New Mixed Phase Y-Ba-Cu-O Compound System at Ambient Pressure. *Phys. Rev. Lett., Vol. 58,* No 9, P. 908-910.

21 Takano, M., Takada, J., & Oda, K., et. al. (1988). High-Tc Phase Promoted and Stabilized in the Bi, Pb-Sr-Ca-Cu-O System. *Jpn. J. Appl. Phys., Vol. 27,* No 6, P. L1041-L1043.

22 Chu, C.W., Gao, L., & Chen, F., et. al. (1993). Superconductivity above 150 K in HgBa2Ca2Cu3O8-δat high pressures. *Nature, Vol. 365,* P. 323-325.

23 Sheng, Z.Z., & Hermann, A.M. (1988). Superconductivity in the rare-earth-free Tl–Ba–Cu–O system above liquid-nitrogen temperature. *Nature, Vol. 332,* No 6159, P. 55-58.

24 Ashoka, N.V., George, T.C., & Srinivasan, K. (2014). Investigation of Structural Formation of Starting Composition 2245 in the Bi-Pb-Sr-Ca-Cu-O System Superconductors. *Journal of Solid State Physics, V. Article ID 716032,* P. 1-7.

25 Meretliev, Sh., Sadykov, K.B., & Berkeliev, A. (2000). *Turk J. Physics,* No 24, P. 39.

26 Panova, G.P., Khlopkin, M.N., Chernoplekov, N.A., & Gorobchenko, V.D. (1990). *Superconductivity: physics, chemistry, technology. Vol. 3.*, No 3. P. 421.

27 Chatterjee, S., Bhattacharya, S., & Chaudhuria, B.K. (1998). *Journal of Chemical Physics, Vol. 108,* No 7, P. 2954.

28 Coskun, A., Ozcelik, B., & Kiymac, K. (2001). Physical Properties of Melt-Cast Annealed Bi{1.6}Pb{0.4}Sr{2}Ca{3}Cu{4}O{12}Compound. *Turk J. Phys., Vol. 25,* No 5, P. 473.

29 Yoshiba, K., Sasakura, H., Tsukuic, S., & Mizokawab, Y. (1999). New Bi-cuprate thin films of $Bi_2(La, Ca)_2Ca_{n-1}Cu_nO_z$ (n=3, 4, 5, 6 and 7) prepared by the laser ablation method. *Physica C: Supercond., Vol. 322,* Iss. 1-2, P. 25-30.

30 Mora, M., Gimeno, F., Angurel, L.A., & De la Fuente, G.F. (2004). Laser zone $Bi_2Sr_2CaCu_2O_{8+\delta}$ thick films on (100) MgO substrate. *Supercond. Sci. Technol. Philadelphia, No 17,* P. 1133-1138.

31 Mora, M., Lopez-Gascon, C., Angurel, L.A., & De la Fuente, G.F. (2004). The influence of support temperature on Bi-2212 monoliths textured by diode laser zone melting. *Supercond. Sci. Technol. Philadelphia, No 17,* P. 1129-1133.

Д.Е. Өскенбаев, А.С. Ноғай, А.Д. Өскенбаев, Э.А. Ноғай

Балқымадан өндірілген Bi-2234 висмут HTSC керамикасының синтезі мен қасиеттері

Мақалада $Bi_{1.6}Pb_{0.4}Sr_2Ca_3Cu_4O_y$ құрамды керамикадағы ток өткізгіштік сипаттамаларға әсер ететін асқын өткізгіш фазаларды алуға, бөлшектердің жоғары құрылымын қалыптастыруға және олардың қасиеттерін зерттеуге бағытталған зерттеу нәтижелері келтірілген. Керамика синтезі бұрын дайындалған бастапқы шыны фазасы үлгілері негізінде ИҚ-сәулелену әсерінен балқыту және өте жоғары жылдам сөндіру арқылы (3000 айналу/мин жылдамдықпен айналатын қондырғыда) жүзеге асырылды. Субстрат ретінде платина сымы қолданылды. Үлгілер 72 сағат ұстау уақытымен (аралығы әрбір 24 сағат сайын ұнтақтаумен) 845-850 температура аралығында термиялық өңдеу арқылы синтезделді. Барлық үлгілерде жоғары температуралы асқын өткізгіш Bi-2223 фаза кристалданды. Асқын өткізгіш үлгілердің критикалық температуралары мен кедергілерін өлшеу төрт зондты әдіспен 300 К-ден 60 К-ге дейінгі диапазондағы кедергінің температураға тәуелділігін өлшеу арқылы жүзеге асырылды.

Кілт сөздер: асқын өткізгіштік, критикалық температура, электр кедергісі, дифрактограмма, шыны фазасы.

Д.Е. Ускенбаев, А.С. Ногай, А.Д. Ускенбаев, Э.А. Ногай

Синтез и свойства висмутовой ВТСП керамики Bi–2234, полученной из расплава

В статье представлены результаты исследования, направленные на образование сверхпроводящих фаз и формирование высокой текстуры частиц, влияющих на токонесущие характеристики в керамике состава $Bi_{1.6}Pb_{0.4}Sr_2Ca_3Cu_4O_y$, и исследования их свойств. Синтез керамик осуществляли на основе стеклофазы, полученной под воздействием ИК излучения путем плавления и сверхбыстрой закалки расплава (на установке, вращающейся со скоростью 3000 об/мин) предварительно подготовленных исходных образцов. В качестве подложки была использована платиновая проволока. При термообработке образцов в интервале температур 845–850 °С и времени выдержки 72 ч (с промежуточным помолом в каждые 24 ч) в исследуемых образцах кристаллизовалась сверхпроводящая высокотемпературная фаза Bi–2223. Измерение критических температур и сопротивлений сверхпроводящих образцов осуществлялось четырехзондовым методом путем измерения зависимости сопротивления от температуры в интервале от 300 К до 60 К.

Ключевые слова: сверхпроводимость, критическая температура, электросопротивление, дифрактограмма, стеклофаза.

DOI 10.31489/2023PH3/171-177

UDC 536.631+546.654:41-31:824-31:713-31

B.K. Kasenov[1], Sh.B. Kasenova [1], Zh.I. Sagintaeva[1], C.O. Baisanov[1], N.Yu. Lu[1], Zh.S. Bekturganov[2], A.K. Zeinidenov[2], E.E. Kuanyshbekov[1]

Thermodynamic properties of titanium-manganite $LaCaTiMnO_6$

[1]Abishev Chemical-Metallurgical Institute, Karaganda, Kazakhstan;
[2]Karaganda University of the name of academician E.A. Buketov, Karaganda, Kazakhstan
*(*E-mail: kasenov1946@mail.ru)*

By the method of dynamic calorimetry in the range of 298.15-673 K, the heat capacity of titanium-manganite LaCaTiMnO6, obtained by solid-phase interaction at 800-1200ºC from lanthanum, titanium (II), manganese (III) and calcium carbonate oxides was studied. On the dependence curve $Cp°\sim f(T)$ in the specified temperature range, a λ-shaped effect was detected at 598 K, probably related to the phase transition of the second kind. A fundamental constant is determined — the standard heat capacity of LaCaTiMnO6, equal to 221±14 J /(mol·K). Its standard entropy, equal to 206±6 J/(mol·K), was estimated by the approximate method of ion increments. Based on experimental data, taking into account the temperature of the phase transition, the equations describing the temperature dependences of $C_p°\sim f(T)$ and the thermodynamic functions $S^o(T)$, $H^o(T) — H^o(298.15)$ and $\Phi^{xx}(T)$ of the investigated titanium-manganite lanthanum and calcium are calculated. The standard heat capacity of LaCaTiMnO6 is also calculated using the Debye method, the value of which is in good agreement with experimental data. According to the developed methodology, the standard enthalpy of titanium-manganite formation was calculated, equal to — 3867.5 kJ/mol.

Keywords: Titanium-manganite, lanthanum, calcium, heat capacity, phase transition, enthalpy of formation, thermodynamic properties.

Introduction

Manganites with an effect of colossal magneto resistance (CMR) have the significant innovative perspectives such as the functional materials for sensors in the consumer and industrial electronics and development of the information technologies [1-3]. Lanthanum manganites doped in B-sublattice with titanium have the high electrical conductivity. They can be applied as cathodes of the high-temperature solid oxide fuel cells, the ceramic membranes of the thermo-resistors and magneto-resistors. Titanium oxides with transition metal impurities fix attention as the advancing materials to use in the spin electronics and catalysis [4]. Many investigations described that the doping with TiO_2 can increase the sensitivity and capacity of devices [5]. Titanates of alkaline earth metals are semiconductors with a large band gap (3.0-3.2 eV). They can also be the potential photocatalysts under UV-irradiation [6]. The intensive studies of perovskite-like manganites of the rare earth metals are a basis of materials for various devices, and however, many fundamental problems of the chemistry of these oxides have not been studied well. Based on the above, the purpose of this investigation is to study the thermodynamic properties of titanium-manganite of $LaCaTiMnO_6$.

This titanium-manganite of $LaCaTiMnO_6$ was synthesized by a method of solid-phase synthesis from oxides of lanthanum (III) (puriss. spec.), titanium (IV), manganese (III) and calcium carbonate (p.a.) in the SNOL furnace in four stages: 1) annealing at 800 °C for 5 h, cooling to 25 °Cand grinding; 2) annealing at 1000 °C for 10 h; 3) annealing at 1200 °C for 4 h and 4) low-temperature annealing at 400 °C for 10 h.

The identification of an equilibrium composition formation was determined through X-ray phase analysis conducted on the DRON-2.0 diffractometer. The indexing of the X-ray photogram was performed by the analytical method. A type of syngony and crystal lattice parameters was determined: $LaCaTiMnO_6$ (cube) — a= 13.35 ± 0.02 Å; V^0 = 2376.3 ± 5.00 Å^3; Z = 4; $V°_{elec.cell}$= 594.08 ± 1.25 Å^3; $\rho_{roent.}$ = 3.96 g/cm^3; $\rho_{pick.}$ = 3.95 ± 0.02 g/cm^3 [7].

1. Experimental technique

The investigation of the isobaric heat capacity of LaCaTiMnO6 titanium-manganite was conducted using an IT-C-400 calorimeter over the temperature range of 298.15 K to 673 K. The calorimeter operates based on the comparative method, using a dynamic calorimeter with a heat meter. Temperature measurements were taken at fixed intervals of 25 °C. The device offers a precision of ±10 %. To ensure

accurate measurements, the device was calibrated based on the determination of the thermal conductivity of the KT heat meter [8, 9].

A standard deviation ($\overline{\delta}$) was computed for the averaged values of the specific heat capacity at each temperature, as explained in [9]:

$$\delta = \sqrt{\frac{\sum_{i=1}^{n}(C_i - \overline{C})^2}{n-1}}, \quad (1)$$

where n represents the number of experiments, C_i denotes a measured value of specific heat capacity, and $\bar{C}$ represents the arithmetic average of the measured values of specific heat capacity.

The random error was determined for the averaged values of the molar heat capacity, as outlined in [9]:

$$\overset{\circ}{\Delta} = \frac{\delta \cdot t_p}{\overline{C}} \cdot 100, \quad (2)$$

where, $\overset{\circ}{\Delta}$ - a random error in %, t_p– Student coefficient (for n = 5, t_p= 2.75 at p = 0.95 of the confidence range).

2. Results and discussion

The operation of the device was confirmed by determining of the heat capacity of α-Al_2O_3 (p.a.) (TU 6.09-426-75)). In order to prove measurements of the heat capacity of α-Al_2O_3, we compare our results with new literature data [10] (Table 1).

Table 1

Comparison of the heat capacity of α-Al_2O_3 used to verify a calorimeter operation with the literature data in [10]

T, K	C_p (T), J/(mol·K)		T, K	C_p (T), J/(mol·K)	
	Our data	Data in [10]		Our data	Data in [10]
180	44,50	43,83	400	94,12	95,21
230	64,86	61,18	450	100,26	101,8
250	70,37	67,08	500	105,47	106,1
280	77,07	74,82	550	110,09	109,7
300	76,31	79,41	600	114,29	112,5
350	86,49	88,86	650	118,20	114,9

The data shows that our scientific results of α-Al_2O_3 heat capacity between of 173-673 K satisfactorily conform to results described in [10] within the operating accuracy of IT-C-400 calorimeter. Liquid nitrogen was as a cooling agent in our experiments.

Results of the calorimetric studies are illustrated in Figure and Table 2.

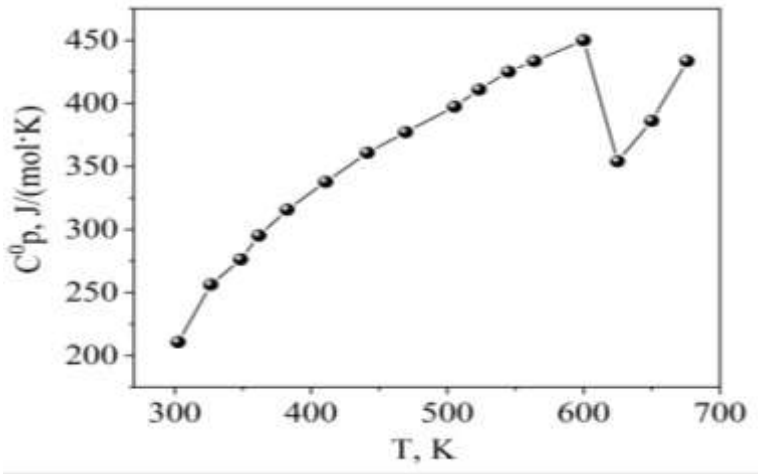

Figure. Diagram of dependence of heat capacity on temperature $LaCaTiMnO_6$

Table 2

Experimental data of the heat capacity of $LaCaTiMnO_6$

T, K	$C_p \pm \overline{\delta}$, J/(g·K)	$C_p \pm \overset{o}{\Delta}$, J/(mol·K)	T, K	$C_p \pm \overline{\delta}$, J/(g·K)	$C_p \pm \overset{o}{\Delta}$, J/(mol·K)
298,15	0,5861 ± 0,0136	221 ± 14	498	1,0018 ± 0,0152	378 ± 16
323	0,7050 ± 0,0188	266 ± 20	523	1,0622 ± 0,0223	401 ± 23
348	0,7805 ± 0,0145	295 ± 15	548	1,0954 ± 0,0211	414 ± 22
373	0,8128 ± 0,0177	307 ± 19	573	1,1096 ± 0,0135	419 ± 14
398	0,8397 ± 0,0149	317 ± 16	598	1,1794 ± 0,0289	446 ± 30
423	0,8835 ± 0,0133	334 ± 14	623	0,9457 ± 0,0190	357 ± 20
448	0,9195 ± 0,0162	347 ± 17	648	1,0880 ± 0,0177	411 ± 19
473	0,9476 ± 0,0216	358 ± 23	673	1,1530 ± 0,0153	436 ± 16

By analyzing the values presented in Figure and Table 2, a distinct and abrupt discontinuity was observed in the temperature-dependent heat capacity of $LaCaTiMnO_6$. The dependence curve, $C_p^0 \sim f(T)$, exhibited a λ-shaped maximum. This remarkable behavior is likely associated with a second-order phase transition occurring at a temperature of 598 K. The transition could be attributed to various factors such as Schottky effects, the Curie and Neel points, alterations in magnetic resistance [12], modifications in electrical conductivity, and changes in dielectric permittivity, and other.

Based on the revealed temperature of the phase transition, the equations of dependencies of $C^0_p \sim f(T)$, [J/(mol·K)] were calculated:

$$C^0_p = (172 \pm 9) + (498.1 \pm 26.4)\ 10^{-3}T - (88.3 \pm 4.7)\ 10^{5}T^{-2}\ (298\text{-}598\ K), \quad (3)$$

$$C^0_p = (2558 \pm 136) - (3532.4 \pm 187.6)\ 10^{-3}T\ (598\text{-}623\ K), \quad (4)$$

$$C^0_p = -(619 \pm 3\ 3) + (1567.0 \pm 83.2)\ 10^{-3}T\ (623\text{-}673\ K). \quad (5)$$

The graph depicted in Figure was generated using the KOMPAS-3D LT program, using experimental data and equations 3-5 as the basis for plotting.

Direct calculation of $S^0(298.15)$ for LaCaTiMnO6 from the experimental data is not feasible with the computational capabilities of the IT-C-400 calorimeter. Therefore, it was estimated using a system of the ionic entropy increments [11]. Then, based on the experimental values on $C^0_p(T)$ and a calculated parameters of $S^0(298.15)$, functions of $S^0(T)$, $H^0(T)-H^0(298.15)$ and $\Phi^{xx}(T)$ were also calculated (Table 3).

Table 3

Thermodynamic parameters of $LaCaTiMnO_6$ in the temperature range of 298.15-675 K

T, K	$C_p°(T) \pm \overset{\circ}{\Delta}$, J/(mol·K)	$S°(T) \pm \overset{\circ}{\Delta}$, J/(mol·K)	$H°(T)-H°(298.15) \pm \overset{\circ}{\Delta}$, J/mol	$\Phi^{xx}(T) \pm \overset{\circ}{\Delta}$, J/(mol·K)
298.15	221 ± 12	206 ± 6	–	206 ± 17
300	224 ± 12	208 ± 17	445 ± 20	206 ± 17
325	251 ± 13	227 ± 19	6380 ± 340	207 ± 17
350	275 ± 15	246 ± 20	12960 ± 700	209 ± 17
375	296 ± 16	266 ± 22	20100 ± 1070	212 ± 18
400	316 ± 17	286 ± 24	27760 ± 1470	216 ± 18
425	335 ± 18	305 ± 25	35910 ± 1910	221 ± 18
450	353 ± 19	325 ± 27	44520 ± 2360	226 ± 19
475	370 ± 20	345 ± 29	53550 ± 2840	232 ± 19
500	386 ± 20	364 ± 30	63000 ± 3340	238 ± 20
525	402 ± 21	383 ± 32	72860 ± 3870	245 ± 20
550	417 ± 22	402 ± 33	83090 ± 4410	251 ± 21
575	432 ± 23	421 ± 35	93710 ± 4980	258 ± 21
600	447 ± 24	440 ± 37	104700 ± 5560	265 ± 22
625	350 ± 19	456 ± 38	114560 ± 6080	273 ± 23
650	400 ± 21	471 ± 39	124060 ± 6590	280 ± 23
675	439 ± 23	487 ± 40	134540 ± 7140	288 ± 24

For comparison with experimental values, the standard heat capacity of LaCaTiMnO6 was also calculated using the Debye method [13]. For this calculation, the Debye characteristic temperatures (Q_D, K) of the constituent elements in the compound and the melting points of the elements in the compound (T_{mp}, K) were utilized. The melting point of $LaCaTiMnO_6$ was determined to be 1273 K. The characteristic temperatures (Q_D) of the elements in $LaCaTiMnO_6$ were computed using the Koref equation [13]:

$$Q'_D = Q_D \cdot \sqrt{T'_{melt.} \div T_{melt.}}, \quad (6)$$

where, $T'_{mp.}$ and $T_{mp.}$ are melting points of the compound and element, respectively. Then the isochoric heat capacities of the elements were calculated using Debye functions. They were summarized together to calculate the isochoric heat capacity of $LaCaTiMnO_6$. Isochoric-isobaric heat capacity transition of $LaCaTiMnO_6$ was made using the Nernst-Lindemann equation:

$$C_p = C_v + 0.0051 \cdot T \cdot C_p^2 / T_{melt}. \quad (7)$$

Based on the above, the following data was used to calculate $C^0_p(298.15)$ of $LaCaTiMnO_6$: $T_{melt.}$, K for La = 1193, Ca — 1112, Ti = 1941, Mn = 1517, O_2 = 54.7; the characteristic temperatures: Q_D, K for La = 135, Ca — 230, Ti = 380, Mn = 303, O_2 = 89 [13]. By equation (9) we calculated Q'_D, K for La = 144.05; Ca — 263.30; Ti = 307.74; Mn = 277.56; O_2 = 429.35. Then, the arguments of the Debye function (Q'_D/T) were calculated using tabular data: (T=298.15) — La = 0.48; Ca — 0.88; Ti = 1.03; Mn = 0.93; and O_2 = 1.44.

The relevant isochoric heat capacities to Q'_D/T on the basis of tabular data are equal to La = 24.64; Ca, 24.02; Ti = 23.76; Mn = 24.02; O_2 = 22.68 J/(mol·K). Then we used the scheme for calculation:

$$C_v\ LaCaTiMnO_6 = C_vLa + C_vCa + C_vTi + C_vMn + 3C_vO_2. \quad (8)$$

We calculated the isochoric heat capacity of $LaCaTiMnO_6$ equal to 164.48 J/(mol·K).

The standard isobaric heat capacity of $C_p^0(298.15)$ of $LaCaTiMnO_6$ equal to 224.9 J/(mol·K) was calculated using the Nernst-Lindemann equation (10). Its value was consistent with the experimental data of 221.0 J/(mol·K) with 1.73 % accuracy.

Based on our developed method [14] and similarly [15], we calculated the standard enthalpy of formation of $LaCaTiMnO_6$ equal to 3867.5 J/(mol·K). The initial data for calculation were applied as described in [13, 16-19].

Conclusions

1. The heat capacity of titanium-manganite of $LaCaTiMnO_6$ was first investigated by the dynamic calorimetry in the interval of 298.15-673 K.

2. Using the experimental data, a fundamental thermochemical constant for the standard heat capacity of $LaCaTiMnO_6$ was determined.

3. The anomalous discontinuity in heat capacity was determined on the dependence curve of $C^o_p \sim f(T)$ at 598 K. This feature is likely attributed to a second-order phase transition. Based on a temperature of the phase transition, the equations of the temperature dependence of the studied titanium-manganite were derived.

4. Using the experimental data obtained for $C^0_p(T)$ and the calculated value of $S^0(298.15)$ with a 25 K step within the temperature range of 298.15 K to 673 K, the temperature dependencies of $C^0_p(T)$, as well as the thermodynamic functions $S^0(T)$, $H^0(T)-H^0(298.15)$, and $\Phi^{xx}(T)$, were calculated for LaCaTiMnO6.

5. The standard heat capacity of $LaCaTiMnO_6$ was calculated by an independent Debye method. It corresponded satisfactorily with the experimental data.

6. According to a method developed by the authors, the standard enthalpy of formation of $LaCaTiMnO_6$ was calculated.

7. The obtained results carry both theoretical and practical significance, enabling the prediction of directed synthesis for similar compounds possessing valuable physical and chemical properties. Furthermore, these results facilitate the analysis of heterogeneous equilibria involving this specific compound and other similar phases. The new thermochemical constants are initial data to load into the fundamental guides and databanks of the thermodynamic constants of substances.

Acknowledgments

This study has been performed within the framework of the program-targeted funding of the scientific and technical program "Development of novel composite materials with high performance properties based on rare and rare-earth elements" of the Industrial Development Committee of the Ministry of Industry and Infrastructure Development of the Republic of Kazakhstan.

References

1 Балакирев В.Ф. Манганиты: Равновесные и нестабильные состояния / В.Ф. Балакирев, В.П. Бархатов, Ю.В. Голиков, С.Г. Майзель. — Екатеринбург: УрО РАН, 2000. — 397 с.

2 Bebenin N.G. Collossal magnetoresistance manganites / N.G. Bebenin, R.I. Zainullina, V.V. Ustinov // Physics — Uspekhi. — 2018. — Vol. 61, No 8. — P. 719-738.

3 Федорова О.М. Влияние кислородной нестехиометрии на фазовое расслоение, структуру и магнитные свойства сложного оксида $NdSr_2Mn_2O_{7\pm\delta}$ / О.М. Федорова, Л.Б. Ведмидь, С.А. Упоров // Перспективные материалы. — 2020. — № 2. — С. 14–21.

4 Mesilov V.V. Soft X-ray absorption spectroscopy of titanium dioxide nanopowders with cobalt impurities / V.V. Mesilov, V.R. Galakhov, N.S. Udintseva, A.Ye. Yermakov, M.A. Uimin, G.S. Zakharova, D.A. Smirnov, A.F. Gubkin, E.A. Sherstobitova // Journal of Experimental and Theoretical Physics. — 2017. — Vol. 124, No 6. — P. 908-913.

5 Селиверстова Е.В. Влияние наночастиц серебра на фотодетектирующие свойства нанокомпозита TiO_2/оксид графена / Е.В. Селиверстова, Н.Х. Ибраев, А.Ж. Жумабеков // Оптика и спектроскопия. — 2020. — Т. 128. — Вып. 9. — С. 1337–1345.

6 Халамейда С.В. Особенности синтеза нанодисперсного титана бария и исследование его свойств / С.В. Халамейда // Химия, физика и технология поверхности. — 2010. — Т. 1. — № 4. — С. 441–449.

7 Касенов Б.К. Способ получения титано-манганитов лантана и щелочноземельных металлов / Б.К. Касенов, Ш.Б. Касенова, Ж.И. Сагинтаева, Б.Т. Ермагамбет, Е.Е. Куанышбеков, М.О. Туртубаева // Патент РК на полезную модель № 7012. Зарегистрирован в Госреестре изобретений РК 15.04.2022 г.

8 Платунов Е.С. Теплофизические измерения и приборы / Е.С. Платунов, С.Е. Буравой, В.В. Курепин, Г.С. Петров. — Л.: Машиностроение, 1986. — 256 с.

9 Техническое описание и инструкции по эксплуатации ИТ-С-400. — Актюбинск, Актюбинский завод «Эталон», 1986. — 48 с.

10 Бодряков В.Ю. Корреляционные характеристики температурного коэффициента объемного расширения и теплоемкости корунда / В.Ю. Бодряков, А.А. Быков // Стекло и керамика. — 2015. — № 2. — С. 30.

11 Кумок В.Н. Проблема согласования методов оценки термодинамических характеристик / В.Н. Кумок // В сб.: Прямые и обратные задачи химической термодинамики. — Новосибирск: Наука, 1987. — С. 108.

12 Резницкий Л.А. Калориметрия твердого тела / Л.А. Резницкий. — М.: Изд-во МГУ, 1981. — 184 с.

13 Морачевский А.С. Термодинамические расчеты в металлургии: справоч. / А.С. Морачевский, И.В. Сладков. — М.: Металлургия, 1985. — 137 с.

14 Касенов Б.К. Двойные и тройные манганиты, ферриты и хромиты щелочных, щелочноземельных и редкоземельных металлов / Б.К. Касенов, Ш.Б. Касенова, Ж.И. Сагинтаева, Б.Т. Ермагамбет, Н.С. Бектурганов, И.М. Оскембеков. — М.: Научный мир, 2017. — 416 с.

15 Kassenov B.K. Calculation of thermodynamic properties of earth metals — copper — zinc (Cu-Zn) / B.K. Kassenov, Sh.B. Kassenova, Zh.I. Sagintaeva, B.T. Ermagambet, E.E. Kuanyshbekov, A.A. Mukhtar // Metallurgija, 2021. — Vol. 60, N 3-4. — P. 454-456.

16 Термические константы веществ: справоч.; под ред. В.П. Глушко. — М.: Наука, 1979. — Вып. IX. — 576 с.

17 Термические константы веществ: справоч.; под ред. В.П. Глушко. — М.: Наука, 1978. — Вып. XII. — Ч. 1. — 536 с.

18 Термические константы веществ: справоч.; под ред. В.П. Глушко. — М.: Наука, 1972. — Вып. VI. — Ч. 1. — 370 с.

19 Термические константы веществ: справоч.; под ред. В.П. Глушко. — М.: Наука, 1974. — Вып. VII. —Ч. 1. — 344 с.

Б.Қ. Қасенов, Ш.Б. Қасенова, Ж.И. Сағынтаева, С.О. Байсанов, Н.Ю. Лу,
Ж.С. Бектұрғанов, А.К. Зейниденов, Е.Е. Қуанышбеков

$LaCaTiMnO_6$ титан манганитінің термодинамикалық қасиеттері

298.15-673 К аралығындағы динамикалық калориметрия әдісімен лантан, титан (II), марганец (III) тотықтары және кальций карбонаты 800-1200°С кезінде қатты фазалық өзара әрекеттесу нәтижесінде алынған $LaCaTiMnO_6$ титан-манганитінің жылу сыйымдылығы зерттелді. Рентгенографиялық әдістермен бұл қосылыс тор параметрлерімен келесідей кубтық сингонияда кристалданатыны анықталды: a = 13,35 ± 0,02 Å; V^0 = 2376,3 ± 5,00 Å^3; Z = 4; $V°_{эл.ұяш}$ = 594,08 ± 1,25 Å^3; $\rho_{рент.}$ = 3,96 г/см^3; $\rho_{пикн.}$ = 3,95 ± 0,02 г/см^3. Көрсетілген температуралық аралықта $C_p°{\sim}f(T)$ тәуелділік қисығында 598 К — де λ-тәрізді әсер айқындалды, бұл II-текті фазалық ауысуға қатысты болуы мүмкін. Осы фазалық ауысу Шоттки эффектілерімен, Кюри, Нель нүктелерінің болуымен, магниттік кедергінің өзгеруімен, электр өткізгіштікпен, диэлектрлік өтімділікпен және т.б. байланысты болуы мүмкін. $LaCaTiMnO_6$ қосылысының 221±14 Дж/(моль·К)-ге тең болатын, іргелілік тұрақтысы — стандартты жылу сыйымдылығы анықталды. Иондық инкременттерінің жуықталған әдісімен оның 206±6 Дж/(моль·К) –ге тең болатын стандартты энтропиясы бағаланды. Фазалық ауысу температурасын ескере және тәжірибелік мәліметтерге сүйене отырып, зетртеліп отырған лантан және кальций титан манганитінің $C_p°{\sim}f(T)$ температураға тәуелділікті сипаттайтын теңдеулері мен қадамы 25 К болатын $S^o(T)$, $H^o(T)$ — $H^O(298.15)$ және $Ф^{xx}(T)$ термодинамикалық функциялар есептелді. $LaCaTiMnO_6$ стандартты жылу сыйымдылығы дебай әдісімен де есептелді, оның мәні тәжірибелік деректермен жақсы үйлеседі. Әзірленген әдістеме бойынша титан-манганиттің стандартты түзілу энтальпиясы есептелді, ол — 3867,5 кДж/моль тең.

Кілт сөздер: титан-манганит, лантан, кальций, жылу сыйымдылығы, фазалық ауысу, түзілу энтальпиясы, термодинамикалық қасиеттері.

Б.К. Касенов, Ш.Б. Касенова, Ж.И. Сагинтаева, С.О. Байсанов, Н.Ю. Лу, Ж.С. Бектурганов,
А.К. Зейниденов, Е.Е. Куанышбеков

Термодинамические свойства титано-манганита $LaCaTiMnO_6$

Методом динамической калориметрии в интервале 298,15–673 К исследована теплоемкость титано-манганита $LaCaTiMnO_6$, полученного твердофазным взаимодействием при 800–1200°С из оксидов лантана, титана (II), марганца (III) и карбоната кальция. Рентгенографическими методами установлено, что данное соединение кристаллизуется в кубической сингонии со следующими параметрами решетки: a = 13,35 ± 0,02 Å; V^0 = 2376,3 ± 5,00 Å^3; Z = 4; $V°_{эл.яч}$ = 594,08 ± 1,25 Å^3; $\rho_{рент.}$ = 3,96 г/см^3; $\rho_{пикн.}$ = 3,95 ± 0,02 г/см^3. На кривой зависимости $C_p°{\sim}f(T)$ в указанном интервале температур обнаружен λ-образный эффект при 598 К, относящийся, вероятно, к фазовому переходу II рода. Данный фазовый переход, возможно, связан с эффектами Шоттки, наличием точек Кюри, Нееля, изменениями магнитного сопротивления, электропроводности, диэлектрической проницаемости и др. Определена фундаментальная константа — стандартная теплоемкость $LaCaTiMnO_6$, равная 221±14 Дж/(моль·К). Приближенным методом ионных инкрементов оценена его стандартная энтропия, равная 206±6 Дж/(моль·К). На основании опытных данных с учетом температуры фазового перехода вычислены уравнения, описывающие температурные зависимости $C_p°{\sim}f(T)$ и шагом через 25 К термодинамические функции $S^o(T)$, $H^o(T)$ — $H^O(298,15)$ и $Ф^{xx}(T)$ исследуемого титано-манганита лантана и кальция. Стандартная теплоемкость $LaCaTiMnO_6$ рассчитана также по методу Дебая, значение которой хорошо согласуется с опытными данными. По разработанной методике вычислена стандартная энтальпия образования титано-манганита, равная 3867,5 кДж/моль.

Ключевые слова: титано-манганит, лантан, кальций, теплоемкость, фазовый переход, энтальпия образования, термодинамические свойства.

References

1 Balakirev, V.F., Barkhatov, V.P., Golikov, Yu.V., & Maisel, S.G. (2000). Manganity: Ravnovesnye i nestabilnye sostoianiia. Ekaterinburg: Uralskoe otdelenie Rossiiskoi akademii nauki, 397 [in Russian].

2 Bebenin, N.G., Zainullina, R.I., & Ustinov, V.V. (2018). Collossal magnetoresistance manganites. *Physics-Uspekhi, Vol. 61,* No 8, pp.719-738. https://doi.org/10.3367/ufne.2017.07.038180.

3 Fedorova, O.M., Vedmid, L.B., & Uporov, S.A. (2020). Vliianie kislorodnoi nestechiometrii na fazovoe rassloenie, strukturu i magnitnye svoistva slozhnogo oksida $NdSr_2Mn_2O_{7 \pm \delta}$. *Perspektivnye materialy — Promising Materials, 2,* 14–21. doi: 10.30791/1028-978x-2020-2-14-21 [in Russian].

4 Mesilov, V.V., Galakhov, V.R., Udintseva, N.S., Yermakov, A.Ye., Uimin, M.A., Zakharova, G.S., Smirnov, D.A., Gubkin, A.F., & Sherstobitova, E.A. (2017). Soft X-ray absorption spectroscopy of titanium dioxide nanopowders with cobalt impurities. *Journal of Experimental and Theoretical Physics, 124,* 6, 908-913. https://doi.org/10.1134/s106377611705003x.

5 Seliverstova, E.V., Ibrayev, N.Kh., & Zhumabekov, A.Zh. (2020). Vliianie nanochastits serebra na fotodetektiruiushchie svoistva nanokompozita TiO_2/oksid grafena [The Effect of Silver Nanoparticles on the Photodetecting Properties of the TiO_2/Graphene Oxide Nanocomposite]. *Optika i spektroskopiia — Optics and spectroscopy, Vol. 128,* 9, 1337-1345. doi:10.1134/s0030400x20090192.

6 Halameyda, S.V. (2010). Osobennosti sinteza nanodispersnogo titana bariia i issledovanie ego svoistv [Features of the synthesis of nanodispersed barium titanium and the study of its properties]. *Khimiia, fizika i tekhnologiia poverkhnosti — Chemistry, physics and technology of the surface, 1,* 4, 441–449 [in Russian].

7 Kasenov, B.K., Kasenova, Sh.B., Sagintaeva, Zh.I., Ermagambet, B.T., Kuanyshbekov, E.E., & Turtubaeva, M.O. (2022). Sposob polucheniia titano-manganitov lantana i shchelochnozemelnykh metallov [Method for producing titanium-manganites of lanthanum and alkaline earth metals]. *Patent RK na poleznuiu model № 7012. Zaregestrirovan v Gosreestre izobretenii RK 15.04.2022 g. — Patent of the Republic of Kazakhstan for Utility Model No. 7012. Registered in the State Register of Inventions of the Republic of Kazakhstan on 15.04.2022* [in Russian].

8 Platunov, E.S., Buravoi, S.E., Kurepin, V.V., & Petrov, G.S. (1986). Teplofizicheskie izmereniia i pribory [Thermophysical measurements and devices]. Leningrad: Mashinostroenie [in Russian].

9 Technicheskoe opisanie i instruktsii po ekspluatatsii IT–S–400 [Technical description and operating instructions IT-S-400] (1986). Aktiubinsk, Aktiubinskii zavod «Etalon», 48 [in Russian].

10 Bodryakov, V.Yu., & Bykov, A.A. (2015). Korelliatsionnye kharakteristiki temperaturnogo koeffitsienta obemnogo rasshireniia i teploemkosti korunda [Correlation Characteristics of the Temperature Coefficient of Volume Expansion and Heat Capacity of Corundum]. *Steklo i keramika — Glass and ceramics, 2,* 30 [in Russian].

11 Kumok, V.N. (1987). Problema soglasovaniia metodov otsenki termodinamicheskikh kharakteristik [The problem of matching methods for evaluating thermodynamic characteristics]. *V sbornike: Priamye i obratnye zadachi khimicheskoi termodinamiki — In the collection: Direct and inverse problems of chemical thermodynamics.* P.. 108. Novosibirsk: Nauka.

12 Reznitsky, L.A. (1981). Kalorimetriia tverdogo tela [Solid body calorimetry]. Moscow: Izdatelstvo Moskovskogo gosudarstvennogo universiteta [in Russian].

13 Morachevsky, A.S., & Sladkov, I.V. (1985). Termodinamicheskie raschety v metallurgii [Thermodynamic calculations in metallurgy]. Moscow: Metallurgiia [in Russian].

14 Kasenov, B.K., Kasenova, Sh.B., Sagintaeva, Zh.I., Ermagambet, B.T., Bekturganov, N.S., & Oskembekov, I.M. (2017). Dvoinye i troinye manganity, ferrity i khromity shchelochnykh, shchelochnozemelnykh i redkozemelnykh metallov [Double and triple manganites, ferrites and chromites of alkaline, alkaline earth and rare earth metals]. Moscow: Nauchnyi mir [in Russian].

15 Kasenov B.K., Kasenova Sh.B., Sagintaeva Zh.I., Ermagambet B.T., Kuanyshbekov E.E., & Mukhtar A.A. (2021). Calculation of thermodynamic properties of earth metals — copper — zinc (Cu-Zn). *Metallurgija, Vol. 60,* 3-4, 454-456.

16 Glushko, V.P. (Ed.). (1979). Termicheskie konstanty veshchestv: spravochnik [Thermal constants of substances: handbook]. Moscow: Nauka, Issue IX, 576 p. [in Russian].

17 Glushko, V.P. (Ed.). (1978). Termicheskie konstanty veshchestv: spravochnik [Thermal constants of substances: handbook]. Moscow: Nauka, Issue XIII, Part 1, 536 p. [in Russian].

18 Glushko, V.P. (Ed.). (1972). Termicheskie konstanty veshchestv: spravochnik [Thermal constants of substances: handbook]. Moscow: Nauka, Issue VI, Part 1, 370 p. [in Russian].

19 Glushko, V.P. (Ed.). (1974). Termicheskie konstanty veshchestv: spravochnik [Thermal constants of substances: handbook]. Moscow: Nauka, Issue VII, Part 1, 344 p. [in Russian].

АВТОРЛАР ТУРАЛЫ МӘЛІМЕТТЕР
СВЕДЕНИЯ ОБ АВТОРАХ
INFORMATION ABOUT AUTHORS

Afroze, Sh. — Postdoc, L.N. Gumilyov Eurasian National University, Astana, Kazakhstan.

Aimukhanov, A.K. — Candidate of Physical and Mathematical Sciences, Associate professor, Professor of the Department of Radiophysics and Electronics, Leading Researcher, Karaganda University of the name of academician E.A. Buketov, Scientific Center for Nanotechnology and Functional Nanomaterials, Karaganda, Kazakhstan; e-mail: a_k_aitbek@mail.ru; ORCID: 0000-0002-4384-5164

Alishin, T.R. — Post-graduate student, School of Advanced manufacturing technology, Tomsk Polytechnic University, Tomsk, Russia; e-mail: tra1@tpu.ru

Amanzholova, G. — Doctoral student, Institute of molecular nanophotonics, Karaganda University of the name of academician E.A. Buketov, Kazakhstan, https://orcid.org/0000-0002-2463-9859

Annie, Ng — PhD holder, Assistant Professor, Nazarbayev University, Astana, Kazakhstan. E-mail: https://orcid.org/0000-0002-5975-2499

Apreleva, A.S. — Post graduate student, Department of low temperature physics and superconductivity, Lomonosov Moscow State University, Russia. E-mail: sasha-apreleva@mail.ru

Apshe, K. — Master of pedagogical psychology, Senior Lecturer of the Department of the Theory and Methodology of foreign language training, Karaganda University of the name of academician E.A. Buketov Karaganda, Kazakhstan. E-mail: gulshira_86kz@mail.ru

Baisanov, S.O. — Doctor of technical sciences, Professor, Director, Zh. Abishev Chemical-Metallurgical Institute, Karaganda, Kazakhstan. E-mail: met.rasplav@mail.ru, ORCID: 0000-0002-7328-2921

Balapanov, M.Kh. — Doctor of physical and mathematical sciences, professor of the Department of General Physics, Ufa University of Science and Technology, Bashkortostan, Russia.

Baptayev, B. — PhD holder, Senior Researcher, National Laboratory of Astana, Astana, Kazakhstan. https://orcid.org/0000-0001-5970-5660

Bayatanova, L.B. — PhD, Senior Lecturer, Department of Physics, Faculty of Basic and Engineering Training, D. Serikbayev East Kazakhstan Technical University, Ust-Kamenogorsk, Kazakhstan. E-mail: leila_1809@mail.ru

Bazarbayeva, T. — PhD holder, Associate Professor, Al-Farabi Kazakh National University, Almaty, Kazakhstan.

Bekmyrza, K.Zh. — Ph.D, Associate Professor of the Department of Technical Physics, L.N. Gumilyov Eurasian National University, Astana, Kazakhstan.

Bekturganov, Z.S. — Doctor of chemical sciences, Professor of the Department of radiophysics and electronics, Karaganda University of the name of academician E.A. Buketov, Karaganda, Kazakhstan. E-mail: zhbekturganov@gmail.com

Berdimuratov, N.E. — Leading researcher of scientific research center “Surface engineering and tribology”, Sarsen Amanzholov East Kazakhstan University, Ust-Kamenogorsk, Kazakhstan; Senior researcher, “PlasmaScience” LLP, Ust-Kamenogorsk, Kazakhstan, e-mail: nurbol.ber@gmail.com

Berkinova, Z. — PhD student, Nazarbayev University. Astana, Kazakhstan. E-mail: zhazira.berkinova@nu.edu.kz, (0000-0001-6032-2851)

Bizhanova, G. — PhD holder, Senior Researcher, National Laboratory of Astana, Nazarbayev University, Astana, Kazakhstan. E-mail: https://orcid.org/0000-0003-0328-6123

Bozada Cengiz — PhD Department of Engineering Physics, Gaziantep University, Gaziantep, Turkey E-mail: b.ankara@yandex.com, ORCID: 0000-0001-5962-860X

Burkov, M.A. (contact person) — 1st year PhD student, Department of engineering thermophysics named after professor Zh.S. Akylbayev, Karaganda University of the name of academician E.A. Buketov, Karaganda, Kazakhstan. Email: maxim19990202@gmail.com.

Deulina, D.E. — student, School of Advanced manufacturing technology, Tomsk Polytechnic University, Tomsk, Russia. E-mail: ded5@tpu.ru; ORCID: 0009-0001-7235-4903

Duisenbayeva, M.S. (contact person) — Master of natural sciences, Department of Engineering Thermophysics named after Professor Zh.S. Akylbayev, Karaganda University of the name of academician E.A. Buketov. E-mail: m_o_l_d_i_r_89@mail.ru

Dvilis, E.S. — Ph.D., Senior researcher, Research Educational Innovation Center "Nanomaterials and Nanotechnologies", School of Advanced manufacturing technology, Tomsk Polytechnic University, Tomsk, Russia; e-mail: dvilis@tpu.ru; ORCID: 0000-0002-6853-6448

Dyusembayeva, A.N. — PhD, Karaganda University of the name of academician E.A. Buketov, Karaganda, Kazakhstan. E-mail:aikabesoba88@mail.ru

Ferraris, J. — PhD holder, Professor, University of Texas at Dallas, Richardson 75080-3021, USA.

Hanlin, Hu. — PhD holder, Associate Professor, Hoffmann Institute of Advanced Materials Postdoctoral Innovation Practice Base Shenzhen, China. E-mail: https://orcid.org/0000-0001-5617-0998

Ibrayev, N. — Doctor of Physics and Mathematical Sciences, Professor, Director of the Institute of Molecular Nanophotonics, Karaganda University of the name of academician E.A. Buketov, Kazakhstan, https://orcid.org/0000-0002-5156-5015

Igamov, B.D. — Professor, Leading Researcher, Scientific and technical center with a design bureau and pilot production of the Academy of Sciences of the Republic of Uzbekistan, Tashkent, Uzbekistan. E-mail: igamov@mail.ru

Ilela, A.E. — Ph.D., Associate professor, School of Advanced manufacturing technology, Tomsk Polytechnic University, Tomsk, Russia; e-mail: 10detahy@tpu.ru; ORCID: 0000-0001-7474-1192

Ilyassov, B.R. — PhD, Associate professor, Head of the Department of Intelligent Systems and Cyber Security, Astana IT University, Kazakhstan; e-mail: baurdinho@mail.ru; ORCID: 0000-0003-4563-2004

Imanova, G.T. — Ph.D. in physics, Associate professor, Leading Researcher, Ministry of Science and Education of the Republic of Azerbaijan, Institute of Radiation Problems, Baku, Azerbaijan. E-mail: gunel_imanova55@mail.ru

Ishembetov, R.Kh. — Candidate of physical and mathematical sciences, docent of the Department of General Physics, Ufa University of Science and Technology, Bashkortostan, Russia.

Ismailov, Zh.T. — Professor, Department of radio physics electronics, Karaganda University of the name of academician E.A. Buketov, Kazakhstan. E-mail: Zhismailov@yandex/kz

Kabyshev, A.M. — Ph.D, Senior Lecturer of the International Department of Nuclear Physics, new materials and technologies, L.N. Gumilyov Eurasian National University, Astana, Kazakhstan.

Kakimzhanov, D.N. — 2nd year doctoral student in Technical Physics, D. Serikbayev East Kazakhstan Technical University, Kazakhstan. E-mail: https://orcid.org/0000-0001-9453-0456

Kasenov, B.K. — Doctor of chemical sciences, professor, head of the laboratory of thermochemical processes, Abishev Chemical-Metallurgical Institute, Karaganda, Kazakhstan. E-mail: kasenov1946@mail.ru, ORCID: 0000-0001-9394-0592

Kasenova, Sh.B. — Doctor of chemical sciences, Professor, Chief researcher of the laboratory of thermochemical processes, Abishev Chemical-Metallurgical Institute, Karaganda, Kazakhstan. E-mail: kasenovashuga@mail.ru, ORCID: 0000-0001-9755-7478

Kamardin, A.I. — Professor, Leading Researcher, Scientific and technical center with a design bureau and pilot production of the Academy of Sciences of the Republic of Uzbekistan, Tashkent, Uzbekistan. E-mail: kamardin89@mail.ru

Khasanov, O.L. — Ph.D., Professor, School of Advanced manufacturing technology, Tomsk Polytechnic University, Tomsk, Russia; e-mail: khasanov@tpu.ru; ORCID: 0000-0003-3746-8259

Kiseleva, T.Yu. — Docent, Department of solid state physics, Lomonosov Moscow State University, Russia. E-mail: Kiseleva.tyu@gmail.com

Kolisnichenko, O.V. — Senior Researcher, D. in Engineering, E.O. Paton Electric Welding Institute of the National Academy of Sciences of Ukraine, Ukraine. E-mail: https://orcid.org/0000-0003-4507-9050

Korsakov, I.E. — Docent, Department of inorganic chemistry, Lomonosov Moscow State University, Russia. E-mail: i.kors@yandex.ru

Kozhanova, R.S. — 3rd year PhD student of Technical Physics, Shakarim University of Semey, researcher of Plasmascience LLP, Ust-Kamenogorsk, Kazakhstan. E-mail: kozhanova.rauan@mail.ru

Kuanyshbekov, E.E. — Master of engineering, leading engineer of the laboratory of thermochemical processes, Abishev Chemical-Metallurgical Institute, Karaganda, Kazakhstan. E-mail: mr.ero1986@mail.ru, ORCID: 0000-0001-9172-9566

Kubenova, M.M. — PhD, Senior Lecturer, Department of Standardization and Certification, L.N. Gumilyov Eurasian National University, Astana, Kazakhstan.

Kulbachinskii, V.A. — Professor, Department of low temperature physics and superconductivity, Lomonosov Moscow State University, Russia. E-mail: kulb@mig.phys.msu.ru

Kupriyanov, E.E. — Post graduate student, Department of low temperature physics and superconductivity, Lomonosov Moscow State University, Russia. E-mail: ee.kupriyanov@physics.msu.ru

Kurbanbekov, Sh.R. — PhD, Associate professor of the Department of Physics, Khoja Ahmed Yasawi International Kazakh-Turkish University, Kazakhstan. E-mail: sherzod.kurbanbekov@ayu.edu.kz

Kuterbekov, K.A. — Doctor of physical and mathematical sciences, professor of the International Department of Nuclear Physics, new materials and technologies, L.N. Gumilyov Eurasian National University, Astana, Kazakhstan.

Kytin, V.G. — Dozent, Department of low temperature physics and superconductivity, Lomonosov Moscow State University, Russia. E-mail: kytin@ mig.phys.msu.ru

Kyzdarbekova, Sh.S. — Senior lecturer, Karaganda University of the name of academician E.A. Buketov, Karaganda, Kazakhstan, e-mail:sholp1@mail.ru

Lu, N.Y. — Candidate of technical sciences, Deputy director for the scientific work, Abishev Chemical-Metallurgical Institute, Karaganda, Kazakhstan. E-mail: hmi_science@mail.ru, ORCID:0000-0002-3624-0984

Magazov, N.M. — 1st year PhD student of Mechanical Engineering in D. Serikbayev East Kazakhstan Technical University, Ust-Kamenogorsk, Kazakhstan. E-mail: magazovn@gmail.com

Mannix, P. Balanay — PhD holder, Associate professor, Nazarbayev University, Astana, Kazakhstan.

https://orcid.org/0000-0003-2479-8582

Mukametkali, T.M. — Master of physics, Doctoral student of the Department of Radiophysics and Electronics, Researcher, Karaganda University of the name of academician E.A. Buketov, Scientific Center of Nanotechnology and Functional Nanomaterials, Karaganda, Kazakhstan; e-mail: tmk625@mail.ru; ORCID:0000-0003-2685-2976

Mukhamedrakhim, A.R. — 2-nd year student, Karaganda University of the name of academician E.A. Buketov, Karaganda, Kazakhstan.

Mukhanova, Zh.A. — Doctoral students, L.N. Gumilyov Eurasian National University, Astana, Kazakhstan.

Muktanova, N. — 2nd year PhD student of Technical Physics in D. Serikbayev East Kazakhstan Technical University, Ust-Kamenogorsk, Kazakhstan. E-mail: nmuktanova@bk.ru

Nogai, A.S. — Doctor of physical and mathematical sciences, Professor, NJSC "S. Seifullin Kazakh Agrotechnical Research University", Faculty of Energy, Astana, Kazakhstan. E-mail:nogay06@mail.ru; https://orcid.org/0000-0003-4235-7246

Nogai, E.A. — Junior Researcher NJSC "S. Seifullin Kazakh Agrotechnical Research University", Faculty of Energy, Astana, Kazakhstan. E-mail: ep-55@mail.ru, https://orcid.org/0000-0002-4900-9482

Nussupbekov, B.R. — Candidate of Technical Sciences, Professor of the Department of Engineering Thermophysics named after Professor Zh.S. Akylbayev, Karaganda University of the name of academician E.A. Buketov. E-mail: bek_nr1963@mail.ru

Palymbetov, R.Sh. — Doctoral students, L.N. Gumilyov Eurasian National University, Astana, Kazakhstan.

Pavlenko, V. – PhD holder, Associate Professor, Al-Farabi Kazakh National University, Almaty, Kazakhstan. E-mail: https://orcid.org/0000-0002-3923-5822

Paygin, V.D. — Ph.D., Scientist, Research Educational Innovation Center "Nanomaterials and Nanotechnologies", School of Advanced manufacturing technology, Tomsk Polytechnic University, Tomsk, Russia. E-mail: vpaygin@mail.ru; ORCID: 0000-0002-8238-4364

Rakhadilov, B.K. — Director of Plasmascience LLP, PhD, Associate Professor, Ust-Kamenogorsk, Kazakhstan. E-mail: rakhadilovb@gmail.com

Rozhkova, X.S. (contact person) — Master of technical science, Lecturer of the Department of Radiophysics and Electronics, Researcher, Karaganda University of the name of academician E.A. Buketov, Scientific Center for Nanotechnology and Functional Nanomaterials, Karaganda, Kazakhstan; e-mail: ksusharogovaya@mail.ru; ORCID: 0000-0003-3048-6171

Sagintaeva, Z.I. — Candidate of chemical sciences, Associate professor, Leading researcher of the laboratory of thermochemical processes. Abishev Chemical-Metallurgical Institute, Karaganda, Kazakhstan. E-mail: kai_sagintaeva@mail.ru, ORCID: 0000-0001-8655-356

Sakenova, R.Ye. — PhD, Head of the Department of Physics and Technology, S. Amanzholova East Kazakhstan Technical University, Ust-Kamenogorsk, Kazakhstan. E-mail: Sakenova_rimma@mail.ru, https://orcid.org/0000-0001-6095-0129

Satbaeva, Z.A. — PhD, Senior Researcher, "PlasmaScience" LLP, Ust-Kamenogorsk, Kazakhstan. E-mail: satbaeva.z@mail.ru

Seitkhanova, A.K. — Associate Professor at the Graduate School of Natural Sciences, PhD, Pavlodar Pedagogical University, Kazakhstan. E-mail: https://orcid.org/0000-0001-8610-5492

Seliverstova, E. — Senior researcher, PhD Physics, Institute of molecular nanophotonics, Karaganda University of the name of academician E.A. Buketov, Kazakhstan, https://orcid.org/0000-0002-9507-8825

Serikova, T. — 3rd year UG student, Nazarbayev University, Astana, Kazakhstan.

Shukalov, E. — Master student, L.N. Gumilyov Eurasian National University, Astana, Kazakhstan.

Stepanova, O.A. — Head of the Department of technical physics and thermal power engineering, D. in Technical Sciences, Shakarim University, Semey, Kazakhstan. E-mail: https://orcid.org/0000-0001-5221-1772

Stepanov, S.A. — Ph.D., Associate professor, School of Advanced manufacturing technology, Tomsk Polytechnic University, Tomsk, Russia; e-mail: stepanovsa@tpu.ru; ORCID: 0000-0002-2692-3722

Suleimenova, D. — PhD Student, L.N. Gumilyov Eurasian National University, Astana, Kazakhstan

Suleimenova, S. — Master of Education, Lecturer, Department of engineering thermophysics named after professor Zh.S. Akylbayev, Karaganda University of the name of academician E.A. Buketov, Karaganda, Kazakhstan.

Syed Fahad Bin Haque — Master holder, PhD candidate, University of Texas at Dallas, Richardson 75080-3021, USA. E-mail: https://orcid.org/0000-0002-7322-430X

Tanasheva, N.K. — PhD, Associate professor, Karaganda University of the name of academician E.A. Buketov, Karaganda, Kazakhstan. E-mail:nazgulya_tans@mail.ru

Tashenov, Ye. — PhD holder, Senior Lecturer, L.N. Gumilyov Eurasian National University. Astana, Kazakhstan. https://orcid.org/0000-0002-9982-4629

Tazhibayeva, T. — PhD holder, Professor, Al-Farabi Kazakh National University, Almaty, Kazakhstan.

Terukov, E. — Doctor of Technical Sciences, Professor, Ioffe Institute, R&D Center of Thin Film Technologies in Energetics, St. Petersburg, Russian Federation, https://orcid.org/0000-0002-4818-4924

Tleubergenova A.Zh. (corresponding author) — PhD 2-nd year doctoral student, Karaganda University of the name of academician E.A. Buketov, Karaganda, Kazakhstan. E-mail: shymkent.a7@mail.ru

Tukesheva A. — Bachelor holder, Research assistant, Institute of Combustion Problems, Almaty, Kazakhstan.

Tussupbaeva, A.S. — Master of Education, Senior lecturer, Department of engineering thermophysics named after professor Zh.S. Akylbayev, Karaganda University of the name of academician E.A. Buketov, Karaganda, Kazakhstan

Tyurin, Yuryi — Senior Researcher, Dr. of Engineering, E.O. Paton Institute of Electric Welding Institute of the National Academy of Sciences of Ukraine, Ukraine.

Uazyrkhanova G.K. — Director of the Department of Research Activities, PhD, Associate Professor of the Department of Physics, Faculty of Basic and Engineering Training, D. Serikbayev East Kazakhstan Technical University, Ust-Kamenogorsk, Kazakhstan. E-mail: guazyrhanova@mail.ru

Uskenbaev, A.D. — Master student, NJSC "S. Seifullin Kazakh Agrotechnical Research University", Faculty of Energy, Astana, Kazakhstan. E-mail: alish_us@mail.ru

Uskenbaev, D.E. — PhD, Associate professor, NJSC "S. Seifullin Kazakh Agrotechnical Research University", Faculty of Energy, Astana, Kazakhstan. E-mail: usdan@mail.ru , https://orcid.org/0000-0001-6265-1376

Valiev, D.T. — Ph.D., Associate professor, School of Advanced manufacturing technology, Tomsk Polytechnic University, Tomsk, Russia; e-mail: rubinf@tpu.ru; ORCID: 0000-0001-6880-7642

Yerbolatova, G.U. — PhD, Associate Professor of the Department of Physics, D. Serikbayev East Kazakhstan Technical University, Ust-Kamenogorsk, Kazakhstan, E-mail: e.gulnara_77@mail.ru, https://orcid.org/0000-0002-5258-4103

Zakharov, A. — Master holder, Research assistant, Institute of Combustion Problems, Almaty, Kazakhstan, E-mail: https://orcid.org/0000-0003-4893-3857

Zakhidov, A. — PhD holder, Professor, University of Texas at Dallas, Richardson 75080-3021, USA.

Zeinidenov, A.K. — PhD, Associate professor, Dean of the Physics and Technology Faculty, Head of Scientific Center for Nanotechnology and Functional Nanomaterials, Karaganda University of the name of academician E.A. Buketov, Karaganda, Kazakhstan; e-mail: asyl-zeinidenov@mail.ru; ORCID: 0000-0001-9780-5072

Zhassulankyzy, A.Zh. — Master student of the 2nd year of study in the specialty "Technical Physics", NPJSC "Shakarim University of Semey", Kazakhstan. E-mail: ainur.99.99.99@mail.ru

Zhurerova, L.G. — PhD, Senior researcher of Scientific Research Center "Surface Engineering and Tribology", S. Amanzholov East Kazakhstan University, Ust-Kamenogorsk, Kazakhstan. E-mail: leila_uka@mail.ru